Investigation of Melt Mixtures and Other Complex Systems

Thesis Submitted for the Degree of

Doctor of Philosophy (Science)

of

Jadavpur University

By

Anuradha Das

Department of Chemical, Biological and Macromolecular Sciences

S. N. Bose National Centre for Basic Sciences

Block – JD, Sector – III, Saltlake, Kolkata-700098

West Bengal, India

May 2015

For my Mother, Father, Sister and Husband

Acknowledgement

I would like to express my earnest thanks and deepest gratitude to my supervisor Prof. Ranjit Biswas for his guidance and immense support. I would especially thank him for giving me the liberty to work independently. Being under his training has been a memorable journey of academic enrichment.

I am thankful to Dr. S. Mahiuddin, NEIST, Jorhat, Assam and Dr. H. Shirota, Chiba University, Japan for their collaborations. My sincere thanks to Prof. M. Maroncelli, Pennsylvania State University, USA for letting us use his spectra analysis softwares. I am thankful to every individual associated with procuring and maintaining the instrumental facility of S. N. Bose National Centre for Basic Sciences (SNBNCBS). I would also like to thank faculty members of the centre who have helped me in learning through questions and discussions.

I am grateful to University Grants Commission, India and SNBNCBS for providing me with the research fellowship.

My days were brightened up by my labmates – Sandipa, Suman, Kallol, Ejaj, Juriti, Kausik, and Atanu to whom I am thankful professionally and personally. I also thank Dr. Tuhin Pradhan, Dr. Hemant Kumar Kashyap, Dr. Harun Al. Rashid Gazi, Dr. Biswajit Guchhait, Dr. Snehasis Daschakraborty and Dr. Tamisra Pal for helping me in my initial days. I am especially thankful to Suman and Kallol for their support.

I also thank Animesh, Nirnay, Sushobhan, Sanchaiyita, Dr. Madhuparna Karmakar and Dr. Rudra Bannerjee who were there to help me whenever required.

I would like to thank Dr. Parijat Das for her caring attitude and cherish the joyous moments spent with little Rwitoban and Arshaman.

I sincerely thank the non-academic members of SNBNCBS for their help in numerous occasions.

I am grateful to my Family-in-Law – Mr. Santanu Bhattacharyya, Mrs. Anasuya Bhattacharyya and Joy for their love, care and immense support. I am also thankful to ‘Vola Kaku’ and ‘Manju Kamma’ for their care and affection. I would like to thank my aunts – Valo Pisi, Mam, Bubu, Chhoto and their families for their endless love and encouragement.

I am thankful to my late. Grandma, Dadavai, Sonama, Boroma, Bapi and Putuma for their love and affection.

I am thankful to my niece (Ankhi) and nephew (Rishi) for giving me wonderful moments to cherish.

I thank Dr. Koushik Das, Dr. Tushar Kanti Das, Dr. Soma Das and Dr. Tamalika Das for being very affectionate and supportive.

I cannot thank enough my husband, Swarnendu Bhattacharyya, who has been a friend and a guide. His support and love are the pillars of my life.

Words will fall short in expressing how much I owe to my parents – Mrs. Ashima Das and Mr. Barun Kumar Das. I am most thankful to them for their love, care, encouragement, patience and blessings.

Abstract

This Thesis is primarily focused on studying structure and dynamics of deep eutectic solvents (DESs) which are fast emerging as important and economically viable alternative media for large-scale use in chemical industry. DESs are multi-component molten mixtures at or near room temperature and made of components with high individual melting points. Extensive intra-species hydrogen-bonding (H-bonding) and entropic gain supports the liquid phase of such multi-component melts. The key question that has been investigated is whether deep depression of freezing points via inter-species H-bonding renders spatio-temporal heterogeneity in such systems. Steady state absorption, fluorescence and time-resolved fluorescence measurements have been performed for a variety of DESs for this purpose. Both ionic and non-ionic DESs have been studied. Effects of solution structure and dynamics on a chemical reaction in such a medium have also been studied.

We have studied presence of spatial heterogeneity in these DESs via following excitation wavelength (λ_{exc}) dependence of emission energy of a dissolved fluorophore. Some systems, particularly those made of amide and electrolyte, have shown strong λ_{exc} dependence, indicating presence of pronounced spatial heterogeneity. Solute-centred relaxation rates, such as solute solvation and rotation rates in these media, have been found to show fractional viscosity dependence. This has been interpreted as due dynamic (temporal) heterogeneity. Interestingly, addition of urea in such DESs have been found to remove signatures of both spatial and temporal heterogeneity. The latter has been termed as urea-induced homogenisation of solution structure and dynamics of these DESs. In addition, how these spatio-temporal heterogeneities are transduced on a simple chemical reaction has also been investigated. Excited state photo induced intramolecular charge transfer reaction has been considered as a model system for this study. Supporting measurements using tera-hertz dielectric relaxation (THz-DR) and Fourier-transformed infra-red (FTIR) spectroscopic techniques have been carried out to better understand H-bonding interactions and subsequent effects on dynamics in these systems.

The Thesis consists of ten chapters, with first chapter presenting a literature survey and a brief-overview of the work carried out. Chapter 2 describes the experimental techniques and

data analysis methods used. Chapter 3 describes the importance of choice of probes for investigating spatio-temporal heterogeneity in DESs made of acetamide and electrolyte. Chapter 4 investigates whether heterogeneity is a generic feature for DESs made via depression of freezing points. Chapter 5 presents spectroscopic results favouring urea-induced 'homogenisation' of structure and dynamics. Chapter 6 correlates reaction timescale with relaxation rates in ionic deep eutectics. Chapter 7 investigates effects of functional groups on solution heterogeneity of ionic deep eutectics. Chapter 8 presents supportive THz and FTIR measurements. Chapter 9 provides results on rate of charge transfer reaction in electrolyte solutions of polar solvents for better explanation of data obtained in ionic DESs. Finally, the Thesis ends outlining very briefly a few interesting problems in Chapter 10 that may be studied in future.

Publications

1. *"Specific Conductivities and Viscosities of $0.1LiNO_3+0.9[xCH_3CONH_2+(1-x)CO(NH_2)_2]$ as Functions of Mole Fraction, x, and Temperature"* by Sanchayita Rajkhowa, **Anuradha Das**, Sekh Mahiuddin and Ranjit Biswas, *Journal of Chemical & Engineering Data*, **2012**, *57*, 3467−3472.

2. *"Fast Fluctuations in Deep Eutectic Melts: Multi-Probe Fluorescence Measurements and All-Atom Molecular Dynamics Simulation Study"* by **Anuradha Das**, Suman Das and Ranjit Biswas, *Chemical Physics Letters*, **2013**, *581*, 47-51.

3. *"Low-Frequency Collective Dynamics in Deep Eutectic Solvents of Acetamide and Electrolytes: A Femtosecond Raman-Induced Kerr Effect Spectroscopic Study"* by Ranjit Biswas, **Anuradha Das**, and Hideaki Shirota, *Journal of Chemical Physics*, **2014**, *141*, 134506 (1-11).

4. *"Density Relaxation and Particle Motion Characteristics in a Non-Ionic Deep Eutectic Solvent, (Acetamide + Urea): Time-Resolved Fluorescence Measurements and All-atom Molecular Dynamics"* by **Anuradha Das**, Suman Das and Ranjit Biswas, *Journal of Chemical Physics*, **2015**, *142*, 034505, 1-9.

5. *"Dielectric Relaxations of (Acetamide + Electrolyte) Deep Eutectic Solvents in the Frequency Window, 0.2 < ν/GHz < 50: Anion and Cation Dependence"* by Kallol Mukherjee, **Anuradha Das**, Samiran Choudhury, Anjan Barman and Ranjit Biswas, *Journal of Physical Chemistry B (Under revision).*

6. *"Urea-Induced 'Homogenization' of Ionic Deep Eutectics: Signatures from Time-Resolved Fluorescence Measurements"* by **Anuradha Das** and Ranjit Biswas (Submitted).

7. *"Dynamic Fluorescence Studies of (Choline chloride+ Urea) Deep Eutectics: Interconnection between Solvent Dynamics and Reaction Kinetics"* by **Anuradha Das** and Ranjit Biswas (Submitted).

8. *"Effects of functional groups of the hydrogen bond donors in choline chloride based DESs – A fluorescence Spectroscopic Outlook"* by **Anuradha Das**, Ejaj Tarif and Ranjit Biswas (Manuscript in preparation).

9. *"Terahertz Dielectric Relaxation and FTIR studies on Deep Eutectic Solvents of Acetamide + Electrolytes: Anion and Cation Identity"* by **Anuradha Das**, Animesh Patra, Rajib Kumar Mitra and Ranjit Biswas (Manuscript in preparation).

10. *"Effects of Mixed Electrolytes on Excited State Intramolecular Charge Transfer Reaction in Common Solvents: Steady State and Time resolved Fluorescence Emission Studies"* by **Anuradha Das** and Ranjit Biswas (Manuscript in preparation).

Contents

Chapter 1

Introduction

Designing solvents for large scale application in chemical industry with minimum ecological footprint yet commercially viable is a non-trivial problem. This is because such an engineering of reaction media not only associates with biasing a chemical reaction toward a desired product but also demands cheap production cost, easy handling and transportation, bio-degradability, stability against moisture, and recyclability. If all or several of these features combine with a facility to prepare such a medium it will by simply mixing two or three components and gentle heating if required, then one is very close to realizing a solvent engineering dream: replacement of conventional organic solvents by a class of 'green' media. Deep eutectic solvents (DESs), which are near-room temperature molten mixtures of two or more high melting solids,[1-8] are examples of one such a class of media. These multi-component melt mixtures are liquids at or near room-temperature due to exhaustive inter-component hydrogen-bonding (H-Bonding). When one of the components is electrolyte, the resulting DES is called ionic DES. Acetamide in combination with electrolytes can constitute examples of such ionic DESs. If all the components are non-electrolyte, then such a molten mixture can be termed as non-ionic DES. Acetamide and urea can form such a DES. As already indicated, interspecies H-bonding leads to depression of freezing points and the subsequent gain in entropy supports the liquid phase at a temperature much lower than the individual melting temperatures. Several of these DESs are characterised by glass transition temperature around ~200K.[9-12]

Typically, amides are one of the main constituents for DESs and the other can be any hydrogen bond donating/accepting group like alcohols/acids/sugars or electrolytes.[1-4,13-17] However, in spite of such flexibility in preparation and scope for application, only a limited range of studies are available that have explored important basic scientific aspects that may have technological relevance. Viscoelastic,[18,19] dielectric,[15-17] nuclear

magnetic resonance[18] and ultrasonic relaxation measurements[15,18] of (alkylamide+electrolyte) systems have indicated presence of microheterogeneity in solution at temperatures above 300K. Fluorescence investigation accompanied by molecular dynamic simulations[20-23] and measurements of collective low frequency dynamics[24] have provided some useful information on the interaction and fast dynamics of some of these DESs. Different interactions such as hydrophobic interactions between the alkyl groups and electrostatic interactions with ions in addition to the H-bond interactions may lead to microscopic phase segregation.[15,25] Rate of a reaction that occurs in such a complex solution environment is expected to be affected by the solution heterogeneity. Also, the time scales of motions of particles in the media can modify the course of a reaction.[26-32] For better and smarter use DESs, therefore, it is important to characterise the medium dynamics and nature of solute –solvent coupling in these media. Time-resolved fluorescence spectroscopy can be a useful experimental method for exploring solution dynamical timescales and environmental effects on them. Steady state spectroscopic method, on the other hand, can provide useful information on interactions. We have extensively utilised these spectroscopic measurements for decoding structural and dynamical information of several deep eutectics. Time-resolved solvation and rotation of a dissolved dipolar solute have been followed to estimate the viscosity coupling to these dynamical quantities. Supportive measurements using terahertz dielectric relaxation spectroscopy (THz-DRS) have been carried out to augment the explanations of fluorescence results. In some representative cases, Fourier-transformed infra red (FTIR) measurements have been carried out to explore the inter-component interactions.

Principle of Solvation Dynamics:

The time dependant response of solvent molecules to a perturbation (generally via irradiating an intense laser pulse on a solute probe dissolved at extremely low concentration) is what is known as "solvation dynamics". If there is a considerable change in dipole moment of the dipolar probe (through charge redistribution in the probe), there will be solvent response to the electronic redistribution of the excited

probe[33] and can supply important information on dynamics and interaction in various media.[34-40] Solvent control on reaction emerges from both interactions and dynamics.

The process of solvation dynamics is pictorially represented in Figure. 1.1. A very dilute solution of a fluorescent probe is prepared in a medium whose dynamics are to be measured. Such low concentration is necessary to avoid solute-solute interactions. Before any laser excitation the system is in equilibrium in reference to solute-solvent interactions. Since the electronic transition in the irradiated solute is instantaneous compared to nuclear motion of the solvent molecules, a non-equilibrium situation appears. Assuming the vibrational cooling is much faster than electronic transition, the emission always occurs from the lowest vibrational state of S_1. Again, the relaxation of the solvent is much faster than the average fluorescence lifetime of the probe, allowing the solvent motions to temporally dictate the fluorescence emission energy. As a result, fluorescence energy emanating from the excited dissolved solute gradually shifts to lower energy with time until the solvent rearrangement is complete.

The relation of solvent and solvation dynamics to reaction rate[26,41-45] is as follows. If the solvation rate is slower compared to the reaction rate, the friction created from the slow solvent motion on the reactive mode will affect the reaction rate. This is known as dynamical solvent effect. Static solvent effect is exerted by the dielectric constant of the solvent (ε_0) that alters the activation barrier of the reaction. Interestingly, the same ε_0 dictates the Stokes shift magnitude, and thus provides an estimate of the solute solvent interactions.[34-36,46-56] Naturally, solvation dynamics bears the impact of several other phenomena, such as, intermolecular H-bonding interactions, solvent confinement, and can provide useful information for catalysis and energy transfer reactions.[33,57-60]

Figure 1.1

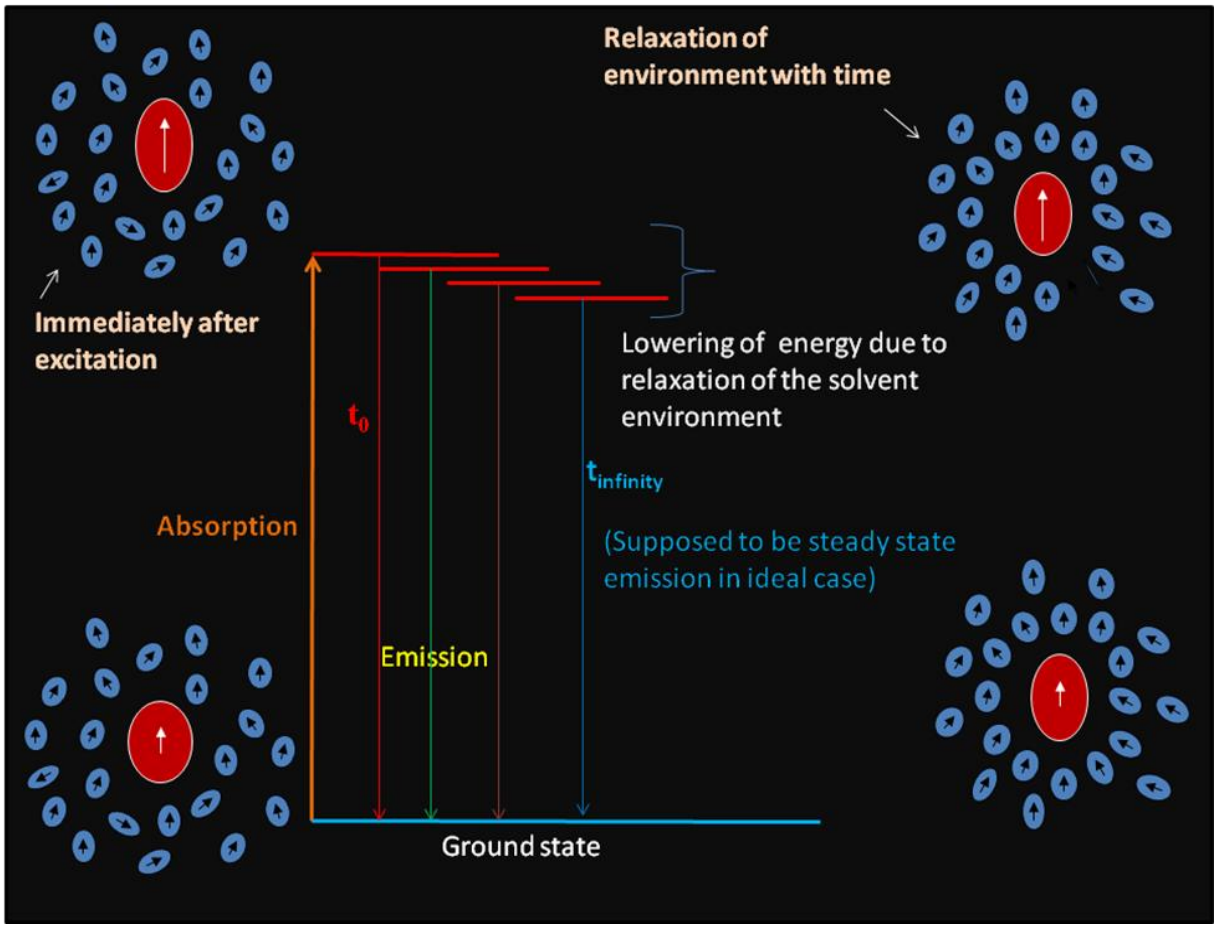

Red large circles: Solute dipole

Blue smaller circles: Solvent dipoles

(This figure is inspired by various sources. Two distinct sources are B. Bagchi, Molecular Relaxation in Liquids, 2012, Oxford University Press and A. Samanta, J. Phys. Chem. Lett., 2010, 1(10), 1557)

Principle of excitation wavelength dependence:

When a dipolar probe is laser-excited, it gains energy and is transferred to the excited state S_1 from the ground state S_0. The well established Kasha's rule then imply that the fluorescence emission should originate from the lowest vibrational level of the first excited singlet (S_1) state irrespective of the excitation energy.[46,61] It has been found that systems like low-temperature liquids, organized assemblies and room temperature ionic liquids show fluorescence emission shifted to longer wavelengths (red shift) with increase in excitation wavelength.[62-65] Figure 1.2 which is a simplified adaptation of ref. 47 describes one such case.

The reason behind such exceptions is as follows.[47] In systems mentioned above, there is a distribution of energetically varying domains, which may be visualized as distribution of inhomogeneous solvation shells. The solute-solvent interaction energies in these domains are unequal and inter-conversions among them are slow. On selective excitation, the population of solute molecules of matching transition energies are excited which undergoes subsequent emission at different wavelengths. Provided a suitable probe is used, signature of this distribution of inhomogeneous solvation environments is reflected in excitation wavelength dependence of fluorescence emission energy. This phenomenon is very useful in studying medium microheterogeneity and is used for studying DESs reported in this thesis.

Figure 1.2

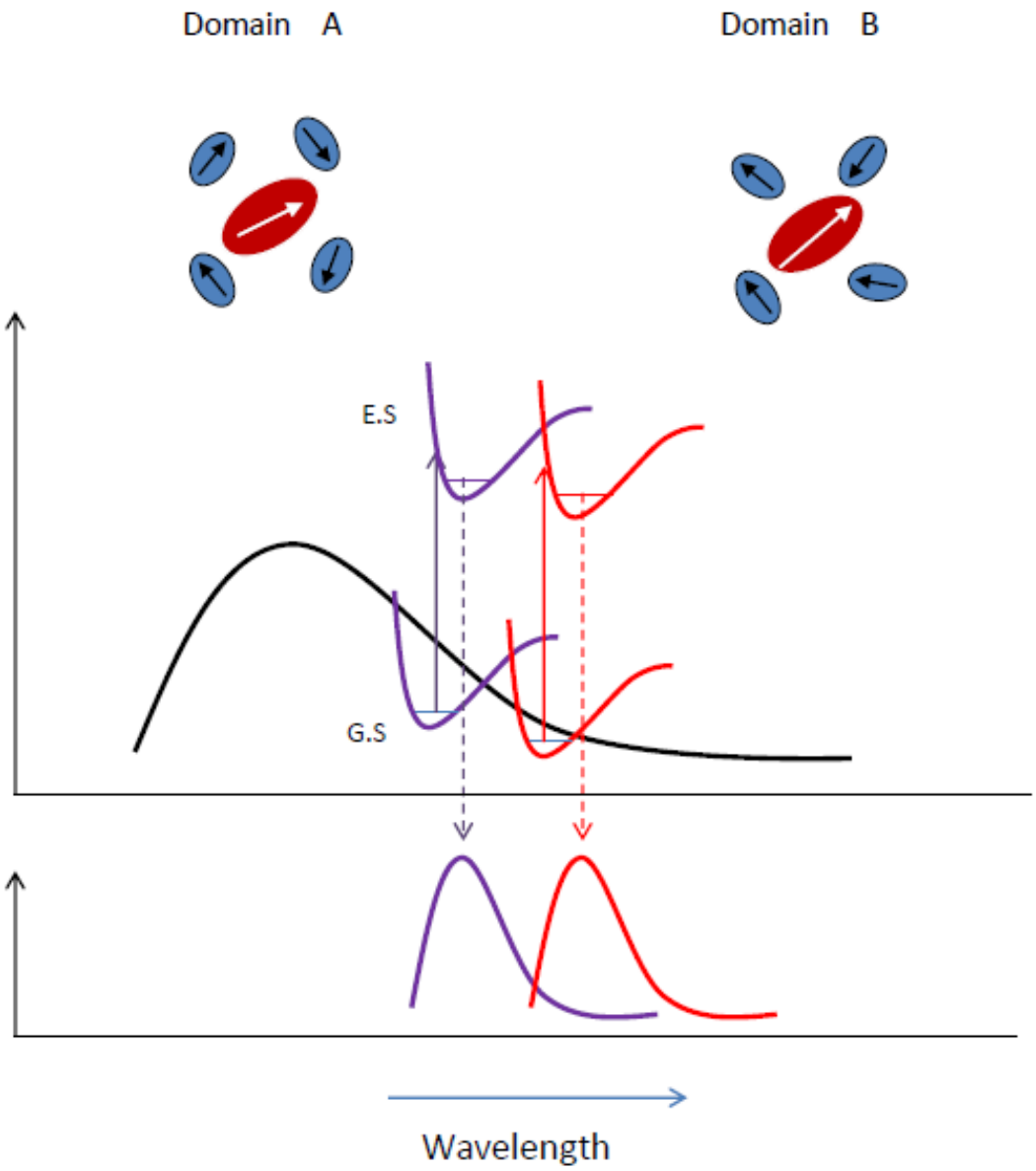

E.S.: Excited State

G.S.: Ground State

Domain A and Domain B are energetically different. Absorption and emission are shown by solid arrows and broken arrows respectively.
Excitation dependant emission envelopes from energetically different domains are shown by violet and red.

Chapter 2 is devoted to the discussion of experimental techniques and methods of data analysis used for the work in this Thesis.

In chapter 3 of this Thesis, degree of temporal heterogeneity in the melt mixture of [0.78CH_3CONH_2 + 0.22{*f*LiBr + (1-*f*) $LiNO_3$}], *f* being Br^- ion concentration, is investigated by a rod like probe molecule p-N,N-dimethylamino-p'-cyanodiphenylacetylene (DTN) of a lifetime of about ~ 0.2-0.5ns[66] and compared with results obtained by using a probe (coumarin 153, abbreviated as C153) having much longer lifetime. Differing extents of excitation wavelength dependent fluorescence emission of chromophores with varying lifetimes suggested distribution of fluctuating timescales for micro-domains in deep eutectic melt. Micro-heterogeneity in solution structure and dynamics is further reflected via more pronounced fractional viscosity dependence of rotation rate for shorter lifetime probe. A probe with much shorter lifetime reports more pronounced fractional viscosity dependence because of stronger coupling between domain fluctuation and solute rotation.[67]

In chapter 4, we have chosen a non-ionic DES made of acetamide (CH_3CONH_2) and urea (NH_2CONH_2). Temperature dependent relaxation dynamics, particle motion characteristics and heterogeneity aspects of deep eutectic solvents have been investigated by employing time-resolved fluorescence measurements. Three different compositions (*f*) for the mixture, [*f* CH_3CONH_2+(1-*f*)NH_2CONH_2], have been studied in a temperature range (328-353 K) which is ~120-145 K above the measured glass transition temperatures (~207 K) of these DESs. Steady state fluorescence emission measurements using probe solutes with sharply different lifetimes do not indicate any dependence on excitation wavelength in these metastable molten systems. Time resolved fluorescence anisotropy measurements reveal near-hydrodynamic coupling between medium viscosity and rotation of a dissolved dipolar solute. Stokes shift

dynamics has been found to be too fast to be detected by the time-resolution (~70 ps) employed, suggesting extremely rapid medium polarization relaxation.[68] Absence of excitation wavelength dependence and fractional viscosity dependence in these DESs suggests that depression of freezing points does not automatically render microheterogeneity (detectable via simple fluorescence technique) in solution structure and dynamics.

Since homogeneity has been identified in non-ionic melt mixtures in presence of urea, we next attempted in Chapter 5 to study whether introduction of electrolyte in addition to acetamide and urea system retains the homogeneity or not. The system of study used was:

0.1$LiNO_3$+0.9[*f* Urea+ (1- *f*) Acetamide] and 0.1LiBr+0.9[*f* Urea+ (1- *f*) Acetamide] Steady state experiments using C153 at all temperatures (303K – 343K) report insensitivity of excitation energy dependence of fluorescence emission. This has not been observed with systems without urea.[20,23] Time resolved studies reveal significant dynamic Stokes' shift[34] with an average solvation time between 120-180ps for $LiNO_3$ and 185-265 ps for LiBr containing systems. Moreover, amount of detected Stokes' shift magnitude is larger in presence of $LiNO_3$ than LiBr. The variation of rotational time with temperature-reduced viscosity shows fraction power dependence as in $\langle \tau_r \rangle \propto \eta^p$ with the power being almost unity, strikingly different from DES sans urea which had p~0.6. The hydrodynamic coupling of the solutes' rotation to the viscosity in these systems also indicates urea-induced homogenisation. Estimated activation energy for solute rotation $E_a(\langle \tau_r \rangle)$ has been found to weakly depend on urea concentration, and follows the activation energy for viscosity ($E_a(\eta)$) of these deep eutectics. Note the homogenisation referred to here is with respect to the excited state lifetime of the solute fluorophore.

Chapter 6 deals with the question whether the homogenisation effect of urea pervades to other DESs as well. Here we chose choline chloride as the second component as choline chloride is also a very potential candidate of industrial application.[7] We have studied a DES made of choline chloride and urea[1] in the mole ratio of 2:1. Two separate fluorescent probes differing in excited state lifetimes have been used for this purpose.

They are coumarin 153 (C153, lifetime ~3-4ns)[34] and trans-2-[4-(dimethylamino)styryl]-benzothiazole (DMASBT) (lifetime ~0.5ns).[69] Spatial heterogeneity aspect of (choline chloride + urea) DES has been investigated by following the excitation wavelength ($\lambda_{exc.}$) dependence of fluorescence emission of these probes. Such a study reveals stronger $\lambda_{exc.}$ dependence for shorter lifetime probe which weakens upon increasing temperature. Time resolved fluorescence emission studies using C153 reveal interesting results. Anisotropy studies give average rotational time ~30 ns at ~300 K and ~2 ns at high temperatures. This result indicates that the probe has been trapped in long lived local structures at regions of high viscosity at lower temperatures.[70,71] Solvation dynamics with C153 produces significant dynamic Stokes' shift with the average solvation time ($< \tau_s >$) varying from 0.15 ns to 1.5 ns. Interestingly, viscosity dependence of $< \tau_r >$ and $< \tau_s >$ indicates fraction power p ~0.8. We have also carried out intramolecular charge transfer reaction of 4-(1-azetidinyl)benzonitrile (P4C) and 4-(1-pyrrolidinyl)benzonitrile (P5C) in these systems to see the effects of these media on reaction rate. Measured average reaction rates for intramolecular charge transfer molecules show a strong dynamic solvent control.

There are various other combinations of choline chloride DESs containing different kinds of hydrogen bond donor (HBD).[2,3,72] In Chapter 7, we have studied the effects of functional groups of hydrogen bond donors on the overall interaction and dynamics on choline chloride DESs. The components other than choline chloride are malonic acid, 3-phenylpropionic acid, ethylene glycol and glycerol.[2,72] Steady state excitation wavelength dependence results (by C153 and DMASBT) at all temperatures (303K – 343K) show varied sensitivity of variation of frequencies and widths for different HBD molecules suggesting different degrees of spatial heterogeneity. Time resolved studies reveal larger dynamic Stokes' shift for –COOH containing HBD than –OH ones. Missing portion of the dynamics also shows interesting change with changing functional groups as well the alkyl chain. Both $< \tau_s >$ and $< \tau_r >$ show fractional viscosity dependence for all the combinations. Activation energies from solute rotation, solvation and viscosity are found to vary with HBDs.

Chapter 8 introduces the use of dielectric spectroscopy in the range of (0.2 THz to 2 THz) for the first time to study the fast processes in the deep eutectic solvent systems of (~0.80acetamide+ ~0.20electrolytes). We have also employed FTIR measurements. The system chosen is (acetamide+electrolyte), which has been previously studied by fluorescence,[20,22,23] Kerr effect spectroscopy,[24] dielectric relaxation[73] and molecular dynamics.[21,74] Different electrolytes used are: lithium nitrate ($LiNO_3$), lithium bromide (LiBr), lithium perchlorate ($LiClO_4$), sodium perchlorate ($NaClO_4$), potassium thiocyante (KSCN) and sodium thiocyanate (NaSCN). 4-Debye process is found to be most suited to fit the real permittivity (ε') and imaginary permittivity (ε'') simultaneously. The different time constants range from 80fs to over 30ps for the systems that are attributed to various origins. There is marked effect of anion and cation identity on these time constants. We have also presented the absorption co-efficient of the acetamide DES for various electrolytes which shows maximum absorption for perchlorate ions. The FTIR spectra clearly show the fingerprints for anions and characteristic –CO and $–NH_2$ bands that undergoes moderate shifts in presence of varying cations and anions.

Reactions initiated by photons are of much interest because of its relevant occurrence in nature and subsequent uses.[27,75-78] Photosynthesis and vision are two such examples that are of utmost importance. This motivated us to study charge transfer reactions that are initiated by light. Two molecules that exhibit such phenomena are P4C and P5C. On photoexcitation, the molecule is first excited to the locally excited (LE) state where charge transfer occurs from the amino group to benzonitrile creating the charge transferred (CT) state. CT state being of polar nature, is stabilized by more polar solvent through dipole –dipole interaction. Concurrent twisting of the bond connecting the amino group and the benzene ring during the charge transfer is the central idea of twisted intramolecular charge transfer (TICT) model.[27,79-82] Evidences of TICT come from the dependence of the reaction on viscosity of the environment from the alteration of the rate of LE to CT transformation.[83,84] The rate of the reaction ($LE \rightarrow CT$) is modified by the dynamical modes as the reaction is influenced by orientational polarisation relaxation. Addition of electrolytes to a solvent can alter the polarity significantly and cause substantial difference in the rate of a reaction.[82,85] In Chapter 9,

we have extended our study of charge transfer reactions in solvents by adding electrolytes to see its effect on the rate. The system used is [xLiClO$_4$+ (0.5-x)NaClO$_4$] in ethyl acetate and acetonitrile. An improvisation in this study is made through choosing mixed electrolytes to see whether the effect of one electrolyte is controlled by the second electrolyte. This idea is guided by the role of Na+/K+ balance in ion channels in biological systems.[86,87]

Chapter 10 which is the final chapter for the present Thesis, enlists several interesting problems that may be studied in future.

References

1. Abbott, A. P.; Capper, G.; Davies, D. L.; Rasheed, R. K.; Tambyrajah, V. *Chem. Commun.* **2003**, 70.

2. Abbott, A. P.; Boothby, D.; Capper, G.; Davies, D. L.; Rasheed, R. K. *J. Am. Chem. Soc.* **2004**, *126*, 9142.

3. Abbott, A. P.; Harris, R. C.; Ryder, K. S.; D'Agostino, C.; Gladden, L. F.; Mantle, M. D. *Green Chem* **2011**, *13*, 82.

4. Smith, E. L.; Abbott, A. P.; Ryder, K. S. *Chem Rev* **2014**, *114*, 11060.

5. Francisco, M.; van den Bruinhorst, A.; Kroon, M. C. *Green Chem.* **2012**, *14*, 2153.

6. Carriazo, D.; Serrano, M. C.; Gutierrez, M. C.; Ferrer, M. L.; del Monte, F. *Chem Soc Rev* **2012**, *41*, 4996.

7. Francisco, M.; Van den Bruinhorst, A.; Kroon, M. C. *Angew. Chem., Int. Ed.* **2013**, *52*, 3074.

8. Francisco, M.; Gonzalez, A. S. B.; de Dios, S. L. G.; Weggemans, W.; Kroon, M. C. *Rsc. Adv.* **2013**, *3*, 23553.

9. McManis, G. E.; Fletcher, A. N.; Bliss, D. E.; Miles, M. H. *J. Electroanal. Chem.* **1985**, *190*, 171.

10. Kalita, G.; Rohman, N.; Mahiuddin, S. *J. Chem. Eng. Data.* **1998**, *43*, 148.

11. Kalita, G.; Sarma, R. G.; Mahiuddin, S. *J. Chem. Eng. Data.* **1999**, *44*, 222.

12. Mahiuddin, S. *J. Chem. Eng. Data.* **1996**, *41*, 231.

13. Vitali, G.; Berchiesi, G.; Barocci, S. *Thermochim. Acta* **1989**, *143*, 205.

14. Berchiesi, G.; Vitali, G.; Plowiec, R.; Barocci, S. *J. Chem. Soc. Faraday Trans. 2* **1989**, *85*, 635.

15. Berchiesi, G.; Deangelis, M.; Rafaiani, G.; Vitali, G. *J. Mol. Liq.* **1992**, *51*, 11.

16. Berchiesi, G. *J. Mol. Liq.* **1999**, *83*, 271.

17. Amico, A.; Berchiesi, G.; Cametti, C.; Di Biasio, A. *J. Chem. Soc. Faraday Trans. 2* **1987**, *83*, 619.

18. Berchiesi, G.; Rafaiani, G.; Vitali, G.; Farhat, F. *J. Therm. Anal.* **1995**, *44*, 1313.

19. Berchiesi, G.; Vitali, G.; Passamonti, P.; Plowiec, R. *J. Chem. Soc., Faraday Trans 2* **1983**, *79*, 1257.

20. Guchhait, B.; Gazi, H. A. R; Kashyap, H. K.; Biswas, R. *J. Phys. Chem. B* **2010**, *114*, 5066.

21. Pal, T.; Biswas, R. *Chem. Phys. Lett.* **2011**, *517*, 180.

22. Guchhait, B.; Das, S.; Daschakraborty, S.; Biswas, R. *J. Chem. Phys.* **2014**, *140*, 104514.

23. Guchhait, B.; Daschakraborty, S.; Biswas, R. *J. Chem. Phys.* **2012**, *136*, 174503.

24. Biswas, R.; Das, A.; Shirota, H. *J. Chem. Phys.* **2014**, *141*, 134506.

25. Castellani, F.; Berchiesi, G.; Pucciarelli, F.; Bartocci, V. *J. Chem. Eng. Data.* **1981**, *26*, 150.

26. Van der zwan, G.; Hynes, J. T. *Chem. Phys.* **1991**, *152*, 169.

27. Dahl, K.; Biswas, R.; Ito, N.; Maroncelli, M. *J. Phys. Chem. B* **2005**, *109*, 1563.

28. Angell, C. A. *J. Chem. Phys.* **1967**, *46*, 4673.

29. Moynihan, C. T. *J. Phys. Chem.* **1966**, *70*, 3399.

30. Chakrabarti, D.; Bagchi, B. *Phys. Rev. Lett.* **2006**, *96*, 187801.

31. Sillescu, H. *J. Non-Cryst. Solids* **1999**, *243*, 81.

32. Ediger, M. D. *Annu. Rev. Phys. Chem.* **2000**, *51*, 99.

33. Lakowicz, J. R. *Principle of Fluorescence Spectroscopy*; Kluwer Academic Pub: New York, 1999; Vol. 2nd Ed.

34. Horng, M. L.; Gardecki, J. A.; Papazyan, A.; Maroncelli, M. *J. Phys. Chem.* **1995**, *99*, 17311.

35. Jimenez, R.; Fleming, G. R.; Kumar, P. V.; Maroncelli, M. *Nature* **1994**, *369*, 471.

36. Bhattacharyya, K. *Acc. Chem. Res.* **2003**, *36*, 95.

37. Thompson, W. H. *Annu. Rev. Phys. Chem.* **2011**, *62*, 599.

38. de Boeij, W. P.; Pshenichnikov, M. S.; Wiersma, D. A. *Annu. Rev. Phys. Chem.* **1998**, *49*, 99.

39. Fayer, M. D. *Acc. Chem. Res.* **2012**, *45*, 3.

40. Shirota, H.; Funston, A. M.; Wishart, J. F.; Castner, E. W. *J. Chem. Phys.* **2005**, *122*, 184512.

41. Maroncelli, M.; Macinnis, J.; Fleming, G. R. *Science* **1989**, *243*, 1674.

42. Liu, M.; Ito, N.; Maroncelli, M.; Waldeck, D. H.; Oliver, A. M.; Paddon-Row, M. N. *J. Am. Chem. Soc.* **2005**, *127*, 17867.

43. Moog, R. S.; Maroncelli, M. *J. Phys. Chem.* **1991**, *95*, 10359.

44. Horng, M. L.; Dahl, K.; Jones, G.; Maroncelli, M. *Chem. Phys. Lett.* **1999**, *315*, 363.

45. Hynes, J. T., Simon, J. D. *Charge -Transfer Reactions and Solvation Dynamics in Ultrafast Dynamics of Chemical Systems*; Kluwer: Dodrecht, **1994**.

46. Samanta, A. *J. Phys. Chem. B* **2006**, *110*, 13704.

47. Karmakar, R.; Samanta, A. *J. Phys. Chem. A* **2002**, *106*, 4447.

48. Karmakar, R.; Samanta, A. *J. Phys. Chem. A* **2003**, *107*, 7340.

49. Sarkar, N.; Das, K.; Datta, A.; Das, S.; Bhattacharyya, K. *J. Phys. Chem.* **1996**, *100*, 10523.

50. Sarkar, N.; Datta, A.; Das, S.; Bhattacharyya, K. *J. Phys. Chem.* **1996**, *100*, 15483.

51. Shirota, H.; Segawa, H. *J. Phys. Chem. A* **2003**, *107*, 3719.

52. Tamoto, Y.; Segawa, H.; Shirota, H. *Langmuir* **2005**, *21*, 3757.

53. Jin, H.; Baker, G. A.; Arzhantsev, S.; Dong, J.; Maroncelli, M. *J. Phys. Chem. B* **2007**, *111*, 7291.

54. Mandal, P. K.; Sarkar, M.; Samanta, A. *J. Phys. Chem. A* **2004**, *108*, 9048.

55. Halder, M.; Headley, L. S.; Mukherjee, P.; Song, X.; Petrich, J. W. *J. Phys. Chem. A* **2006**, *110*, 8623.

56. Burai, T. N.; Datta, A. *J. Phys. Chem. B* **2009**, *113*, 15901.

57. Horng, M. L.; Gardecki, J. A.; Maroncelli, M. *J. Phys. Chem. A* **1997**, *101*, 1030.

58. Dutt, G. B. *Chemphyschem* **2005**, *6*, 413.

59. Lee, H.; Lee, G.; Jeon, J.; Cho, M. *J. Phys. Chem. A* **2012**, *116*, 347.

60. Aziz, E. F.; Rittmann-Frank, M. H.; Lange, K. M.; Bonhommeau, S.; Chergui, M. *Nat Chem* **2010**, *2*, 853.

61. Birks, J. B. *Photophysics of Aromatic Molecules;*; Wiley-Interscience: : London, **1970**.

62. Demchenko, A. P. *Luminescence* **2002**, *17*, 19.

63. Lakowicz, J. R.; Keating-Nakamoto, S. *Biochemistry-Us* **1984**, *23*, 3013.

64. Itoh, K.; Azumi, T. *J. Chem. Phys.* **1975**, *62*, 3431.

65. Chattopadhyay, A.; Mukherjee, S. *Biochemistry-Us* **1993**, *32*, 3804.

66. Hirata, Y.; Kanemoto, Y.; Okada, T.; Nomoto, T. *J. Mol. Liq.* **1995**, *65*, 421.

67. Das, A.; Das, S.; Biswas, R. *Chem. Phys. Lett.* **2013**, *581*, 47.

68. Das, A.; Das, S.; Biswas, R. *J. Chem. Phys.* **2015**, *142*, 034505.

69. Maroncelli, M. *Private communication.*

70. Perkins, S. L.; Painter, P.; Colina, C. M. *J. Chem. Eng. Data.* **2014**, *59*, 3652.

71. D'Agostino, C.; Harris, R. C.; Abbott, A. P.; Gladden, L. F.; Mantle, M. D. *Phys. Chem. Chem. Phys.* **2011**, *13*, 21383.

72. Perkins, S. L.; Painter, P.; Colina, C. M. *J. Phys. Chem. B* **2013**, *117*, 10250.

73. Mukherjee, K.; Das, A.; Choudhury, S; Barman, A; Biswas, R. *J. Phys. Chem. B* **2015**, *xxxx*, xxxx.

74. Das, S.; Biswas, R.; Mukherjee, B. *J. Phys. Chem. B* **2015**, *119*, 274.

75. Grabowski, Z. R.; Rotkiewicz, K.; Rettig, W. *Chem. Rev.* **2003**, *103*, 3899.

76. Lippert, E.; Rettig, W.; Bonacickoutecky, V.; Heisel, F.; Miehe, J. A. *Adv. Chem. Phys.* **1987**, *68*, 1.

77. Techert, S.; Zachariasse, K. A. *J. Am. Chem. Soc.* **2004**, *126*, 5593.

78. Zachariasse, K. A.; Druzhinin, S. I.; Bosch, W.; Machinek, R. *J. Am. Chem. Soc.* **2004**, *126*, 1705.

79. Pradhan, T.; Gazi, H. A. R; Biswas, R. *J. Chem. Phys.* **2009**, *131*, 054507.

80. Pradhan, T.; Gazi, H. A. R.; Biswas, R. *The Journal of Chemical Physics* **2009**, *131*, 054507.

81. Pradhan, T.; Ghoshal, P.; Biswas, R. *J. Phys. Chem. A* **2008**, *112*, 915.

82. Pradhan, T.; Biswas, R. *J. Phys. Chem. A* **2007**, *111*, 11524.

83. Rettig, W. *J. Luminesc.* **1980**, *26*, 21.

84. Rettig, W. *J. Phys. Chem.* **1982**, *86*, 1970.

85. Pradhan, T.; Biswas, R. *J. Phys. Chem. A* **2007**, *111*, 11514.

86. French, R. J.; Wells, J. B. *The Journal of General Physiology* **1977**, *70*, 707.

87. Korn, S.; Ikeda *Science* **1995**, *269*, 410.

Chapter 2

Experimental Techniques and Data Analysis Methods

2.1. Experimental Techniques

Absorbance, Steady State and Time Resolved Fluorescence are the most frequently used techniques to investigate physical problems in this thesis.

2.1.1. Absorption Data collection: We have used UV-2450 (Shimadzu) for our experimental data collection. Figure 2.1 is a basic schematic representation of absorption spectrophotometer. Tungsten and Deuterium are used as lamp source for visible and ultra-violet region respectively. The emitted light focussed by a mirror, passes through a filter reaching the monochromator. The diffraction grating in a monochromator is used to select a specific wavelength from the collected light. The light is then split into two beams before it reaches the sample. One beam is used as the reference and the other beam passes through the sample. The transmitted light from the sample and reference cells reach the detector (photodiode). After signal enhancement, the light reaches the data processor where analog to digital converter is used to convert the signal. Finally, after the processing of the signal we get the absorbance spectra.

Absorbance is dependent on the path length of the sample, l, concentration of the sample, c, and the extinction co-efficient of the sample, ε (constant for each species at particular wavelength) according to Beer-Lambert Law : $A = \log_{10}(I_0 / I) = \varepsilon.c.l$.

I_0 = Intensity of incident light at a given wavelength

I = Intensity of transmitted light

For our measurement, $l = 1cm$ and $c \approx 10^{-5} M$.

Figure 2.1

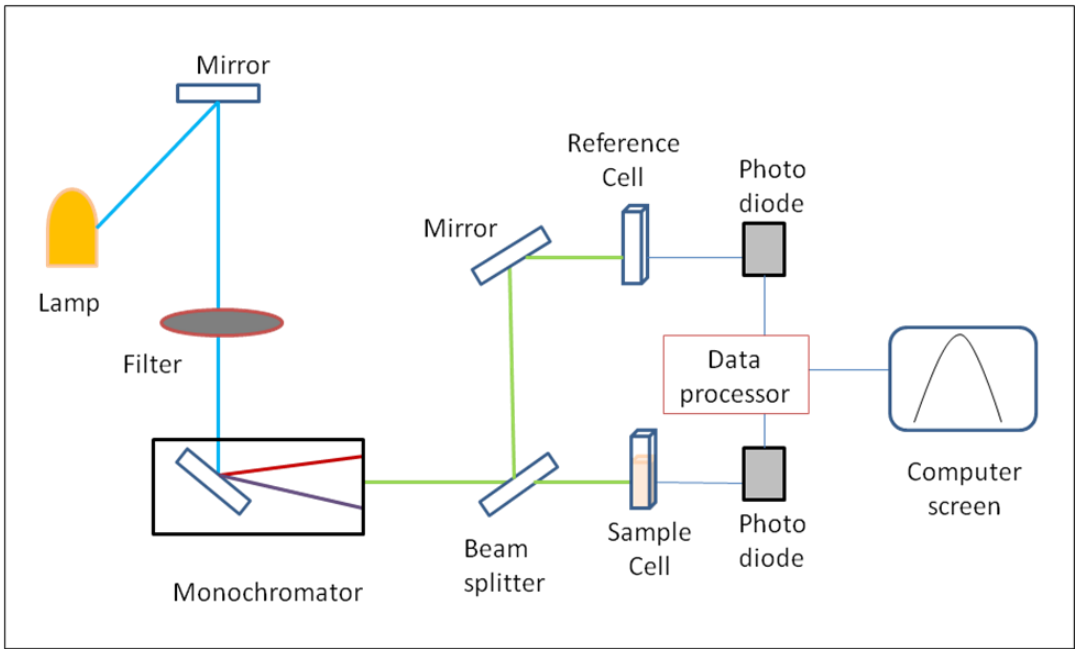

Figure 2.1: Schematic diagram of an absorption spectrophotometer.

2.1.2. Fluorescence Data collection: Fluorescence is classified in two categories – Steady State fluorescence and Time Resolved fluorescence. In steady state fluorescence measurements, the sample is illuminated with a continuous source of light and the emission intensity spectrum is recorded whereas in time resolved measurements, the emission decay is recorded. For the time resolved measurements the pulse width is of a shorter lifetime than the decay lifetime of the sample[1-3].

We have used Fluoromax-3 (Jobin-Yvon, Horiba) for our steady state fluorescence measurements. The source is generally a Xenon lamp. The monochromators are equipped with gratings that decrease the stray light and select specific wavelength. Shutter and polariser is provided in the path of the light after the excitation and emission monochromaor. The optical paths of the excitation and the emission light paths are along the orthogonal axis to ensure minimal leakage of excitation light into the detection side[3].

A basic schematic diagram of fluorimeter is shown in Figure 2.2.

Figure 2.2

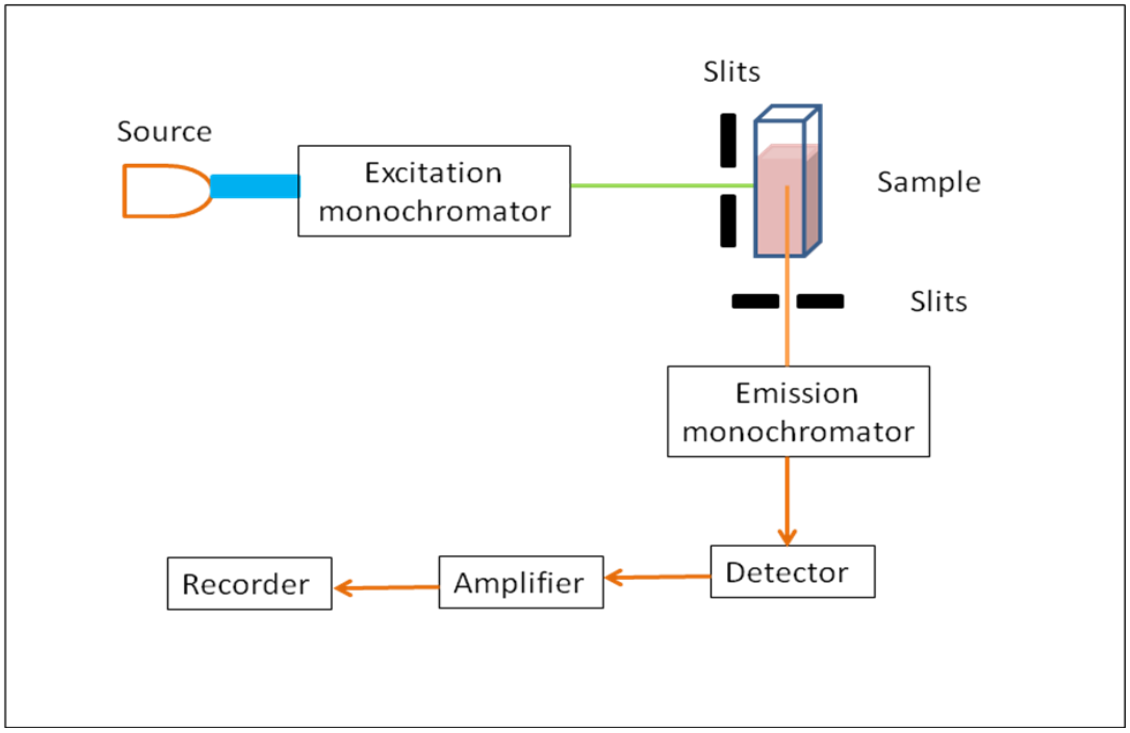

Figure 2.2: Schematic diagram of a steady state fluorescence spectrophotometer.

For time resolved fluorescence measurements, Time Correlated Single Photon Counting (TCSPC) technique has been used. This chapter describes TCSPC technique along with the data analysis methods for solvation, rotation and charge transfer dynamics.

2.1.3. TCSPC Technique: The TCSPC technique is much more complex than other two techniques described above. Here each single photon emitted by fluorophore is detected after the excitation with a short pulse laser light.[1,2] The principle of TCSPC relies on the concept that the probability distribution for emission of single photon from a fluorophore molecule following its excitation is identical to the time-dependent fluorescence intensity change of all photons emitted by the fluorophore molecules

after excitation. Figure 2.3 shows a schematic block diagram of a typical TCSPC system. We have used the TCSPC set up from Edinburgh (U.K.) for fluorescence decay measurements. An excitation pulse excites the sample placed in the sample chamber and creates a start signal. The signal is then passes through Constant Fraction Discriminator (CFD), which accurately measures the arrival time of laser pulse.

Figure 2.3

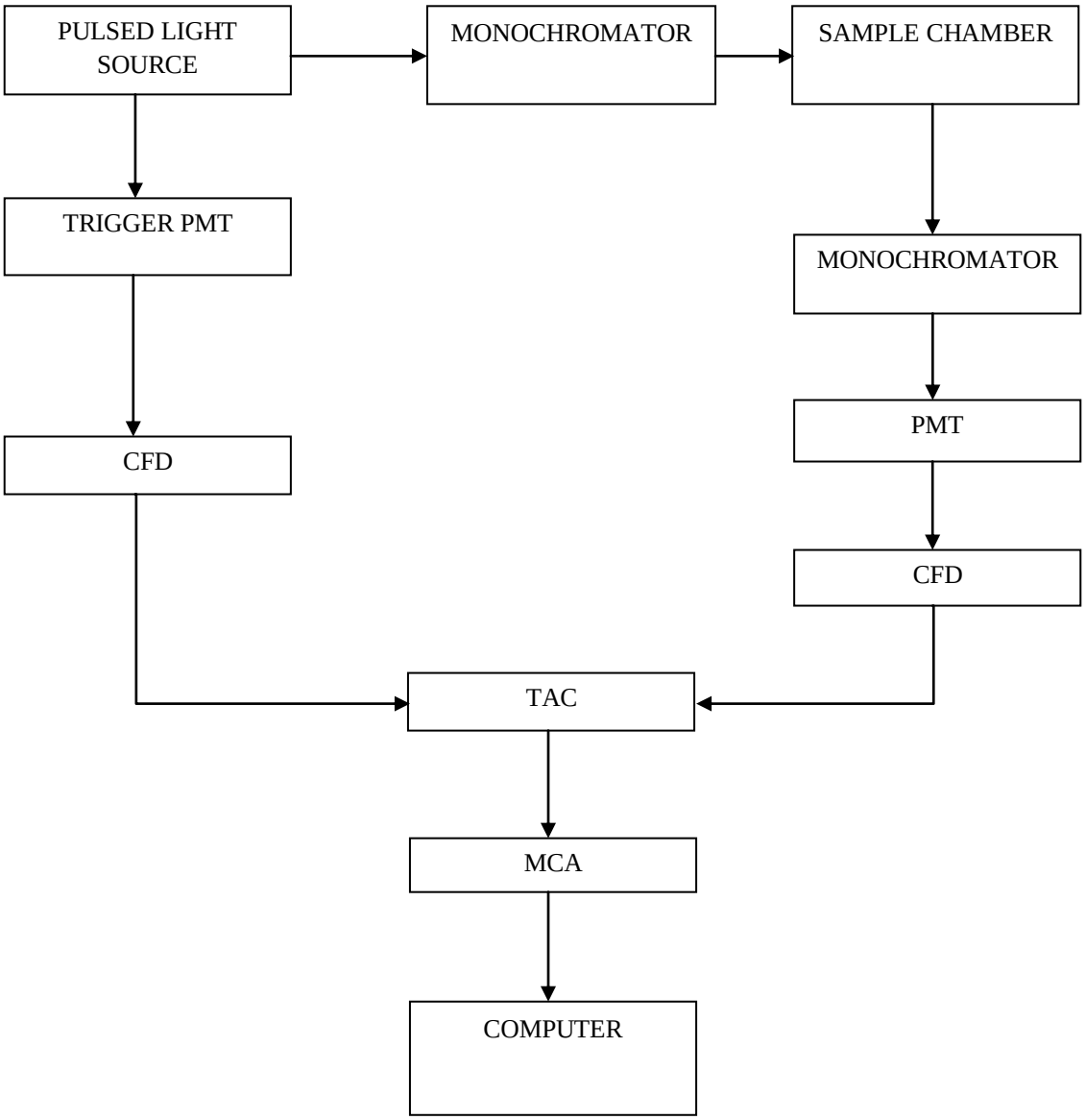

Figure 2.3: Schematic diagram for a time correlated single photon counting system. This figure is taken from the thesis of Dr. Guchhait (Spectroscopic studies of molten electrolyte mixtures, binary polar solvent mixtures and solvents under confinement.)

Subsequently, the signal is passed to Time-to-Amplitude Converter (TAC), which triggers the voltage ramp, i.e. voltage increases linearly with time. The voltage ramp is stopped when the first photon emitted by the sample fluorophore is detected. An output pulse from the TAC is proportional to the time delay (Δt) between the excitation and emission signals. This output pulse then passes through the Multichannel Analyzer (MCA) where Analog-to-Digital Converter (ADC) generates the numerical transformation. On repeating this process for numerous times, a histogram of the decay which is the photon count versus time channel is built in MCA.[3]

2.2. Data Analysis

2.2.1. Solvation Dynamics

Steady state absorption and fluorescence spectra were collected by using respectively a UV-visible spectrophotometer (UV-2450, Shimadzu) and Fluorimeter (Fluoromax-3, Jobin-Yvon, Horiba) and solvent blanks were subtracted to start with the analysis.

To study the solvation dynamics, a series of 18-20 magic angle (54.7^0) decays are collected at equally spaced wavelengths across the steady-state emission spectrum of solute (fluorophore) dissolved in medium.[4] We have used Coumarin 153 (C153) as the fluorophore in our measurements. So, 409 nm dye laser was used as light source and the full width at half maximum (FWHM) of instrument response function (IRF) was ~ 70 ps. The fluorescence transients were typically characterised by only decay in blue end and a rise followed by decay in the red end. The fluorescence decay [$N(t)$] collected from the instrument is a convolution of IRF [$R(t)$] and sample response [$I(t)$]. To extract $I(t)$ from the measured $N(t)$ and $R(t)$ data, the iterative reconvolution method[5] using a nonlinear least square analysis is used. A sum of exponential, $I(t) = \sum_{i=1}^{N} \alpha_i \exp(-t/\tau_i)$, (where α_i and τ_i are the amplitudes or the pre-exponential factors and characteristic life times respectively) is usually required to fit the TCSPC decays.

On fitting the decays at various wavelengths (λ_j), we get the amplitudes [$\alpha_i(\lambda_j)$] and lifetimes [$\tau_i(\lambda_j)$], with $\sum_i \alpha_i(\lambda_j) = 1$ according to the multi-exponential function,

$$I(\lambda_j, t) = \sum_{i=1}^{N} \alpha_i(\lambda_j) \exp(-t/\tau_i(\lambda_j)) \tag{2.1}$$

To construct the Time Resolved Emission Spectra (TRES) the conventional literature method have been adopted.[3-5]

A new set of normalized intensity decays are computed so that the time integrated intensity at each wavelength is equal to the steady state intensity at that wavelength ($F(\lambda_j)$). The normalization factor is

$$H(\lambda_j) = \frac{F(\lambda_j)}{\int_0^\infty I(\lambda_j, t)dt} = \frac{F(\lambda_j)}{\sum_i \alpha_i(\lambda_j)\tau_i(\lambda_j)} \tag{2.2}$$

The appropriate normalized intensity decay function is obtained by,

$$I'(\lambda_j, t) = H(\lambda_j) I(\lambda_j, t) = \sum_{i=1}^{N} \alpha_i'(\lambda_j) \exp(-t/\tau_i(\lambda_j)), \tag{2.3}$$

where $\alpha_i'(\lambda_j) = H(\lambda_j)\alpha_i(\lambda_j)$. The values of $I'(\lambda_j, t)$ are used to calculate the intensity at any wavelength and time, and thus the time resolved emission spectra (TRES) are obtained. The TRES are then converted to frequency representation for further analysis.[4] Each time resolved emission spectrum is fitted with log normal line shape function for continuous representation of spectrum. The time dependent emission peak frequencies are extracted from the fitted spectra, and are used to construct the normalized solvation response function [$S(t)$],

$$S(t) = \{\nu(t) - \nu(\infty)\} / \{\nu(0) - \nu(\infty)\}, \tag{2.4}$$

Where $\nu(0)$, $\nu(t)$ and $\nu(\infty)$ denote some measure (usually peak) of frequency for the reconstructed emission spectrum at $t = 0$ (that is, immediately after excitation), at any

given instant (t), and at a time sufficiently long ($t=\infty$) respectively to allow for complete solvent relaxation. $S(t)$ is a normalized function decaying from unity to zero as the environment rearranges with time in response to the instantaneous alteration of the equilibrium charge distribution of the solute via laser excitation. The emission frequency (ν_{fl}) of the steady state emission spectrum of the solute probe should ideally be equal to $\nu(\infty)$ for a given system. However, when the solvent reorganisation is not complete within the excited state lifetime of the probe, the ν_{fl} is blue shifted from $\nu(\infty)$. Integration of the multi-exponential fits to the measured $S(t)$ decay yields average solvation time ($<\tau_s>$) as follows:

$$\langle \tau_s \rangle = \int_0^\infty dt S(t) = \int_0^\infty dt[\textstyle\sum_i a_i \exp(-t/\tau_i)] = \sum_i a_i \tau_i \ , \qquad (2.5)$$

where $\sum_i a_i = 1$, and a_i and τ_i respectively denote the amplitude and time constant associated with the *i*-th component of the total decay.

2.2.2. Rotational Dynamics

Reorientational dynamics of fluorophore[3,5,6] is also measured by TCSPC. This measurement is based on the principle of photoselective excitation of those fluorophore molecules whose absorption transition dipoles are parallel to the electric vector of polarized excitation light. The fluorescence intensity decays at parallel and perpendicular emission polarizations depend on reorientation of the excitated fluorophore. If the reorientation time and fluorescence life time of fluorophore are comparable, then the depolarization of fluorescence anisotropy with time can be used to measure reorientation dynamics of fluorophore. Time dependent fluorescence anisotropy ($r(t)$) is defined[3] as

$$r(t) = \{I_{\parallel}(t) - I_{\perp}(t)\} / \{I_{\parallel}(t) + 2I_{\perp}(t)\} \qquad (2.6)$$

To minimize any effects on anisotropy of fast decay or rise due to solvent reorganization,[6] emission decays for time-resolved anisotropy studies are collected at

the peak wavelength of steady state emission bands. The vertically ($I_{\parallel}$), horizontally ($I_{\perp}$) and magic angle polarized fluorescence decays (with respect to the sample being excited with the vertically polarized light) are recorded. The polarization characteristics of optical setup have important consequences to the measured anisotropy. It is inevitably necessary when using such instruments to correct for the anisotropy in response. This correction factor is usually termed as G-factor and is defined as the ratio of the transmission efficiency for vertically polarized light to that of horizontally polarized light ($G = I_{\parallel} / I_{\perp}$). Hence, the corrected time dependent fluorescence anisotropy, $r(t)$ can be represented as

$$r(t) = \{I_{\parallel}(t) - GI_{\perp}(t)\} / \{I_{\parallel}(t) + 2GI_{\perp}(t)\} \tag{2.7}$$

The magic angle decay was first deconvoluted from the IRF and fitted to multi-exponential function of time. Subsequently, the parallel (I_{II}) and the perpendicular ($I_{\perp}$) decays were simultaneously fitted by using an iterative reconvolution method.[3,5] In this fluorescence anisotropy method,[6] the longest life time obtained from the fitting of magic angle decay was used during the fit. $r(t)$ decays, so obtained, are fitted with multiexponential function of the following form:

$$r(t) = r(0)\sum_i \alpha_i \exp(-t/\tau_i), \tag{2.8}$$

where τ_i (i = 1, 2) represents the time constants for the decay components (a_i). In this Thesis, the value for the initial anisotropy, $r(0)$, was fixed at 0.376 while fitting the $r(t)$ for C153 in all the solutions studied here.[6] The average rotational correlation time $\langle \tau_r \rangle$ was then determined as follows:

$$\langle \tau_r \rangle = \int_0^{\infty} dt[r(t)/r(0)] = \sum_i \alpha_i \tau_i \tag{2.9}$$

2.2.3. Intramolecular Charge Transfer Reaction

Photo-induced intramolecular charge transfer is an important fundamental process and has been carried in pure[7] and mixtures of solvents,[8,9] ionic liquids[10] and in confined environments.[11,12] In this Thesis, we carried out excited state intramolecular charge transfer reaction of 4-(1-azetidinyl)benzonitrile (P4C) and 4-(pyrrolidinyl)benzonitrile (P5C) in melt mixture of choline chloride+urea (Chapter 6) and in acetonitrile and ethyl acetate in presence of two electrolytes – $LiClO_4$ and $NaClO_4$ (Chapter 9). Upon photo-excitation, these molecules (P4C and P5C) exhibit an anomalous fluorescence band which is red-shifted in addition to normal fluorescence in polar solvents. The appearance of the red-shifted fluorescence has been a matter of considerable debate and discussion.[7,13-28] Various existing models[7,13-28] clearly indicate that the anomalous fluorescence occurs from an electronic state which has charge transfer (CT) character. The state that exhibits normal fluorescence is assumed to possess charge distribution similar to that of the ground state and is termed as locally excited (LE) state. Upon photo-excitation, a substantial amount of charge is transferred from donor (amino group) to the acceptor (benzonitrile ring) moiety shown in SCHEME 1.

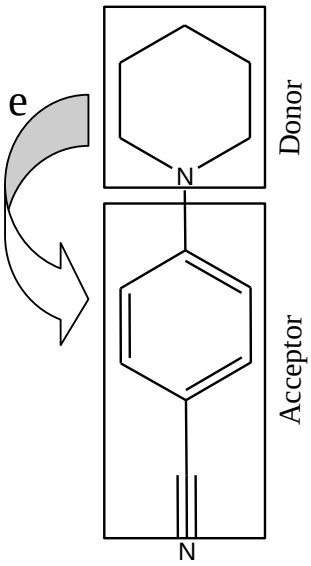

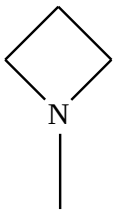

P4C

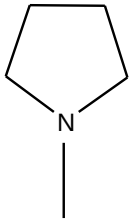

P5C

SCHEME 1

Recent study[7] of photo-induced intramolecular charge transfer reaction of substituted benzonitrile derivatives in several solvents of varying polarity reported that the rate of reaction in those derivatives is substantially modified by the dynamical modes of the solvents in which the reaction is studied.

The photo-excitation of intramolecular charge transfer (ICT) molecule (P4C/P5C≡PnC) and the subsequent charge transferred (CT) state formation is shown in SCHEME 2, where k_f and k_r are the forward and backward rate constants respectively.

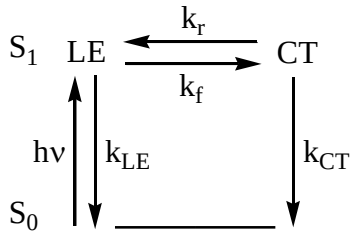

SCHEME 2

k_{LE} and k_{CT} denote the net rate constants (radiative and non-radiative) for LE and CT states, respectively. The interconversion between LE and CT states, which is the intramolecular charge transfer reaction, is much faster in polar solvents near room temperature than the time constants associated with the population decays (inverse of k_{LE} and k_{CT}) to the ground state (S_0). Note that these rate constants are time independent quantities. As seen earlier[7] and also later in this Thesis that inter-conversion between LE and CT states is the charge transfer reaction. Naturally therefore, modification of one of these factors affects the rate at which the reaction progresses. This molecule possesses higher dipole moments in CT states and hence formation of CT population is favored in polar solvents.[7] We have synthesized the intramolecular charge transfer molecule (PnC) in our laboratory following the literature method.[17]

Figure 2.4

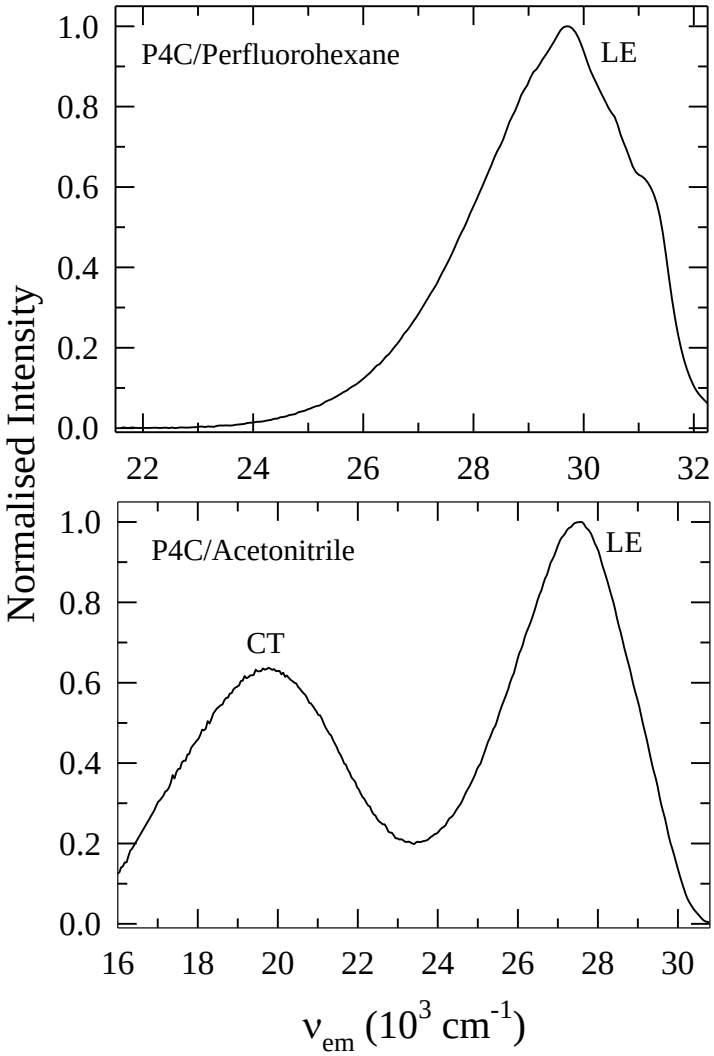

Figure 2.4. Representative emission spectra of P4C in non-polar (perfluorohexane) and polar (acetonitrile) solvents.

Representative fluorescence spectra of P4C molecule in polar (acetonitrile) and non-polar (perfluorohexane) solvents are shown in Figure 2.4. The presence of two distinct peaks in the fluorescence spectrum of P4C in acetonitrile and the absence of it in perfluorohexane clearly indicate that non-polar solvent does not support the formation of the CT state in this molecule. Considering the kinetic framework (SCHEME 2) of

intramolecular charge transfer of P4C molecule, the time evolution of LE and CT intensities can be obtained[7,29,30] as follows :

$$I_{LE}(t) \propto k_{LE}^{rad} \frac{[LE(t)]}{[LE(0)]} = k_{LE}^{rad} \frac{1}{\lambda_1 - \lambda_2} \left\{ (Y - \lambda_2) e^{-\lambda_2 t} + (\lambda_1 - Y) e^{-\lambda t_1} \right\} \quad (2.10)$$

and $$I_{CT}(t) \propto k_{CT}^{rad} \frac{[CT(t)]}{[LE(0)]} = k_{CT}^{rad} \frac{k_f}{\lambda_1 - \lambda_2} \left\{ e^{-\lambda_2 t} - e^{-\lambda t_1} \right\} , \quad (2.11)$$

where k_{LE}^{rad} and k_{CT}^{rad} represent respectively the rate constants associated with the LE and CT population decays to the ground state. Eqs. 2.10 and 2.11 suggest that in polar environments the time evolution of the LE intensity should be comprised by a fast and a slow decay components with very distinct time constants whereas that of CT intensity should show a fast rise followed by a slow decay. In earlier study[7] and also in the present Thesis, the time constants associated to the rise of CT state match well with those fast decays of LE state. So, the fast decay time of LE or the rise time of CT are associated to the reaction rate of LE $\rightarrow$ CT interconversion.[7] The slow time constants of the LE and CT intensity decays describe the time scales associated with the population decay from the S_1 to the S_0 state. This should be the scenario irrespective of the monitoring wavelength across either the LE or CT bands. However, in non-polar solvents where the charge transfer reaction is not supported, one expects a single exponential decay across the fluorescence emission spectrum of the ICT molecule.

The two-state reversible interconversion reaction shown in SCHEME 2 considered above can successfully describe the time dependence of the LE and CT emission intensities of ICT molecule (P4C/P5C) in the systems considered in this thesis.

In this Thesis, the fluorescence spectra of P4C and P5C in melt mixtures and electrolyte containing solvents show dual peak. Subsequently, the fluorescence spectrum of P4C/P5C in perfluorohexane (reference spectrum) was used to deconvolute each fluorescence spectrum into two fragments.[7] The areas under the LE and CT band were obtained after the deconvolution. Fluorescence peak frequencies of LE and CT were calculated by adding the shifts of peak frequencies (with respect to reference spectra) in solvent with reference frequency in perfluorohexane. Time-resolved fluorescence intensity decay measurements were carried out using a time

correlated single photon counting (TCSPC) as discussed above. A light emitting diode (LED) of 299 nm was used as an excitation source for monitoring charge transfer solute (PnC). The full width at half-maximum (FWHM) of the instrument response function (IRF) was ~ 475 ps. The LE and CT fluorescence decays were recorded at magic angle (54.7°) with a band-pass of 8 nm. Decays were then deconvoluted from the IRF and fitted to biexponential function using an iterative reconvolution algorithm.[3,5] This allows one to detect decay component with a time constant as fast as ~100 ps with reasonable accuracy.[7]

References

1. O'Cronnor, D. V.; Phillips, D. *Time Correlated Single Photon Counting*, Academic Press, London, **1984**.

2. Chang, M. C.; Courtney, S. H.; Cross, A. J.; Gulotty, R. J.; Petrich, J. W.; Fleming, G. R. *Analytical Instrumentation* **1985**, *14*, 433.

3. Lakowicz, J. R. *Principle of Fluorescence Spectroscopy*, 2nd ed.; Kluwer Academic Pub: New York, **1999**.

4. Horng, M. L.; Gardecki, J. A.; Papazyan, A.; Maroncelli, M. *J. Phys. Chem.* **1995**, *99*, 17311.

5. Birch, D. J. S.; Imhof, R. E. Time-Domain Fluorescence Spectroscopy Using Time Correlated Single Photon Counting, Topics in Fluorescence Spectroscopy; Lakowicz, J. R., Ed.; Plenum: New York, **1991**; *Vol 1*.

6. Horng, M. L.; Gardecki, J. A.; Maroncelli, M. *J. Phys. Chem. A* **1997**, *101*, 1030.

7. Dahl, K.; Biswas, R.; Ito, N.; Maroncelli, M. *J. Phys. Chem. B* **2005**, *109*, 1563.

8. Pradhan, T.; Ghoshal, P.; Biswas, R. *J. Phys. Chem. A* **2008**, *112*, 915.

9. Gazi, H. A. R.; Biswas, R. *J. Phys. Chem. A* **2011**, *115*, 2447.

10. Sahu, K.; Kern, S. J.; Berg, M. A. *J. Phys. Chem. A* **2011**, *115*, 7984.

11. Biswas, R.; Rohman, N.; Pradhan, T.; Buchner, R. *J. Phys. Chem. B* **2008**, *112*, 9379.

12. Pradhan, T.; Gazi, H.; Guchhait, B.; Biswas, R. *J. Chem. Sci.* **2012**, *124*, 355.

13. Zachariasse, K. A.; Druzhinin, S. I.; Bosch, W.; Machinek, R. *J. Am. Chem. Soc.* **2004**, *126*, 1705.

14. Techert, S.; Zachariasse, K. A., *J. Am. Chem. Soc.* **2004**, *126*, 5593.

15. Zachariasse, K. A. *Chem. Phys. Lett.* **2000,** *320*, 8.

16. Zgierski, M. Z.; Lim, E. C. *Chem. Phys. Lett.* **2004,** *393*, 143.

17. Rettig, W. *J. Luminesc*. **1980**, *26*, 21.

18. Rettig, W. *J. Phys. Chem*. **1982**, *86*, 1970.

19. Rettig, W.; Gleiter, R.; *J. Phys. Chem*. **1985**, *89*, 4674.

20. Rettig, W.; Wermuth, G. *J. Photochem.* **1985**, *28*, 351.

21. Al-Hassan, K. A.; Rettig, W. *Chem. Phys. Lett.* **1986**, *126*, 273.

22. LaFemina, J. P.; Duke, C. B.; Rettig, W. *Chem. Phys*. **1990**, *87*, 2151.

23. Braun, D.; Rettig, W. *Chem. Phys*. **1994**, *180*, 231.

24. Braun, D.; Rettig, W. *Chem. Phys. Lett*. **1997**, *268*, 110.

25. Rettig, W. *Ber. Bunsen-Ges. Phys. Chem.* **1991**, *95*, 259.

26. Yatsuhashi, T.; Trushin, S. A.; Fuss, W.; Rettig, W.; Schmid, W. E.; Zilberg, S. *Chem. Phys*. **2004**, *296*, 1.

27. Zachariasse, K. A.; Grobys, M.; von der Haar, T.; Hebecker, A.; Il'ichev, Y. V.; Jiang, Y.-B.; Morawski, O.; Kuhnle, W.; *J. Photochem. Photobiol. A* **1996**, *102*, 59.

28. Rettig, W.; Zeitz, B. *Chem. Phys. Lett.* **2000**, *317*, 187.

29. Pradhan, T.; Biswas, R. *J. Phys. Chem. A* **2007**, *111*, 11514.

30. Pradhan, T.; Biswas, R. *J. Phys. Chem. A* **2007**, *111*, 11524.

Chapter 3

Fast Fluctuations in Deep Eutectic Melts: Multi-Probe Fluorescence Measurements and All-Atom Molecular Dynamics Simulation Study

3.1. Introduction

Micro-heterogeneity in solution structure of (amide + electrolyte) deep eutectic (DU) melts is known for a long time.[1-4] However, characterization of this micro-heterogeneity and understanding its impact on a chemical event occurring in these media are still at the developing stage.[5-8] Dielectric relaxation measurements extending up to 100 MHz frequency range have reported pronounced non-Debye relaxation mechanism with extremely slow timescales, suggesting collective nature of the relaxation.[4] The length-scale involved in such collective relaxation has not been understood in terms of spatial correlations as scattering measurements using radiations of atomic resolution have not been performed yet. Recent fluorescence measurements[5-7] have explored solution structure and dynamics of several (acetamide + electrolyte) deep eutectics where pronounced excitation wavelength (λ_{exc}) dependence of fluorescence emission of a dissolved solute and a strong decoupling between solute rotation rate and medium viscosity have been observed. The above decoupling is manifested via fractional viscosity dependence of the measured average rotation time, $\langle \tau_r \rangle \propto \eta^p$, with p much less than unity. Similar fraction power dependence on viscosity has also been observed for the average time for solute solvation with fraction power less than the corresponding p obtained for solute rotation. The latter may be interpreted as a sort of translation-rotation decoupling as the average solute solvation rate is governed by the center-of-mass diffusion of the solvating particles.[9-13] The fractional viscosity dependence and the translation-rotation decoupling mentioned above, which resemble closely to those for deeply super-cooled liquids,[14-16] have been attributed to the dynamic (temporal) heterogeneity of these deep eutectic melts. A computer simulation study using model potentials for acetamide and

electrolytes predicts strong dynamic heterogeneity via pronounced non-Gaussian character of particle displacement in these complex melts and collective blockage of ion movement.[8] In addition, the simulated diffusion coefficients have been found to be much larger than those predicted by hydrodynamics using experimental viscosity as input, hinting at diffusion-viscosity decoupling in these DU melts.

Against such a backdrop the recent fluorescence results[7] on DU melt, [0.78CH_3CONH_2 + 0.22{*f* LiBr + (1-*f*) $LiNO_3$}] appear to be more interesting as fluorescence emission of coumarin 153 (C153) exhibits significant λ_{exc} dependence which was absent in [CH_3CONH_2 + K/NaSCN) melts,[6] suggesting more extensive solute-sensing of inhomogeneous density fluctuations in presence of lithium salts. This is further supported by the more pronounced fractional viscosity dependence of solute solvation and rotation rates in DU containing lithium salts than in presence of thiocyanates. The scenario turns out to be even more interesting as both the spatial (λ_{exc} dependence) and temporal (η^p dependence) heterogeneities exhibit Br^- ion concentration dependence which becomes stronger with a solute having excited state lifetime shorter than that of C153. Curiously, λ_{exc} dependence has been found to be dominating at the NO_3^- rich region whereas η^p dependence becomes more severe at the Br^- ion enriched composition. These results once again support the view that emergence of temporal heterogeneity does not necessitate observation of spatial heterogeneity.[17-19] For the present melt, this may also mean that inhomogeneous density fluctuation timescales largely remain unchanged across the Br^- ion concentration; it is the competition between the solute lifetime (τ_{life}) and solvent density fluctuation that brings out the observed difference in η^p dependence for different solutes. Characterization of this density fluctuation and subsequent coupling to solute via experiments and simulations constitute the theme of the present work.

Note that the interaction of amide (-$CONH_2$) groups with ions (cations and anions) can lead to formation of co-ordinated complexes in such DU melts. Infrared measurements[20] have already indicated interaction between amide groups and ions in similar multi-component mixtures. Dielectric relaxation measurements[21] have also provided an estimation for the domain size that may have formed in (amide + electrolyte) melts. Interestingly, the chelating effects of cation via coordination with

oxygen atoms in polymer-electrolyte composites have been demonstrated both in simulations[22] and experiments.[23-25] Here we plan to study the effects of such micro-domains or density inhomogeneities, if formed via interaction between ions and acetamide as discussed above, through fluorescence measurements and all-atom molecular dynamics simulations. For fluorescence study, we have used a dye molecule, p-N,N-dimethylamino-p'-cyano-diphenylacetylene (DTN), whose τ_{life} is much shorter than that of C153. Note the molecular volume of DTN[26] and C153[27] are respectively 230 $Å^3$ and 246 $Å^3$ and thus a significant difference in viscosity coupling is not expected from size variation. However, difference in shape (DTN being prolate and C153 ellipsoid) may have some effects. Fluorescence quenching by NO_3^- or Br^- can be a concern here but our earlier measurements using C153 have suggested secondary importance of such processes.[7]

In this Chapter, we have investigated the solute-medium coupling in [$0.78CH_3CONH_2$ + $0.22\{f$ LiBr + $(1\text{-}f)$ $LiNO_3\}$] DU melts by following the composition and temperature dependent dynamic fluorescence anisotropy of DTN. For this, six different values of f covering no Br^- concentration (f =0) to full (f =1) have been considered at five different temperatures between ~303 K and ~348 K. Measured average rotation times describing the fractional viscosity dependence are then compared with our earlier data for C153[7] by showing as a function of temperature-reduced viscosity, η/T. In addition, composition dependence of p is also compared for these two solutes and the difference between them is interpreted in terms of differing sensitivity of these probes to environmental fluctuations. Simulated wavenumber dependent incoherent and coherent scattering functions (ISF and CSF) reveal distributed relaxation kinetics and fast timescales which support an explanation for the observed stronger viscosity decoupling of DTN rotation rate (in comparison to that of C153) in terms of dynamic (temporal) heterogeneity and larger coupling to fast density fluctuations.

3.2. Experimental Details

Acetamide (>99%, Sigma-Aldrich), lithium nitrate (≥99.5%, Sigma Aldrich), and lithium bromide (≥99%, Sigma Aldrich) were vacuum-dried at ~~325 K for 24 hours

before use. Because of strong hygroscopic nature of these salts, samples were prepared with the best possible care to minimize moisture absorption. Formamide (99%, Sigma Aldrich) was used as received. DTN was synthesized following a literature method[28-30] and purity checked by NMR analyses. Temperature of the sample chamber was maintained by preheated water circulation. Absorption and emission spectra of DTN were collected by using the standard absorption spectrophotometer and fluorimeter and processed with care.[31-32] Time dependent fluorescence decays were collected by using a set-up based upon time correlated single photon counting method described elsewhere[31-32] and in Chapter 2 and using 375 nm light for excitation producing an instrumental response function (IRF) of full-width-at-half-maximum ~70 ps.

Rotation time (τ_r) of the solute was then determined from the simultaneous fitting of the collected parallel ($I_{\parallel}(t)$) and perpendicular ($I_{\perp}(t)$) decays after deconvolution from the IRF as follows:[26,33,34]

$$I_{\parallel}(t) = A_{\parallel}(t) I_{fl}(t)[1+2r(t)], \quad (3.1)$$

$$I_{\perp}(t) = A_{\perp}(t) I_{fl}(t)[1-r(t)], \quad (3.2)$$

where $I_{fl}(t)$ denotes the relative fluorescence intensity in the absence of any rotational contribution and obtained by using the collected magic angle intensity decays. $A_{\parallel}$ and $A_{\perp}$ are fit parameters for normalizing the effects due to different detection efficiencies and acquisition times. Measured anisotropy decays were found to be adequately described by single exponentials, $r(t) = r_0 \exp(-t/\tau_r)$, where the value of the initial anisotropy, r_0, was allowed to vary. We found r_0 to vary between 0.35 and 0.38 which agree well with earlier observations.[26-33]

3.3. Results and Discussion

Figure 3.1 displays representative absorption and emission spectra of DTN dissolved in the above DU melt at f =0.4 at ~303 K along with those in formamide. Note that both the absorption and emission spectra of DTN in this DU melt at f =0.4 are red-shifted than those in formamide. Similar behaviour can also been seen if spectra of

C153 in formamide and (acetamide + K/NaSCN) are compared.[5] This indicates that these DU melts are somewhat more polar than formamide. Since absorption and emission spectral peak frequencies do not show any f dependence (Figure A1, Appendix A), the above observation remains unaltered for any Br^- ion concentration in this melt. Interestingly, emission of C153 in (acetamide + $LiBr/NO_3$) melt is blue-shifted than that of C153 in formamide,[7] suggesting a reverse polarity trend. This

Figure 3.1

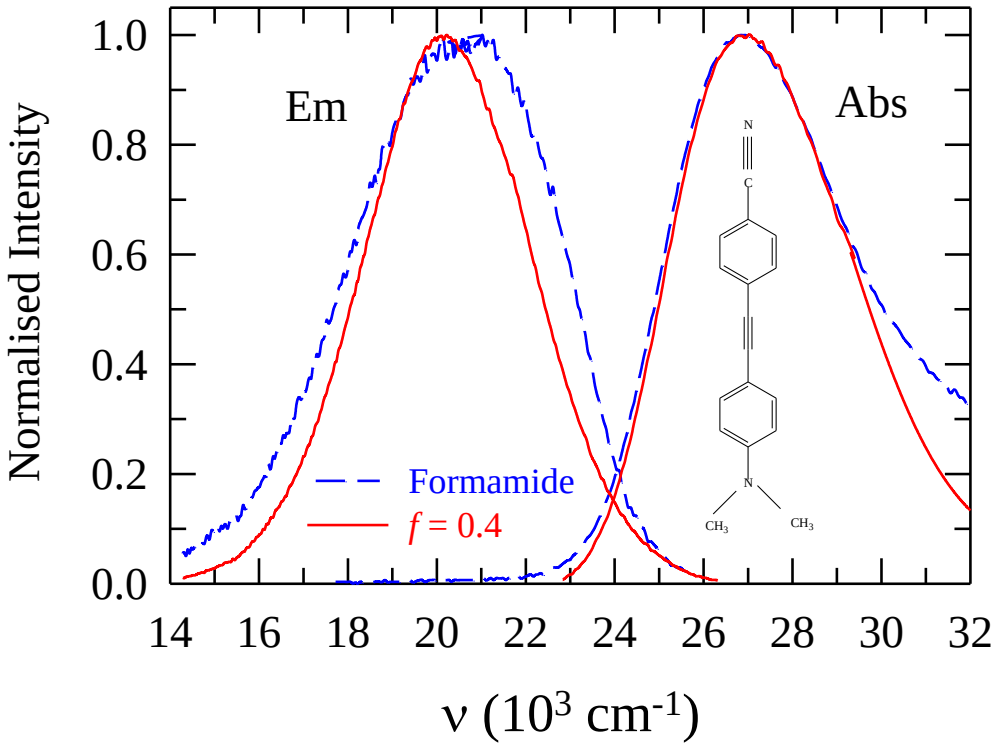

Figure 3.1: Comparison between the steady state absorption and emission spectra of DTN in [0.78CH_3CONH_2+ 0.22{*f*LiBr+ (1-*f*)$LiNO_3$}] deep eutectic (DU) melt with *f*= 0.40 (solid lines), and in formamide (broken line) at ~303 K. Chemical structure of DTN is also shown as inset.

contrasting result is probably more associated with the strong intra-molecular charge transfer character of DTN[35] and interaction of the excited solute with the medium than

anything related to the vast difference in τ_{life} between these two probes.[9,30,35] The lifetime of DTN in this melt has been determined by analyzing the fluorescence intensity decays collected at magic angle, representative of which is displayed in Figure A2 (Appendix A). As seen earlier for DTN and a closely related molecule in common organic solvents,[26,30] the magic angle decays have been found to be bi-exponential functions of time. The composition and temperature dependent τ_{life} of DTN is summarized respectively in Table B1 and Table B2 (Appendix B) and reflect the viscosity sensitivity as depopulation also involves intramolecular rotation.

Figure 3.2 reflects on the spatial heterogeneity aspect of this melt where excitation wavelength (λ_{exc}) dependence of fluorescence emission and the corresponding spectral width (full-width-at-half-maximum) of DTN are shown and compared with earlier results obtained using C153 and another short life-time probe, trans-2-[4-(dimethylamino)styryl]benzothiazole (DMASBT).[7] Note that changing λ_{exc} from 330 nm to 430 nm induces a redshift of ~1200 cm^{-1} in fluorescence emission peak frequency (ν_{em}) of DTN which is very similar to that found for DMASBT and nearly double of the amount observed for C153. The fact that λ_{exc}-induced shift in ν_{em} is larger for DTN and DMASBT than for C153 provides further support for the conjecture that the inhomogeneous density fluctuation timescales in this melt are fast and overlap better with the excited state lifetime of DTN. The increased sensitivity to medium spatial heterogeneity for fast-probes is further reflected in the larger variation of the spectral width (Γ_{em}) with λ_{exc}. More specifically, DTN is showing ~2000 cm^{-1} narrowing upon 100 nm redshift in λ_{exc} which is ~5 times larger than that for C153 for the same change in λ_{exc}. Note the redshift in ν_{em} with concomitant spectral narrowing observed here are in accordance with the trend already observed for various chromophores in bulk solvents,[9] electrolyte solutions[36] and confined media.[37,38]

Figure 3.2

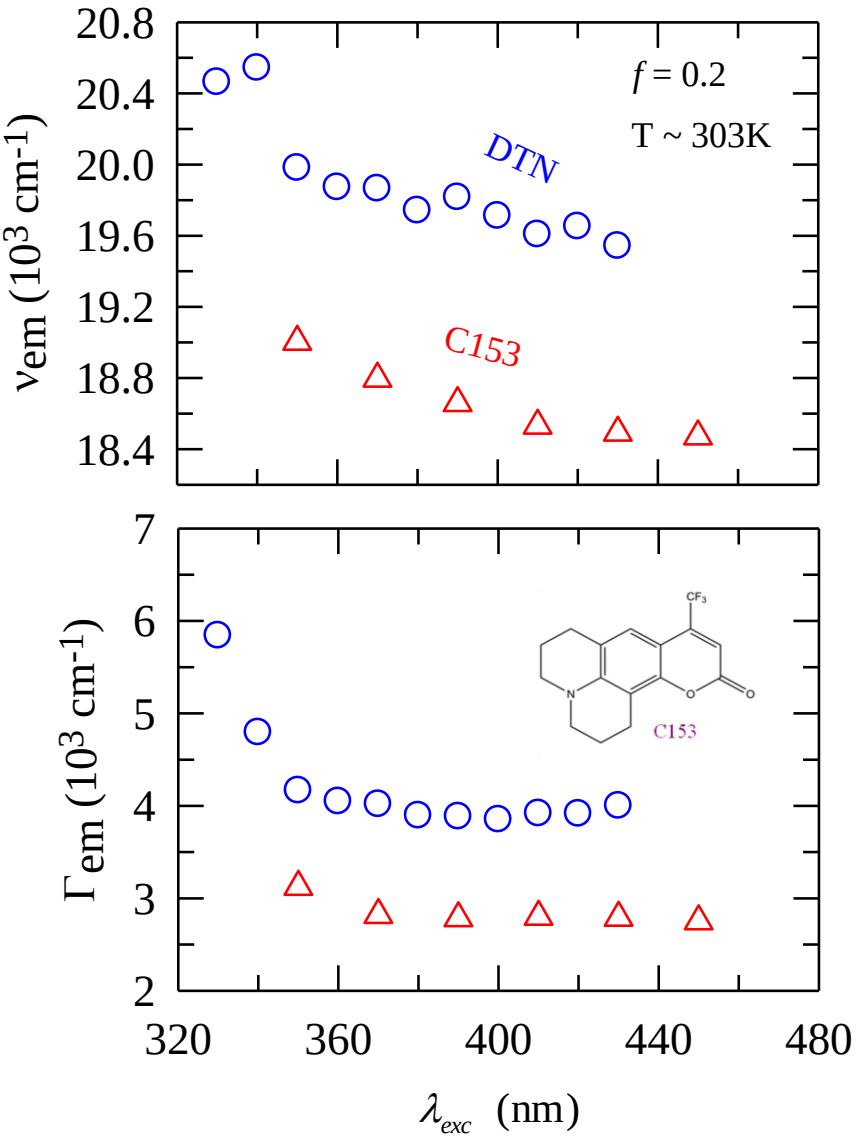

Figure 3.2: Excitation wavelength (λ_{exc}) dependence of fluorescence emission peak frequencies, ν_{em} (upper panel) and full-width-at-half-maxima, Γ_{em} (lower panel) for DTN and C153 in DU melt, [0.78CH_3CONH_2+ 0.22{*f*LiBr+ (1-*f*)$LiNO_3$}], with f = 0.2 at ~303 K. Chemical structure of C153 is also shown in the lower panel.

We next present the temperature dependent rotation times ($<\tau_r>$) for DTN in this melt at various values of f and connect it to fast inhomogeneous density fluctuations while exploring the viscosity coupling. Table B3 (Appendix B) summarizes the $<\tau_r>$ obtained from fits described earlier along with the experimental viscosity.[7] As data in this table suggest, $<\tau_r>$ for DTN lies between ~0.5 ns and ~4 ns for all the f values considered in the temperature range, ~303-348 K. Note τ_r values for DTN in this melt are somewhat smaller than but similar to those for C153 in the same melt.[7] The viscosity coupling of DTN rotation is investigated in Figure 3.3 where the measured $<\tau_r>$ are shown as a function of η/T. Also for comparison are shown the predicted rotation times from the modified Stokes-Einstein-Debye (SED) relation,[39] $\tau_r = (V\eta/k_B T) f_s C$, with shape factor, f_s =2.94, and C =0.418[26] and 1 for slip stick

Figure 3.3

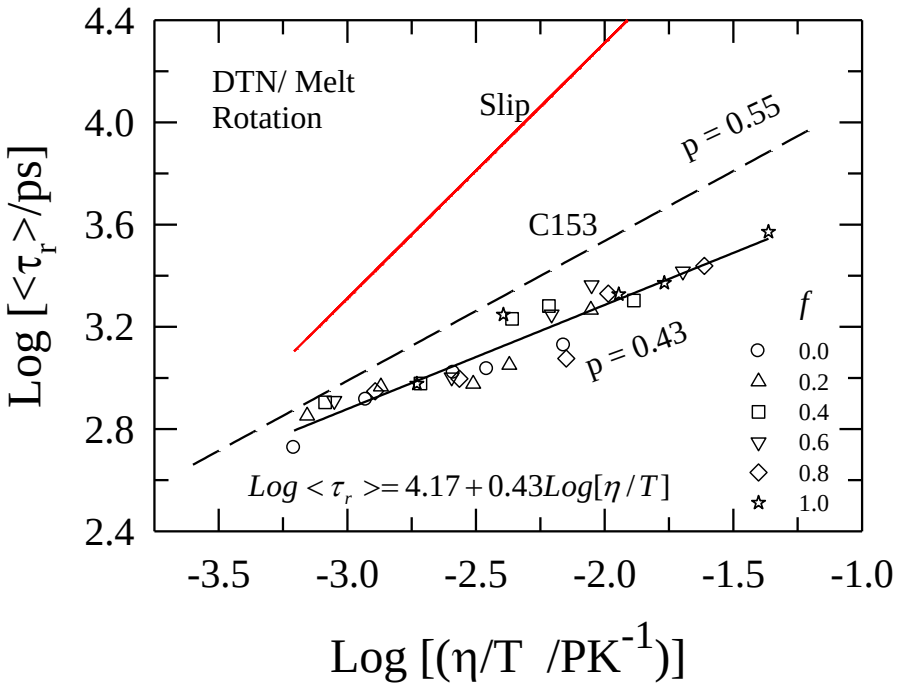

Figure 3.3: Viscosity decoupling of rotation times ($\langle\tau_r\rangle$) for DTN and C153 in the DU melt, [0.78CH_3CONH_2+ 0.22{*f*LiBr+ (1-*f*)$LiNO_3$}], and comparison. Temperature dependent measured times (symbols) at various f values are shown as a function of temperature-reduced viscosity (η/T) in a log-log fashion. The line going through

these symbols represent a fit to an expression which is also shown as inset. Similar fit through C153 data is shown by the broken line where p = 0.55 (from Ref. 7). Calculated rotation times for DTN from the slip hydrodynamics at various η/T values are also shown (solid line) for a comparison. Corresponding stick values are not shown as they are simply larger by a proportionality factor and do not convey anything extra.

boundary conditions, respectively. Note the measured $<\tau_r>$ values are not only much faster than the SED predictions but the extent of slowing down of $<\tau_r>$ with viscosity found in measurements also differs. This is quantified by the line going through the measured $<\tau_r>$ representing a viscosity dependence of the following type, $\tau_r = A(\eta/T)^p$, with p = 0.43. This value of f -averaged fraction power (p) is substantially deviated from unity and signifies strong viscosity decoupling. This kind of fractional viscosity dependence is reminiscent of what has been observed for deeply supercooled liquids and often considered as diagnostics for temporal heterogeneity.[14-16,19] Following this we ascribe the viscosity decoupling of DTN rotation to the temporal (dynamic) heterogeneity of the medium eventhough solute shape anisotropy can also contribute partially to the observed decoupling.[40,41] This assignment derives further support from our model simulation studies[8] where signature of temporal heterogeneity via pronounced non-Gaussian character of particle displacements has been observed in similar (acetamide + electrolyte) DU melts.

Interestingly, p value obtained above for DTN is ~20-25% less than that found for C153 (p =0.55, shown by the broken line in Figure 3.3) and suggests relatively stronger decoupling. Note such a 'small' difference in p can represent significantly different solute-solvent coupling as it originates from a power-law dependence. Such a different coupling can be seen even after 'normalizing' the shape factor via comparing the η/T dependence of the ratios between the experimental and theoretical rotation times ($\langle\tau_r\rangle_{expt}/\langle\tau_r\rangle_{theo}$) for these two solutes. We propose that relatively stronger decoupling for DTN results from more effective sensing of 'fast' environmental fluctuations due to its shorter lifetime. Dynamic fluorescence anisotropy

measurements provide ensemble-averaged rotation time because the detected signal is composed of contributions from a number of excited chromophores distributed in different kinds of solvation environments (environmental inhomogeneity). Since $\tau_{life}^{C153} > \tau_{life}^{DTN}$, a more effective environmental averaging of C153 rotation is expected. This weakens the degree of decoupling for C153, leading to a larger value for p than that associated with DTN rotation in the same medium. It should be noted here that fractional viscosity dependence (or temporal heterogeneity) does not guarantee the presence of environmental inhomogeneity in a given medium; the latter requires confirmation through further spatial information.[42,43] Excitation wavelength dependence of probe emission frequency and spectral width shown in Figure 3.2 provides this critical information.

The above proposition that a competing τ_{life} with fast density fluctuations produces greater decoupling is further investigated in Figure 3.4 where fraction power (p) obtained using DTN is shown as a function of Br^- ion concentration (f) in the melt and compared with that from earlier C153 measurements.[7] In contrast to C153 results, p associated with DTN does not show any f dependence. In addition, the f-insensitive value of p for DTN (~0.4) is close to that (~0.5) for C153 at f=1, suggesting the temporal heterogeneity sensed by DTN across f is what is shown by C153 as the 'maximum' in the same melt. This may occur if either of the two following reasons prevails. First, the timescales associated with environmental fluctuation remain largely unaltered across f. This is possible if density inhomogeneity is caused by Li^+ whose concentration is not changing with f. Second, a slower fluctuating timescale develops upon increasing f which C153 can sense but not DTN. A support for the second mechanism may be accessed via exploring the f dependence of the λ_{exc}-induced total change (Δx) in ν_{em} and Γ_{em} by exciting the dissolved solute at the most blue ($\lambda_{exc,b}$) and most red ($\lambda_{exc,r}$) wavelengths at a given temperature, T: $\Delta x(f, \mathrm{T}) = x(\lambda_{exc,b}, f, \mathrm{T}) - x(\lambda_{exc,r}, f, \mathrm{T})$. Figure A3 (Appendix A) depicts the results for such an investigation with DTN in this melt where both the

changes in emission frequency and spectral width ($\Delta\nu_{em}$ and $\Delta\Gamma_{em}$, respectively) show initial increase with f and then saturates. The initial increase may suggest enhancement of spatial heterogeneity via slowing down of fluctuating timescale upon replacing NO_3^- by Br^-. The saturation in these quantities then suggests the inability of DTN (due its shorter τ_{life}) to sense and report the subsequent slower fluctuations which can be picked up by a longer lifetime probe such as C153.

Figure 3.4

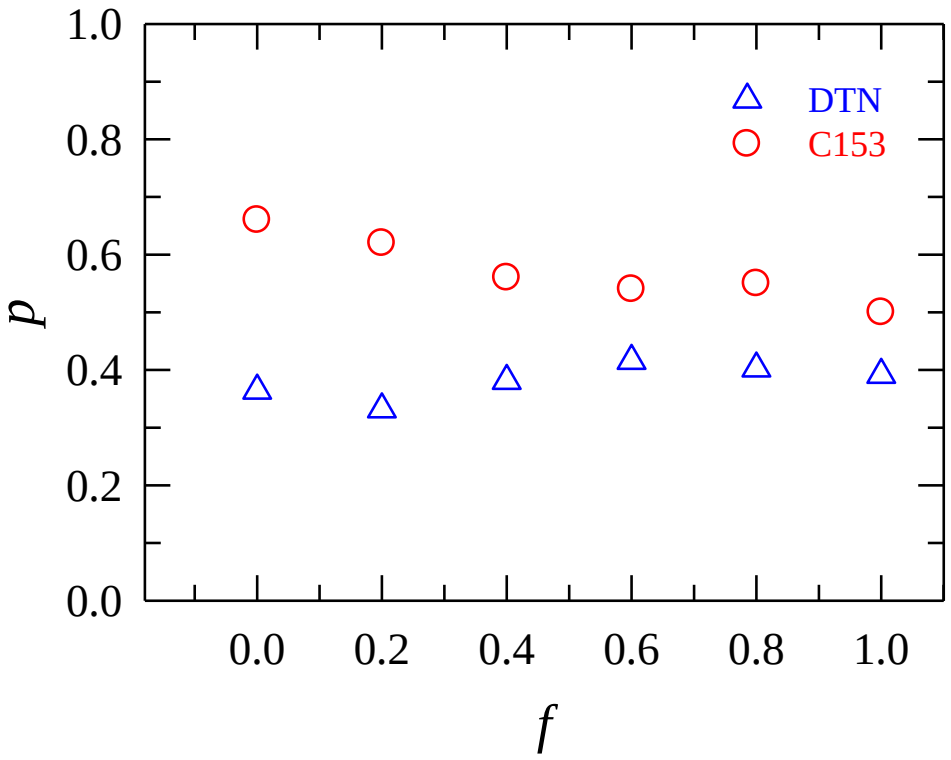

Figure 3.4: Br^- ion concentration dependence of the fraction power, *p*, obtained via fit of the measured rotation times for DTN (triangles) in the DU melt, [0.78CH_3CONH_2+ 0.22{*f*LiBr+ (1-*f*)$LiNO_3$}], and a comparison with the corresponding values for C153 (circles, from Ref. 7).

3.4. Conclusion

To summarize, the present work reveals the degree of temporal heterogeneity as reflected by the fraction power dependence of solute rotation in a given medium depends upon the excited state lifetime of the probe used. In a spatially inhomogeneous medium such as this DU melt, this dependence arises from a competition between the timescales of inhomogeneous density fluctuation and the excited state lifetime of the reporter chromophore. This assumption, however, does not preclude the contributions from those dynamic solute-environment interactions which cannot be described by the conventional hydrodynamics. In addition, quantitative understanding of the fractional viscosity dependence requires careful inclusion of solute shape anisotropy.

References

1. Castellani, F.; Berchiesi, G.; Pucciarelli, F.; Bartocci, V. *J. Chem. Eng. Data.* **1981**, *26*, 150.
2. Berchiesi, G.; Angelis, M.D.; Rafaiani, G.; Vitali, G. *J. Mol. Liq.* **1992**, *51*, 11.
3. Berchiesi, G.; Rafaiani, G.; Vitali, G.; Farhat, F. *J. Therm. Anal.* **1995**, *44*, 1313.
4. Berchiesi, G.; Vitali, G.; Passamonti, P.; Plowiec, R. *J. Chem. Soc., Faraday Trans. 2*, **1983**, *79*, 1257.
5. Guchhait, B.; Gazi, H. A. R; Kashyap, H. K.; Biswas, R. *J. Phys. Chem. B* **2010**, *114*, 5066.
6. Gazi, H. A. R; Biswas, R. *J. Phys. Chem. A* **2011**, *115*, 2447.
7. Guchhait, B.; Daschakraborty, S.; Biswas, R. *J. Chem. Phys.* **2012**, *136*, 174503.
8. Pal, T.; Biswas, R. *Chem. Phys. Lett.* **2011**, *517*, 18.
9. Horng, M. L.; Gardecki, J. A.; Papazyan, A.; Maroncelli, M. *J. Phys. Chem.* **1995**, *99*, 17311.
10. Bagchi, B.; Biswas, R. *Adv. Chem. Phys.* **1999**, *109*, 207.
11. Kashyap, H. K.; Biswas, R. *J. Phys. Chem. B* **2010**, *114*, 254.
12. Daschakraborty, S.; Biswas, R. *Chem. Phys. Lett.* **2010,** *510*, 202.
13. Daschakraborty, S.; Biswas, R. *Chem. Phys. Lett.* **2012**, *545*, 54.
14. Ediger, M. D. *Annu. Rev. Phys. Chem.* **2000**, *51*, 99.
15. Sillescu, H. *J. Non-Cryst. Solids* **1999**, *243*, 81.
16. Ediger, M. D; Angell, C. A.; Nagel, S.R. *J. Phys. Chem.* **1996**, *100*, 13200.
17. Harris, K. R. *J. Chem. Phys.* **2009,** *131*, 054503.
18. Daschakraborty, S.; Biswas, R. *J. Chem. Sci.* **2012,** *124*, 763.
19. Richert, R. *J. Phys: Condens. Matter*, **2002,** *14*, R703.
20. Diorio, A. F.; Lippincott, E.; Mandelkern, L. *Nature* **1962**,*195*, 1296.
21. Berchiesi, G. *J. Mol. Liq*. **1999**, *83*, 271.
22. Muller-Plathe, F., van Gunsteren, W. F. *J. Chem. Phys.* **1995**, *103*, 4745.
23. Guchhait, B.; Biswas, R. *J. Chem. Phys.* **2013**, *138*, 114909.

24. Gadjournova, Z.; Andreev, Y. G.; Tunstall, D. P.; Bruce, P. G. *Nature* **2001**, *412*, 520.
25. MacGlashan, G. S.; Andree, Y. G.; Bruce, P. G. *Nature* **1999**, *398*, 792.
26. Imeshev, G.; Khundkar, L. R. *J. Chem. Phys.* **1995**, *103*, 19.
27. Jin, H.; Baker, G. A.; Arzhantsev, S.; Dong, J.; Maroncelli, M. *J. Phys.Chem. B* **2007**, *111*, 7291.
28. Stiegman, A. E.; Graham, E.; K. J. Perry, Khundkar, L. R.; Cheng, L.-T.; Perry, J. W. *J. Am. Chem. Soc.* **1991**, *113*, 7658.
29. Borch, R.; Hassid, A. *J. Org. Chem.*, **1972**, *37*, 1673.
30. Takahashi, S.; Kuroyama, Y.; Sonogashira, K.; Hagihara, N. *Synthesis* **1980**, 627.
31. Pradhan, T.; Ghoshal, P.; Biswas, R. *J. Phys. Chem. A* **2008**, *112*, 915.
32. Pradhan, T.; Ghoshal, P.; Biswas, R. *J. Chem. Sci.* **2008**, *120*, 275.
33. Hirata,Y.; Kanemoto, Y., Okada, T., Nomoto, T. *J. Mol. Liq.* **1995**, *65/66*, 421.
34. Cross, A. J.; Fleming, G. R. *Biophys. J.* **1984**, *46*, 45.
35. Hirata,Y.; Okada, T., Nomoto, T. *Chem. Phys. Lett.* **1997**, *278*, 133.
36. Pradhan, T.; Gazi, H. A. R.; Biswas, R. *J. Chem. Phys.* **2009**, *131*, 054507.
37. Biswas, R.; Rohman, N.; Pradhan, T.; Buchner, R. *J. Phys. Chem. B* **2008**, *112*, 9379.
38. Biswas, R.; Das, A. R.; Pradhan, T.; Touraud, D.; Kunz, W.; Mahiuddin, S. *J. Phys. Chem. B* **2008**, *112*, 6620.
39. Horng, M. L.; Gardecki, J. A.; Maroncelli, M. *J. Phys. Chem.A* **1997**, *101*, 1030.
40. Jas, G. S.; Larson, E. J.; Johnson, C. K.; Kuczera, K. *J. Phys. Chem. A* **2000**, *104*, 9841.
41. Hue, Y.; Fleming, G. R. *J. Chem. Phys.* **1991**, *94*, 3857.
42. Richert, R. *J. Non-Cryst. Solids* **1994**, *172-174*, 209.
43. Richert, R.; Heuer, A. *Macromolecules* **1997**, *30*, 4038.

Chapter 4

Density Relaxation and Particle Motion Characteristics in a Non-Ionic Deep Eutectic Solvent, (Acetamide + Urea): Time-Resolved Fluorescence Measurements

4.1. Introduction

Deep eutectic solvents (DESs) are increasingly finding a variety of industrial and technological applications due to their exquisite solvent properties, economical viability and easy synthetic accessibility.[1-5] The bio-degradable nature of these multi-component melts makes these non-aqueous melt mixtures suitable candidates for green solvent engineering and sustainable media for biomass processing.[6-8] DESs are molten mixtures at temperatures much below than the individual melting temperatures (T_m) of the constituents and may contain both ionic and non-ionic species. Extensive H-bond interaction among the components is believed to be reason for the observed depression of freezing points. Such multi-component mixtures, when contain electrolytes, are termed as ionic DESs.[1-4] Non-ionic DESs, on the other hand, are composed of dipolar molecules and amphiphiles. DESs made of acetamide and urea are representative examples of the latter kind and constitute the subject of the present study. Note that although a few fast spectroscopic measurements combined with computer simulations have attempted to illustrate the solute-solvent coupling in and relaxation dynamics of several ionic DESs,[9-15] similar studies are yet to be carried out for non-ionic members, such as, (acetamide + urea) DESs. Here we investigate, via employing both time-resolved fluorescence measurements and molecular dynamics simulations, the density relaxation timescales of the DESs, [f CH_3CONH_2+(1-f)NH_2CONH_2], and coupling between a dissolved solute and density fluctuations in them at three different compositions (f) for the temperature range, 328 – 353 K.

The reasons that motivated us to take up the present study are as follows. First, pulsed field gradient nuclear magnetic resonance (PFG-NMR) measurements of DES made of choline chloride ($[HOC_2H_4N(CH_3)_3]^+ Cl^-$) and urea have suggested particle diffusion via jumps rather than through stochastic Brownian moves.[16] Interestingly, support for presence of such a non-hydrodynamic transport mode for mixture components has been provided also by time-resolved fluorescence measurements of (acetamide + electrolyte) DESs which reported fractional viscosity dependence of average rotation and solvation rates ($\left\langle \tau_{r/s}^{-1} \right\rangle \propto \eta^{-p}$, $p < 1$) of a solute dissolved in them.[10-12,15] In such a situation one would be naturally curious to know how density relaxes in deep eutectics made of acetamide and urea. As individual components, both acetamide and urea possess tremendous industrial and biological relevance. For example, molten acetamide (T_m ~353 K[17]) is known to solubilise a large number of organic and inorganic compounds except cellulose, and may be utilised as a simple model system for understanding the role of hydrogen bonding interactions in determining the three dimensional structure of proteins and nucleic acids.[17-19]

Urea is, on the other hand, one of the most commonly used nitrogenous fertilizers, and known to critically impact protein stability and function.[20-24] Although the T_m of urea is ~406 K, (acetamide + urea) exhibits a eutectic temperature ~319 K at 0.62 mole fraction of acetamide.[25,26] This makes (acetamide + urea) DESs accessible for studying structure and dynamics in molten condition at a temperature range much lower than the individual T_ms of the components but more than 100 K above the thermodynamic glass transition temperature (T_g ~207 K) of the corresponding DES. This fact assumes even more importance as signatures of pronounced dynamic heterogeneity have been observed earlier[10-13] for (acetamide + electrolyte) DESs at a temperature ~100-150 K above the corresponding T_gs. Apart from this basic scientific aspect, a smart application of (acetamide + urea) DESs as designer solvents for tailoring chemical reactions necessitates a thorough understanding of structure-dynamics relationship for these media. Here the importance stems from the well-known solvent control of chemical reactions.[27-33] Interestingly, acetamide and urea, though can act as both H-bond donors and acceptors, possess vastly different molecular properties. For example, while the static dielectric constant (ε_0) of

acetamide is ~60 and molecular dipole moment (μ) 3.2 D,[34,35] those values for urea are ~3 (measured in solid state) and 4.56 D,[36] respectively. Besides forming inter-species H-bonding, urea and acetamide also support intra-species H-bonding, leading to formation of dimers at low concentrations and polymers at high concentrations.[37,38] Given that the collective H-bonding network and polarity critically influences solvation timescales,[39-45] alteration of composition mixture provides an easy handle to regulate medium effects on a chemical reaction occurring in these media. Presence of polymeric as well as inter-species H-bonded molecules may give rise to medium heterogeneity sustaining slow dynamics in these systems.[46] More importantly, creation of liquid phase via extensive depression of freezing points of the mixture components may lead to microscopic heterogeneity in structure and dynamics of such media. These complexities of (acetamide + urea) DESs have been explored here via time-resolved fluorescence measurements of solute-centred dynamics, and atomistic simulations of density relaxation and displacement distribution profiles.

4.2. Experimental Details

4.2.1 Sample Preparation

Laser grade coumarin 153 (C153) was used as received (Exciton). Trans-2-[4-dimethylamino)styryl]benzothiazole (DMASBT), a fluorescence probe with much shorter excited state average lifetime[12,47] than that of C153, was used (as received[48]) for an investigation of solution spatial heterogeneity via monitoring the excitation wavelength ($\lambda_{exc.}$) dependence of fluorescence emission of dissolved DMASBT. Acetamide ($\geq$99%, SRL, India), urea (>99%, SRL, India) were dried (~300 K) under mild vacuum overnight before use.

Samples were prepared by following the method described in details elsewhere.[9-12,14,15] In brief, the required amount of DES components were mixed together in volumetric flasks, sealed, and heated using a hot water bath at a temperature around ~355 K (Julabo, model F32) until the mixtures became completely molten. An aliquot of a given molten DESs was then quickly transferred into a pre-heated quartz cuvette (1 cm path length) which was pre-stained with dye (C153/DMASBT) grains and sealed. A few drops of (dye+hexane) solution was used for this 'dye-staining' followed by

removal of the career solvent (hexane) by gently blowing mild-hot air through the cuvette. Subsequently, the cuvette containing the sample and dye was brought near the experimental temperature via using a water-bath. Care was taken to ensure complete dissolution of the probe into the DES sample, maintain a dye (C153/DMASBT) concentration $\leq 10^{-5}$ M in the solution under investigation. Spectral data were recorded after allowing the sample for about half-an-hour to equilibrate with pre-heated sample chamber at a designated temperature (328 K to 353 K at an interval of 5 K). A few samples were bubbled with dry N_2 gas before data collection but did not produce any difference in data with those collected with the un-bubbled samples.

4.2.2. Data Collection and Analyses for Absorption, Steady State and Time Resolved Fluorescence Studies

Steady state absorption spectra and fluorescence spectra were collected with a UV-visible spectrophotometer (UV-2450, Shimadzu) and a Fluoromax-3, Jobin-Yvon (Horiba) fluorimeter respectively. Time correlated single photon counting (TCSPC) based set-up was used as before[10-12] (LifeSpec-ps, Edinburgh Instruments) for time-resolved fluorescence measurements which produced a pulse-width (full-width-at-half-maximum) of ~70 ps when an aqueous solution of non-dairy creamer was used as a scattering medium at the excitation wavelength of 409 nm. For measurements using C153, we used 409 nm light for excitation. Steady state spectroscopic data were then processed and analysed by following the method described elsewhere.[49-53]

Time resolved fluorescence anisotropy ($r(t)$) measurements were performed via following the standard protocol[54-56] mentioned in Chapter 2. An iterative reconvolution algorithm[57] was used to simultaneously fit the collected parallel (I_{para}) and perpendicular (I_{perp}) decays. The geometric factor (G) was obtained via tail matching and found to be 1.15 ± 0.1. Dynamic anisotropic decays thus obtained were found to fit to bi-exponential functions of time, and the average rotation times ($\langle \tau_r \rangle$) were then obtained via time-integration, $\langle \tau_r \rangle = \int_0^\infty dt \left[r(t)/r(0) \right] = \int_0^\infty dt \sum_{i=1}^{2} a_i \exp(-t/\tau_i)$, with $\sum_i a_i = 1$ and the initial anisotropy, $r(0) = 0.376$ for C153.[54] Note here that Stokes shift

dynamics[45] in these DESs was found to be too fast to be detected by the present set-up. However, magnitudes of dynamic Stokes shifts for C153 were estimated[58] using steady state absorption and emission spectra. Density, viscosity and glass transition temperature (T_g) for these systems were measured by following the procedures described elsewhere.[14] While Table B4 (Appendix B)[59] summarizes the composition dependent density and viscosity values for the temperature range considered, Figure A4 provides a representative scan obtained from differential scanning calorimetric measurements of T_g for these DESs.

4.3. Results and Discussion

4.3.1. Steady state spectral characteristics

Steady state absorption and emission spectra of C153 in these DESs at different compositions (at a fixed temperature) and temperatures (at a fixed composition) are presented in Figures A5 and A6[59] which indicate a near-invariance with both mixture composition and temperature. A more clear representation of this insensitivity (within ± 100 cm^{-1}) is provided in Figure 4.1 where the absorption and emission spectral peak frequencies, and widths (full-width-at-half-maxima)[60,61] are shown as a function of temperature. Although these measurements are done within a narrow composition range, the observed spectral insensitivity is probably reflecting preferential solvation of dissolved C153 by the more polar component (ε_0 of acetamide and urea are ~60 and ~3, respectively) in the solution mixture. A more interesting aspect here is the temperature-independence of the spectral frequencies because temperature is known to frustrate the static correlations at the collective (that is, long wavelength) limit and hence reduce ε_0.[62-64] Note however that these spectral characteristics (frequencies and widths) are similar in magnitudes to those obtained for C153 in (acetamide + electrolyte) DESs[10,12] as acetamide has been the dominant component in all these melt mixtures.

Figure 4.1

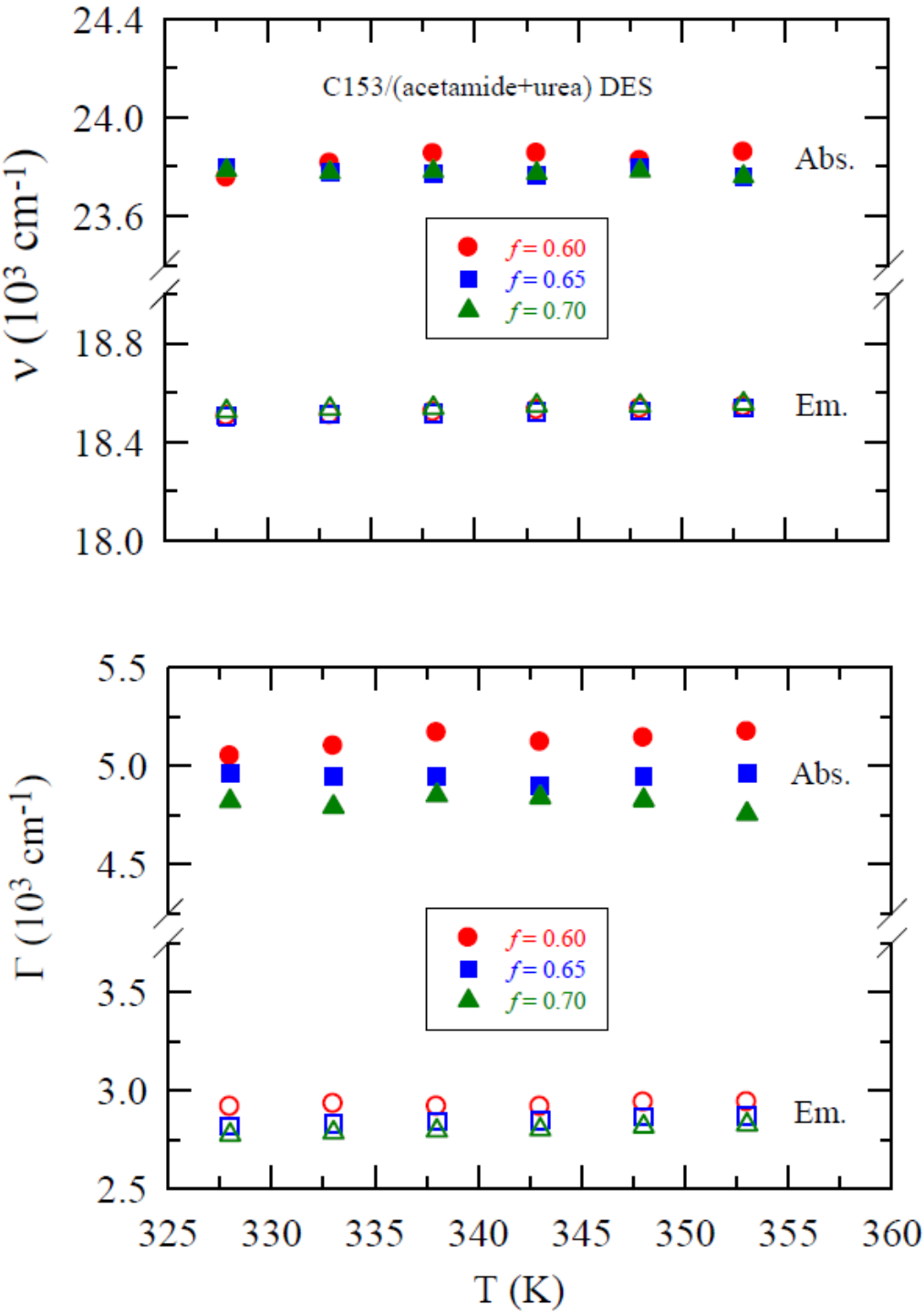

Figure 4.1: Temperature dependent spectral characteristics of C153 in [$f$$CH_3CONH_2$+ (1-$f$)$NH_2CONH_2$] DESs at three different acetamide mole fractions (f). Upper panel shows the variation of peak frequency (ν) and lower presents the variation in spectral width (Γ, full width at half maximum) of absorption (filled symbols) and emission

spectra (open symbols) of C153 in these DESs at *f*= 0.6 (circles), 0.65 (squares) and 0.7 (triangles).

We next explore the presence of spatial heterogeneity in these (acetamide + urea) DESs as $\lambda_{exc.}$ dependent fluorescence emission measurements (of a dissolved probe) of (acetamide + electrolyte) DES[10,12] have revealed inhomogeneous solution state. Probe dependence of the extent of emission shift induced by $\lambda_{exc.}$ observed there suggests presence of domains with a distribution of relaxation times. As a competition between domain relaxation and probe's average excited state lifetime (τ_{life}) critically controls the detection of spatial heterogeneity through $\lambda_{exc.}$ dependence, we have employed two fluorescent probes (C153 and DMASBT) with sharply different τ_{life} (~5 ns for C153[45] and ~0.5 ns for DMASBT[12,47]) for our $\lambda_{exc.}$ dependent study of these DESs. Representative results are summarized in Figure 4.2 where a change in $\lambda_{exc.}$ by ~120 nm (see Figure A7 for the chosen $\lambda_{exc.}$ across the absorption spectra of these probes[59]) produces a variation of only ~100 cm^{-1} in the emission peak frequencies and widths for both these probes. Interestingly, a much larger variation in these spectral properties was observed earlier for (CH_3CONH_2 + $LiNO_3$/Br/ClO_4) DESs and attributed to the presence of spatial heterogeneity of solution structure.[65,66] Given the spectral resolution of our measurements ($\pm$ 200 cm^{-1}), a variation of only 100 cm^{-1} suggests that the associated density relaxation timescales are much faster than τ_{life} of these probes, making these systems to appear as 'homogeneous' within the lifetime of these probes.

Figure 4.2

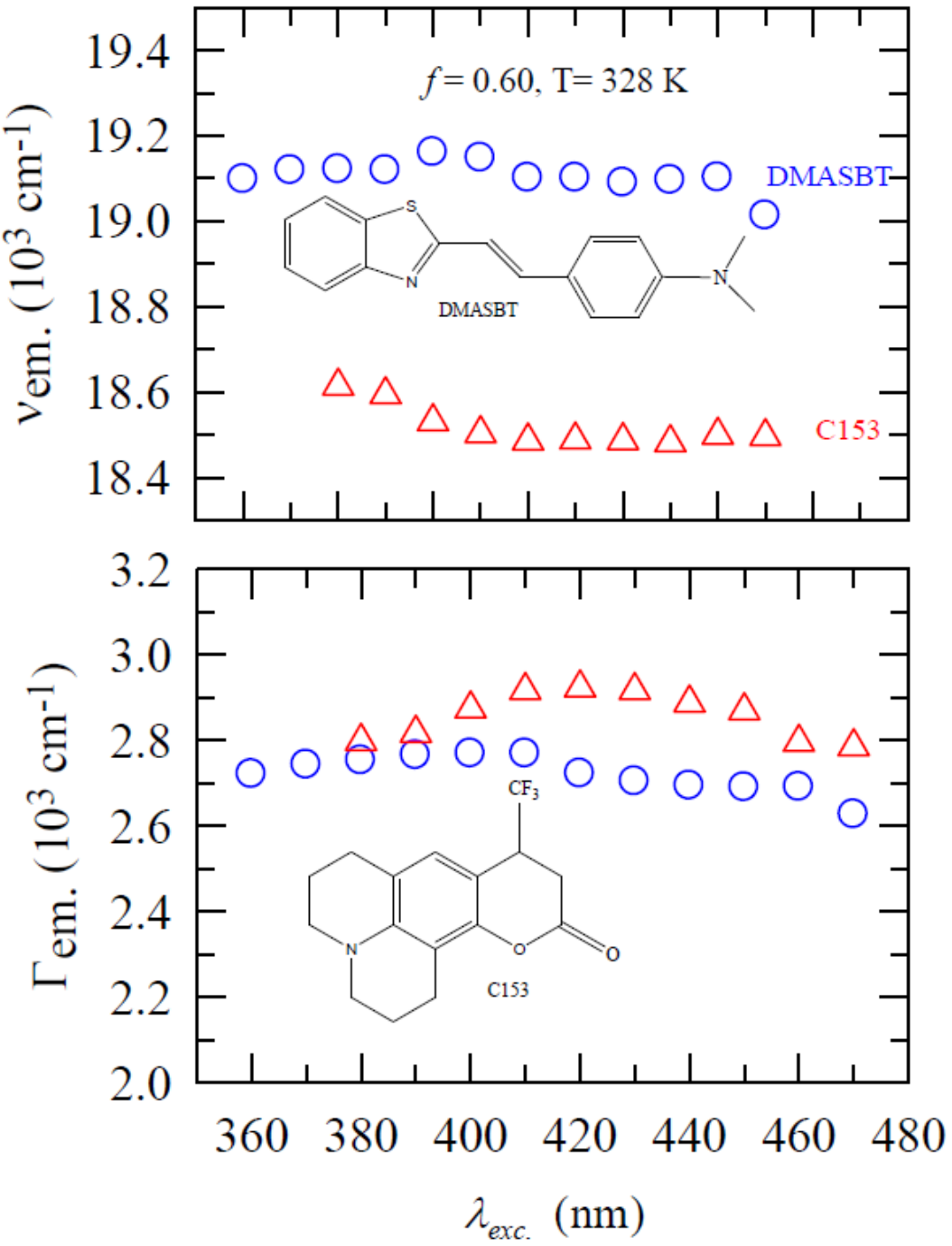

Figure 4.2: Excitation wavelength ($\lambda_{exc.}$) dependence of fluorescence emission peak frequencies, ν_{em} (upper panel), and full-width-at-half-maxima, Γ_{em} (lower panel) for DMASBT (circles) and C153 (triangles) in [$f$$CH_3CONH_2$+ (1-$f$)$NH_2CONH_2$] with f = 0.6 at ~328 K. Chemical structures of DMASBT and C153 are also shown as insets.

4.3.2. Time-resolved fluorescence measurements

As already shown,[10-12,87] fractional viscosity dependence of average solvation and rotation times measured via time-resolved fluorescence measurements may indicate presence of temporal (or dynamic) heterogeneity in a given medium. Since solvation dynamics is too fast to be detected by the present set-up, we can provide only the estimated magnitudes of dynamic Stokes shift for C153 in these systems. Table B5[59] summarizes the estimated shift values at three different compositions for the temperature range, 328-353 K. Note in this table that the estimated shift values are within the range, ~750-900 cm^{-1}, which is similar to those reported[10] for (amide +electrolyte) DESs at higher temperatures. Although hydrodynamics predict presence of a nanosecond diffusive timescale in these systems ($\sigma^2/D_T \approx 1$ ns at ~330 K for a particle of diameter, $\sigma \sim 4$Å, diffusing through a medium with viscosity, $\eta \sim 10$ cP), it is interesting to note the absence of such a slow component in the present measurements. This is in contrast to our earlier findings for (amide + electrolyte) systems,[10,12,14,15] and may arise due to the extensive participation of the collective H-bond network of the present DESs and other fast modes[39-42] to the solvation process. Suitable dielectric relaxation measurements and simulations of density relaxations are required to understand the origin of such fast solvation response in these systems.

Rotational relaxation of the same dissolved solute is, however, much slower and can be detected in our experiments. Figure 4.3 provides a representative example where collected $r(t)$ decays at two different temperatures for C153 in the present DES at 0.6 acetamide mole fraction are shown. As indicated by dynamic Stokes shift measurements, these and other anisotropy decays collected at different compositions and temperatures contain a component much faster than the time-resolution (~70 ps) of our set-up, and are bi-exponential functions of time. Reasonable bi-exponential description of all the collected $r(t)$ decays have been found after constraining the faster time constant to 15 ps whose amplitude, depending upon composition and temperature, varies between ~25-75%. The rest is constituted by a slower component with time constant in 100-300 ps range (see Table B6).[59] Subsequently, the coupling between the solute rotation and the medium viscosity is explored in Figure 4.4 where the logarithm of average rotation times measured at all the compositions and temperatures considered are shown as a function of logarithm of temperature-reduce

viscosity. For a comparison, hydrodynamic slip predictions for rotation times of C153, with its shape factor incorporated,[54] in these DESs are also shown in the same figure. The increase of the measured average rotation times ($\langle \tau_r \rangle$) with viscosity can be

Figure 4.3

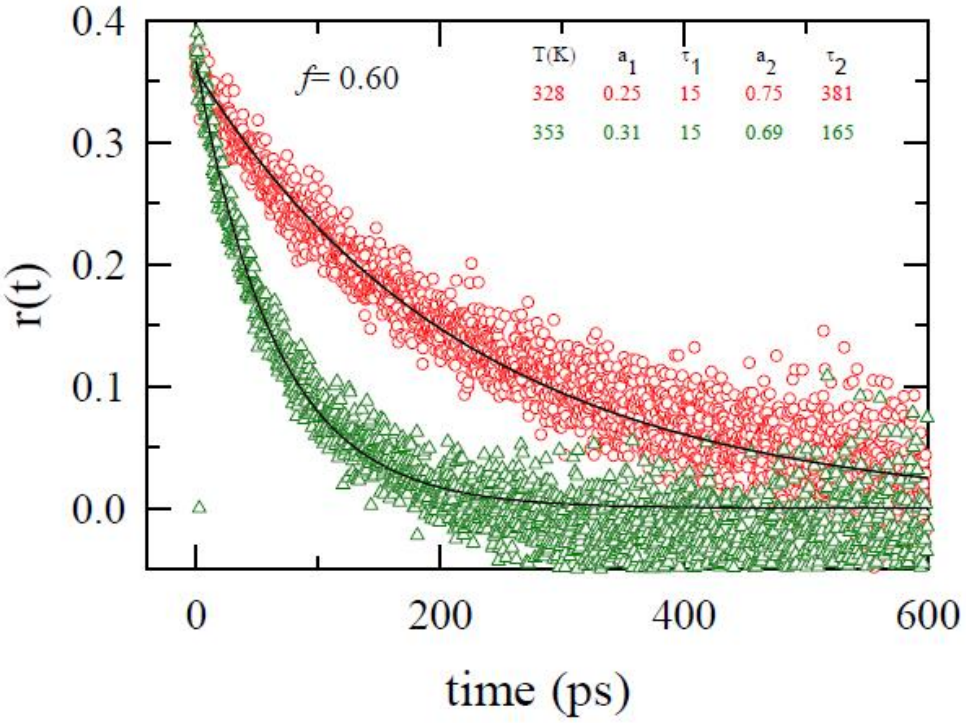

Figure 4.3: Representative anisotropy decays at 328 K (red) and 353K (green) for C153 in [$f$$CH_3CONH_2$+ (1-$f$)$NH_2CONH_2$] with f = 0.6. Circles denote the experimental data and solid lines fits through them. Fit parameters are shown in the inset. Time constants (τ_i) are in the unit of picoseconds. The Goodness-of-fit parameters (χ^2) in these two temperatures are 1.06 and 1.09 for 328 and 353K respectively.

described by an average linear fit (shown in the inset) which suggests a viscosity dependence of the following form, $\langle \tau_r \rangle \propto (\eta/T)^p$ with $p = 0.96$. The fraction power (p) maintained its value of near unity even when the measured $\langle \tau_r \rangle$ data were analysed separately (see Figure A8).[59] Such a near-hydrodynamic viscosity

dependence for average rotation times strongly suggests temporal homogeneity of the DESs under study, and is in sharp contrast with our earlier findings for (amide + electrolyte) systems.[10,12,15] Arrhenius-type of temperature dependence for the average rotation rates ($\langle \tau_r \rangle^{-1}$) has been observed (see Figure A9)[59] and the associated average activation energy (E_a) is found to be ~31.6 kJmol^{-1}. Interestingly, a similar E_a has been found earlier for (CH_3CONH_2 + $LiBr/NO_3$) DESs[12] where pronounced heterogeneity characterized the solution structure and dynamics.

It is evident, therefore, that both the steady state and time-resolved fluorescence measurements of [$f$$CH_3CONH_2$+(1-$f$)$NH_2CONH_2$] DESs using a dipolar solute suggest homogeneity in solution structure and dynamics. It would be instructive to learn, via simulations, whether such homogeneity is also preserved for the un-doped system, that is, the DESs in the absence of any dipolar solute.

Figure 4.4

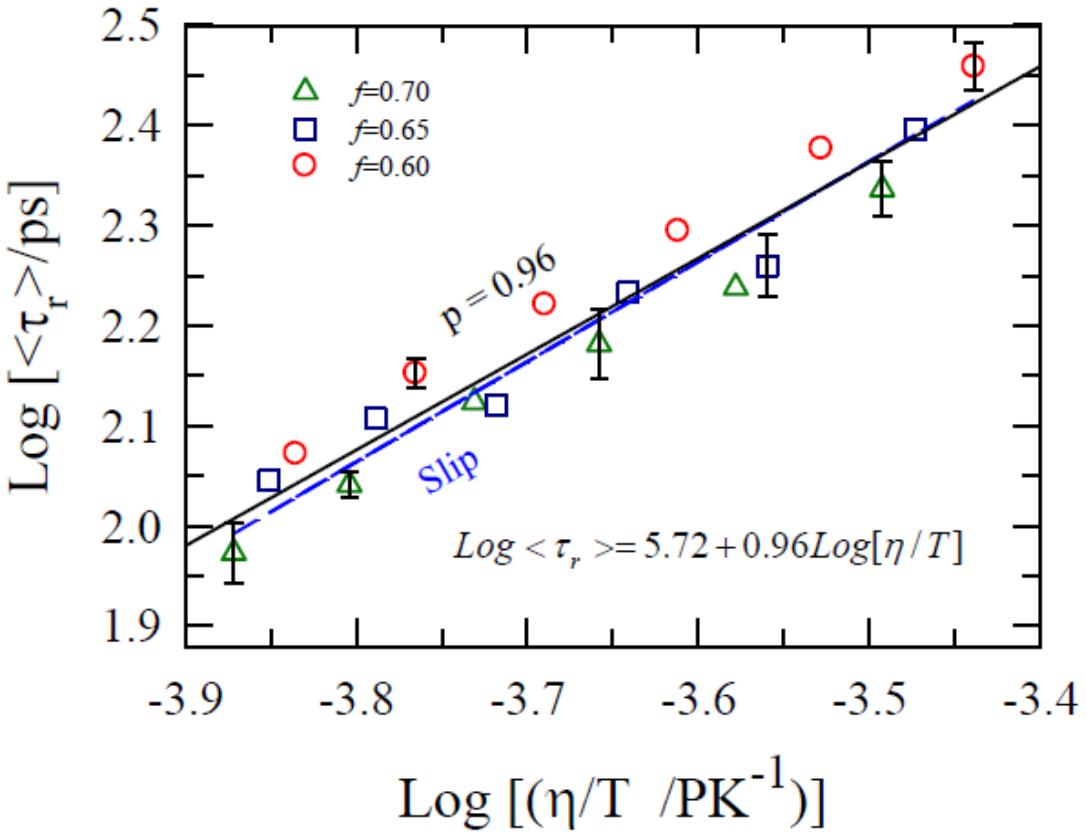

Figure 4.4: Viscosity dependence of measured rotation times ($\langle \tau_r \rangle$) for C153 in [*f*CH_3CONH_2+ (1-*f*)NH_2CONH_2] at various temperatures, and comparison to hydrodynamic predictions using slip boundary condition (SBC). Measured rotation times are shown as a function of temperature-reduced viscosity (η/T) in a log-log fashion. Broken blue lines represent the hydrodynamic (Debye-Stokes-Einstein, DSE) predictions, $\tau_r^{DSE} = (V\eta/k_BT)fC$, with C153 volume V=246 Å^3, shape factor (assuming ellipsoid) f = 1.71, and solute-solvent coupling parameter C = 0.24 (for SBC). Solid black line denotes the fit through the measured data. Stick predictions are much slower and thus not shown.

4.4. Conclusion

In conclusion, our combined steady state and time-resolved fluorescence study indicate that the (acetamide + urea) deep eutectics studied here are both spatially and dynamically homogeneous systems although these systems have been studied at a temperature range much lower than the individual melting temperatures of the constituents. This is in sharp contrast to earlier findings for (acetamide + electrolyte) deep eutectics, and indicates qualitative difference between these two classes of deep eutectic systems. The observation of the Stokes' shift dynamics in these DESs is too fast to be detected by the present measurements.

The qualitative difference between these two classes of DESs may be understood by comparing the H-bond formation and dynamics[19] between these DESs. Study of low frequency collective dynamics employing Kerr spectroscopic measurements[19] and orientational motions via dielectric relaxation measurements of these systems can reveal important information on inter- and intra-species association of these systems. Development of semi-molecular theories for understanding the orientational relaxation and Stokes shift dynamics along the line of what has been done for binary mixtures of ionic liquids with common solvents[68-71] are required to provide microscopic

understanding of relaxation dynamics of these exciting media. Smart applications of DESs as designer solvents demand such a robust knowledge.

References

1. Wagle, D. V.; Zhao, H.; Baker, G. A. *Acc. Chem. Res.* **2014**, *47*, 2299.
2. Zhang, Q. H.; Vigier, K. D.; Royer, S.; Jerome, F. *Chem. Soc. Rev.* **2012**, *41*, 7108.
3. Abbott, A. P.; Capper, G.; Davies, D. L.; Rasheed, R. K.; Tambyrajah, V. *Chem. Commun.* **2003**, 70.
4. Abbott, A. P.; Boothby, D.; Capper, G.; Davies, D. L.; Rasheed, R. K. *J. Am. Chem. Soc.* **2004**, *126*, 9142.
5. Francisco, M.; Van den Bruinhorst, A.; Kroon, M. C. *Angew. Chem., Int. Ed.* **2013**, *52*, 3074.
6. Francisco, M.; Van den Bruinhorst, A.; Kroon, M. C. *Green Chem.* **2012**, *14*, 2153.
7. Zhao, H.; Baker, G. A. *J. Chem. Technol. Biotechnol* **2013**, *88*, 3.
8. Carriazo, D.; Serrano, M. C.; Gutierrez, M. C.; Ferrer, M. L.; del Monte, F. *Chem Soc Rev* **2012**, *41*, 4996.
9. Biswas, R.; Das, A.; Shirota, H. *J. Chem. Phys.* **2014**, *141*, 134506..
10. Guchhait, B.; Das, S.; Daschakraborty, S.; Biswas, R. *J. Chem. Phys.* **2014**, *140*, 104514.
11. Das, A.; Das, S.; Biswas, R. *Chem. Phys. Lett.* **2013**, *581*, 47.
12. Guchhait, B.; Daschakraborty, S.; Biswas, R. *J. Chem. Phys.* **2012**, *136*, 174503.
13. Pal, T.; Biswas, R. *Chem. Phys. Lett.* **2011**, *517*, 180.
14. Gazi, H. A. R.; Guchhait, B.; Daschakraborty, S.; Biswas, R. *Chem. Phys. Lett.* **2011**, *501*, 358.
15. Guchhait, B.; Gazi, H. A. R; Kashyap, H. K.; Biswas, R. *J. Phys. Chem. B* **2010**, *114*, 5066.
16. D'Agostino, C.; Harris, R. C.; Abbott, A. P.; Gladden, L. F.; Mantle, M. D. *Phys. Chem. Chem. Phys.* **2011**, *13*, 21383..
17. Kerridge, D. H. *Chem. Soc. Rev.* **1988**, *17*, 181.

18. Dixon, D. A.; Dobbs, K. D.; Valentini, J. J. *J. Phys. Chem.* **1994**, *51*, 13435.
19. Das, S.; Biswas, R.; Mukherjee, B. *J. Phys. Chem. B* **2015**, *119*, 274.
20. Hua, L.; Zhou, R.; Thirumalai, D.; Berne, B. J. *Proc. Natl. Acad. Sci. USA* **2008**, *105*, 16928.
21. Das, A.; Mukhopadhyay, C. *J. Phys. Chem. B.* **2009**, *113*, 12816.
22. Bandyopadhyay, D.; Mohan, S.; Ghosh, S. K.; Choudhury, N. *J. Phys. Chem. B.* **2014**, *118*, 11757.
23. Sagle, L. B.; Zhang, Y.; Litosh, V. A.; Chen, X.; Cho, Y.; Cremer, P. S. *J. Am. Chem. Soc.* **2009**, *131*, 9304.
24. Bennion, B. J.; Daggett, V. *Proc. Natl. Acad. Sci. USA* **2003**, *100*, 5142.
25. Walbrugh, L. *Amitraj Solid Dosage Form*. Master of Science Thesis, University of Pretoria, Pretoria, South Africa, **2006**.
26. Rajkhowa, S.; Das, A.; Mahiuddin, S.; Biswas, R. *J. Chem. Eng. Data* **2012**, *57*, 3467.
27. Van der zwan, G.; Hynes, J. T. *Chem. Phys.* **1991**, *152*, 169.
28. Van der Zwan, G.; Hynes, J. T. *J. Chem. Phys.* **1983**, *78*, 4174.
29. Nitzan, A. *Chemical Dynamics in Condensed Phases*; Oxford Univ. Press: Oxford, 2006.
30. Pradhan, T.; Biswas, R. *J. Phys. Chem. A* **2007**, *111*, 11514.
31. Pradhan, T.; Gazi, H. A. R; Biswas, R. *J. Chem. Phys.* **2009**, *131*, 054507.
32. Biswas, R.; Bagchi, B. *J. Chem. Phys.* **1996**, *105*, 7543.
33. Murarka, R. K.; Bhattacharyya, S.; Biswas, R.; Bagchi B. *J. Chem. Phys.* **1999**, *110*, 7365.
34. Stafford, O. F. *J. Am. Chem. Soc.* **1933**, *55*, 3987.
35. Wallace, R. A. *Inorg. Chem.* **1972**, *11*, 414.
36. Kumler, W. D.; Fohlen, G. M *J. Am. Chem. Soc.* **1942**, *64*, 1944.
37. Subha Mahadevi, A.; Indra Neela, Y.; Narahari Sastry, G. *Phys. Chem. Chem. Phys.* **2011,** ***13***, 15211.
38. Carr, J. K.; Buchanan, L. E.; Schmidt, J. R.; Zanni, M. T.; Skinner, J. L. *J. Phys. Chem. B* 2013, *117*, 13291.
39. Bagchi, B.; Biswas, R. *Adv. Chem. Phys.* **1999**, *109*, 207.
40. Roy, S.; Bagchi, B. *J. Chem. Phys.* **1993**, *99*, 1310.
41. Roy, S.; Bagchi, B. *J. Chem. Phys.* **1993**, *99*, 9938.
42. Biswas, R.; Bagchi, B. *J. Phys. Chem.* **1996**, *100*, 1238.

43. Kashyap, H. K.; Pradhan, T.; Biswas, R. *J. Chem. Phys.* **2006**, *125*, 174506.
44. Daschakraborty, S.; Pal, T.; Biswas, R. *J. Chem. Phys.* **2013**, *139*, 164503.
45. Horng, M. L.; Gardecki, J. A.; Papazyan, A.; Maroncelli, M. *J. Phys. Chem.* **1995**, *99*, 17311.
46. Pal, T.; Biswas, R. *J. Chem. Phys.* 2014, *141*, 104501.
47. Kondo, M.; Li, X.; Maroncelli, M. *J. Phys. Chem. B* **2013**, *117*, 12224.
48. DMASBT was used as received as a gift from Prof. Mark Maroncelli., Penn. State University, USA.
49. Pradhan, T.; Ghoshal, P.; Biswas, R. *J. Phys. Chem. A* **2008**, *112*, 915.
50. Gazi, H. A. R; Biswas, R. *J. Phys. Chem. A* **2011**, *115*, 2447.
51. Biswas, R.; Das, A. R.; Pradhan, T.; Touraud, D.; Kunz, W.; Mahiuddin, S. *J. Phys. Chem. B* **2008**, *112*, 6620.
52. Guchhait, B.; Biswas, R. *J. Chem. Phys.* **2013**, *138*, 114909.
53. Guchhait, B.; Biswas, R.; Ghorai, P. K. *J. Phys. Chem. B* **2013**, *117*, 3345.
54. Horng, M. L.; Gardecki, J. A.; Maroncelli, M. *J. Phys. Chem. A* **1997**, *101*, 1030.
55. Pradhan, T.; Ghoshal, P.; Biswas, R. *J. Chem. Sci.* **2008**, *120*, 275.
56. Sarma, N.; Borah, J. M.; Mahiuddin, S.; Gazi, H. A. R.; Guchhait, B.; Biswas, R. *J. Phys. Chem. B* **2011**, *115*, 9040.
57. Cross, A. J.; Fleming, G. R. *Biophys. J.* **1984**, *46*, 45.
58. Fee, R. S.; Maroncelli, M. *Chem. Phys.* **1994**, *183*, 235.
59. See Appendix for composition dependent density and viscosity values for the temperature range 328-353 K, a representative DSC scan showing T_g, absorption and emission spectra of C153 at various compositions (at a given temperature) and temperatures (at a given composition), estimated dynamic Stokes shifts for C153 at three different compositions, figure showing plots of measured $\langle \tau_r \rangle$ versus η/T at different acetamide mole fractions, and Arrhenius plots for measured $\langle \tau_r \rangle$.
60. Biswas, R.; Lewis, J. E.; Maroncelli, M. *Chem. Phys. Lett.* **1999**, *310*, 485.
61. Lewis, J. E.; Biswas, R.; Robinson, A. G.; Maroncelli, M. *J. Phys. Chem. B* **2001**, *105*, 3306.
62. Ronne, C.; Thrane, L.; Astrand, P. -O.; Wallqvist, A.; Mikkelsen, K. V.; Keiding, S. O. *J. Chem. Phys.* **1997**, *107*, 5319.

63. Petrowsky, M.; Frech, R. *J. Phys. Chem. B* **2009**, *113*, 16118.

64. Hunger, J.; Stoppa, A.; Schrödle, S.; Hefter, G.; Buchner, R. *Chemphyschem* **2009**, *10*, 723.

65. Mandal, P. K.; Sarkar, M.; Samanta, A. *J, Phys. Chem. A* **2004**, *108,* 9048.

66. Hu, Z.; Margulis, C. J. *Proc. Natl. Acad. Sci. U. S. A.* **2006**, *103,* 831.

67. Ediger, M. D. *Annu. Rev. Phys. Chem.* **2000**, *51*, 99.

68. Pal, T.; Biswas, R. *J. Chem. Phys.* **2014**, *141,* 164502.

69. Daschakraborty, S.; Biswas, R. *J. Phys. Chem. B* **2014**, *118,* 1327.

70. Daschakraborty, S.; Biswas, R. *J. Phys. Chem. B* **2011**, *115*, 4011.

71. Daschakraborty, S.; Biswas, R. *J. Chem. Phys.* **2014**, *140,* 014504.

Chapter 5

Urea-Induced 'Homogenization' of Ionic Deep Eutectics: Signatures from Time-Resolved Fluorescence Measurements

5.1. Introduction

Molten mixtures composed of amide and electrolyte are industrially important reaction media because of economic viability, easy to prepare and transport, low moisture-sensitivity, and in some cases for their biodegradable nature[1-9]. These systems are known as deep eutectics as multiple constituents of high individual melting temperatures (T_ms), upon mixing and heating, create stable liquid solutions at a temperature much lower than individual T_ms[3,6-8,10-13]. Acetamide in presence of electrolytes can be brought into liquid phase at or around room temperature and serves as an example of ionic deep eutectics. Exquisite solvent properties[14-18] of acetamide due to the presence of several functional groups- methyl, carbonyl, amide and tautomeric hydroxyl group – have rendered acetamide/electrolyte deep eutectics tremendous application potential. The high dielectric constant ($\varepsilon_0 \approx 60$) combined with high dipole moment (3.7 D) makes acetamide excel over water as a solvent[17]. Note acetamide is a room temperature solid which melts at 353 K, and boils at 495 K[19]. Applications of these deep eutectics can be found in thermal salt cells, electricity production and electrodeposition.[20,21] Of late, these deep eutectics have also found applications in synthesis of nanomaterials, semi-conductors, and other functional materials.[1-5,22,23].

Because of extensive interaction between ions and acetamide molecules, and inter-amide hydrogen bonding (H-bonding), experimental studies have found signatures of solution micro-heterogeneity reminiscent of those in supercooled systems near glass transition.[24] Experimental results have often been rationalized in terms of microscopic regions consisting of amorphous and liquid-like domains.[25]. Viscoelastic, dielectric relaxation and nuclear magnetic resonance studies have repeatedly provided evidences

for such micro-heterogeneous solution structures.[11,25-27] These experiments suggest a high static dielectric constant and extremely slow relaxation times.[11-13,25-27] Recent fluorescence measurements using a dipolar solute probe,[28-33] in contrast, have suggested average polarity of these ionic deep eutectics is similar to that of liquid formamide at ambient condition. In addition, these measurements have provided strong evidences for both spatial and temporal heterogeneities. Fractional power-law dependence of solute rotation and solvation rates on solution viscosity reported by these experiments also reflect a sort of translation-rotation decoupling, a feature typical of deeply super-cooled liquids near glass transition.[24,34-37]

In this chapter we have investigated how urea ($CO(NH_2)_2$) alters the heterogeneity aspect of acetamide/electrolyte ionic deep eutectics. Lithium nitrate ($LiNO_3$) and lithium bromide (LiBr) have been chosen as electrolytes here because pronounced signatures of both spatial and temporal heterogeneities have been found in presence of these salts[30]. The composition of the system studied is as follows: $0.1LiNO_3$+0.9[*f* Urea+ (1- *f*) Acetamide] where '*f* ' is varied from 0.25 to 0.60 and 0.1LiBr+0.9[*f* Urea+ (1- *f*) Acetamide] where '*f* ' is varied from 0.20 to 0.60. We have not varied *f* further because beyond this *f*-range the system is no more a liquid at convenient temperatures. Temperature dependant studies are then carried out in the range, $303 \le T/K \le 343$, in order to examine the nature of viscosity coupling to relaxation rates in these systems. Density, viscosity and electrical conductivity data for these systems in the similar temperature range are already available for $LiNO_3$[38] where the trends of transport properties are analyzed according to the Vogel-Fulcher-Tammann[39-41] description. Addition of urea has been found to introduce remarkable influence on the steady state and time-resolved spectral data, promoting dramatic difference in solution effects on relaxation kinetics between ionic acetamide deep eutectics in the presence and absence of urea. For example, significant excitation wavelength ($\lambda_{exc.}$) dependence of steady state fluorescence emission and departure from hydrodynamics of average relaxation rates found in the absence of urea is removed completely upon addition of urea.

5.2. Experimental Sections

5.2.1. Sample Preparation

Laser grade C153 from Exciton was used without further purification. Acetamide (≥ 99%, SRL, India), lithium nitrate (≥99.5%, Sigma Aldrich), lithium bromide (≥99%, Sigma Aldrich) and urea (>99%, Merck Specialties, India) were vacuum-dried (300 K) for 24 hours before use. Since LiBr is very hygroscopic it is better to represent it as $LiBr.xH_2O$, where 'x' stands for the unknown amount of water absorbed during handling, although care was exercised during sample preparation and subsequent measurements. Formamide (99%, Sigma Aldrich) is used without further purification. Samples were prepared by quick transferring of the pre-weighed amounts of each of these compounds into a suitable volumetric flask for a given composition, and sealed by teflon tape and parafilm. Each volumetric flask containing sample was then heated on a hot plate at ~330 K to initiate melting of the solid mixture. Once molten and transparent liquid phase obtained, heat-source was removed and the liquid solutions were allowed to cool down to room temperature (~298 K) slowly. An aliquot (~3 ml) of this stock sample solution was then transferred into a pre- heated quartz cuvette having 1 cm path length containing C153 grains and sealed. The concentration of C153 in the measured solution was always maintained at $\leq 10^{-6}$ M. Spectral data collection began only after allowing sufficient time for temperature equilibration of the sample-containing cuvette in the sample-chamber. Random check with samples bubbled with dry N_2 gas did not produce data any different from those collected with the un-bubbled cases.

Densities (ρ) of the samples were measured by an automated temperature-controlled density-cum-sound velocity analyzer (Anton Paar, model DSA 5000) at required temperatures ($\pm$ 0.5K). Viscosities (η) of the DES systems were measured by AMVn automated micro-viscometer from Anton Paar (falling ball method). The composition dependent viscosities and densities at different temperatures are provided in Table B7.

5.2.2. Data Collection and Analyses for Stokes' Shift Dynamics

Steady state absorption spectra were collected with UV-visible spectrophotometer (UV-2450, Shimadzu) whereas steady state fluorescence spectra were collected with Fluoromax-3, Jobin-Yvon (Horiba) fluorimeter. Time Correlated Single Photon Counting spectrophotometer (LifeSpec-ps) from Edinburgh Instruments (Livingston), U.K was used to collect time resolved fluorescence decays. To excite solute probe (C153) excitation source of 409 nm was used. All data were collected with a bandpass of ±2nm. The full width at half maximum (FWHM) of instrument response function (IRF) collected using water was ~ 70 ps. Other details can be found in Chapter 2. Desired experimental temperature was maintained via a temperature-controller (Julabo, F32) and a Peltier heater (LFI-3751).

For solvation dynamics studies, we collected typically 18-20 decays at equally spaced wave-lengths throughout the steady-state emission spectrum of the dissolved solute in these molten mixtures at magic angle (54.7˚) with a vertically polarized excitation beam. Data collection was continued until the peak count reached 5000 (dark count~ 10). This provides a good statistics for fitting of the collected data. Collected emission decays were first deconvoluted from the instrument response function (IRF) and fitted to multi-exponential functions of time using an iterative reconvolution algorithm.[42,43] Time resolved emission spectra (TRES) were reconstructed from these fitted decays by normalizing with steady state emission spectra. Such fitting procedure[42-46] can significantly sharpen the effective resolution for capturing dynamics even ~3-4 times faster than the IRF. With this instrumental resolution we might still miss the faster components of solvent response but is expected to capture the long time dynamics well.

Time dependent solvation of the laser excited probe was then followed by constructing the normalized spectral or solvation response function:[42]

$$S(t) = \frac{\nu(t) - \nu(\infty)}{\nu(0) - \nu(\infty)}, \qquad (5.1)$$

where ν(x) denotes the emission frequency at time t; ν(0) denotes emission frequency immediately after excitation when solvent relaxation have yet not started but the vibrational relaxation is supposed to be completed; ν(∞) denotes frequency of the emission spectrum after solvent relaxation is complete. Therefore, it is expected that ν(∞) should be equal to steady state emission frequency of the same probe. But there may be discrepancy where the steady state emission doesn't come from the completely relaxed state. This may happen in slow viscous systems where microscopic spatial heterogeneity is also present. For the systems studied here, the difference between the steady state and time resolved spectra was about 150-400 cm^{-1} (± 250cm^{-1}). Subsequently, average solvation time, $\langle \tau_s \rangle$ was obtained via multi-exponential fits to the measured S(t) as follows, $\langle \tau_s \rangle = \int_0^\infty dt\, S(t) = \int_0^\infty dt \sum_{i=1}^{n} a_i \exp(-t/\tau_i) = \sum_i^n a_i \tau_i$, where $\sum_i^n a_i = 1$.

5.2.3. Data Collection and Analyses for Time Resolved Anisotropy, $r(t)$

Emission decays for time resolved fluorescence anisotropy measurements were collected at the peak of steady state emission spectrum to ensure that there is minimum loss of anisotropy of fast decay due to solvent reorganization. Three decays namely the vertical (I_{para}), horizontal (I_{perp}) and magic angle polarized emission with respect to the excitation of the solute by vertically polarized light were collected for each measurements. The magic angle decay was first deconvoluted from the IRF and fitted to multi-exponential function of time, followed by fitting parallel (I_{para}) and perpendicular (I_{perp}) decays using an iterative reconvolution algorithm.[47] Time resolved fluorescence anisotropy, $r(t)$ was then constructed as follows:[47]

$$r(t) = \frac{I_{para}(t) - GI_{perp}(t)}{I_{para}(t) + 2GI_{perp}(t)} \quad , \tag{5.2}$$

The geometric factor (G-factor) was obtained by tail matching the parallel and perpendicular intensity decays. The larger time constant of the magic angle decay fit was used for subsequent parallel and perpendicular decay fitting. Then we fit the anisotropy decay data by biexponential function of time of the following form

$$r(t) = r(0)[a_1 \exp(-t/\tau_1) + a_2 \exp(-t/\tau_2)] \, , \tag{5.3}$$

Where $a_1 + a_2 = 1$, and τ_1 and τ_2 are the two time constants associated with decay amplitudes a_1 and a_2 respectively. The initial anisotropy denoted by *r(0)* for C153 is fixed at 0.376 for all decay fitting.[48] The average rotational correlation time, $\langle \tau_r \rangle$, was then obtained via integrating the normalized function, $r(t)/r(0)$, and thus calculated analytically as, $\langle \tau_r \rangle = a_1\tau_1 + a_2\tau_2$

5.3. Results and Discussion

5.3.1. Steady State Absorption and Fluorescence Spectral Characteristics

A comparison between the steady state absorption and fluorescence emission spectra of C153 dissolved in deep eutectics with composition $0.10LiNO_3$+ 0.90[*f* Urea+ (1-*f*) Acetamide] at *f*= 0.60 and ~303 K with that of formamide (FA) is presented in Figure 5.1. Note spectra in these deep eutectics are both narrower and red-shifted than that in FA. This indicates added complexity in solute-medium interactions in these molten multi-component systems. Absorption and emission peak frequencies of C153 in melt mixture are 23.222 and 18.310 respectively (in the unit of $10^3 cm^{-1}$) and FA are 23.91 and 17.96; spectral widths, that is, full-widths-at-half-maxima are (in the unit of $10^3 cm^{-1}$): for absorption 4.261 (deep eutectics) versus 4.77 (FA) , and for emission 2.868 (deep

eutectics) versus 3.44 (in FA). Consequently, the relative Stokes' shift magnitudes

Figure 5.1

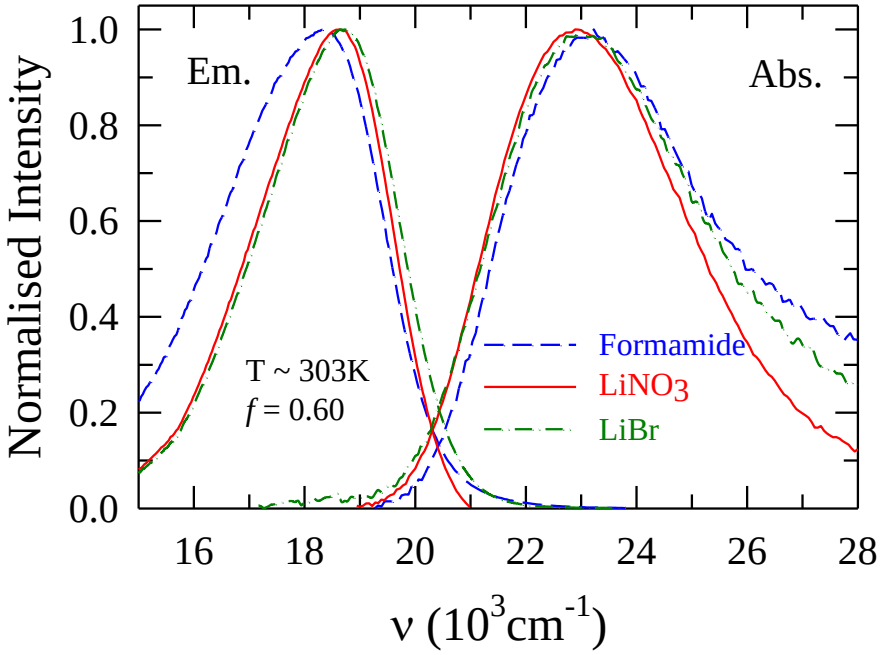

Figure 5.1: Steady state absorption and fluorescence emission spectra (color coded) of C153 (solute) dissolved in molten mixture 0.10$LiNO_3$/ LiBr + 0.90[*f* Urea+ (1-*f*) Acetamide] at *f* = 0.6 and formamide at 303K are shown.

(relative to that of heptane[49]) differs widely, being ~ 450cm^{-1} in the deep eutectics studied and ~1500cm^{-1} in FA. This is somewhat different from earlier observations in ionic acetamide deep eutectics[28-30,33] where a much closer resemblance to the formamide spectral properties was detected. This difference can be explained if we recall that the deep eutectics at this composition is a urea-dominated mixture, and the static dielectric constant of urea (solid)[50,51] is approximately 3.5 which is much lower than that of molten acetamide ($\varepsilon_0 \approx 60$)[17]. What is striking here is, however, the

absorption and emission spectral red-shifts are relative to those both in FA whose ε_0 is ~110[52] at ~300 K, and in the ionic acetamide deep eutectics in the absence of urea. These relative red-shifts indicate direct and enhanced solute-electrolyte/ion interaction in these urea containing deep eutectics. Note spectral widths in presence of urea in these ionic deep eutectics are narrower than those in the absence of urea. This suggests urea-induced homogeneity in solution structure of these deep eutectics.

Urea concentration dependence of spectral characteristics for C153 in these deep eutectics are presented in Figure 5.2 where absorption and emission peak frequencies (ν), spectral widths (Γ) and relative Stokes' shift are shown as a function of f. The f dependence of emission frequency at $t = \infty$ measured in dynamic Stokes shift experiments ($\nu(\infty)$) is also shown in the same figure. Interestingly, all these frequencies and widths exhibit near-insensitivity to the urea concentration in these molten mixtures, reflecting a very weak dependence of average solution polarity and structure on f. Note $\nu(\infty)$ for these deep eutectics are, however, slightly red-shifted (~ 200 cm^{-1}) than the corresponding steady state emission frequencies ($\nu_{em.}$) in these systems. This difference, $\nu_{em.} - \nu(\infty)$, is a signature of steady state emission arising from excited solute possessing incompletely solvent-relaxed configuration. The difference being limited within 200 cm^{-1} also suggests that the extent of slow solvent relaxation is not large in these molten mixtures. Urea concentration dependence of estimated[49] dynamic Stokes shift magnitudes, $\Delta\nu^t = \nu(0) - \nu(\infty)$, is shown in the lower panel of Figure 5.2 and compared against the relative steady state Stokes shift magnitudes, $\Delta\Delta\nu = \left[\nu_{abs.} - \nu_{em.}\right]^{deep\,eutectics} - \left[\nu_{abs.} - \nu_{em.}\right]^{heptane}$, for these molten mixtures. The effects of f - dependent slow solvent relaxation is reflected more quantitatively here.

Figure 5.2

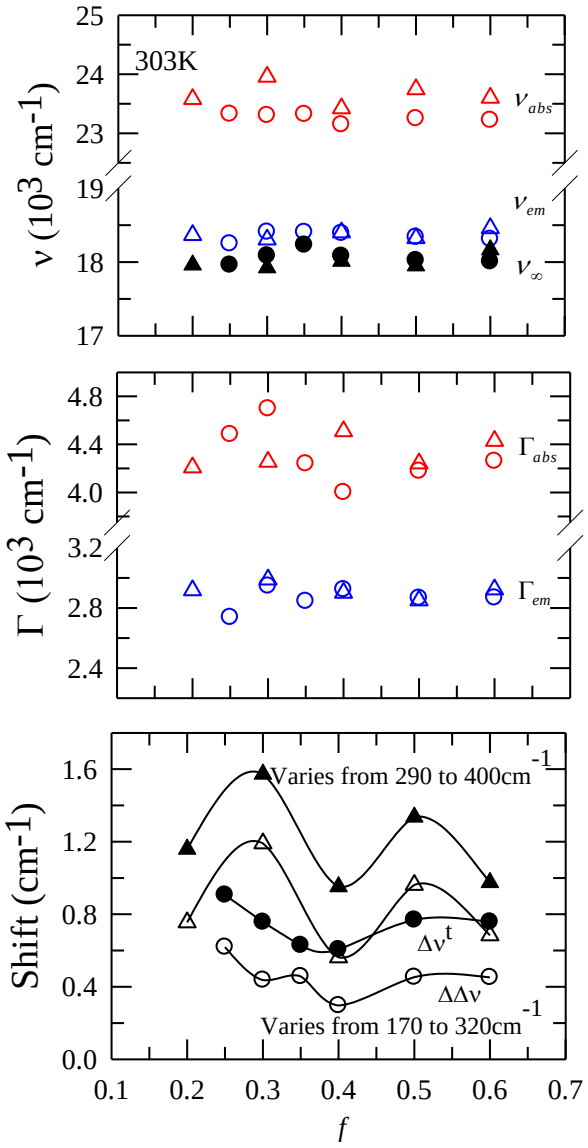

Figure 5.2: Spectral parameters at different fractions of Urea (color coded) are shown in this figure (circles for $LiNO_3$ and triangles for LiBr). Absorption and emission frequencies are shown in the upper panel, the full width at half maxima (Γ) in the middle panel and both steady state (unfilled symbols) and time resolved Stokes' shift (filled symbols) are shown in the lower panel.

The two shifts are defined as: $\Delta\Delta\nu = \left[\nu_{abs.} - \nu_{em.}\right]^{Mixture} - \left[\nu_{abs.} - \nu_{em.}\right]^{heptane} = \Delta\nu^{Mixture} - \Delta\nu^{heptane}$ and $\Delta\nu^{t} = \left[\nu(t=0)\right] - \left[\nu(t=\infty)\right]$, $\Delta\nu^{t}$ is essentially the Fee-Maroncelli method (Ref. 49) and $\Delta\nu^{heptane}$ is measured as 4230 cm^{-1}.

Excitation wavelength ($\lambda_{exc.}$) dependences of $\nu_{em.}$ for C153 in these deep eutectics and the associated spectral widths (Γ) are shown in Figure 5.3. These results correspond to f =0.3 and 0.6 at ~303 K and is a representative of f -dependence of these quantities at other urea concentrations. Note the $\lambda_{exc.}$ -induced variation for these spectral properties are limited within ~200-300 cm^{-1}, suggesting a weak dependence on excitation energy. Such a dependence of $\nu_{em.}$ and Γ for these urea containing deep eutectics are very different from those observed earlier in the corresponding (acetamide+$LiBr/NO_3$) deep eutectics in the absence of urea[30]. This is somewhat surprising given that these systems, being not particularly low viscous media $(10 < \eta/cP < 450)$, are expected to support slower solvent relaxation. This in turn means that the inhomogeneous solvation shells around the dipolar solute inter-converts too rapidly, forcing the solute probe to report only the effects of fluctuation-averaged environments during its excited state lifetime. A probe with shorter lifetime may serve as a better reporter of spatial inhomogeneity present in these in these systems.[32]

Figure 5.3

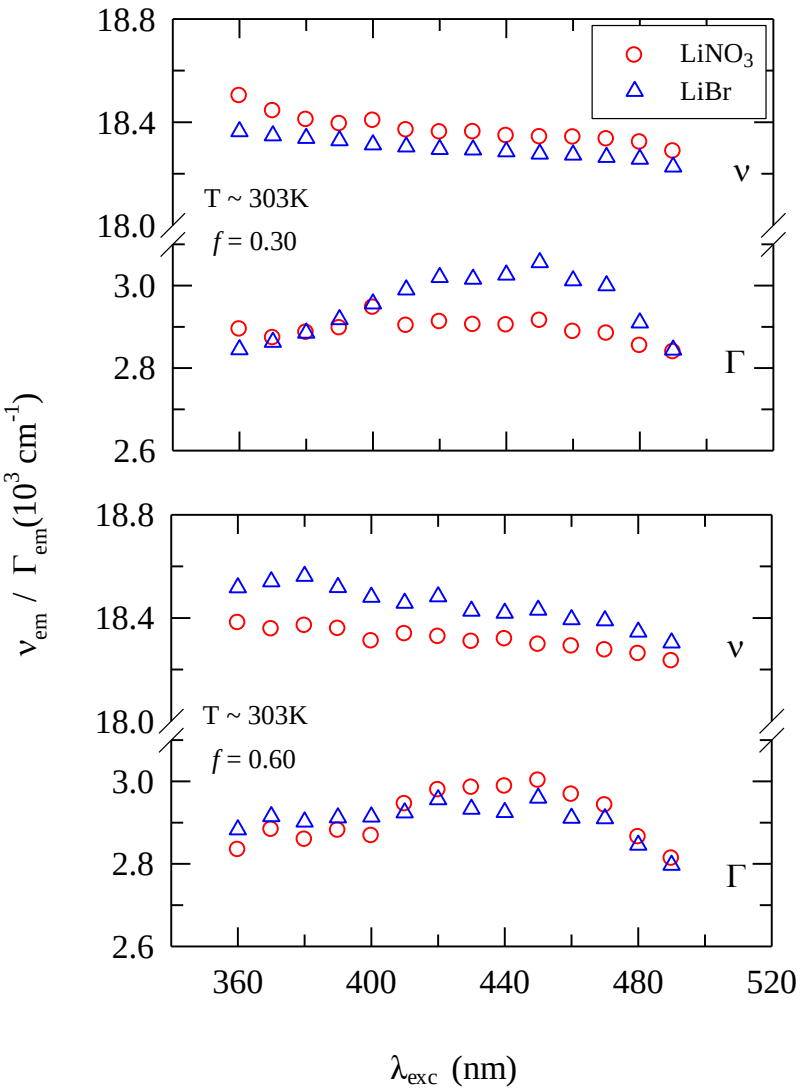

Figure 5.3: A representative plot of spectral parameters for the 0.10$LiNO_3$/ LiBr + 0.90[*f* Urea+ (1-*f*) Acetamide] at *f* = 0.3 (upper panel) and *f* = 0.6 (lower panel) at 303K for excitation wavelength dependence ($\lambda_{exc.}$) is shown here. The upper halves of each of the panels show the variation of emission peak frequency, (ν_{em}) whereas the lower halves show that of full width at half maxima (FWHM), (Γ_{em}) of the emission spectrum for C153 in the mentioned systems.

5.3.2. Time- Resolved Fluorescence Stokes Shift Measurements

Representative fluorescence emission intensity decays collected at blue end (470nm) and red end (650nm) of emission spectrum for C153 in $0.1LiNO_3$+0.9[*f* Urea+ (1- *f*) Acetamide] with *f*= 0.35 at 303K are shown in Figure A10. Multiexponential fits through these decays along with the instrumental response function and residuals are also shown here. Rise followed by decay at the red wavelength and decay only at the blue wavelength suggest presence of dynamic Stokes shift in these systems. Fit parameters shown in the upper panel indicate presence of a nanosecond component in these systems which is expected considering viscosity of these media and presence of ions in them. A heavy ion like Br^- is known to be a fluorescence quencher[53] and thus it is important to examine whether dynamic quenching has contributed to the decay characteristics. This has been confirmed by following the f -dependence of the longest time constants obtained via fits to the magic angle decays at emission peak wavelengths in these deep eutectics. The fits in Figure A11 summarize the results. The end-to-end difference has been found to be only ~225 ps for NO_3^- and ~375 ps for Br^- containing systems in presence of urea. Since these variations are only within a few percent of the longest time constants, we assume dynamic quenching effects to be negligible. Also, no significant changes in intensity of the steady state experiments have been found at a fixed probe concentration. Therefore, it is safe to consider that the decay characteristics primarily represent rearrangement of the environment in response to the laser excitation of the solute probe dissolved in these media.

Representative TRES (time resolved emission spectra) constructed[49,54] are shown in Figure 5.4 for the system $0.1LiNO_3$+0.9[*f* Urea+ (1- *f*) Acetamide] at *f*=0.35 and ~ 303K. The magnitude of the observed dynamic Stokes shift ($\Delta\nu_{obs}$) here is ~500cm^{-1} . The estimated[49] "true" dynamic Stokes shift is ~630 cm^{-1} at this composition which indicates missing of ~ 20% of the total dynamics in the present measurements. Also note in Figure 5.4 that the constructed emission spectrum at $t = \infty$ is ~250cm^{-1} red-shifted from the steady state emission spectrum. A combination of slow movement of the environmental particles and interaction-induced subtle changes in the underlying

vibronic structure of the solute in these viscous media can account for this difference $\nu(\infty)$ and $\nu_{em.}$.

Figure 5.4

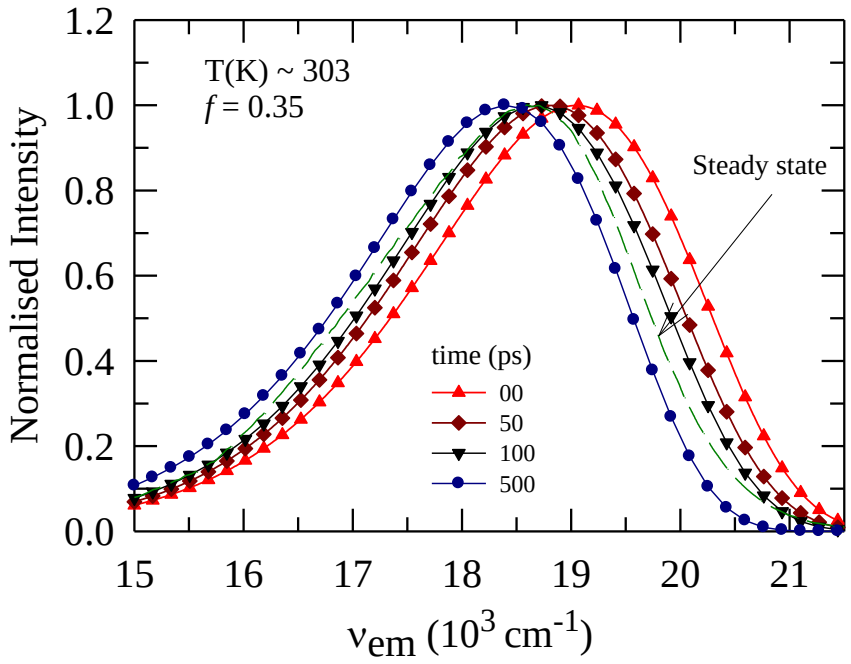

Figure 5.4: Synthesized time resolved emission spectra (TRES) of C153 at different time from the experimentally obtained decays in 0.10 $LiNO_3$+0.90 [*f* Urea+(1- *f*) Acetamide] at *f* = 0.35 (T= 303 K). TRES shown are at the following time intervals after solute excitation: 0 ps (triangles), 50 ps (diamonds), 100 ps (inverted triangles) and 500 ps(circles). The steady state emission spectrum of the same is shown in broken line.

Dynamic Stokes' shift magnitudes, observed and estimated, at the urea concentrations considered here are listed in Table 5.1 along with the corresponding missing components. Note a significant portion of the total dynamics in both the systems has remained undetected in the present experiments and the magnitude of this missing component increases with increasing urea concentration. In addition, Br^- containing systems report relatively larger (~45-75%) missing amplitude than that (~20-65%) in NO_3^- containing deep eutectics. Such a large missing component suggests presence of

Table 5.1: Dynamic Stokes' shift for C153 in molten mixtures of $0.10LiNO_3$/ LiBr + 0.90[*f* Urea+ (1-*f*) Acetamide] at 303 K.

	$LiNO_3$			LiBr		
f	ν^t_{est} $(cm^{-1})^a$	ν^t_{obs} $(cm^{-1})^a$	% missed	ν^t_{est} $(cm^{-1})^a$	ν^t_{obs} $(cm^{-1})^a$	% missed
0.20				1159	547	53
0.25	906	688	24			
0.30	757	571	25	1514	516	66
0.35	629	503	20			
0.40	945	423	55	952	509	46
0.50	1037	367	65	1336	602	55
0.60	1080	473	56	975	236	76

a) The estimated and observed Stokes' shifts are calculated by using the Fee-Maroncelli method which is described in Ref.49. The error bar associated with the measurements is approximately ± 250 cm^{-1}.

solvent dynamics much faster than the detection limit of the present set-up. Collective intermolecular libration modes in amides,[55,56] as found in many H-bonded systems can produce ultrafast solvation response with timescales in pico and sub-picoseconds[57-62]. Therefore, it is only natural that the broad time-resolution employed here would miss the initial faster response in these acetamide-based deep eutectics. A modification of the collective H-bond network in amides ('amides' include both acetamide and urea) due to a competition between formation of ion-amide and amide-amide H-bonds then leads to the observed ion-dependence of the missing amplitudes at the early time. The anion dependence of the slower part of the solvation response in these urea containing ionic deep eutectics are shown in Figure 5.5 at f =0.3 and 0.5 whereas Table 5.2 summarises the $\langle \tau_s \rangle$ obtained for different compositions. Medium viscosity can explain this ion dependence of the slower solvation component.

Figure 5.5

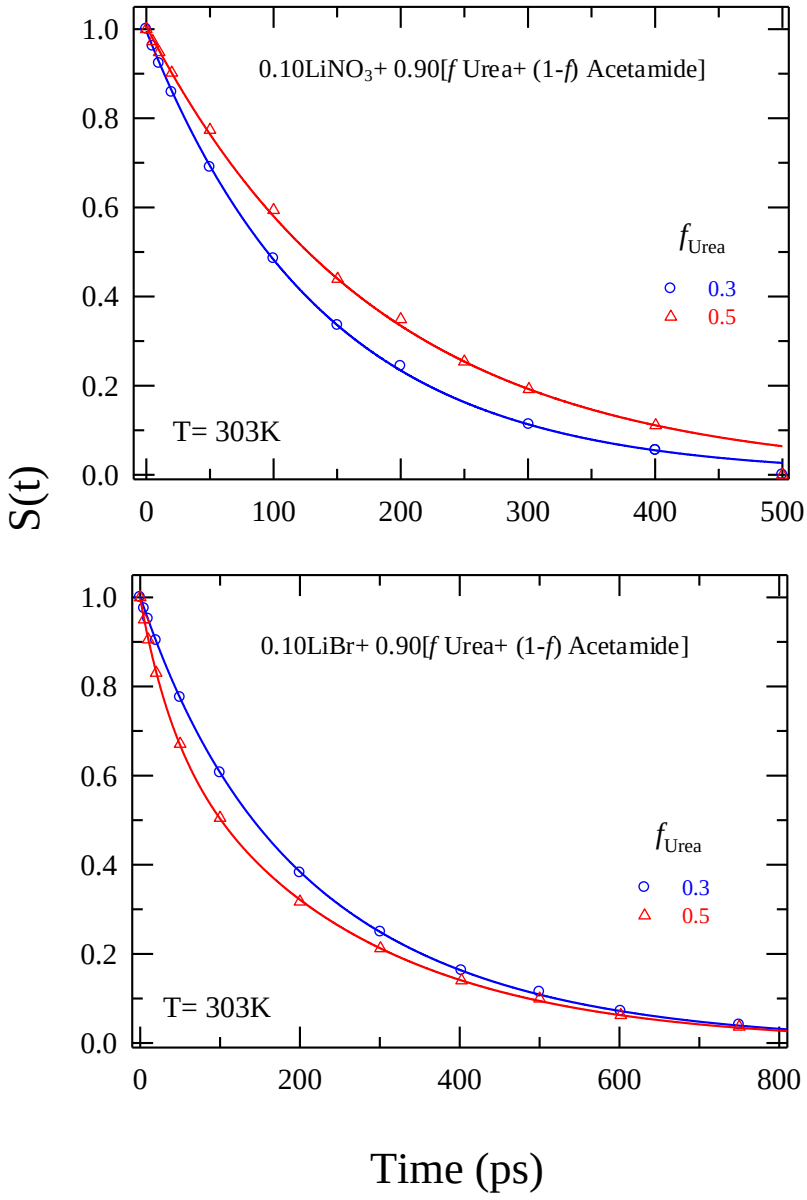

Figure 5.5: Decays of solvation response function, $S(t)$, measured using C153 at 303K in $0.1LiNO_3$+0.9[f Urea+ (1- f) Acetamide] molten mixtures for f = 0.3 (red) and 0.5 (blue) are shown in the upper panel. The same for LiBr is shown is shown in the lower panel.

Table 5.2: Solvation response function measured from experiment in the molten mixtures of $0.10LiNO_3$/ LiBr + 0.90[*f* Urea+ (1-*f*) Acetamide] at 303K. $\langle \tau_s \rangle$ are better than $\pm$ 10% of the reported values (estimated based on limited data sets).

(a) $0.10LiNO_3$ + 0.90[*f* Urea+ (1-*f*) Acetamide]

f	$\langle \tau_s \rangle$ (ps)
0.25	118
0.30	139
0.35	125
0.40	156
0.50	182
0.60	141

(b) 0.10LiBr + 0.90[*f* Urea+ (1-*f*) Acetamide]

f	$\langle \tau_s \rangle$ (ps)
0.20	240
0.30	217
0.40	189
0.50	187
0.60	263

5.3.3. Time resolved Anisotropy Measurements

Emission decays for time resolved anisotropy were collected at the maxima of the steady state emission spectra for parallel, perpendicular and magic angle**.** For fit to the collected dynamic anisotropy data at all compositions and temperatures, the initial value for anisotropy (r_0) for C153 is fixed at 0.38[48,63]. A representative bi-exponential fit to the data is shown in Figure A12 which corresponds to C153 rotation in $0.1LiNO_3$+0.9[*f* Urea+ (1- *f*) Acetamide] at *f* = 0.35 at 303K. Fit parameters summarized in the upper panel and residual shown in the lower panel indicate adequate description of the experimental data by the mathematical expression used. Note our attempt to fit the collected data by using stretched exponential, $r(t) = r_0 \exp\left[-\left(t/\tau_{rot}\right)^{\beta_{rot}}\right]$, has resulted poorer fits uniformly at all urea concentrations and temperatures considered. Interestingly, bi-exponentials were found to be adequate for C153 rotation in the urea-free ionic acetamide deep eutectics as well.[28-30] The non-observation of stretched exponential were ascribed to the broad time resolution used[64] and relatively longer lifetime of the probe used in comparison to the trapping time of the solute in heterogeneous solvation environments present in these molten mixture.[40,41,43] Also, multi-exponential $r(t)$ decays have been observed earlier even for neat liquid solvents.[26] Non-Markovian nature of the underlying time-dependent friction rather than the microscopic heterogeneity of solutions was thought[65,66] to be a more appropriate reason for the observed bi-exponential character.

Next, temperature dependent dynamic anisotropy measurements have been carried out at various urea concentrations to explore the viscosity coupling of C153 rotation in these media and examine the validity of the corresponding hydrodynamic relations. Figure A13 displays the representative temperature dependent $r(t)$ decays for $LiNO_3$ and LiBr containing deep eutectics at $f = 0.3$. Bi-exponential fit parameters for the collected decays are summarised in Table B8 (a and b). Effects of addition of urea in these ionic deep eutectics are shown in Figure 5.6 where average rotation times ($\langle \tau_r \rangle$) are compared between urea-free[30] and urea-added systems. Line going through these

data in both the panels represent fit of the data to the following form: $\langle \tau_r \rangle = A(\eta/T)^p$. Note in both the cases addition of urea brings the numerical value of p closer to unity. As fractional viscosity dependence (that is, p significantly less than unity) of relaxation rates is often ascribed to medium dynamic heterogeneity[24,34-36], these results may be interpreted as a consequence of urea-induced homogenization of the medium. This also parallels our observation for $\lambda_{exc.}$ dependence of fluorescence emission of C153 in these urea-added deep eutectics.

Figure 5.6

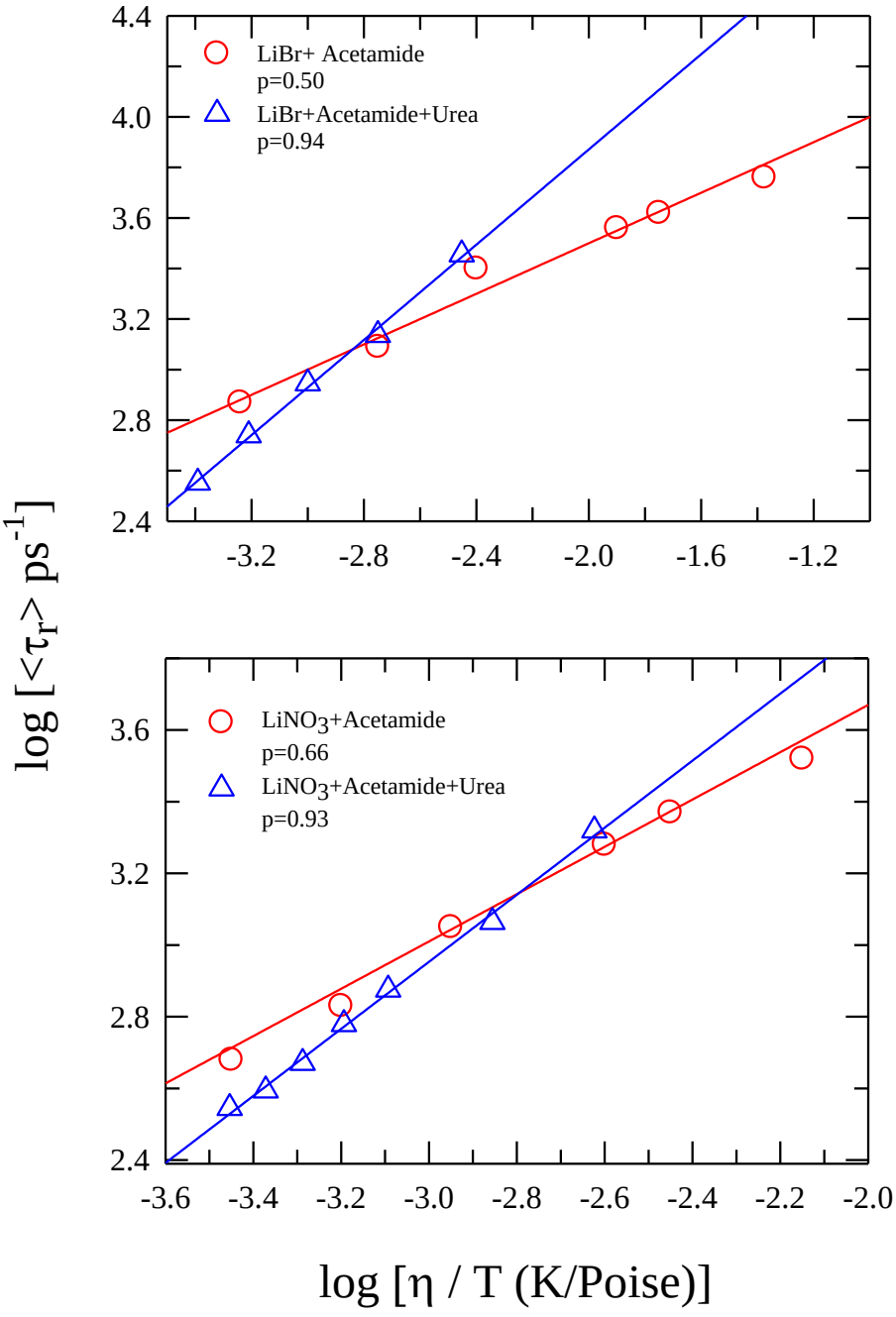

Figure 5.6: Temperature reduced viscosity dependence of average rotational time of C153 of the molten mixture 0.10$LiNO_3$/ LiBr + 0.90[*f* Urea+ (1-*f*) Acetamide] denoted by the triangles is shown as the log-log plot. In the same respective panels the plot of

the mixture without urea denoted by circles is shown. The '*p*' values are indicated for both the composition.

A comparison between composition dependent p values obtained for urea-added and urea-free (acetamide+$LiNO_3$/Br) deep eutectics[30] are shown in Figure 5.7. Note at all concentrations of urea studied here, p for urea-added systems remain not only closer to unity but are also uniformly larger than those found in urea-free deep eutectics. This indicates that urea 'homogenizes' the dynamics of (acetamide+$LiNO_3$/Br) deep eutectics irrespective of the anion identity of the electrolyte used. This range for urea concentration dependent p values ($0.8 \leq p \leq 1.01$, tabulated in Table B9) prompt us to investigate the validity of hydrodynamic description of solute rotation in these deep eutectics. Figure 5.8 presents a comparison between our measured temperature dependent $\langle \tau_r \rangle$ at all urea concentrations and those calculated from Debye-Stokes-Einstein (DSE) relation[34], $<\tau_r>= \frac{V\eta}{k_B T} fC$, for these systems. For calculations we have used solute volume V = 246 $Å^3$ and shape factor f= 1.71[65]. DSE predictions at both the stick (C=1) and slip (C= 0.24) limits are also shown. Clearly, C153 rotation in these media are closer to slip than stick predictions. In addition, the lines going through the data indicate $f-$averaged value for p between ~1 and ~0.8, reflecting hydrodynamic description being semi-quantitative for C153 rotation in these multi-component molten mixtures.

Figure 5.7

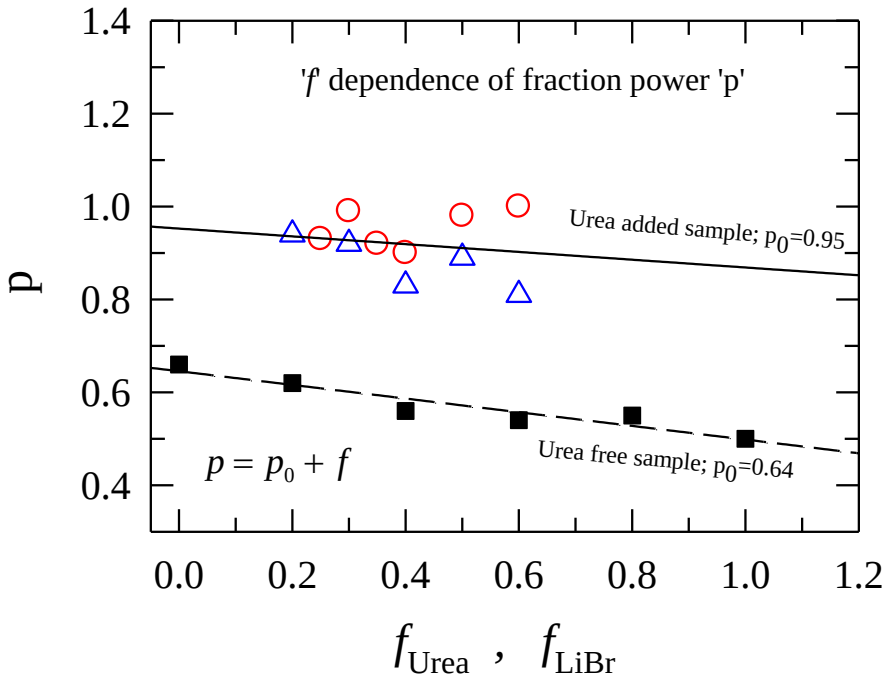

Figure 5.7: The X-axis represents f_{Urea} for urea added systems whereas f_{LiBr} for urea-free samples[30].

Composition (f) dependence of p with the measured $<\tau_r>$ in the system 0.1$LiNO_3$/LiBr+0.9[f Urea+ (1- f) Acetamide] for $LiNO_3$ (red circles) and LiBr (blue triangles) is plotted in the log-log form of the equation: $\tau_r = A(\eta/T)^p$. The value of 'p' is seen to be near unity for all fractions of urea for both salts. The linear fit (solid black line) through the urea added sample data yields an overall p-value of 0.95.

The black squares indicate 'p'-values in the system [0.78Acetamide+0.22{f LiBr + (1-f) $LiNO_3$}][30] which are far from unity. Note that this system is urea-free.

The linear fit (broken black line) through the urea free sample data yields an overall p-value of 0.64.

Figure 5.8

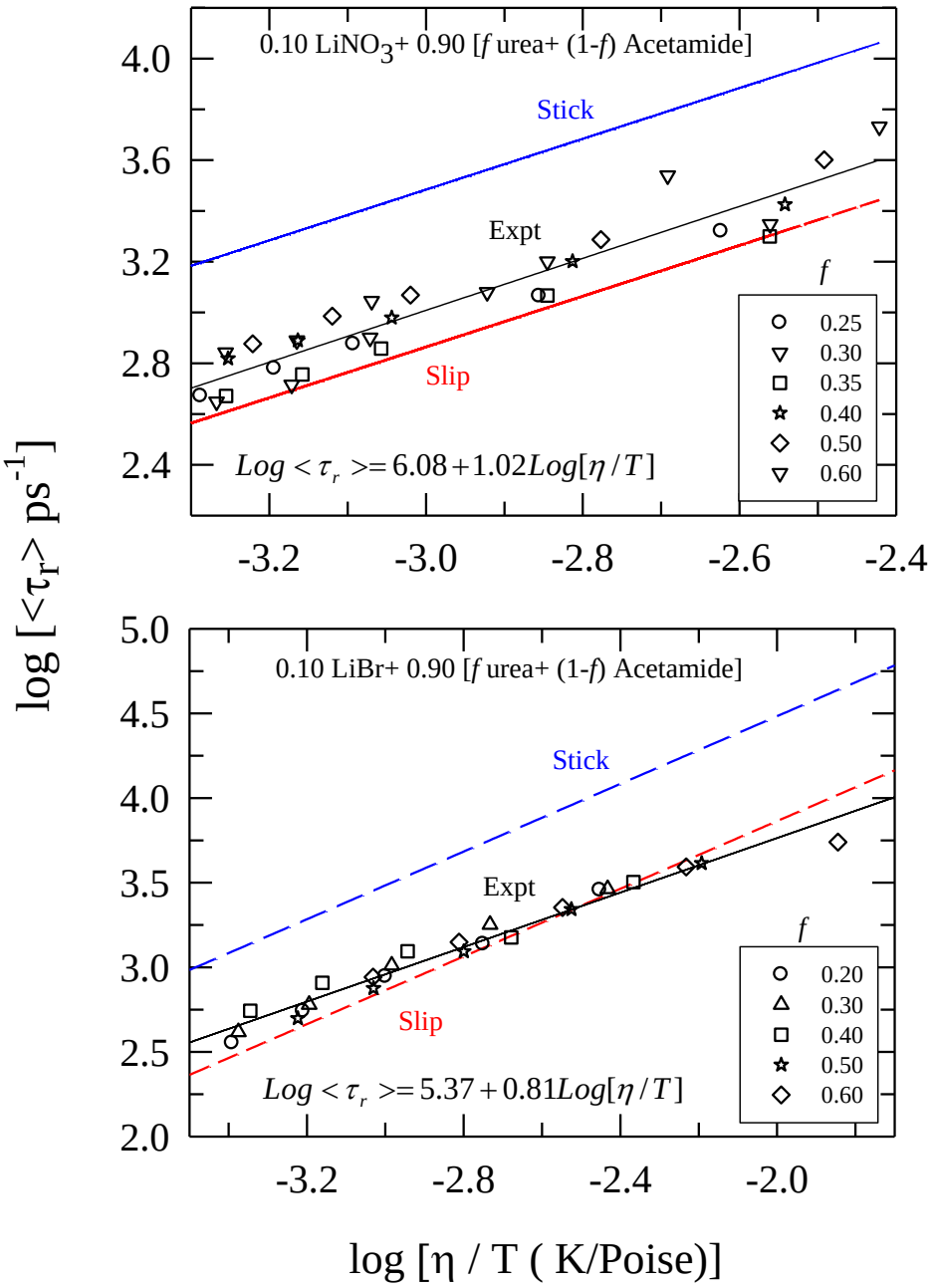

Figure 5.8: Theoretically calculated values of rotational time as obtained from modified DSE equation for slip boundary (red broken line) and stick boundary (blue broken line) are shown along with experimentally obtained values (solid line).

Subsequently, urea concentration dependences of activation energies associated with C153 rotation and solution viscosity - $E_a(\langle\tau_r\rangle)$ and $E_a(\eta)$ respectively – have been investigated. Arrhenius type of temperature dependence of both rotation time ($\langle\tau_r\rangle$) and viscosity (η) are shown in Figure A14 and A15 respectively. Results displayed in Figure 5.9 indicate a weak urea concentration dependence of both the activation energies for these deep eutectics. In addition, similar range for both $E_a(\langle\tau_r\rangle)$ and $E_a(\eta)$ suggests C153 rotation in these media is governed by the frictional resistance from the bulk medium viscosity. This is more quantitatively shown in Figure 5.10 where a linear relationship between $E_a(\langle\tau_r\rangle)$ and $E_a(\eta)$ provides further support to the above conjecture. Also note that $E_a(\langle\tau_r\rangle)$ estimated for these urea-added systems are ~10 kJ/mol larger than those found earlier for the corresponding urea-free (acetamide + $LiNO_3$/Br) deep eutectics.[30] This is expected on the ground that viscosity coupling to solute rotation in these urea-added systems is stronger than in the urea-free counterparts as substantial dynamic heterogeneity in the later softened the frictional resistance to solute rotation.

Figure 5.9

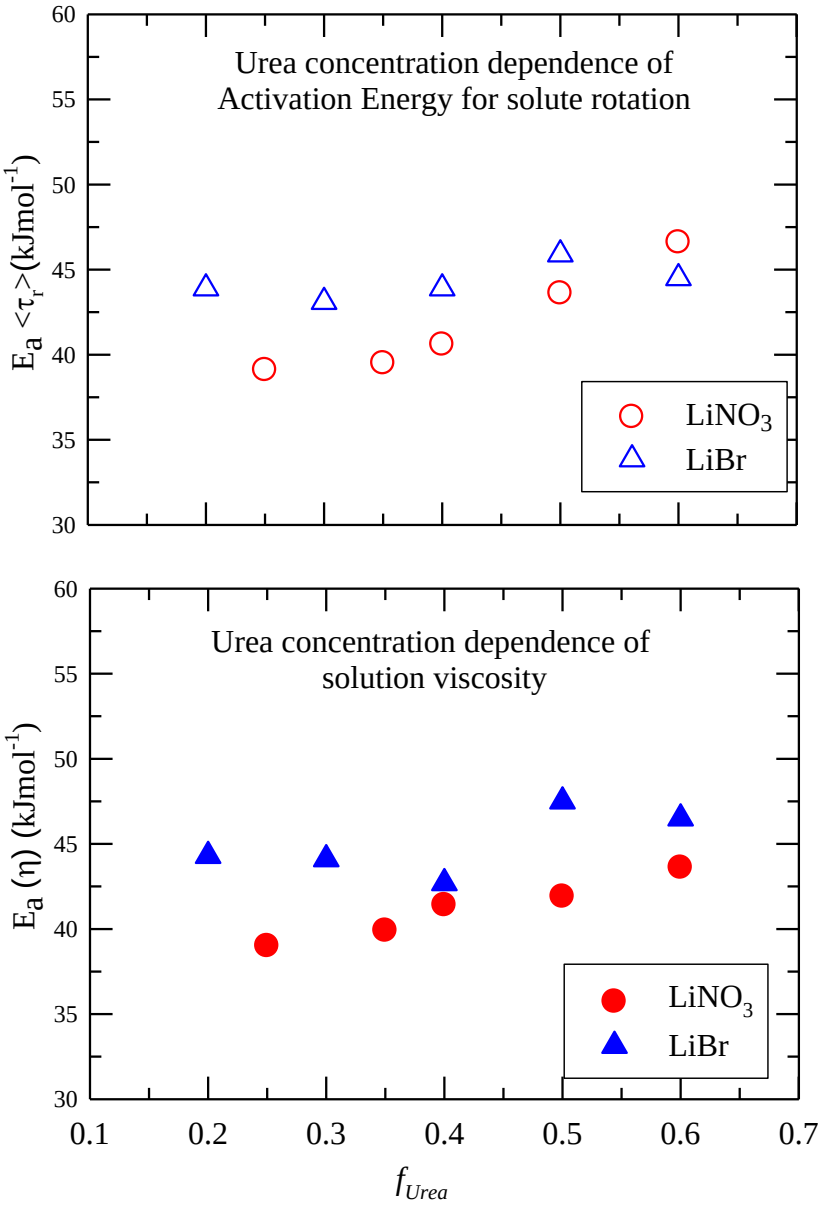

Figure 5.9: Activation energies obtained from Arrhenius type plot of $\ln(1/\langle\tau_r\rangle)$ vs *1/RT* for rotation of C153 and viscosity dependence in the system 0.10$LiNO_3$/ LiBr + 0.90[*f* Urea+ (1-*f*) Acetamide] for temperature range of 303K-343K, are plotted as a function '*f*'. Circles represent data for $LiNO_3$ and triangles for LiBr.

Figure 5.10

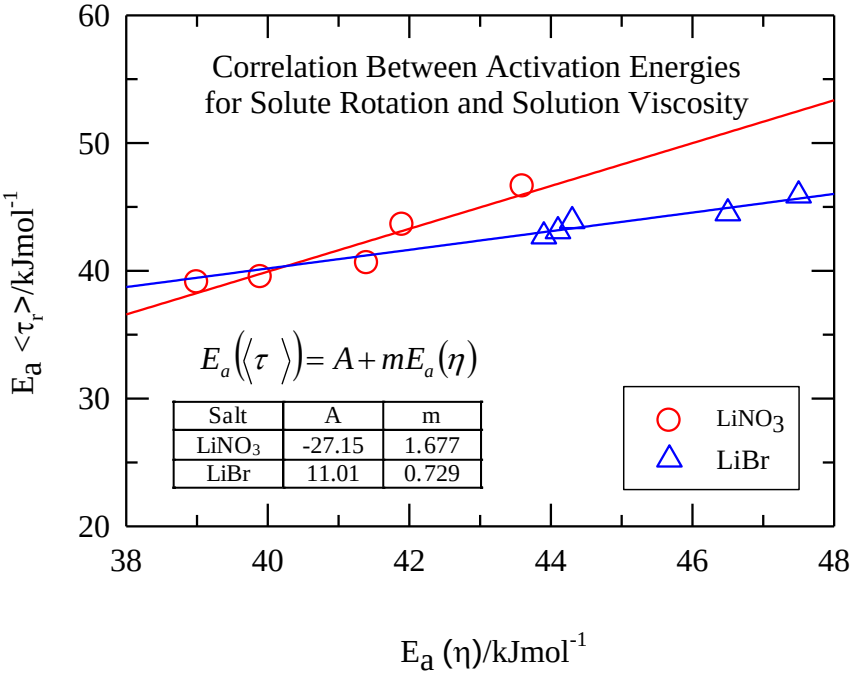

Figure 5.10: Activation energies obtained from Arrhenius plot of $\ln(1/\langle\tau_r\rangle)$ vs *1/RT* for rotation of C153 is plotted against Arrhenius type plots of viscosity dependence in the system 0.10$LiNO_3$/ LiBr + 0.90[*f* Urea+ (1-*f*) Acetamide] for temperature range of 303K-343K. Circles represent data for Li NO_3 and triangles for LiBr.

5.4. Conclusion

In conclusion, spectroscopic results presented in this chapter strongly suggest addition of urea induces homogenization of structure and dynamics of (acetamide + electrolyte) deep eutectics studied here. This homogenization signature is reflected via insensitivity of excitation energy dependence of fluorescence emission of a dissolved fluorescent solute, and near-hydrodynamic coupling of its rotation to medium viscosity. Estimated activation energy for solute rotation ($E_a(\langle\tau_r\rangle)$) has been found to weakly depend on urea concentration, and follows the activation energy for viscosity ($E_a(\eta)$) of these

deep eutectics. $E_a(\langle\tau_r\rangle)$ has been found to be, on an average, ~10 kJ/mol larger in presence of urea in these deep eutectics than in urea-free condition. This is attributed to the difference in viscosity-coupling of solute rotation between the urea-added and urea-free ionic acetamide deep eutectics studied here. Dynamic Stokes' shift measurements suggest shift magnitudes of ~500-1500 cm^{-1}, significant portion of which occurs at a timescale much faster than the detection limit of the time-resolution employed. Participation of collective intermolecular H-bonding network between acetamide, urea and acetamide-urea molecules can give rise to picoseconds and faster solvation response in these mixtures and this can lead to missing of initial fast solvation response in the present measurements.

While interpreting the present fluorescence data in terms of urea-induced homogenization of solution structure and dynamics of these (acetamide + $LiNO_3$/Br) deep eutectics, it should be kept in mind that such an interpretation is strongly linked to the excited state lifetime of the fluorescent probe used. For example, one may still find signatures of heterogeneity in these deep eutectics in presence of urea by employing a fluorescent probe with lifetime faster than that of C153 because observation of heterogeneity critically depends upon a competition between the heterogeneity timescale (timescale for inter-conversion among inhomogeneous solvation shells) and fluorescence lifetime. Further experimental studies using shorter lifetime probes, suitably aided by computer simulations are therefore required to fully understand the structural and dynamical aspects of these complex yet very important solvent systems.

References

1. Wagle, D. V.; Zhao, H.; Baker, G. A. *Acc. Chem. Res.* **2014**, *47*, 2299.

2. Francisco, M.; Gonzalez, A. S. B.; de Dios, S. L. G.; Weggemans, W.; Kroon, M. C. *Rsc. Adv.* **2013**, *3*, 23553.

3. Francisco, M.; van den Bruinhorst, A.; Kroon, M. C. *Angew. Chem., Int. Ed.* **2013**, *52*, 3074.

4. Francisco, M.; van den Bruinhorst, A.; Kroon, M. C. *Green Chem.* **2012**, *14*, 2153.

5. Zhang, Q. H.; Vigier, K. D.; Royer, S.; Jerome, F. *Chem. Soc. Rev.* **2012**, *41*, 7108.

6. Abbott, A. P.; Boothby, D.; Capper, G.; Davies, D. L.; Rasheed, R. K. *J. Am. Chem. Soc.* **2004**, *126*, 9142.

7. Abbott, A. P.; Harris, R. C.; Ryder, K. S.; D'Agostino, C.; Gladden, L. F.; Mantle, M. D. *Green Chem* **2011**, *13*, 82.

8. Abbott, A. P.; Capper, G.; Davies, D. L.; Rasheed, R. K.; Tambyrajah, V. *Chem. Commun.* **2003**, 70.

9. Smith, E. L.; Abbott, A. P.; Ryder, K. S. *Chem Rev* **2014**, *114*, 11060.

10. Castellani, F.; Berchiesi, G.; Pucciarelli, F.; Bartocci, V. *J. Chem. Eng. Data.* **1981**, *26*, 150.

11. Berchiesi, G.; Vitali, G.; Passamonti, P.; Plowiec, R. *J. Chem. Soc., Faraday Trans. 2*, **1983**, *79*, 1257.

12. Berchiesi, G.; Vitali, G.; Plowiec, R.; Barocci, S. *J. Chem. Soc. Faraday Trans. 2* **1989**, *85*, 635.

13. Berchiesi, G.; Angelis, M.D.; Rafaiani, G.; Vitali, G. *J. Mol. Liq.* **1992**, *51*, 11.

14. Stafford, O. F. *J. Am. Chem. Soc.* **1933**, *55*, 3987.

15. Yntema, L. F.; Audrieth, L. F. *J. Am. Chem. Soc.* **1930**, *52*, 2693.

16. Dawson, L. R.; Sears, P. G.; Graves, R. H. *J. Am. Chem. Soc.* **1955**, *77*, 1986.

17. Wallace, R. A. *Inorg. Chem.* **1972**, *11*, 414.

18. Wallace, R. *J. Phys. Chem.* **1971**, *75*, 2687.

19. Kerridge, D. H. *Chem. Soc. Rev.* **1988**, *17*, 181.

20. Jander, G.; Winkler, G. J. *Inorg. Nucl. Chem.* **1959**, *9*, 24.

21. Wallace, R.; Bruins, P. *J. Electrochem. Soc.* **1967**, *114*, 212.

22. Zhao, H.; Baker, G. A. *J. Chem. Technol. Biotechnol* **2013**, *88*, 3.

23. Carriazo, D.; Serrano, M. C.; Gutierrez, M. C.; Ferrer, M. L.; del Monte, F. *Chem Soc Rev* **2012**, *41*, 4996.

24. Ediger, M. D. *Annu. Rev. Phys. Chem.* **2000**, *51*, 99.

25. Berchiesi, G. *J. Mol. Liq.* **1999**, *83*, 271.

26. Berchiesi, G.; Rafaiani, G.; Vitali, G.; Farhat, F. *J. Therm. Anal.* **1995**, *44*, 1313.

27. Amico, A.; Berchiesi, G.; Cametti, C.; Di Biasio, A. *J. Chem. Soc. Faraday Trans. 2* **1987**, *83*, 619.

28. Guchhait, B.; Gazi, H. A. R; Kashyap, H. K.; Biswas, R. *J. Phys. Chem. B* **2010**, *114*, 5066.

29. Guchhait, B.; Das, S.; Daschakraborty, S.; Biswas, R. *J. Chem. Phys.* **2014**, *140*, 104514.

30. Guchhait, B.; Daschakraborty, S.; Biswas, R. *J. Chem. Phys.* **2012**, *136*, 174503.

31. Gazi, H. A. R; Biswas, R. *J. Phys. Chem. A* **2011**, *115*, 2447.

32. Das, A.; Das, S.; Biswas, R. *Chem. Phys. Lett.* **2013**, *581*, 47.

33. Gazi, H. A. R.; Guchhait, B.; Daschakraborty, S.; Biswas, R. *Chem. Phys. Lett.* **2011**, *501*, 358.

34. Sillescu, H. *J. Non-Cryst. Solids* **1999**, *243*, 81.

35. Angell, C. A. *J. Chem. Phys.* **1967**, *46*, 4673.

36. Moynihan, C. T. *J. Phys. Chem.* **1966**, *70*, 3399.

37. Chakrabarti, D.; Bagchi, B. *Phys. Rev. Lett.* **2006**, *96*, 187801.

38. Rajkhowa, S.; Das, A.; Mahiuddin, S.; Biswas, R. *J. Chem. Eng. Data* **2012**, *57*, 3467.

39. Vogel, H. *Phys. Z.* **1921**, *22*, 645.

40. Fulcher, G. S. *J. Am. Ceram. Soc.* **1923**, *8*, 339.

41. Tammann, G. H.; W. Z. *Anorg. Allgem. Chem.* **1926**, *156*, 245.

42. Horng, M. L.; Gardecki, J. A.; Papazyan, A.; Maroncelli, M. *J. Phys. Chem.* **1995**, *99*, 17311.

43. Chapman, C. F.; Maroncelli, M. *J Phys Chem-Us* **1991**, *95*, 9095.

44. Dahl, K.; Biswas, R.; Ito, N.; Maroncelli, M. *J. Phys. Chem. B* **2005**, *109*, 1563.

45. Pradhan, T.; Biswas, R. *J. Phys. Chem. A* **2007**, *111*, 11514.

46. Pradhan, T.; Ghoshal, P.; Biswas, R. *J. Phys. Chem. A* **2008**, *112*, 915.

47. Cross, A. J.; Fleming, G. R. *Biophys. J.* **1984**, *46*, 45.

48. Horng, M. L.; Gardecki, J. A.; Maroncelli, M. *J. Phys. Chem. A* **1997**, *101*, 1030.

49. Fee, R. S.; Maroncelli, M. *Chem. Phys.* **1994**, *183*, 235.

50. Kumler, W. D.; Fohlen, G. M. *J. Am. Chem. Soc.* **1942**, *64*, 1944.

51. Das, A.; Das, S.; Biswas, R. *J. Chem. Phys.* **2015**, *142*, 034505.

52. Riddick, J. A.; Bunger, W. B.; Sakano, T. K. *Organic Solvents*; Wiley: New York, 1986.

53. Bolen, E. J.; Holloway, P. W. *Biochemistry-Us* **1990**, *29*, 9638.

54. Maroncelli, M.; Fleming, G. R. *J. Chem. Phys.* **1987**, *86*, 6221.

55. Shirota, H.; Castner, E. W. *J. Am. Chem. Soc.* **2001**, *123*, 12877.

56. Chang, Y. J.; Castner, E. W. *J. Phys. Chem.* **1994**, *98*, 9712.

57. Kashyap, H. K.; Biswas, R. *J. Phys. Chem. B* **2010**, *114*, 16811.

58. Kashyap, H. K.; Biswas, R. *J. Phys. Chem. B* **2008**, *112*, 12431.

59. Kashyap, H. K.; Pradhan, T.; Biswas, R. *J. Chem. Phys.* **2006**, *125*, 174506.

60. Biswas, R.; Bagchi, B. *J. Phys. Chem.* **1996**, *100*, 1238.

61. Biswas, R.; Bagchi, B. *J. Phys. Chem. A* **1999**, *103*, 2495.

62. Bagchi, B.; Biswas, R. *Adv. Chem. Phys.* **1999**, *109*, 207.

63. Jin, H.; Li, X.; Maroncelli, M. *J. Phys. Chem. B* **2007**, *111*, 13473.

64. Arzhantsev, S.; Jin, H.; Baker, G. A.; Maroncelli, M. *J. Phys. Chem. B* **2007**, *111*, 4978.

65. Jin, H.; Baker, G. A.; Arzhantsev, S.; Dong, J.; Maroncelli, M. *J. Phys. Chem. B* **2007**, *111*, 7291.

66. Ito, N.; Arzhantsev, S.; Heitz, M.; Maroncelli, M. *J. Phys. Chem. B* **2004**, *108*, 5771.

Chapter 6

Dynamic Fluorescence Studies of (Choline chloride+ Urea) Deep Eutectics: Interconnection between Solvent Dynamics and Reaction Kinetics

6.1. Introduction

During the past few decades, there have been many attempts to satisfy the ever increasing quest for environmental friendly solvents. Ionic liquids qualified as a good industrial solvent but slowly lost its importance to a more benign class of solvent systems known as deep eutectic solvents (DESs). DESs become the preferred alternatives primarily due to less toxicity and expense[1-8]. When biodegradability couples with cost-effectiveness and reduced toxicity of this class of solvents, DESs qualifies to be treated as 'green solvents' for industrial applications. DES are easily prepared by mixing two or more compounds at a certain mole ratio and heating to convert the solid mixture into the stable liquid phase at a temperature much lower than the individual melting temperatures of the constituents.[5] Extensive inter-species H-bonding and gain in entropy are the main factors that drive the depression of freezing points, producing liquids that may even sometime show properties reminiscent of supercooled liquids near glass transition.[9-11]

There is a wide window of choice for constituents resulting in the formation of neutral and ionic DESs.[7] For example, neutral DESs can be obtained by mixing amides like acetamide and urea, whereas the ionic ones can be obtained by choosing electrolyte as one of the components. A new set of DESs can be synthesized by mixing a quaternary ammonium salt like choline chloride with any of the following species: amides, salts,

acids, sugars, and alcohols.[2,7] This provides a unique and easy handle for changing important medium properties, such as, polarity, viscosity and conductivity , which play key roles in deciding rate of a reaction (and product) conducted in liquid phase.[12-18] In addition, freedom of choice for constituents makes solvent engineering easy with DESs as a reaction medium can be tailored with much less effort to drive a reaction for an intended product.

Acetamide based DES have been already investigated by fast spectroscopic methods like fluorescence[9-11,19]. In addition nuclear magnetic resonance,[20] viscoelastic,[21,22] ultrasonic[21,22] and dielectric relaxation[23,24] measurements have also been employed. All these studies suggest presence of microheterogeneity in these media even far above their glass transition temperatures. Multi-probe steady state excitation wavelength dependence of fluorescence emission study have provided further information on spatial heterogeneity of these systems.[25] Dynamic Stokes' shift and anisotropy measurements have revealed deviation from hydrodynamic description of diffusion in these media through displaying fractional viscosity dependence of solute rotation and solvation times.[9-11,26] All atom molecular dynamics simulations[19,25,27,28] then explored the origin of the observed fractional viscosity dependence. Faster relaxation processes related to collective low frequency librational modes have recently been identified via Raman-induced Kerr effect spectroscopy (RIKES) measurements.[29]

Towards the beginning of twenty-first century,[5,6] choline chloride based DESs had been introduced and were accepted as green solvent systems. This is because choline chloride, being a vitamin, is both biocompatible and biodegradable.[30-33] Phase diagrams for several such DESs have been studied along with transport properties, providing a temperature range for subsequent use.[6-8,34] The most widely studied system of choline chloride based DESs is that of with urea which forms liquid at 285 K in the ratio of 1:2.[5] SCHEME 1 provides the chemical structures for both choline chloride and urea. The melting point of choline chloride is 575 K[5] and urea is 406 K[5]. The mixture is found to be moderately polar[35]. Molecular dynamics simulation study of choline chloride and urea system has shown that the co-ordination number of urea

around chloride ion is found to be greater than that for choline cation.[36] In addition, the H-bonding preference of the cis-H and trans-H are also investigated which is further supported by infra-red measurements.[36] Theoretical treatments for investigating H-bond mechanism and lifetimes have also been attempted[37]. NMR studies have been performed to explore the coupling between viscosity and particle diffusion.[37] Recently, qualitative study for determining the average polarities of choline chloride containing DESs have been initiated.[35] However, no study has been carried out so far exploring the medium dynamics and its effects on a chemical reaction occurring in them. This is what is investigated in this chapter.

The glass transition temperature (T_g) of the DES (choline chloride+ urea) is found to be ~200 K (Figure A16) which is similar to what we have already got for acetamide based DESs.[11,19] Here we explore, using steady state and time-resolved fluorescence spectroscopy, signatures of spatial and temporal heterogeneities of (choline chloride + urea) deep eutectics at a temperature range much above the measured T_g. We have seen earlier in ionic deep eutectics that avoidance of crystallization via freezing point depression has introduced heterogeneity signatures, such as, excitation wavelength and fractional viscosity dependencies.[9-11] We would also like to investigate how temporal heterogeneity, if present in these DESs, affects a simple chemical reaction occurring in such a medium.

We have considered photo-induced excited state intramolecular charge transfer (ICT) reaction for investigating the heterogeneity effects on a chemical reaction in such a medium. Two ICT molecules investigated here are: 4-(1-azetidinyl)benzonitrile (P4C) and 4-(1-pyrrolidinyl)benzonitrile (P5C) (SCHEME 1). These molecules have previously been studied in several solvents of varying polarity[38] and also in electrolyte solutions.[13-15] Twisted intramolecular charge-transfer (TICT) model (SCHEME 2) was used in these studies for rationalizing the solvent dependence of the kinetics. The conversion between the locally excited (LE) and charge transferred (CT) states of these molecules involves a barrier of ~$5k_BT$[38] which is considered as an example of low barrier reaction. SCHEME 3 presents the transformation of the LE state to CT state via TICT process on photo-illumination. The LE state is naturally favoured in

low polarity condition while the more polar CT state is further stabilized via increased dipole-dipole interaction. The rate of conversion is therefore expected to be affected by both solvent dependence of reaction barrier and coupling of solvent dynamics to reaction timescale.[17,18,39] Temperature may also cause a change in the polarity in addition to the change of viscosity.[40] Hence we aim at monitoring the charge transfer reactions at elevated temperatures also.

The rest of the chapter is structured as follows. We have presented a detailed report on the interaction and solvation dynamics of [*f* Choline chloride+ (1-*f*) Urea)] at *f*= 0.33 and 0.40 near the eutectic composition (1:2) at temperatures from ~293 K to ~333 K by carrying out steady state and time-resolved fluorescence spectroscopic measurements. Choice of this composition is guided by its eutectic behaviour[5]. Probes used for dynamic fluorescence studies are coumarin 153 (C153) (lifetime ~3-5ns)[41] and trans-2-[4-(dimethylamino)styryl]-benzothiazole (DMASBT) (lifetime of ~0.5ns)[10] (SCHEME 1). Discussion on the behaviour of the system in accordance with Stokes Einstein Debye law is followed by the study of charge transfer reactions of P4C and P5C and solvent effects on their kinetics.

SCHEME 1:

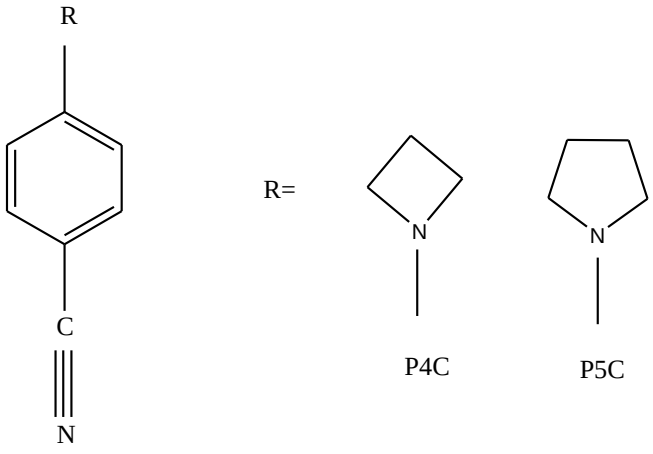

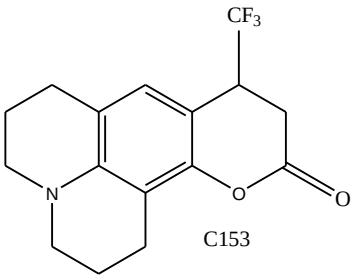

C153

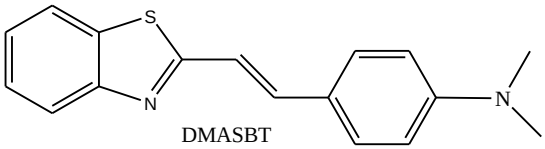

DMASBT

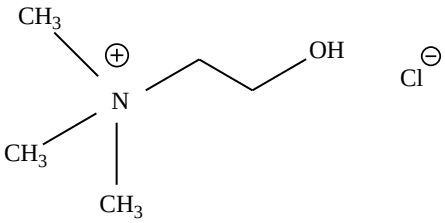

Choline chloride

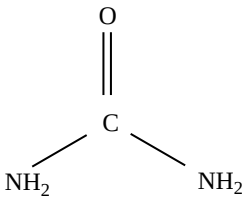

Urea

SCHEME 2:

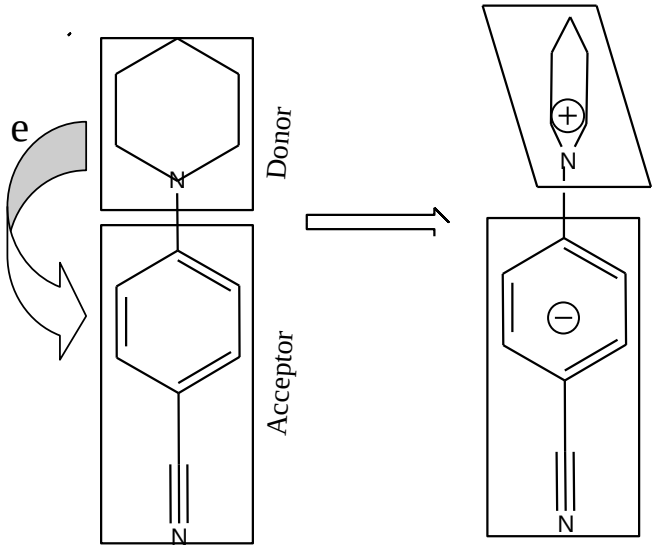

LE CT

SCHEME 3:

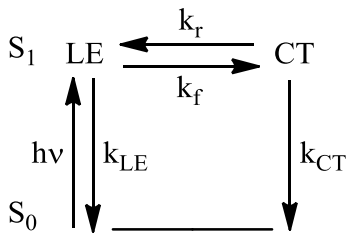

6.2. Experimental section

6.2.1. Materials

Choline chloride (≥99%, Sigma Aldrich) and urea (≥99%, SRL) were vacuum dried at room temperature for ~48 hours before use. C153 (laser grade, Exciton) and DMASBT[42] were used as received. P4C and P5C were synthesized and purified using the method reported earlier.[14]

6.2.2. Sample Preparation

Choline chloride and urea was weighed as required in a sample vial of 20ml and heated at ~340K until it was completely molten . It was then removed from heat and kept at room temperature to cool. 3ml of this cooled molten mixture was transferred to a transparent quartz cuvette (path length= 1 cm). The concentration of the fluorophore probe was maintained at ~10^{-5} M. A temperature controller (Julabo, model-F32) was connected to the cuvette chamber for temperature equilibration (+/- 0.5 K). Few samples were bubbled with dry nitrogen gas but produced results no different from those obtained for un-bubbled samples.

6.2.3. Data collection and analysis

Steady state absorption spectra and fluorescence spectra were collected with a UV-visible spectrophotometer (UV-2450, Shimadzu) and a Fluoromax-3, Jobin-Yvon (Horiba) fluorimeter, respectively. Time resolved fluorescence measurements were carried out with a time correlated single photon counting set-up (LifeSpec-ps) from

Edinburgh Instruments (Livingston), U.K. A laser excitation source of 409 nm has been used to excite the fluorophore solute C153 using a bandpass of ± 2nm. The full width at half maximum (FWHM) of instrument response function (IRF) of the used LASER was ~ 70 ps. To maintain the experimental temperature, a Peltier Heater (LFI-3751) was used for steady state fluorescence measurements. Spectral data for steady state measurements and time resolved studies were collected and analysed by methods described elsewhere[9,41] and in Chapter 2.

The following equation was used to construct the solvation response function [S(t)]:[43]

$$S(t) = \{\nu(t) - \nu(\infty)\}/\{\nu(0) - \nu(\infty)\} \tag{6.1}$$

where $\nu(0)$, $\nu(t)$ and $\nu(\infty)$ denote frequency (usually peak) for the reconstructed emission spectrum respectively at $t = 0$ (that is, immediately after excitation), at any given instant (t), and at a sufficiently long time ($t = \infty$). Integration of the multi-exponential fits to $S(t)$ gives us average solvation time ($< \tau_s >$) as:

$$\langle \tau_s \rangle = \int_0^\infty dt S(t) = \int_0^\infty dt[\textstyle\sum_i a_i \exp(-t/\tau_i)] = \sum_i a_i \tau_i \tag{6.2}$$

Where $\sum_i a_i = 1$, and a_i and τ_i respectively denote the amplitude and time constant associated with the *i*-th component of the total decay.

Fluorescence intensity decay for time resolved anisotropy measurement has been taken at the peak wavelength of the steady state fluorescence spectra of C153. Three types of decay of each sample and temperature have been collected - vertically (I_{para}), horizontally (I_{perp}) and magic angle polarized emission with respect to the excitation of the solute by vertically polarized light. The anisotropy analysis was again obtained by standard protocol[44] described in Chapter 2. Time resolved fluorescence anisotropy, *r*(t) was constructed by following the equation given bellow.

$$r(t) = \frac{I_{para}(t) - GI_{perp}(t)}{I_{para}(t) + 2GI_{perp}(t)} \tag{6.3}$$

The G-factor was obtained by tail matching. The larger time constant of the magic angle decay fit was used for subsequent parallel and perpendicular decay fitting. Then we fitted the anisotropy decay data by biexponential function of time of the following form

$$r(t) = r(0)[a_1 \exp(-t/\tau_1) + a_2 \exp(-t/\tau_2)] \ , \qquad (6.4)$$

where $a_1 + a_2 = 1$, and τ_1 and τ_2 are the two time constants associated with amplitudes a_1 and a_2 respectively. The initial anisotropy, r(0), was fixed at 0.376 for[45] all the samples used here. The average rotational correlation time, $\langle \tau_r \rangle$, was obtained via integrating the normalized function, $r(t)/r(0)$, as,

$$\langle \tau_r \rangle = \int_0^\infty dt \sum_{i=1}^{2} a_i \exp[-t/\tau_i] = a_1\tau_1 + a_2\tau_2 \ , \qquad (6.5)$$

Steady state absorption, emission, and time-resolved fluorescence measurements of P4C and P5C were carried out following methods described[15,14] earlier in Chapter 2. Concentration of P4C in solutions was always maintained at $\leq 10^{-5}$M. Fluorescence spectra of PnC in polar solutions were deconvoluted using standard software to get peak frequency, widths and areas under the LE and CT bands for further analyses. Error associated with the peak frequency and width are typically ±150 cm^{-1} and ±200 cm^{-1}, respectively. Time resolved fluorescence intensity decays were measured using a laser diode (producing excitation light of ~300 nm coupled to the TCSPC set-up).

Densities (ρ) of the samples were measured by an automated temperature-controlled density-cum-sound velocity analyzer (Anton Paar, model DSA 5000) at required temperatures ($\pm$ 0.5K). Viscosities (η) of the DES systems were measured by AMVn automated micro-viscometer from Anton Paar (falling ball method). Refractive indices are measured by Rudolph J357 Automated Refractometer. Glass transition temperature (T_g) shown in Figure A16 for this system was measured by Density Scanning Calorimter (DSC Q200).

Measured densities, viscosity coefficients and refractive indices are summarized in Table B10 (Appendix B).

6.3. Results and discussions

6.3.1. Steady state spectroscopic results

Figure 6.1 displays the absorption and emission spectra of C153 dissolved in [*f* choline chloride+ (1-*f*) urea] at *f* =0.33 and compares with those in 1-pentanol. Among many solvents, we found the spectral properties of this deep eutectics is close to that for 1-pentanol (ε_0 ~14).[41] Note the emission spectrum almost overlap while the absorption spectrum is slightly shifted from 1-pentanol. Similar shapes and peak energies of these spectra therefore suggest very similar solute-medium interactions in both the systems under comparison. In this context we would like to mention that (acetamide + electrolyte) DESs[9-11,19] were found to be more polar than the present DES as the corresponding spectra resembled those in formamide (ε_0 ~110).[46]

Figure 6.1

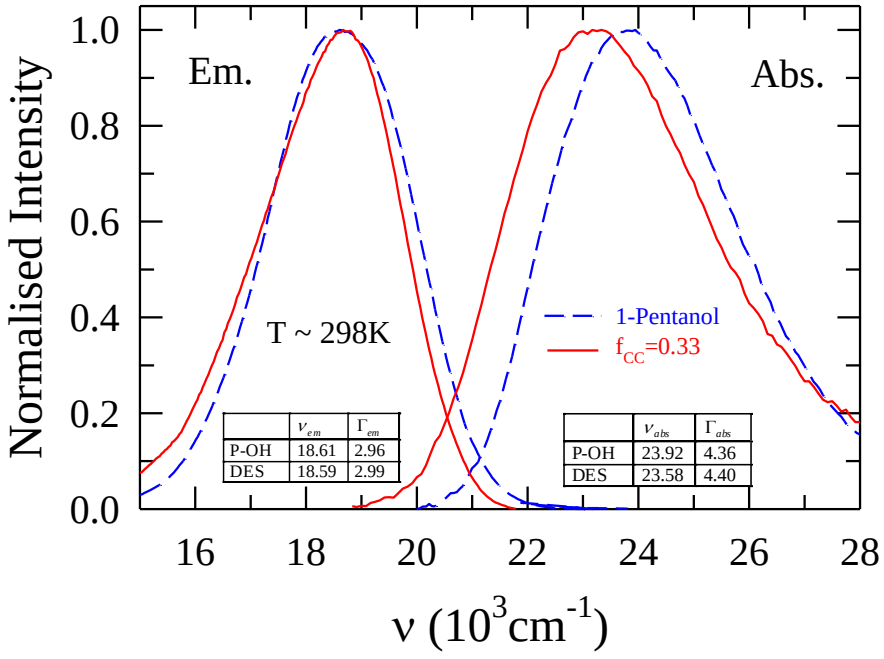

Figure 6.1: Comparison between steady state absorption and emission spectra (color coded) of the dissolved solute (C153) at 298 K in [*f* Choline chloride**+** (1-*f*) Urea] molten mixtures at *f***=** 0.33 and 1-pentanol (P-OH). The tables in the insets provide the values of the frequency (ν_{abs}, ν_{em}) and width (fwhm, $\Gamma_{abs}, \Gamma_{em}$).

Figure 6.2 show the variation of spectral parameters of [*f* choline chloride+ (1-*f*) urea] at varying temperatures at two different '*f*'. The absorption peak frequencies (ν_{abs}) shows a very weak dependence in the temperature range considered, while a red-shift in emission peak frequencies (ν_{em}) of ~450 cm^{-1} upon increasing temperature is noticed. This may imply enhancement of local polarity upon increase of temperature. On the other hand, increasing temperature is known to reduce ε_0,[47-49] and such an observation has been made for imidazolium ionic liquids and conventional solvents.[41,50] However, emission frequencies obtained after extrapolating the time-resolved emission spectra to $t = \infty$ (that is, $\nu(\infty)$) do not show any shift with temperature, excluding thereby the aspect of temperature-enhanced solution polarity. Therefore, the relatively blue-shifted emission frequencies at lower temperatures are due to incomplete relaxation of the solvent configurations because of the solution high viscosity ($80 \leq \eta/\mathrm{cP} \leq 1250$) in the temperature range studied, ($298 \leq T/\mathrm{K} \leq 333$). Spectral widths (full-widths-at-half-maxima) shown in the middle panel also do not show any dependence on temperature and resemble to those for spectra in 1-pentanol. A comparison between the measured dynamic Stokes' shift ($\Delta\nu^t$) and the relative steady state Stokes' shift ($\Delta\Delta\nu$) values, shown in the lower panel, also support this view of incomplete solvent relaxation due to large solution viscosity.

Figure 6.2

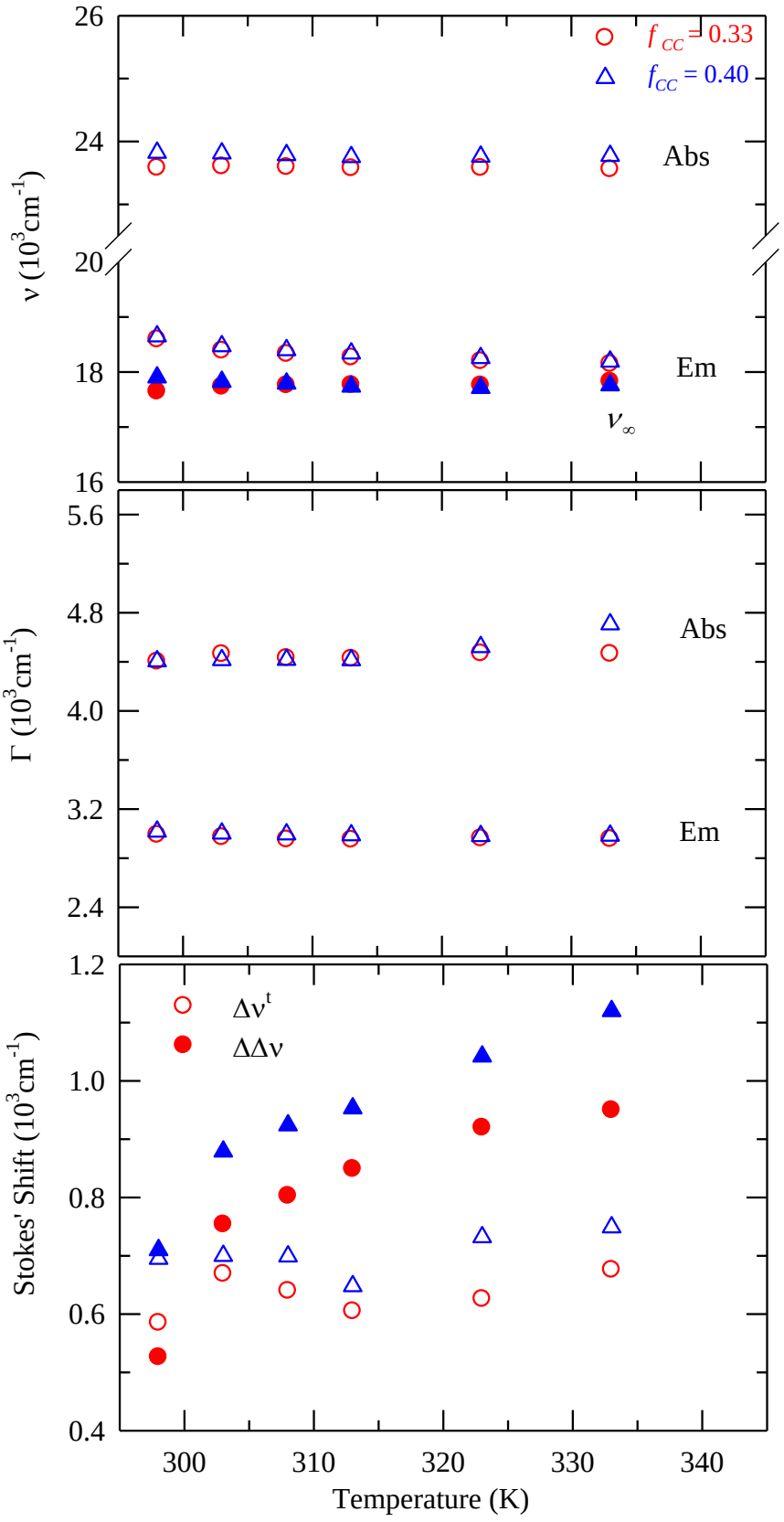
f_{CC} = 0.33
f_{CC} = 0.40
Abs
Em
ν_∞
ν (10^3cm^{-1})
Γ (10^3cm^{-1})
Stokes' Shift (10^3cm^{-1})
Δν^t
ΔΔν
Temperature (K)

Figure 6.2: Spectral parameters at two different fraction of '*f*' in [*f* Choline chloride**+** (1-*f*) Urea] (color coded) are shown here. Temperature dependencies of absorption and emission frequencies (ν) are shown in the upper panel, the full width at half maxima (Γ) in the middle panel and both steady state and time resolved Stokes' shift are shown in the lower panel. The two shifts are defined as $\Delta\Delta\nu = \left[\nu_{abs.} - \nu_{em.}\right]^{mixture} - \left[\nu_{abs.} - \nu_{em.}\right]^{heptane} = \Delta\nu^{mixture} - \Delta\nu^{heptane}$ and $\Delta\nu^{t} = \left[\nu_{.}(t=0)_{.} - \nu(t=\infty)\right]^{mixture}$ by the Fee-Maroncelli method (Ref. 43) and $\Delta\nu^{heptane}$ is measured as 4230 cm^{-1}.

While discussing Figure 6.1, we had mentioned that the system of (choline chloride+ urea) resembles the spectral characteristics of 1-pentanol of dielectric constant ~14. We have estimated the dielectric constant of this deep eutectic system using standard liquid correlation method using refractive indices and steady state results[51]. Refractive indices (n) and the value of emission frequencies (ν_{em}) are experimentally obtained. Temperature dependent ε_0 values are tabulated in Table B11. There is a steady increase in ε_0 as we move from lower to higher temperature. Note the value (ε_0 =14) at near room temperature is very close to what has been reported earlier from a qualitative comparison between emission frequencies (ν_{em}) using a different fluorescent solute.[35] Note ε_0 values estimated from fluorescence emission frequencies this way are expected to differ from direct measurements via dielectric relaxation spectroscopy because ν_{em} is influenced by both dipole-dipole and dipole-ion interactions between the dipolar probe (C153 here) and the surrounding environment in such ionic deep eutectics.

Figure 6.3

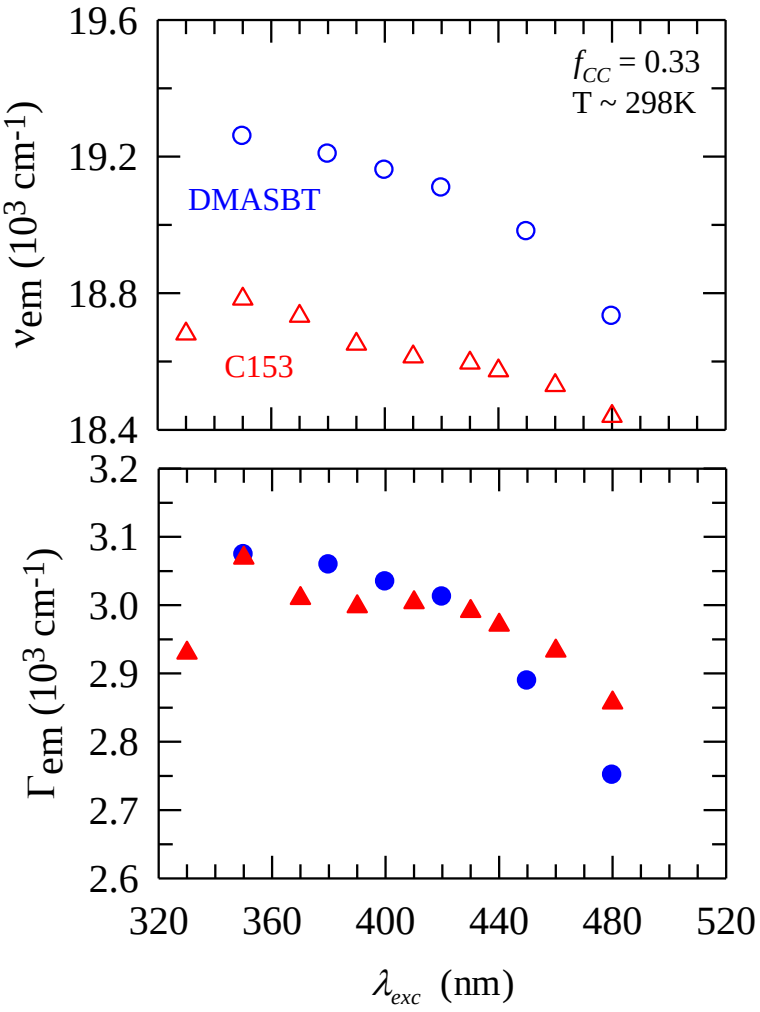

Figure 6.3: Emission peak frequencies (ν_{em}) and full width at half maxima, *fwhm* (Γ_{em}) for DMASBT and C153 in the system of [*f* Choline chloride**+** (1-*f*) Urea] at *f*= 0.33 (298 K) are plotted against different excitation wavelengths (λ_{exc}).

Figure 6.4

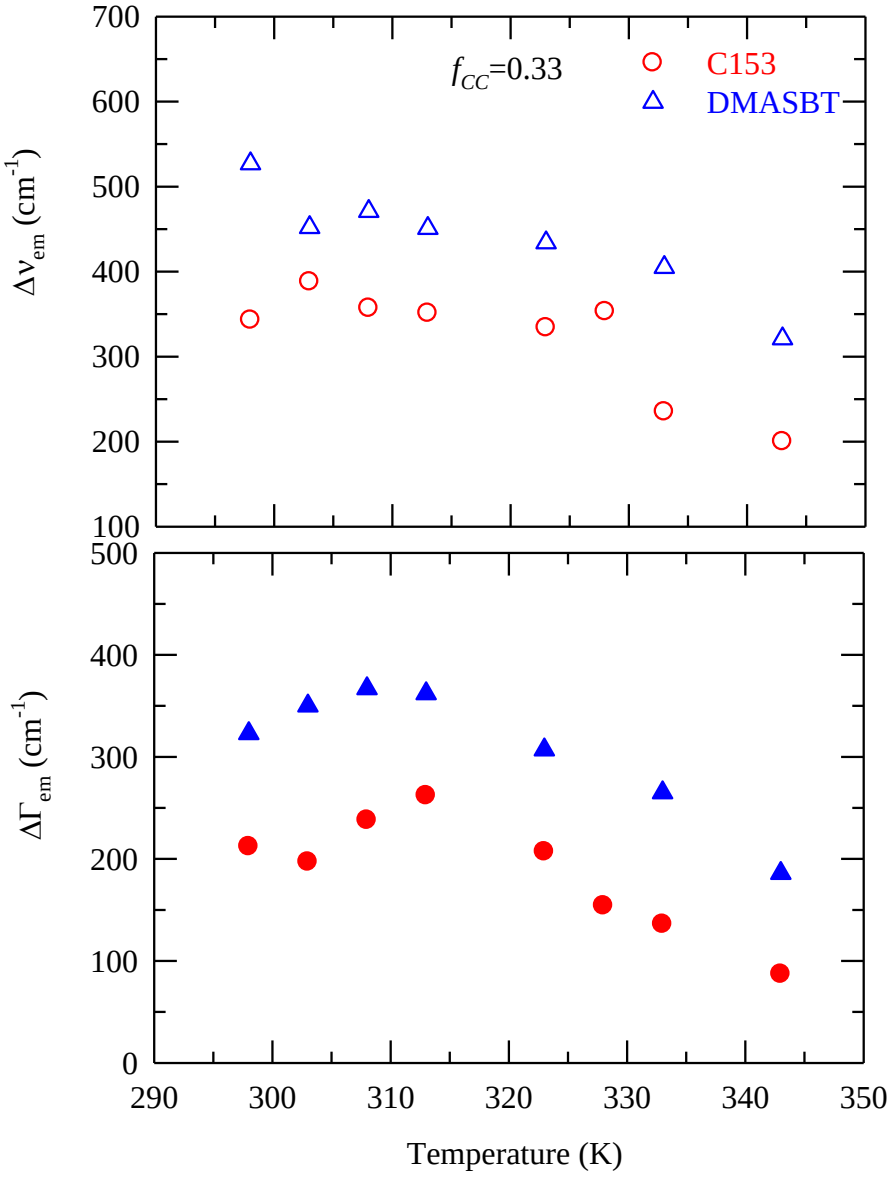

Figure 6.4: Temperature dependent total differences (Δx) in ν_{em} and Γ_{em} for f= 0.33 in [f Choline chloride**+** (1-f) Urea] are shown in the lower panel. This is defined as $\Delta x(T) = x(T, \lambda_{exc,\,b}) - x(T, \lambda_{exc,\,r})$, x being ν_{em} or Γ_{em}. $\lambda_{exc,\,b}$ and $\lambda_{exc,\,r}$ are the shortest (bluest) and longest (most red) wavelengths used for solute excitation.

Next, spatial heterogeneity is investigated via following the excitation wavelength ($\lambda_{exc.}$) dependence of fluorescence emission of two probes, C153 and DMASBT. Note τ_{life} for DMASBT is much shorter[52] than that for C153,[53] and hence faster density fluctuations are expected to be reported better[25] by DMASBT. Figure 6.3 displays $\lambda_{exc.}$ dependence of fluorescence emission frequencies (ν_{em}) and widths (Γ_{em}) for these probes at *f*= 0.33 in [*f* choline chloride + (1-*f*) urea)] deep eutectics at ~298K. Note ν_{em} red shifts by 527 cm^{-1} for DMASBT and 343 cm^{-1} for C153 as $\lambda_{exc.}$ moves from the highest (340 nm) to the lowest (480 nm) energies with concomitant spectral narrowing. Larger $\lambda_{exc.}$-induced spectral shift for DMASBT suggests, as before,[10,25] microheterogeneous domains formed in (choline chloride+ urea) DES fluctuate/interconvert at a timescale much faster than the average lifetime for C153. This provides a qualitative sense of density fluctuation timescales in these deep eutectics and forms the basis for solute dependence of solvent coupling to solute-centered relaxation dynamics in a given medium. Figure 6.4 shows temperature dependencies of total $\lambda_{exc.}$-induced changes in ν_{em} and Γ_{em} for these two solutes in this deep eutectic medium at *f*=0.33. Note over-all decrease of these spectral parameters (ν_{em} and Γ_{em}) with temperature suggests lower viscosity at higher temperature removes heterogeneity and facilitates relaxation. The trend remains the same at higher f as well (see Figure A17).

6.3.2. Dynamics from time resolved fluorescence studies

6.3.2.1. Dynamic Stokes' Shift Measurements

The intensity decays collected at the blue edge of the emission spectrum (steady state) show decay component and fit to triexponential function of time. On the other hand, intensity decays at the red edge fit to biexponentials, showing a rise and decay components. Representative decays with fitted parameters and residuals are shown in Figure 6.5. These representative decays indicate presence of dynamic Stokes' shift in these media as well as dynamical timescales in picoseconds and nanoseconds. Timescale faster than this can also be present as the current set-up is not equipped to quantitatively detect sub-picosecond response. Figure A18 summarize temperature effects on fluorescence lifetime and reflect a small (~20% at most) change.

Figure 6.5

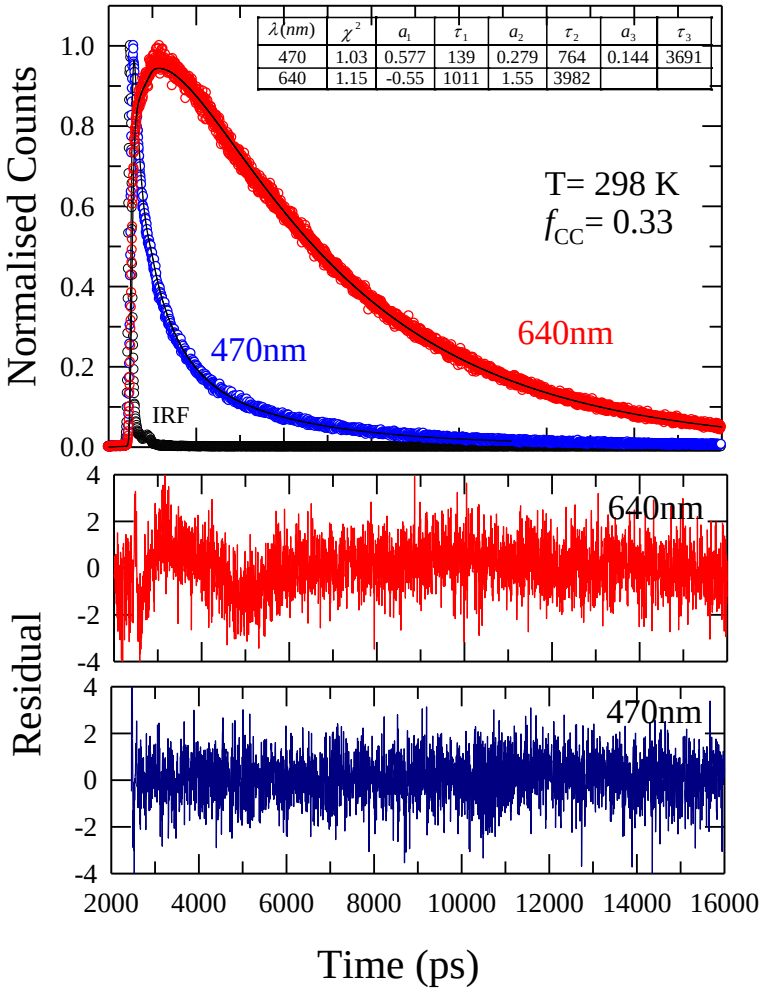

Figure 6.5: Representative fluorescence intensity decays at blue (470nm) and red (640nm) wavelengths for C153 in molten mixtures at f_{CC}= 0.33 (T= 298 K). Circles denote the experimental data and solid lines fits through them. Instrument response function (IRF) is also shown in the same figure (broken lines). The respective residuals (color coded) are presented in the bottom panels. The fit parameters are shown in the inset of the upper panel. Time constants (τ_i) are in the unit of picosecond. The goodness-of-fit parameters (χ^2) in these two wavelengths are 1.03 and 1.15, respectively.

Figure 6.6

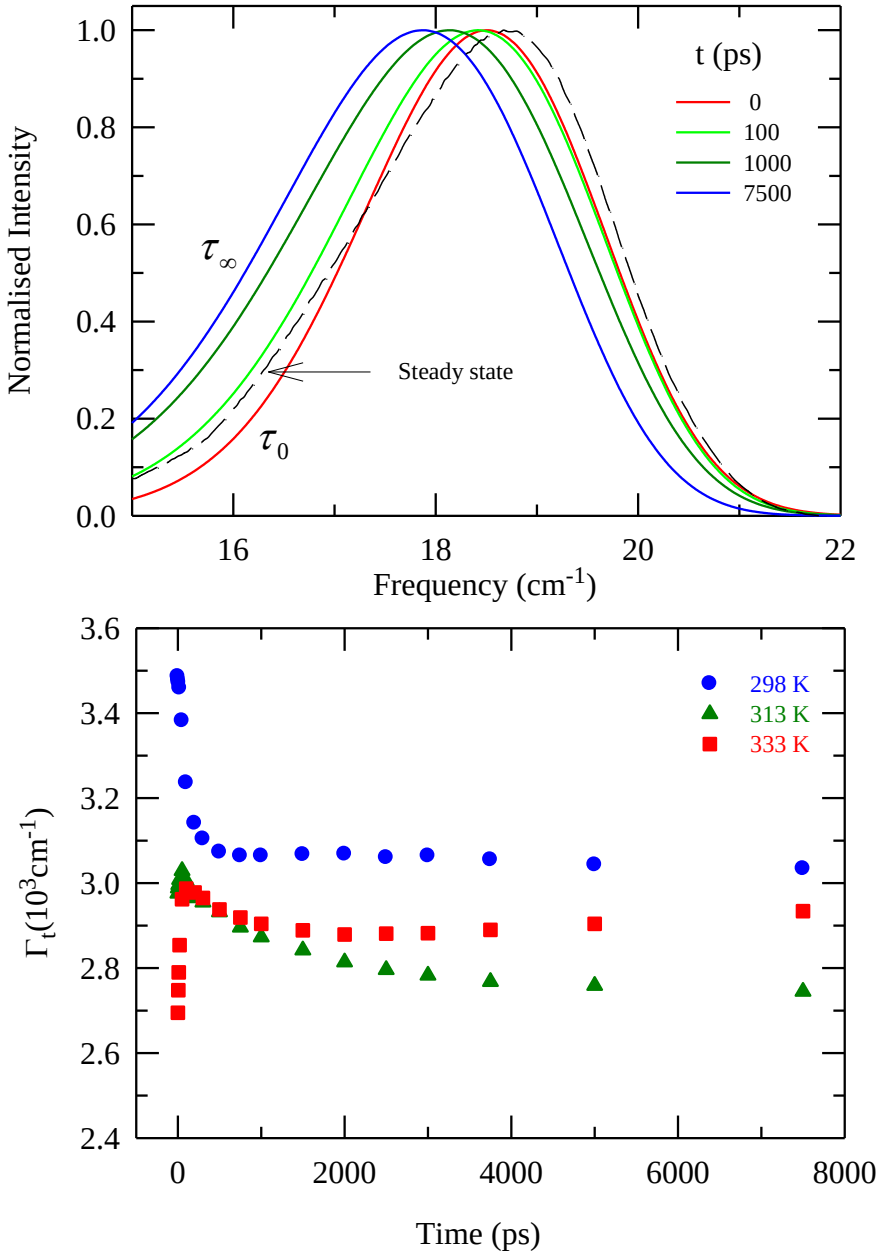

Figure 6.6: Synthesized time resolved emission spectra (TRES) of C153 at different times from the experimentally obtained decays at *f* = 0.33 in [*f* Choline chloride**+** (1-*f*) Urea] (T= 298 K). TRES shown (upper panel) are at the following time intervals after solute excitation: 0 ps (red), 100 ps (green), 1000 ps (deep green) and 7500 ps(blue). The steady state emission spectrum of the same is shown in broken line. Note that t=7500ps is also the τ_∞ spectrum. The lower panel shows the variation of widths of the spectra at three representative temperatures.

Next we show in Figure 6.6 the time-resolved emission spectra (TRES) of C153 in this system at f =0.33 and ~ 298K.[41] Interestingly, steady state emission spectrum (ν_{em}) is blue shifted by 900cm^{-1} relative to the emission spectrum (ν_{∞}) at $\tau = \infty$ from time-resolved measurements. This indicates pronounced effects from incomplete solvent relaxation during steady state emission. This has been already discussed in the steady state section and has been observed to be a common phenomenon for DESs.[9-11] As expected, this difference between ν_{∞} and ν_{em} decreases upon increasing temperature. The observed dynamic shift is ~600 cm^{-1} ($\Delta\nu^{t}_{obs}$) in the present measurements whereas the estimated shift ($\Delta\nu^{t}_{est}$) is found to be ~1500 cm^{-1}. Therefore, ~60% of the total response is being missed here which has a timescale much faster than the employed detection limit. Lower panel of Figure 6.6 shows the time evolution of widths for three temperatures. In the initial part we see $\Gamma(t)$ shows different trend for different temperatures. However, one common feature is little change in $\Gamma(t)$ in the initial period (0-10) followed by a plateau. Note $\Gamma(t)$ at $\tau = \infty$ is similar to Γ_{em} obtained from steady state measurements. The overall initial increase/decrease in $\Gamma(t)$ is within ~300-400 cm^{-1} and amounts to a small percentage of the full spectral width. This has been a common observation in dynamic Stokes' shift studies involving polar solvents,[35] ionic liquids[54-56] and DESs.[9-11]

Table 6.1 summarizes the temperature-dependent observed ($\Delta\nu^{t}_{obs}$) and estimated ($\Delta\nu^{t}_{est}$) dynamic Stokes' shift magnitudes and missing amplitudes in this deep eutectic solvent. Note these shift magnitudes are less than those obtained with the same solute (C153) in (acetamide + Na/KSCN)[9] and (acetamide +LiBr/NO_3)[10] deep eutectics. This is probably due to the presence of urea whose ε_0 is much less than that of acetamide.

Table 6.1: Dynamic Stokes' shift for C153 in [*f* Choline chloride+ (1-*f*) Urea] at different temperatures for f_{CC} =0.33.

T (K)	Estimated $\Delta\nu^t$ ($10^3 cm^{-1}$)	Observed $\Delta\Delta\nu$ ($10^3 cm^{-1}$)	Missed %
298	1.477	0.585	60
303	1.411	0.669	52
308	1.408	0.640	54
313	1.348	0.605	55
323	1.360	0.626	54
333	1.272	0.676	47

Figure 6.7 shows S(t) decays at three different temperatures which indicates faster decays at higher temperatures. Table 6.2 summarizes fit parameters required to describe the measured temperature dependent S(t) decays. For all temperatures, the decays are found to be bi-exponential function of time – with a faster component varying from ~50 to ~300 ps and slower one varying from ~200 ps to ~2300 ps. With rise in temperature, both the components become faster, suggesting diffusive mechanism being their origin. This can be understood as follows. For raising the solution temperature from ~ 298K to ~333K, the viscosity reduces from 1000 cP to 80 cP (at *f*= 0.33). Thus, approximately an order of magnitude reduction in viscosity accounts for similar shortening of the slowest timescale (τ_2) - from 2.2 ns to 0.2 ns. However, this diffusive mechanism may not follow the conventional hydrodynamics. For example, Stokes-Einstein (SE) relation predicts ~435 ns as diffusion time scale (σ^2/D) for choline cation at ~298K (using $\sigma = 2r = 3.29$Å[37], $\eta = 1008$ cP). Similarly, SE timescales for urea or chloride ions have been found too much longer than the slowest ~2 ns timescale measured in the present experiments. Therefore, it is

clear that particle translation very different from hydrodynamic diffusion, such as jumps are involved.[11,36]

Figure 6.7

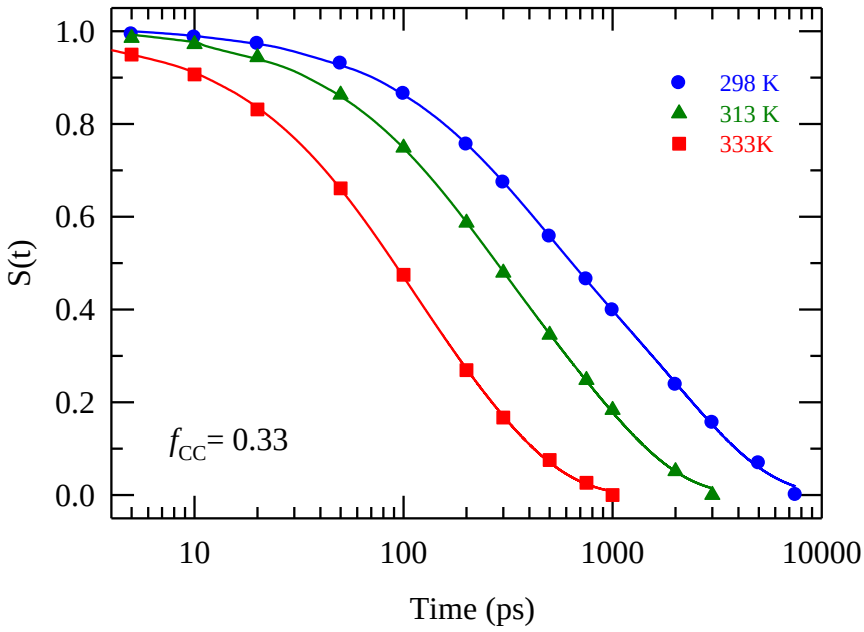

Figure 6.7: Decays of solvation response function, $S(t)$, measured using C153 at f= 0.33 in [f Choline chloride**+** (1-f) Urea] at three different temperatures (color coded).

Table 6.2: Solvation response function measured from experiment in [*f* Choline chloride+ (1-*f*) Urea] at different temperatures for f_{CC} =0.33: Fit parameters[a]

T (K)	a_1	τ_1 (ps)	a_2	τ_2 (ps)	$\langle \tau_s \rangle$ (ps)
298	0.46	294	0.54	2230	1339
303	0.44	278	0.56	2000	1242
308	0.40	204	0.60	1250	834
313	0.38	154	0.62	769	535
323	0.41	130	0.59	496	345
333	0.38	60	0.62	233	166

[a]These numbers are better than $\pm 10\%$ of the reported values (estimated based on limited data sets).

Figure 6.8 explores more quantitatively the viscosity coupling of the average solvation times in this these media at different temperatures. Here a log-log plot of the $< \tau_s >$ against temperature-reduced viscosity (η / T) is shown. These data suggest the following viscosity dependence: $< \tau_s > \propto (\eta / T)^p$, where *p*=0.81 and 0.71 for *f*=0.33 and 0.40, respectively. Such a fractional viscosity dependence indicates dynamic heterogeneity in the medium, and is a result of non-hydrodynamic centre-of-mass movement. Similar results have also been found for (acetamide+ electrolyte) deep eutectics, and resurrection from fraction to near unity for *p* upon replacement of ions by urea to these ionic acetamide deep eutectics.[19]

We have also estimated the activation energies (E_a) associated with the process of solvation and this is shown in Figure A19 by methods described in our earlier works.[10,19] The figure indicates Arrhenius-type temperature dependence of average solvation rates, and produces ~42 kJ/mole and ~51 kJ/mole as E_a values at f=0.4 and 0.33, respectively.

Figure 6.8

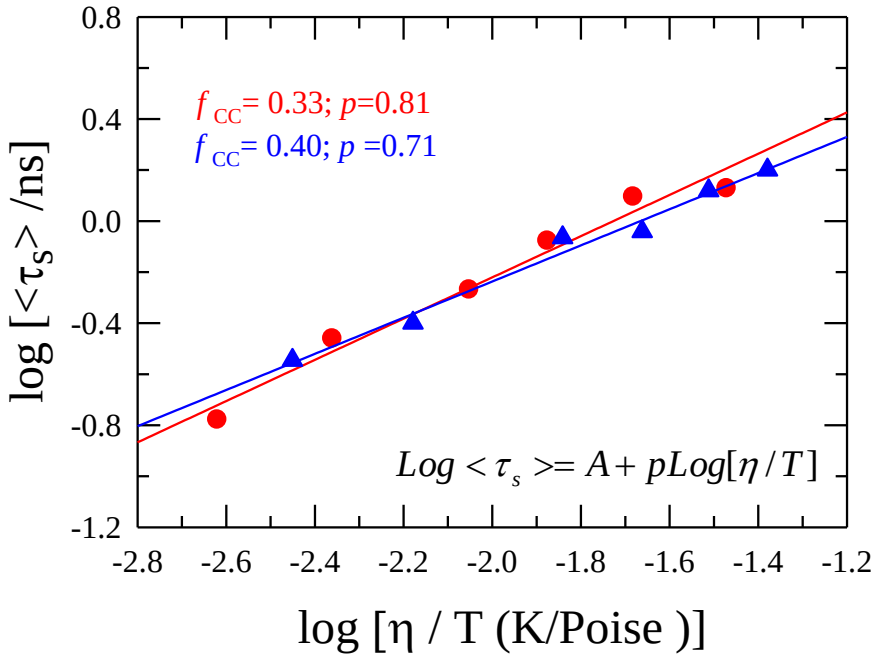

Figure 6.8: Medium viscosity (η) dependence of average solvation time, $\langle \tau_s \rangle$, for C153 in [f Choline chloride**+** (1-f) Urea] (Circles represent f=0.33, Triangles denote f=0.40). The η dependence of $\langle \tau_s \rangle$ in these media can be described by $\langle \tau_s \rangle = A(\eta / T)^p$ where A = 1.39 (f=0.33) and 1.18 (f =0.40).

6.3.2.2. Dynamic Anisotropy Measurements

Table 6.3 lists the bi-exponential fit parameters required to describe the measured $r(t)$ decays. It is clear that all fits are characterised by a slower time scale ranging from 3-40 ns contributing 80-70% of the $\langle \tau_r \rangle$ and a much faster component ranging between 20-100 ps. The slower time constant decreases with increase in temperature and is in accordance with viscosity trend. Note slower time constants at lower temperatures are ~7-8 times longer than than the τ_{life} of the probe C153 (~3-5 ns). Similar observation has also been found for C153 in ionic liquids with relaxation time scales as sluggish as ~100 ns[57].

Table 6.3: Parameters Obtained from Biexponential Fits to *r*(*t*) of C153 [*f* Choline chloride+ (1-*f*) Urea] at different temperatures.

T (K)	$\eta(cP)$	χ^2	a_1	τ_1 (ns)	a_2	τ_2 (ps)	$\langle \tau_r \rangle$ (ns)
f_{CC} =0.33							
298	1008	1.09	0.72	38.53	0.28	18	27.92
303	631	1.06	0.70	24.91	0.30	18	17.45
308	411	1.07	0.59	13.96	0.41	19	8.291
313	278	1.19	0.68	9.54	0.32	16	6.514
318	195	1.08	0.73	6.96	0.27	15	5.117
323	141	1.12	0.79	5.58	0.21	12	4.403
333	80	1.16	0.82	3.39	0.18	74	2.777

f_{CC} =0.40							
298	1244	1.09	72	38.53	28	18	38.9
303	932	1.06	70	24.91	30	18	22.83
308	671	1.07	59	13.96	41	19	11.16
313	451	1.19	68	9.54	32	16	8.484
323	214	1.08	73	6.96	27	15	3.768
333	118	1.12	79	5.58	21	12	2.911

The coupling to the viscosity and validity of Stokes-Einstein-Debye (SED) relation for solute rotation is tested next in Figure 6.9 where temperature dependent average rotational times ($\langle \tau_r \rangle$) are shown as a function of temperature- reduced viscosity (η / T) in a double-logarithmic plot. SED predictions from the relation, $\tau_r = (V\eta / k_B T) f_s C$, are also shown for a comparison. Note for SED calculations, shape factor, f_s =1.71, and C =0.24 (slip) and 1(stick)[50] have been used along with solute volume, V = 246 Å^3. In addition, average times obtained by fitting 100%, 90%, 80% and 70% of the collected r(t) decays are shown to examine the fidelity of the long time constants obtained in our fits. As the figure suggests, there is not much difference in the array of the four considerations. Obviously, measured times are better predicted by slip hydrodynamics than the stick counter-part. A fit of these data to $\langle \tau_r \rangle \propto (\eta/T)^p$ leads to an f-averaged value p=0.86. This value of p is larger than that found in solvation measurements, and thus suggests rotation-translation decoupling of sort. Figure A20 (Appendix A) shows the rotational- translational decoupling for the higher fraction of Choline chloride ad f =0.40 also. Figure 6.10 demonstrates this more vividly where the extent of decoupling, as expected, becomes stronger at lower temperature due to larger viscosity.

Figure 6.9

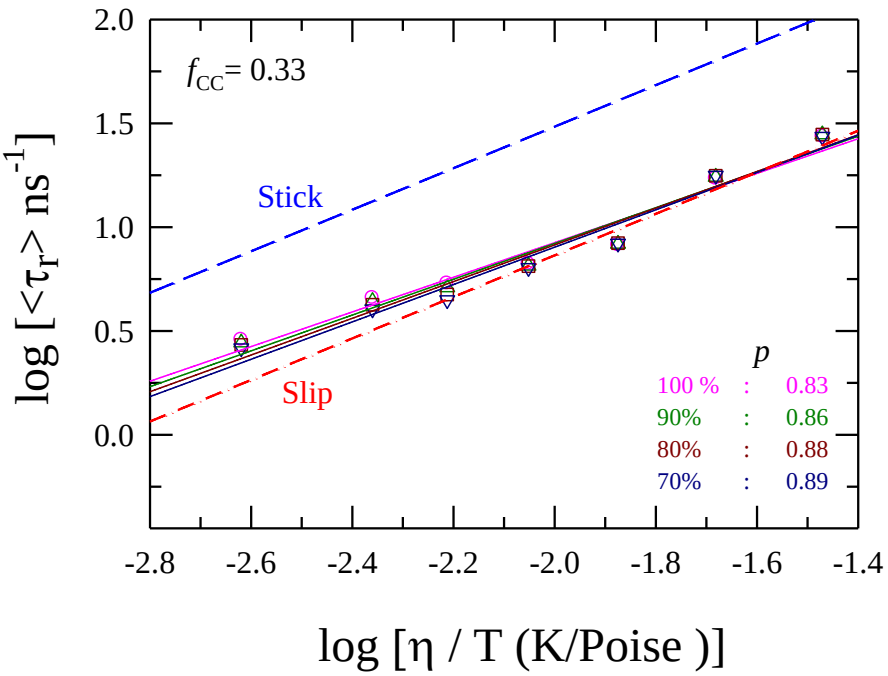

Figure 6.9: Viscosity coupling of rotation times ($\langle \tau_r \rangle$) for C153 in the system [*f* Choline chloride**+** (1-*f*) Urea] (*f*=0.33) and comparison to hydrodynamic theory is shown in this figure. Temperature dependent measured times (color codes are for fittings with different range as explained in the text) are shown as a function of temperature-reduced viscosity (η/T) in a log-log fashion [$Log\langle \tau_r \rangle = A + pLog(\eta/T)$]. Rotation times for C153 at various η/T values from calculation by SED equation are also shown (broken red line) at the slip boundary for a comparison. Corresponding stick values are in broken blue line.

Figure 6.10

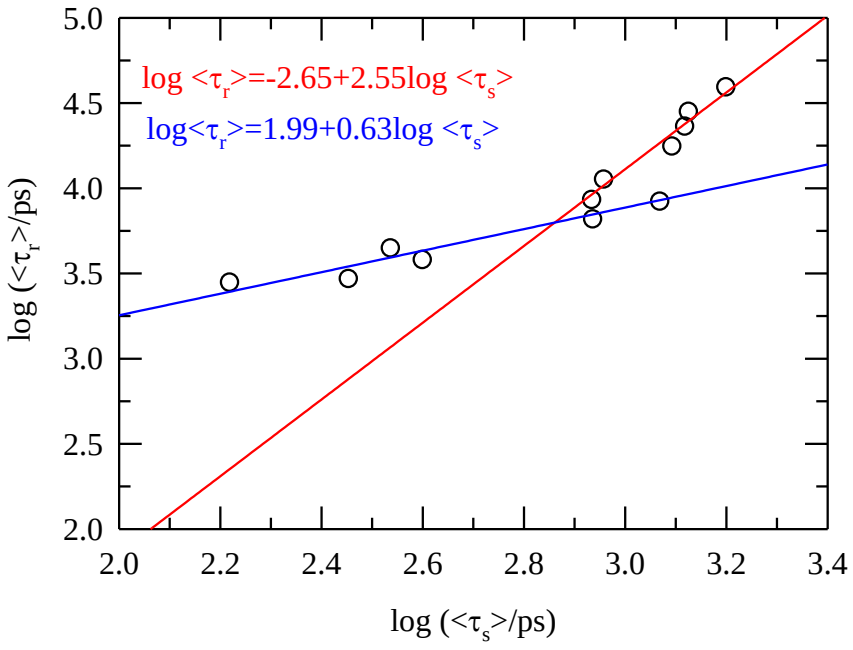

Figure 6.10: Experimental average rotational correlation times ($\langle \tau_r \rangle$) versus solvation times ($\langle \tau_s \rangle$) in log-log form for C153 in the DES is shown here. The line going through the circles represents a fit to the relation shown in the panel. The correlation is different at higher and lower temperature regimes.

6.3.2.3. Charge transfer reaction kinetics and correlation with solvation timescale

Next we explore how solvation affects rate of intra-molecular charge transfer reaction in P4C and P5C in these DESs. The reaction time (τ_{rxn}) is calculated from LE decays from the following general formula:[38]

$$\tau_{rxn} = \frac{\sum_{i=1}^{n-1} a_i \tau_i}{\sum_{i=1}^{n-1} a_i} \qquad (6.7)$$

Where a_i and τ_i are the fractional amplitudes and time constants observed in *n*-exponential fits. Representative decays for LE and CT states for P4C is shown in Figure A21 and some fit values are summarised in Table B12. Relevant steady state results are described in Appendix C.

Figure 6.11 depicts the reaction timescales for P4C and P5C in [*f*Choline chloride + (1-*f*) urea] DES at *f*=0.33 at various temperatures via showing the temperature dependence of average reaction rates, $\langle \tau_{rxn} \rangle^{-1}$. Clearly, the measured rates show Arrhenius-type temperature dependence with activation energies (E_a) ~26 and ~18 kJ/mole for P4C and P5C, respectively. These activation energies are very similar to what have been found earlier while studying ICT reactions in these molecules in neat ambient solvents.[38] In addition, the decay kinetics have also remained qualitatively similar (bi or tri-exponential) as those in normal solvents.

Figure 6.11

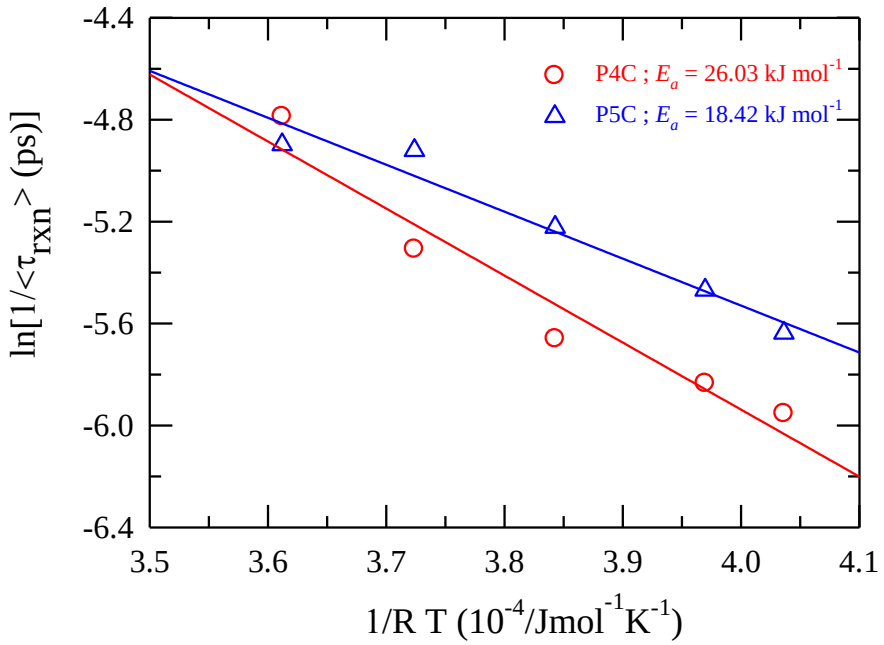

Figure 6.11: Arrhenius type plot of $\ln(1/\langle\tau_{rxn}\rangle)$ vs *1/RT* for reaction time of P4C and P5C in [*f* Choline chloride+(1-*f*) Urea] at f_{CC}= 0.33. The solid lines are the linear fits through the data points. Circles represent natural logarithm of inverse of reaction times for P4C, and triangles for P5C. The respective activation energies are indicated along the legends.

The solvent dynamical control on reaction time scale, $\langle\tau_{rxn}\rangle$, is then explored in Figure 6.12 where measured $\langle\tau_{rxn}\rangle$ are shown as a function of experimental $\langle\tau_s\rangle$ in double-logarithmic fashion. Linear fits going through the data indicate the following dependence, $\langle\tau_{rxn}\rangle = a(<\tau_s>)^b$, for both the ICT molecules. Values for *b* found here suggest stronger dynamic solvent control for ICT reaction of P4C in these DESs than that for P5C. Note this is opposite to what has been found earlier for neat solvents[38] and thus warrants explanation. The coupling to medium dynamic friction via $\langle\tau_s\rangle$ is expected to be stronger for reaction times that are relatively slower because solvation

response in this DES possesses a nanosecond component (see Table 6.2). Since $\langle \tau_{rxn} \rangle$ in P4C is longer than that in P5C, the reactive mode in the former experiences stronger solvent fluctuations (and thus friction) while crossing the reaction barrier. Note also that such a nanosecond component is completely absent in solvation response measured for neat solvents,[41] and as a result, reaction rate in P4C showed no dynamical solvent control.[38] This is a novel finding here.

Figure 6.12

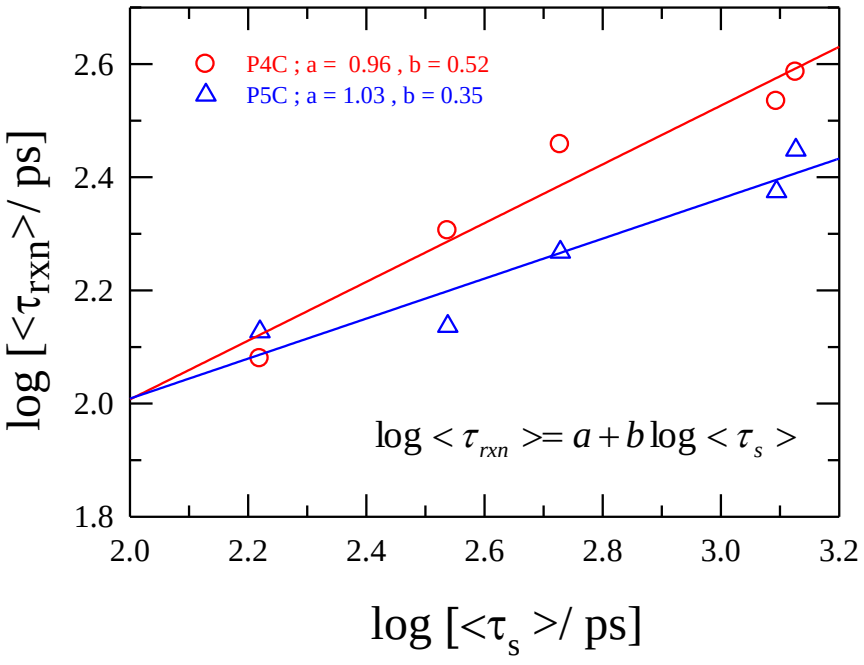

Figure 6.12: The correlation of reaction time (τ_{rxn}) for P4C and P5C is plotted with the solvation time ($\langle \tau_s \rangle$) in the system [*f* Choline chloride+(1-*f*) Urea] at f_{CC}= 0.33.

6.4. Conclusion

In summary, the ionic deep eutectics made of choline chloride and urea studied here indicates moderate presence of both spatial and temporal heterogeneities, showing that presence of urea cannot completely remove the heterogeneity signatures. ICT reaction timescales show evidences for significant solvent dynamical control in these DESs which occurs because of competitive reaction and solvation timescales. Activation energies have been found to be similar to those in normal solvents.

References

1. Jessop, P. G.; Jessop, D. A.; Fu, D. B.; Phan, L. *Green Chem.* **2012**, *14*, 1245.

2. Zhang, Q. H.; Vigier, K. D.; Royer, S.; Jerome, F. *Chem. Soc. Rev.* **2012**, *41*, 7108.

3. Liao, J.-H.; Wu, P.-C.; Bai, Y.-H. *Inorganic Chemistry Communications* **2005**, *8*, 390.

4. Nockemann, P.; Thijs, B.; Driesen, K.; Janssen, C. R.; Van Hecke, K.; Van Meervelt, L.; Kossmann, S.; Kirchner, B.; Binnemans, K. *J. Phys. Chem. B* **2007**, *111*, 5254.

5. Abbott, A. P.; Capper, G.; Davies, D. L.; Rasheed, R. K.; Tambyrajah, V. *Chem. Commun.* **2003**, 70.

6. Abbott, A. P.; Boothby, D.; Capper, G.; Davies, D. L.; Rasheed, R. K. *J. Am. Chem. Soc.* **2004**, *126*, 9142.

7. Francisco, M.; Van den Bruinhorst, A.; Kroon, M. C. *Angew. Chem., Int. Ed.* **2013**, *52*, 3074.

8. Wagle, D. V.; Zhao, H.; Baker, G. A. *Acc. Chem. Res.* **2014**, *47*, 2299.

9. Guchhait, B.; Gazi, H. A. R; Kashyap, H. K.; Biswas, R. *J. Phys. Chem. B* **2010**, *114*, 5066.

10. Guchhait, B.; Daschakraborty, S.; Biswas, R. *J. Chem. Phys.* **2012**, *136*, 174503.

11. Guchhait, B.; Das, S.; Daschakraborty, S.; Biswas, R. *J. Chem. Phys.* **2014**, *140*, 104514.

12. Pradhan, T.; Gazi, H. A. R.; Biswas, R. *J. Chem. Phys.* **2009**, *131*, 054507.

13. Pradhan, T.; Ghoshal, P.; Biswas, R. *J. Phys. Chem. A* **2008**, *112*, 915.

14. Pradhan, T.; Biswas, R. *J. Phys. Chem. A* **2007**, *111*, 11514.

15. Pradhan, T.; Biswas, R. *J. Phys. Chem. A* **2007**, *111*, 11524.

16. Hynes, J. T., Simon, J. D. *Charge -Transfer Reactions and Solvation Dynamics in Ultrafast Dynamics of Chemical Systems*; Kluwer: Dodrecht, **1994**.

17. Van der zwan, G.; Hynes, J. T. *Chem. Phys.* **1991**, *152*, 169.

18. Van der Zwan, G.; Hynes, J. T. *J. Chem. Phys.* **1983**, *78*, 4174.

19. Das, A.; Das, S.; Biswas, R. *J. Chem. Phys.* **2015**, *142*, 034505.

20. Berchiesi, G.; Rafaiani, G.; Vitali, G.; Farhat, F. *J. Therm. Anal.* **1995**, *44*, 1313.

21. Berchiesi, G.; Vitali, G.; Passamonti, P.; Plowiec, R. *J. Chem. Soc., Faraday Trans 2* **1983**, *79*, 1257.

22. Berchiesi, G.; Vitali, G.; Plowiec, R.; Barocci, S. *J. Chem. Soc. Faraday Trans. 2* **1989**, *85*, 635.

23. Amico, A.; Berchiesi, G.; Cametti, C.; Di Biasio, A. *J. Chem. Soc. Faraday Trans. 2* **1987**, *83*, 619.

24. Mukherjee, K; Das, A.; Choudhury, S.; Barman, A.; Biswas, R.; *J. Phys. Chem. B* **2015**, *xxxx*, xxxx.

25. Das, A.; Das, S.; Biswas, R. *Chem. Phys. Lett.* **2013**, *581*, 47.

26. Gazi, H. A. R.; Guchhait, B.; Daschakraborty, S.; Biswas, R. *Chem. Phys. Lett.* **2011**, *501*, 358.

27. Pal, T.; Biswas, R. *Chem. Phys. Lett.* **2011**, *517*, 180.

28. Das, S.; Biswas, R.; Mukherjee, B. *J. Phys. Chem. B* **2015**, *119*, 274.

29. Biswas, R.; Das, A.; Shirota, H. *J. Chem. Phys.* **2014**, *141*, 134506.

30. Abbott, A. P.; Capper, G.; Davies, D. L.; Rasheed, R. K. *Chem. Eur. J.* **2004**, *10*, 3769.

31. Abbott, A. P.; Capper, G.; Davies, D. L.; Rasheed, R. *Inorg. Chem.* **2004**, *43*, 3447.

32. Hayyan, M.; Hashim, M. A.; Hayyan, A.; Al-Saadi, M. A.; AlNashef, I. M.; Mirghani, M. E. S.; Saheed, O. K. *Chemosphere* **2013**, *90*, 2193.

33. Dai, Y.; Van Spronsen, J.; Witkamp, G.-J.; Verpoorte, R.; Choi, Y. H. *Anal. Chim. Acta.* **2013**, *766*, 61.

34. Hayyan, A.; Mjalli, F. S.; AlNashef, I. M.; Al-Wahaibi, Y. M.; Al-Wahaibi, T.; Hashim, M. A. *J. Mol. Liq.* **2013**, *178*, 137.

35. Pandey, A.; Rai, R.; Pal, M.; Pandey, S. *Phys. Chem. Chem. Phys* **2014**, *16*, 1559.

36. Perkins, S. L.; Painter, P.; Colina, C. M. *J. Phys. Chem. B* **2013**, *117*, 10250.

37. D'Agostino, C.; Harris, R. C.; Abbott, A. P.; Gladden, L. F.; Mantle, M. D. *Phys. Chem. Chem. Phys.* **2011**, *13*, 21383.

38. Dahl, K.; Biswas, R.; Ito, N.; Maroncelli, M. *J. Phys. Chem. B* **2005**, *109*, 1563.

39. Nitzan, A. *Chemical Dynamics in Condensed Phases*; Oxford Univ. Press: Oxford, 2006.

40. Lakowicz, J. R. *Principle of Fluorescence Spectroscopy*; Kluwer Academic Pub: New York, 1999; Vol. 2nd ed.

41. Horng, M. L.; Gardecki, J. A.; Papazyan, A.; Maroncelli, M. *J. Phys. Chem.* **1995**, *99*, 17311.

42. *DMABST was received as a gift from Prof. Maroncelli, Penn. State University, USA.*

43. Fee, R. S.; Maroncelli, M. *Chem. Phys.* **1994**, *183*, 235.

44. Cross, A. J.; Fleming, G. R. *Biophys. J.* **1984**, *46*, 45.

45. Arzhantsev, S.; Jin, H.; Baker, G. A.; Maroncelli, M. *J. Phys. Chem. B* **2007**, *111*, 4978.

46. Riddick, J. A.; Bunger, W. B.; Sakano, T. K. *Organic Solvents*; Wiley: New York, 1986.

47. Hunger, J.; Stoppa, A.; Schrödle, S.; Hefter, G.; Buchner, R. *Chemphyschem* **2009**, *10*, 723.

48. Petrowsky, M.; Frech, R. *J. Phys. Chem. B* **2009**, *113*, 5996.

49. Petrowsky, M.; Frech, R. *J. Phys. Chem. B* **2009**, *113*, 16118.

50. Jin, H.; Baker, G. A.; Arzhantsev, S.; Dong, J.; Maroncelli, M. *J. Phys. Chem. B* **2007**, *111*, 7291.

51. Biswas, R.; Lewis, J. E.; Maroncelli, M. *Chem. Phys. Lett.* **1999**, *310*, 485.

52. Maroncelli, M. *Private communication.*

53. Horng, M. L.; Gardecki, J. A.; Maroncelli, M. *J. Phys. Chem. A* **1997**, *101*, 1030.

54. Khara, D. C.; Paul, A.; Santhosh, K.; Samanta, A. *J. Chem. Sci.* **2009**, *121*, 309.

55. Paul, A.; Samanta, A. *J. Phys. Chem. B* **2007**, *111*, 1957.

56. Jin, H.; Li, X.; Maroncelli, M. *J. Phys. Chem. B* **2007**, *111*, 13473.

57. Funston, A. M.; Fadeeva, T. A.; Wishart, J. F.; Castner, E. W. *J. Phys. Chem. B* **2007**, *111*, 4963.

58. Li, X.; Maroncelli, M. *J. Phys. Chem. A* **2011**, *115*, 3746.

Chapter 7

Effects of functional groups of the hydrogen bond donors in choline chloride based DESs – A fluorescence Spectroscopic Outlook

7.1. Introduction

With the increasing quest for more benign class of solvents, immense importance has been given to the production of ecologically safe solvents. For this purpose, deep eutectic solvents (DES) have received intense attention.[1-4] These media possess physico-chemical solvent properties required for large scale industrial and technological applications.[5-7] Moreover, these solvents are easy to prepare, cost effective, and can be easily tuned for desired medium properties by varying the mixture compositions. DESs are actually mixtures of two or more constituents that form stable liquid phase upon melting at a temperature much lower than the individual melting temperatures of the constituents. Extensive H-bond interaction among the constituents is the key for the deep depression of freezing points, and increased entropy upon melting provides further energetic support to stabilize the liquid phase.

Amides and quarternary salts of amides with electrolytes, urea, alcohol and sugars can combine to produce DESs. When electrolytes are used as one of the constituents, ionic DESs are formed. On the other hand, amphiphiles/dipolar constituents are present in a molten mixture containing amides, the resultant molten mixtures are known as non-ionic DESs. Acetamide based DESs[8-16] have already been in use for quite some time now. Choline chloride mixed with urea, poly-hydroxy alcohols or carboxylic acids produce[3,4] DESs which are much less hazardous than acetamide containing ones. Although properties like viscosity, conductivity and surface tension have been measured for many of these systems,[3,4,17-22] microscopic information regarding structure and dynamics is still lacking. In the present work, we have studied four different types of DES with varying functional groups of the hydrogen bond donor to understand the effects of the same on

solution structure and dynamics using steady state and time-resolved fluorescent spectroscopic techniques.

Phase diagram studies on choline chloride based DESs with varying hydrogen bond donors have shown that malonic acid, which has two carboxylic acid (-COOH) groups, can form DES with choline chloride at 1:1 mole ratio whereas other hydrogen bond donors (HBDs) form at 2:1 ratio.[3,18] Molecular dynamics simulations and pulsed field gradient nuclear magnetic resonance (PFG-NMR) measurements of choline chloride based DESs have revealed varying diffusion co-efficient of the choline cations and anions in presence different HBD molecules.[19] The interaction between choline cation and HBD decreases with increase in temperature, producing a large change in viscosity. We investigate this change via probing the viscosity coupling of solute-centred dynamics, such as, excited solute solvation and rotation. Note (choline chloride+ urea) DESs have already been studied by time resolved fluorescence,[22] simulation[17] and NMR[19] measurements. Therefore, results obtained for DESs made of choline chloride and different carboxylic acids will be compared to those for (choline chloride+ urea) in order to better understand these exotic and bio-degradable media.

Chemical structures of the components for the DESs considered here are provided in SCHEME 1. Choline chloride (‘a’) is used in association with vitamin B in health drinks and thus is of tremendous importance. Malonic acid (‘b’) has two –COOH groups whereas 3-phenylpropionic acid (‘c’) has a single such group along with a phenyl group at the hydrocarbon tail. The eutectic composition for the respective acids with choline chloride is 1:1 and 1:2. Such a variation in mixture composition clearly indicates difference in interaction in the resultant DESs. Effects of functional groups emanate from number of groups that can participate in H-bonding with choline chloride. Note malonic and 3-phenylpropionic acids possess two and one carboxylic acid groups, respectively. Ethylene glycol (‘d’) and glycerol (‘e’) contains two and three hydroxyl (-OH) groups, respectively. However, these polyols form DESs with choline chloride at 1:2 mole ratio, indicating mere presence of larger number of functional groups cannot exclusively dictate DES composition.

SCHEME 1

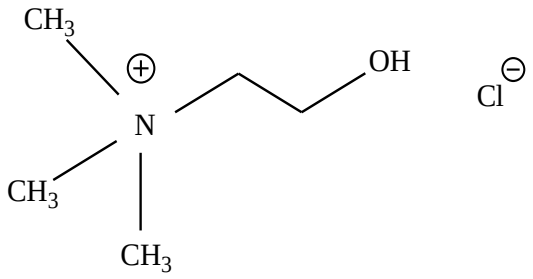

(a)

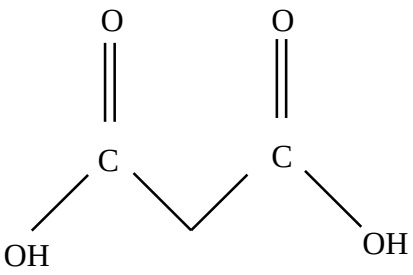

(b)

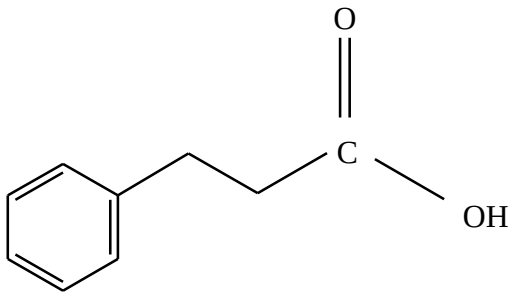

(c)

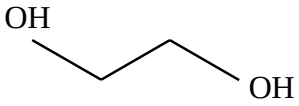

(d)

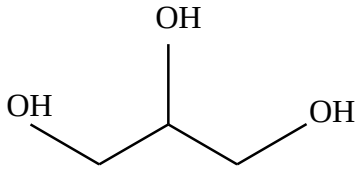

(e)

7.2. Experimental Details

7.2.1. Sample Preparation

Coumarin 153 (C153) was used as received (Exciton). Trans-2-[4-dimethylamino)styryl]benzothiazole (DMASBT), a fluorescence probe with much shorter excited state average lifetime[23] than that of C153, was also used as received.[24] Choline chloride (≥ 99%, Sigma Aldrich), Malonic acid (>99%, Sigma Aldrich) and 3-Phenylpropionic acid (>99%, Sigma Aldrich) were dried (~300 K) in mild vacuum overnight before use. Ethylene glycol (>99%, Sigma Aldrich) and Glycerol (>99%, Sigma Aldrich) were used as received.

Samples were prepared by following the method described in details elsewhere.[10,11] In brief, the required amount of DES components were mixed together in volumetric flasks, sealed, and heated using a hot water bath at a temperature around ~355 K (Julabo, model F32) until the mixtures became completely molten. An aliquot of a given molten DESs was then quickly transferred into a pre-heated quartz cuvette (1 cm path length) which was pre-stained with dye (C153/DMASBT) grains and sealed. A few drops of (dye+hexane) solution was used for this 'dye-staining' followed by removal of the career solvent (hexane) by gently blowing warm air through the cuvette. Subsequently, the cuvette containing the sample and dye was brought to the experimental temperature via using a water-bath. Care was taken to ensure complete dissolution of the probe into the DES sample, maintaining a dye (C153/DMASBT) concentration $\leq 10^{-5}$ M in the solution under investigation. Spectral data were recorded after allowing the sample for about half-an-hour to equilibrate with pre-heated sample chamber at a designated temperature (328 K to 353 K at an interval of 5 K). A few samples were bubbled with dry N_2 gas before data collection but did not produce any difference in data with those collected with the un-bubbled samples.

7.2.2. Data Collection and Analyses for Absorption, Steady State and Time Resolved Fluorescence Studies

Steady state absorption spectra and fluorescence spectra were collected with a UV-visible spectrophotometer (UV-2450, Shimadzu) and a Fluoromax-3, Jobin-Yvon (Horiba) fluorimeter respectively. The spectral data for steady state measurements were analysed and normalized to get the average peak frequency and full width at half maximum (fwhm) by methods described earlier.[25,26] Time correlated single photon counting spectrophotometer (LifeSpec-ps) from Edinburgh Instruments (Livingston), U.K was used for time-resolved experiments. A laser excitation source of 409 nm has been used to excite C153 using a band-pass of $\pm$ 2nm. A pulse-width (full-width-at-half-maximum) of ~70 ps was obtained using an aqueous solution of non-dairy creamer at the excitation wavelength.[9-11] To maintain the experimental temperature, a Peltier heater (LFI-3751) was used for steady state fluorescence measurements whereas a temperature-controller attachment (Julabo F32) was used for steady state absorption and time resolved measurements.

To collect data for solvation dynamics, time resolved emission spectra (TRES) were reconstructed from a series of 18-20 decays collected at magic angle (54.7°) at wavelengths spaced evenly over the full steady state emission spectrum of C153 in the systems. Details of fitting procedure are discussed in Chapter 2 and other relevant works.[26] Solvation response function , S(t), was then constructed from the time-resolved emission spectra as follows:[27]

$$S(t) = \{\nu(t) - \nu(\infty)\} / \{\nu(0) - \nu(\infty)\} \tag{7.1}$$

where $\nu(0)$, $\nu(t)$ and $\nu(\infty)$ denote frequency (usually peak) for the reconstructed emission spectrum respectively at $t = 0$ (that is, immediately after excitation), at any given instant (t), and at a sufficiently long time ($t = \infty$). Average solvation time ($\langle \tau_s \rangle$) was then obtained from the multi-exponential fits to S(t) as follows:

$$\langle \tau_s \rangle = \int_0^\infty dt S(t) = \int_0^\infty dt [\sum_i a_i \exp(-t/\tau_i)] = \sum_i a_i \tau_i \,, \tag{7.2}$$

where $\sum_{1}^{i} a_i = 1$, and a_i and τ_i respectively denote the amplitude and time constant associated with the *i*-th component of the total decay.

Time resolved fluorescence anisotropy [$r(t)$] measurements were performed via following the standard protocol.[11,28,29] An iterative reconvolution algorithm[30] was used to simultaneously fit the collected parallel (I_{para}) and perpendicular (I_{perp}) decays. The geometric factor (G) was obtained via tail matching and found to be 1.15 ± 0.1. The dynamic anisotropic decays obtained were found to fit to bi-exponential functions of time, and the average rotation times ($\langle \tau_r \rangle$) were then obtained via time-integration,

$$\langle \tau_r \rangle = \int_0^\infty dt\,[r(t)/r(0)] = \int_0^\infty dt \sum_{i=1}^{2} a_i \exp(-t/\tau_i), \quad \text{with} \quad \sum_{1}^{i} a_i = 1$$

and the initial anisotropy, r(0)=0.376 for C153.[31,28] Such a value of r(0) of C153 has been used previously in DESs[9,11] and ionic liquids.[32]

Densities (ρ) of the samples were measured by an automated temperature-controlled density-cum-sound velocity analyzer (Anton Paar, model DSA 5000) at required temperatures (± 0.5K). Viscosities (η) of the DES systems were measured by AMVn automated micro-viscometer from Anton Paar (falling ball method). Refractive indices were measured by using an automated refractometer (Rudolph J357). Glass transition temperatures (T_gs) for these DESs were measured by density scanning calorimter (DSC Q200). While Table B13 (Appendix B) summarizes the measured temperature-dependent densities, refractive indices and viscosities, Figure A22 provides a representative DSC scan for T_g for these DESs.

Figure 7.1

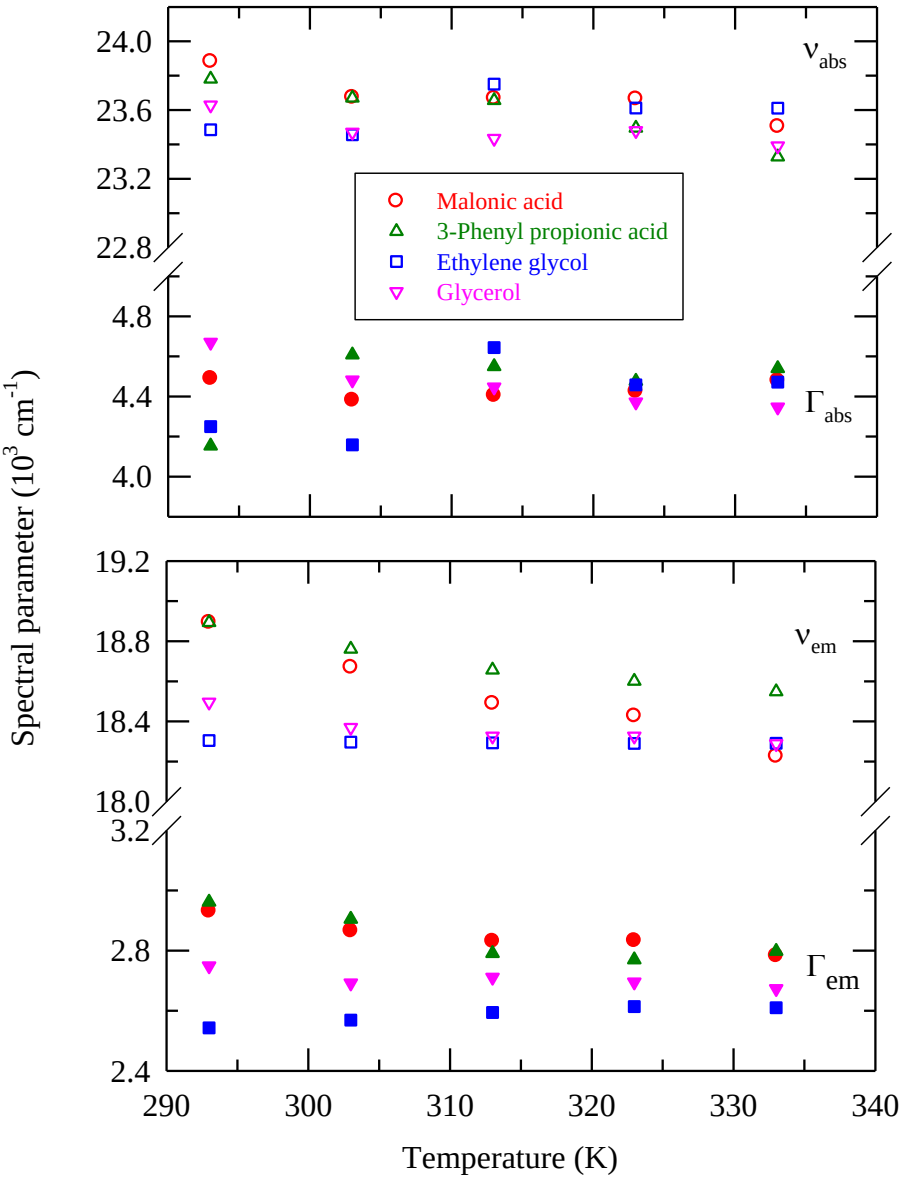

Figure 7.1: Spectral parameters for different combinations of deep eutectic solvent as in [*f* Choline chloride**+** (1-*f*) HBD] (color coded) are shown here. Temperature dependencies of absorption frequencies and the full width at half maxima (Γ) are shown in the upper panel whereas the same for emission are shown in the lower panel.

Specifications of HBD types: *f*=0.50 for malonic acid (red circles), *f*=0.33 for 3-phenylpropionic acid (green triangles), ethylene glycol (blue squares), glycerol (pink inverse triangles).

7.3. Results and Discussion

7.3.1. Steady state spectral characteristics

Steady state absorption and emission spectra of all the four DESs are collected at their respective eutectic composition at various temperatures. Representative absorption and emission spectra are shown in Figure A23 (Appendix A). Average absorption and emission peak frequencies[33] (ν_{abs} and ν_{em}) and the corresponding spectral widths (full-widths-at-half-maxima, Γ_{abs} and Γ_{em}) are shown as a function of temperature in Figure 7.1. Except for ethylene glycol containing DES, ν and Γ show narrowing, the variation being more for emission than absorption. Increase of temperature is expected to decrease the static dielectric constant (ε_0) by frustrating the static orientational correlations at the long wavelength limit.[34,35] Therefore, the observed red shift upon increasing temperature is probably connected to the better solvent relaxed configuration around the excited solute at higher temperature. A comparison in Figure A24 (Appendix A) of spectral frequencies between the temperature dependent steady state fluorescence emission (ν_{em}) and the time-resolved emission at $t=\infty$ (ν_∞) supports this view where ν_∞ are found to be red shifted compared to ν_{em} in all these DESs.

Next, excitation wavelength ($\lambda_{exc.}$) dependence of fluorescence emission has been carried out to investigate the presence of spatial heterogeneity in these DESs.[36,37] Figure A23 shows the selected wavelengths for probe excitation. Figure 7.2 shows the $\lambda_{exc.}$ dependence of ν_{em} and Γ_{em} for C153 ($\tau_{life} \approx 5$ns)[26] in these DESs at ~293 K. DES containing malonic acid shows the maximum $\lambda_{exc.}$-induced shift (~1100 cm^{-1}) in ν_{em} and Γ_{em}, followed by glycerol containing DES (~250 cm^{-1}) and 3-phenylpropionic acid containing one (~200 cm^{-1}). In contrast, ethylene glycol containing DES shows insensitivity to $\lambda_{exc.}$ dependence. Use of a shorter lifetime probe, DMASBT ($\tau_{life} \approx 0.5$ns),[23] produces similar results for DESs containing glycerol and ethylene glycol. This is shown in Figure A25. It is interesting to note that $\lambda_{exc.}$ dependence in 3PPA and glycerol DESs are not as pronounced as expected based

on viscosities of these systems at ~293 K (see Table B13). This may occur due to preferential location of the fluorescent probe. This warrants further study because random probe distribution among various solution environments is what is usually expected, and factors inhibiting such a distribution need to be known.

Figure 7.2

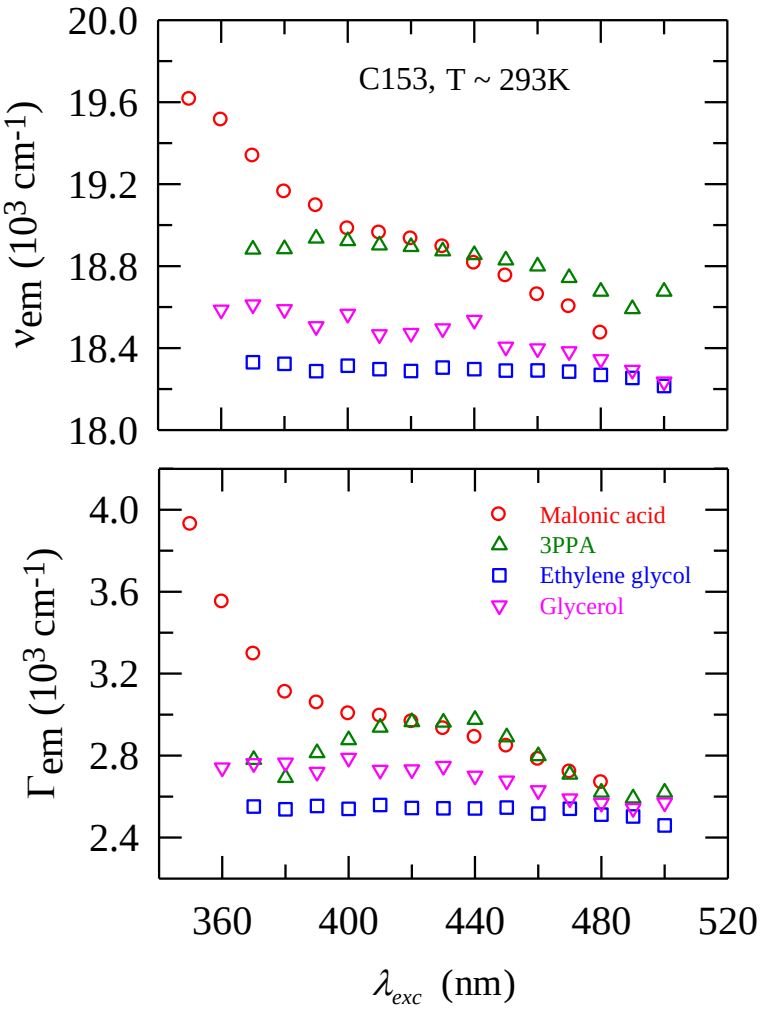

Figure 7.2: Emission peak frequencies (ν_{em}) and full width at half maxima, *fwhm* (Γ_{em}) for C153 in the system of [*f* Choline chloride**+** (1-*f*) HBD] at 293K are plotted against different excitation wavelengths (λ_{exc}).

Specifications of HBD types: *f*=0.50 for malonic acid (red circles), *f*=0.33 for 3-phenylpropionic acid (green triangles), ethylene glycol (blue squares), glycerol (pink inverse triangles).

7.3.2. Stokes shift dynamics: Signature of changing hydrogen bond donors

Representative fluorescence emission intensity decays at a blue and a red wavelengths are shown in Figure 7.3 along with the residuals and fit parameters. As usual, only decay at the blue wavelength, and rise followed by decay at the red end marks presence of dynamic Stokes shift. Figure A26 depicts temperature effects on the longest time constant associated with the decays for (0.5Choline chloride+0.5Malonic acid) DES. It has been similarly checked for other DESs as well. In all cases we did not find any drastic temperature effects on the longest lifetime. Therefore, the temperature dependence of decays are associated with the temperature dependence of solvation energy relaxation.

Figure 7.4 represents typical time-resolved emission spectra[38] and their widths obtained in the present study. Data shown here are for DES of choline chloride and malonic acid made at 1:1 mole ratio at ~293 K. Lower panel of Figure 7.4 also shows temperature effects on widths of the time-dependent spectra. This kind of variation has been observed previously for acetamide deep eutectics[9-11,15], supercooled media[39], confined systems,[40] conventional solvents[26] and ionic liquids.[47] Note in the upper panel that the $t = \infty$ spectrum does not coincide with that of the steady state, and the difference is found to be as large as ~400 cm^{-1} at ~293K. This difference has been found to be the smallest for ethylene glycol containing DES where viscosity is comparatively lower than those for other DESs considered. Measured dynamic Stokes shifts ($\Delta\nu_{obs}^{t}$) has been obtained from the time-resolved emission spectra[27] using the average frequency as $\Delta\nu_{obs}^{t} = \nu(t=0) - \nu(t=\infty)$ of TRES. The total shift could not be observed experimentally due to the limited time-resolution (~70ps) employed.

Figure 7.3

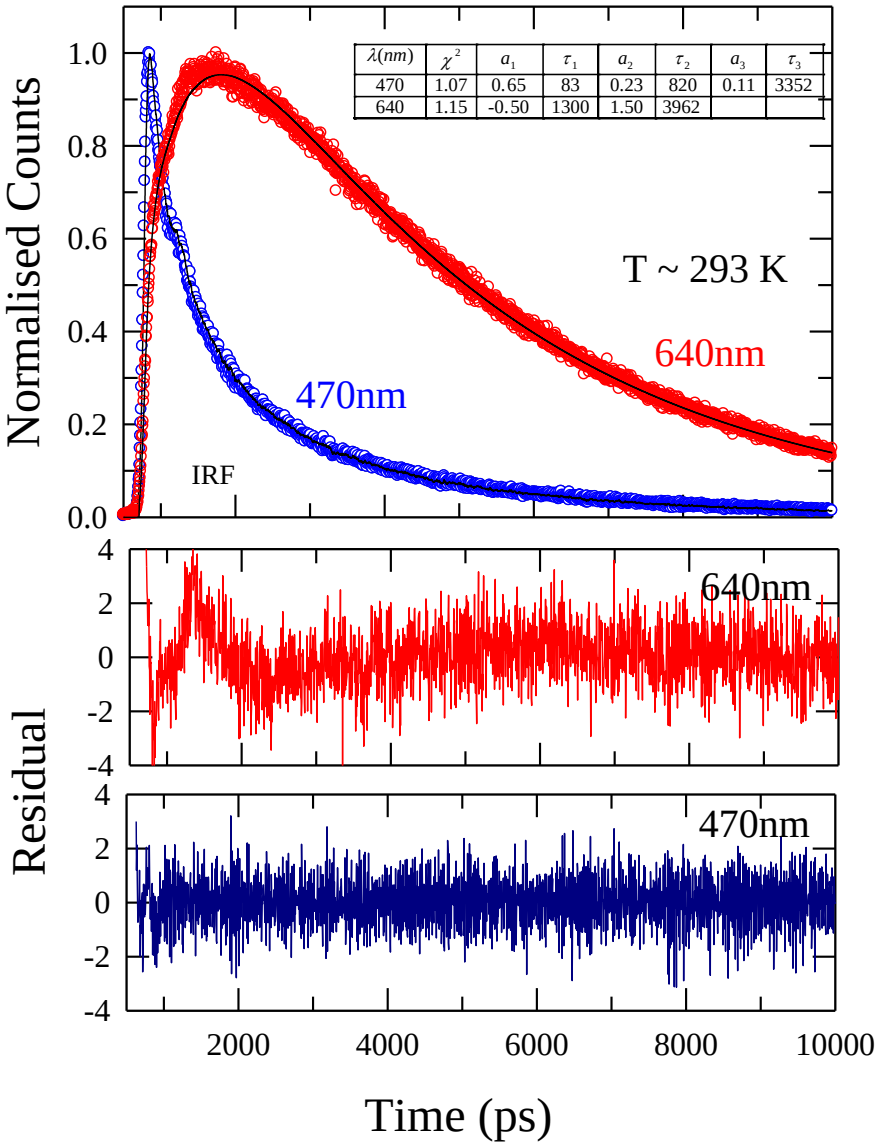

Figure 7.3: Representative fluorescence intensity decays at blue (470nm) and red (640nm) wavelengths for C153 in [*f* Choline chloride**+** (1-*f*) HBD] for HBD= Malonic acid at *f*= 0.50 (T= 293 K). Circles denote the experimental data and solid lines fits through them. The respective residuals (color coded) are presented in the bottom panels. The fit parameters are shown in the inset of the upper panel. Time constants (τ_i) are in the unit of picosecond. The goodness-of-fit parameters (χ^2) in these two wavelengths are 1.07 and 1.15, respectively.

Figure 7.4

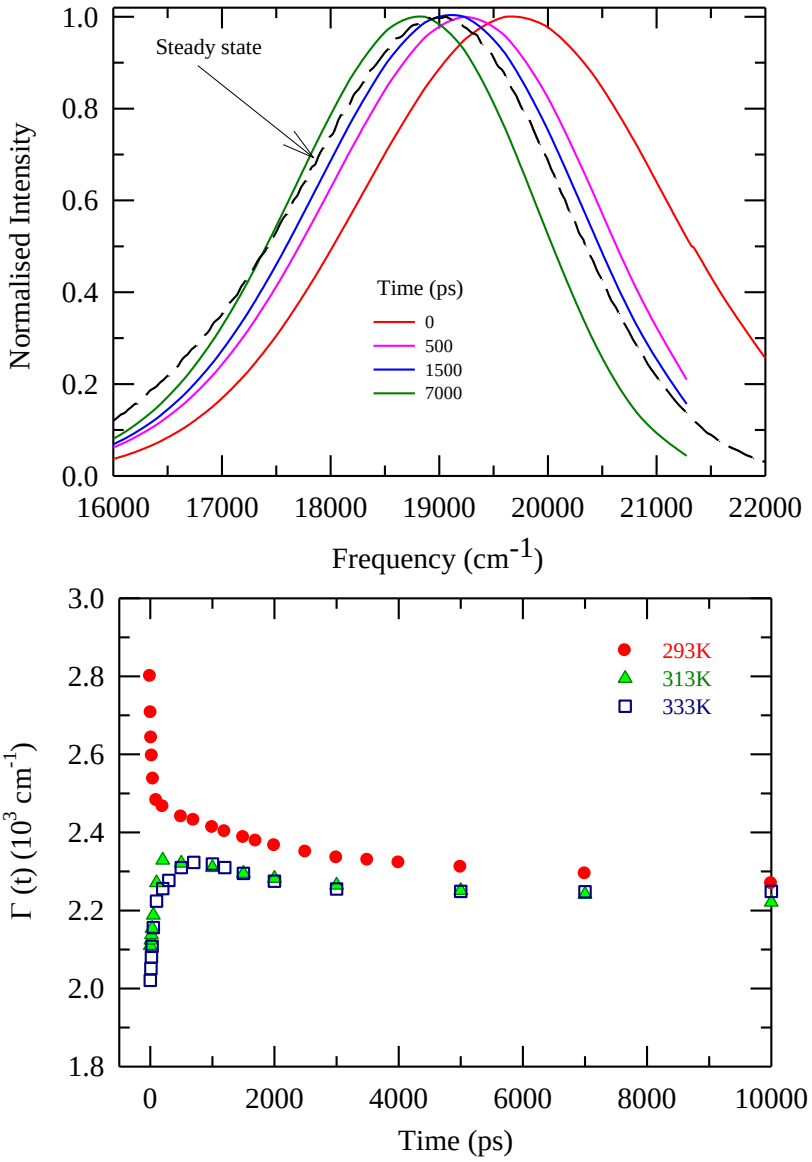

Figure 7.4: Synthesized time resolved emission spectra (TRES) of C153 at different times from the experimentally obtained decays at f = 0.50 in [f Choline chloride**+** (1-f) HBD] (T= 293 K) for HBD= Malonic acid are shown in the upper panel. The time intervals are color coded. The steady state emission spectrum of the same system is shown in broken line. Note that t=7000ps is also the $t = \infty$ spectrum. The lower panel shows the variation of widths of the spectra at different time slices at three representative temperatures.

Table 7.1: Dynamic Stokes' shift for C153 in [*f* Choline chloride+ (1-*f*) HBD] at different temperatures.

T (K)	Estimated $\Delta\nu^t$ ($10^3 cm^{-1}$)	Observed $\Delta\Delta\nu$ ($10^3 cm^{-1}$)	Missed %
Malonic acid, *f*=0.50			
293	1.182	0.962	35
303	1.152	0.774	50
313	1.103	0.732	51
323	1.165	0.710	55
333	1.082	0.691	53
3-Phenylpropionic acid, *f*=0.33			
293	0.932	0.814	38
303	0.936	0.884	34
313	0.659	0.639	40
323	0.755	0.654	43
333	0.798	0.733	39
Ethylene glycol, *f*=0.33			
293	0.859	0.423	66
298	0.738	0.300	74
303	0.779	0.243	79
313	0.627	0.130	87
Glycerol, *f*=0.33			
293	0.898	0.582	55

303	0.856	0.532	58
313	0.804	0.456	62
323	0.638	0.337	70
333	0.728	0.313	72

Estimated total shifts ($\Delta\nu^{t}_{est}$) using the Fee-Maroncelli method[27] are also provided in Table 7.1 along with the components missing in the present experiments. The overall trend shows that there is an increase in difference between $\Delta\nu^{t}_{obs}$ and $\Delta\nu^{t}_{est}$ shifts as temperature increases.

The HBDs with –OH group shows comparatively lesser observed shift compared to the ones containing –COOH although there is not much variation in the estimated shifts. Consequently, the missing percentage for ethylene glycol and glycerol is as high as upto 90 and 75% respectively whereas it is around 50% at the most for malonic acid and 3PPA combinations of choline chloride DESs. This trend of observed shift is unconventional as the estimated dielectric constant[41] from steady state emission frequency (Figure 7.1) predicts higher dielectric constant for ethylene glycol containing DES (~22) and glycerol containing DES (~16) than 3PPA containing DES(~10) and malonic acid containing DES (~11). The origin for the missing component in these systems lies in the low frequency (~100 cm^{-1}) collective intermolecular solvent modes. Such modes in amide systems[42,43] and other hydrogen-bonded solvents[44-46] have been found to significantly contribute to the initial part of solvation energy relaxation.[47-51] If we consider the number of hydrogen bond donating groups, glycerol has the maximum of it. With three –OH groups, the effects of collective modes will be the strongest here. Ethylene glycol has two –OH groups and hence contributions from low frequency solvent modes are also expected here accordingly. On the other hand, malonic acid is the most viscous with two –COOH groups. Due to dimerisation[18,19] and H-Bonding with choline chloride molecules, the

H-bond motions are restricted. 3-PPA is also moderately viscous with a single –COOH group. This probably explains the difference in missing components between acid containing and alcohol containing DESs studied.

Figure 7.5 presents the S(t) decays for C153 in the four DESs at ~293 K. Table 7.2 summarizes the fit parameters and average solvation times ($\langle \tau_s \rangle$) for S(t) decays measured at various temperatures. Note decays for malonic acid and 3PPA containing DESs are characterised by two components – a faster part ranging between ~100-300 ps and a long time constant between ~500-2000 ps. Studies involving polyethylene glycol[52] has shown that it is the end groups of the alkyl chain and not the whole body movement that is involved in the slow long time relaxation. Hence it is expected that the heavy phenyl group at the end of alkyl chain in 3PPA will slow down the solvation rate at long time. From Table 7.2 it can be seen that τ_2 for 3PPA is larger than that for malonic acid although viscosity of the former is lower than the latter. This may be explained in terms of non-hydrodynamic moves such as jumps.[19,53] However, temperature effects on solvation rate in these DESs follow the temperature dependence of viscosity.

Table 7.2: Solvation response function measured from experiment in [*f*Choline chloride+ (1-*f*) HBD] at different temperatures: Fit parameters[a]

T (K)	a_1	τ_1 (ps)	a_2	τ_2 (ps)	$\langle \tau_s \rangle$ (ps)
Malonic acid, *f*=0.50					
293	0.40	256	0.60	1673	1140
303	0.41	323	0.59	1416	969
313	0.59	185	0.61	769	461
323	0.58	68	0.42	756	357
333	0.72	91	0.28	400	178

3-Phenylpropionic acid, *f*=0.33					
293	0.05	120	0.95	1667	1591
303	0.06	99	0.94	1429	1349
313	0.19	333	0.81	1428	1217
323	0.21	250	0.79	1250	1041
333	0.14	145	0.86	909	806
Ethylene glycol, *f*=0.33					
293	0.44	81	0.56	370	241
298					151
303	0.19	22	0.81	151	127
313					82
Glycerol, *f*=0.33					
303	0.17	98	0.83	588	505
313	0.27	97	0.73	556	432
323	0.09	47	0.91	286	264
333	0.08	34	0.92	141	132
293	0.13	29	0.87	140	123

[a]These numbers are better than $\pm 10\%$ of the reported values (estimated based on limited data sets).

Figure 7.5

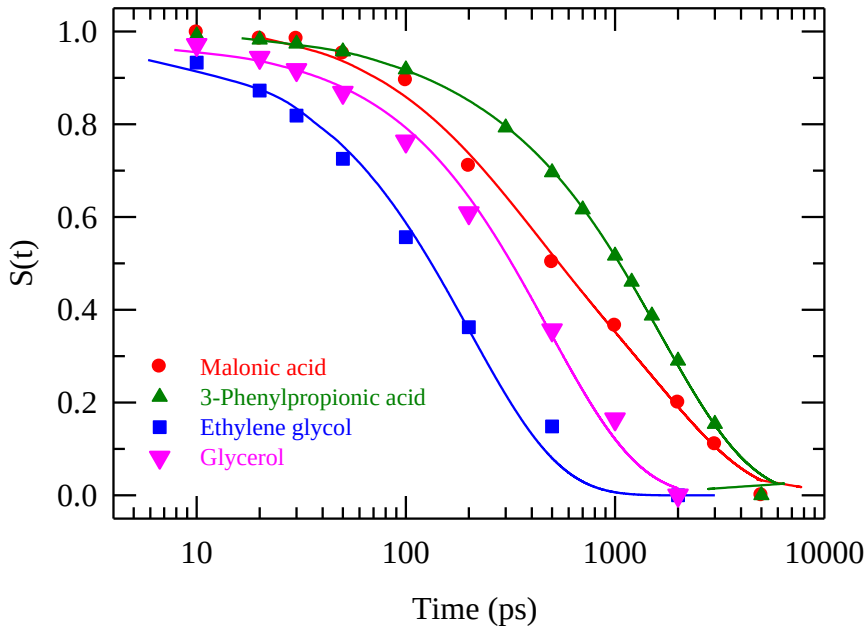

Figure 7.5: Decays of solvation response function, $S(t)$, measured using C153 in [f Choline chloride**+** (1-f) HBD] for different combinations (color coded) at 293K.

Specifications of HBD types: f=0.50 for malonic acid (red circles), f=0.33 for 3-phenylpropionic acid (green triangles), ethylene glycol (blue squares), glycerol (pink inverse triangles).

Next, the coupling between $\langle \tau_s \rangle$ and the medium viscosity is investigated in Figure 7.6 where the measured temperature dependent $\langle \tau_s \rangle$ for these four DESs are shown as a function of temperature-reduced viscosity, η/T, in a double-logarithmic fashion. Fits to the measured $\langle \tau_s \rangle$ values obeying the equation, $\langle \tau_s \rangle \propto (\eta / T)^p$, are also shown and the resulting fraction power (p) indicated. Note in all cases deviation from hydrodynamic description (corresponds to $p=1$) is observed, deviation being the strongest for PPA containing DES and least for the ethylene glycol containing DES. This behaviour is a manifest for dynamic heterogeneity which may arise from jump

motions[53] and diffusion of small particles through medium of bigger particles.[54] This result is in contrast to what has been observed during excitation wavelength dependence of steady state fluorescence emission, and suggests once again that spatial heterogeneity is not a pre-requisite for dynamic heterogeneity.

Figure 7.6

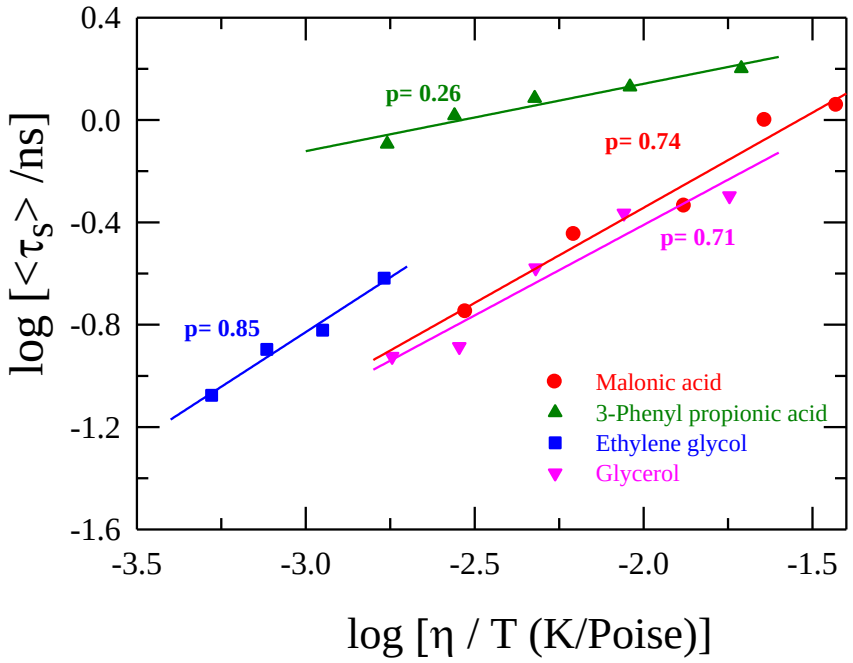

Figure 7.6: Medium viscosity (η) dependence of average solvation time, $\langle \tau_s \rangle$, for C153 in [*f* Choline chloride**+** (1-*f*) HBD] for different combinations (color coded).

Specifications of HBD types: *f*=0.50 for malonic acid (red circles), *f*=0.33 for 3-phenylpropionic acid (green triangles), ethylene glycol (blue squares), glycerol (pink inverse triangles).

7.3.3. Dynamic fluorescence anisotropy: Hydrogen bond Donors and the alkyl chain effects on solute rotation

Dynamic anisotropy ($r(t)$) decays for C153 in these four DESs at ~293 K are shown in Figure 7.7 along with bi-exponential fits through them. Similar fits have been obtained for other temperatures as well. Since these DESs are characterized by heterogeneity of varying degree, attempts were made to fit the $r(t)$ decays to stretched exponentials[55] but produced worse fits. The figure shows that the decays are faster in the order of glycerol, malonic acid, 3PPA, followed by ethylene glycol. Bi-exponential fit parameters and the resulting average rotational times ($\langle \tau_r \rangle$) are summarized in Table 7.3. A closer inspection of Table 7.3 indicate that these decays are characterized by a faster time constant in the range ~50-700 ps, and a slower time constant spread between ~1-10 ns. It may be noted that at low temperatures the $\langle \tau_r \rangle$ values of C153 is few times larger than the lifetime of the same (~5ns). This is not unnatural because large rotational times (2-20 times of the lifetime of the respective probe) have been reported earlier for ionic liquids.[32,56,57]

Figure 7.7

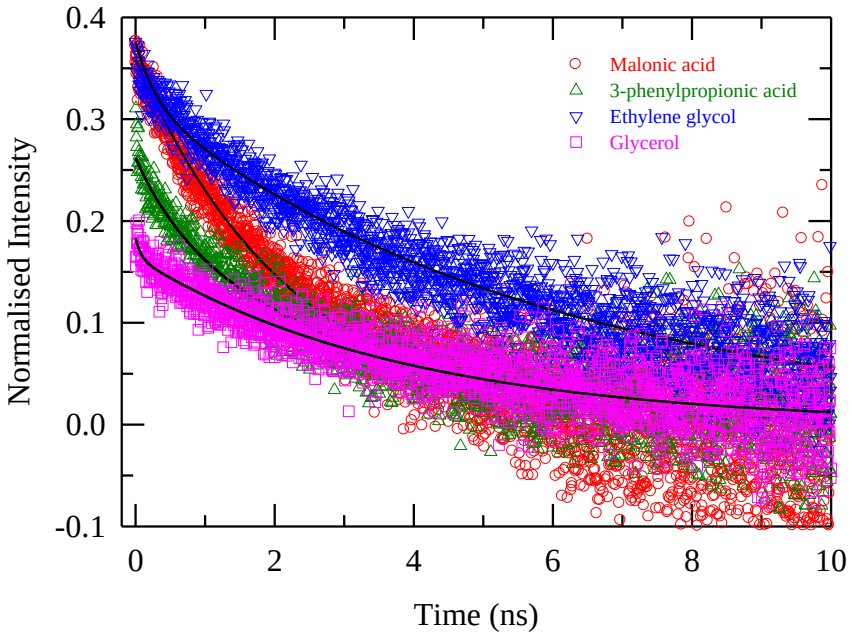

Figure 7.7: Representative anisotropy decays at 293K for [*f* Choline chloride**+** (1-*f*) HBD] for different combinations for C153 are shown : Malonic acid (red, *f*=0.50), phenylpropionic acid (green, *f*=0.33), ethylene glycol (blue, *f*=0.33), glycerol (pink, *f*=0.33) .

Symbols denote the experimental data and solid lines fits through them. The fit parameters are shown in Table 7.3.

Table 7.3: Parameters Obtained from Biexponential Fits to *r*(*t*) of C153 [*f* Choline chloride+ (1-*f*) HBD] at different temperatures.

T (K)	χ^2	a_1	τ_1 (ps)	a_2	τ_2 (ns)	$\langle\tau_r\rangle$ (ns)
Malonic acid, *f*=0.50						
293	1.19	0.35	44	0.65	9.76	6.34
303	0.91	0.29	86	0.71	5.10	3.64
313	0.99	0.41	151	0.59	3.23	2.91
323	0.99	0.39	556	0.61	2.79	1.92
333	1.02	0.53	638	0.47	1.89	1. 22
3-Phenylpropionic acid, *f*=0.33						
293	0.97	0.11	79	0.89	3.84	3.43
303	0.91	0.27	174	0.73	3.67	2.73
313	0.96	0.34	266	0.66	3.37	2.31
323	0.97	0.38	371	0.62	2.70	1.82
333	1.03	0.40	401	0.60	2.20	1.47

Ethylene glycol, *f*=0.33						
293	0.97	0.12	630	0.89	1.59	1.48
303	0.95	0.19	532	0.81	1.19	1.06
313	0.98	0.30	370	0.70	0.97	0.77
323	1.04	0.36	247	0.64	0.79	0.59
333	1.03	0.46	159	0.56	0.64	0.43
Glycerol, *f*=0.33						
293	1.03	0.28	351	0.72	13.45	9.78
303	1.19	0.32	438	0.68	8.49	5.93
313	1.06	0.32	388	0.68	4.36	3.09
323	1.19	0.35	199	0.65	2.91	1.96
333	1.11	0.40	71	0.60	2.74	1.67

Figure 7.8 depicts the coupling between the measured $\langle \tau_r \rangle$ and medium viscosity at various temperatures for C153 in all these DESs. As before, fits to these data describing the viscosity dependence, $\langle \tau_r \rangle \propto (\eta / T)^p$, are also shown along with the Stokes-Einstein-Debye (SED) predictions following hydrodynamic stick and slip boundary conditions. The SED values for $\langle \tau_r \rangle$ have been calculated by using $\langle \tau_r \rangle = (V\eta / k_B T) fC$, with V= 246 Å^3, f (shape factor) = 1.71 and C(solute-solvent coupling parameter) = 0.24 (for slip) and 1 (for stick).[32] Numerical values for p provided in each panel clearly indicate stronger deviation from hydrodynamics for acid containing DESs than the polyol containing ones. Fractional viscosity dependence seen here and that observed for solvation, therefore, clearly suggest that these DESs are dynamically heterogeneous, and the extent of heterogeneity can be tuned by selecting suitably the hydrogen bond donor for a given DES.

Figure 7.8

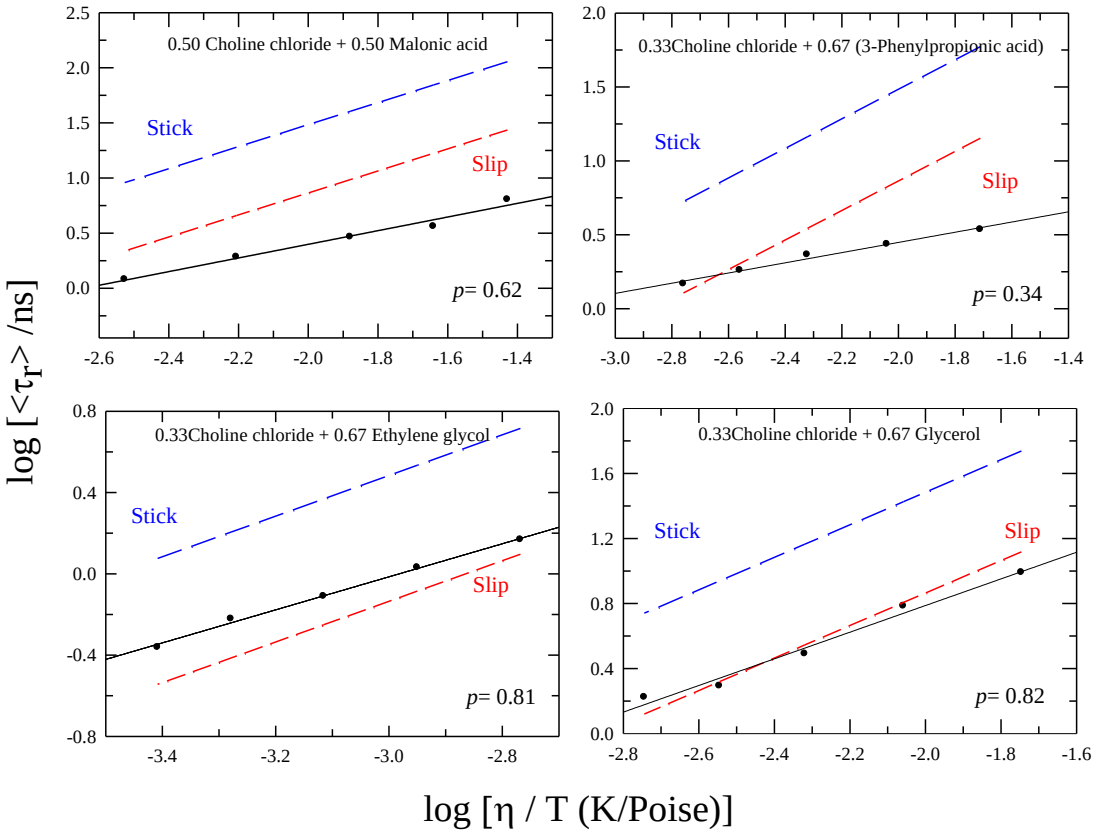

Figure 7.8: Viscosity coupling of rotation times ($\langle \tau_r \rangle$) for C153 in the system [*f* Choline chloride**+** (1-*f*) HBD] for different combinations for C153 and comparison to hydrodynamic theory are shown in different panels. Temperature dependent measured times (symbols) at various *f* values are shown as a function of temperature-reduced viscosity (η/T) in a log-log fashion [$Log\langle \tau_r \rangle = A + pLog(\eta/T)$]. Rotation times for C153 at various η/T values from calculation by SDE equation are also shown (broken blue line) at the slip boundary for a comparison. Corresponding stick values are shown in red.

Figure 7.9

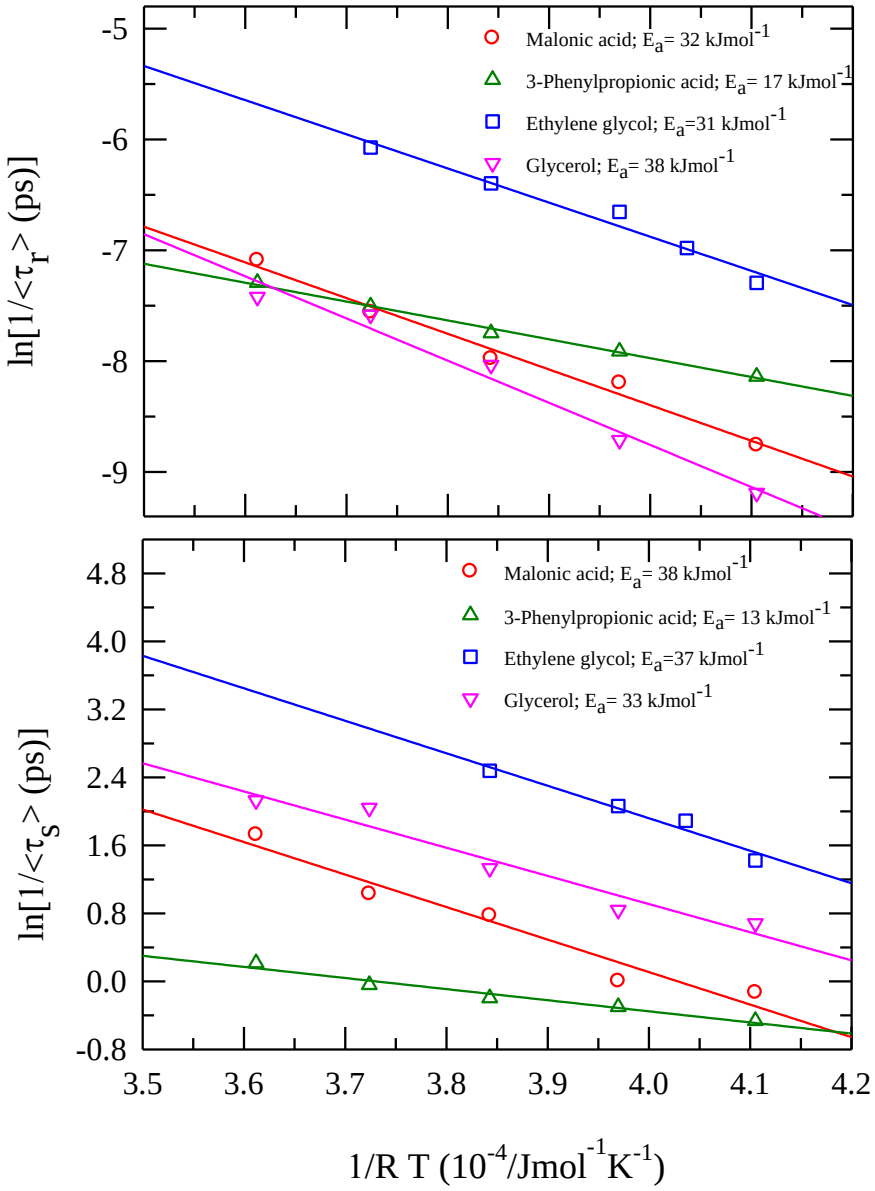

Figure 7.9: Arrhenius plot of $\ln(1/\langle\tau_r\rangle)$ and $\ln(1/\langle\tau_s\rangle)$ vs *1/RT* for rotational dynamics of C153 (upper panel) and solvation (lower panel) in the system [*f* Choline chloride**+** (1-*f*) HBD] are shown in this figure. Respective activation energies are indicated in the insets.

Specifications of HBD types: *f*=0.50 for malonic acid (red circles), *f*=0.33 for 3-phenylpropionic acid (green triangles), ethylene glycol (blue squares), glycerol (pink inverse triangles).

Next, activation energies for rotation and solvation of C153 in these DESs have been estimated via Arrhenius-type analyses of the measured temperature-dependent average rotation and solvation times. Figure 7.9 displays the Arrhenius-type plots for these quantities along with linear fits through them. Except for PPA containing DES, activation energies for both rotation and solvation lie in the ~30-40 kJ/mol range. Such a range was found earlier for solute solvation and rotation in acetamide/electrolyte deep eutectics.[10,11] For PPA containing DES, these barriers are nearly half of what has been estimated for other DESs. Note earlier studies with a different solute probe have indicated activation energy ~30 kJ/mole range for solute rotation in normal alcohols with longer alkyl chain, and nearly half of it for rotation in ethanol.[58] Arrhenius-type plots of viscosity are also presented in Figure A27. A comparison of activation energies obtained from Arrhenius-type analyses of temperature-dependent viscosity, average rotation and solvation times is given in Table 7.4.

Table 7.4: A comparison of activation energies obtained from Arrhenius-type analyses of temperature-dependent average rotation [Ea $\langle \tau_r \rangle$**] solvation [**Ea $\langle \tau_s \rangle$**] and viscosity [**Ea (η)**] is given.**

HBD	Ea $\langle \tau_r \rangle$ (kJ/mol)	Ea $\langle \tau_s \rangle$ (kJ/mol)	Ea (η) (kJ/mol)
Malonic acid	32	38	32
3-PPA	17	13	17
Ethylene glycol	31	37	25
Glycerol	38	33	38

Figure 7.10 explores the correlation between the measured $\langle \tau_s \rangle$ and $\langle \tau_r \rangle$ for C153 in these media. Fits through these data describing $\langle \tau_r \rangle = a(\langle \tau_s \rangle)^b$ dependence are also shown. Such plot provides a qualitative idea about how much of the friction that regulates solute solvation also dictates solute rotation in these media. A deviation from simple proportionality would indicate decoupling between solute solvation and rotation, and in turn support the presence of dynamic heterogeneity. It is evident in Figure 7.10 that substantial decoupling between $\langle \tau_s \rangle$ and $\langle \tau_r \rangle$ exists in these systems which are a result of microscopic heterogeneity present in these systems.

Figure 7.10

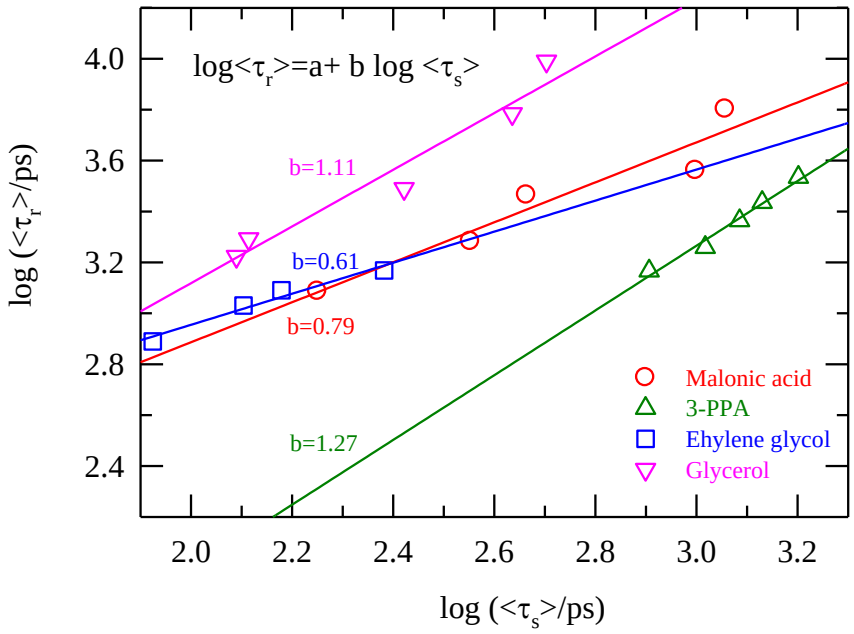

Figure 7.10: Experimental average rotational correlation times ($\langle \tau_r \rangle$) versus solvation times ($\langle \tau_s \rangle$) in log-log form for C153 in [*f* Choline chloride**+** (1-*f*) HBD] for different combinations (color coded) are shown here. The line going through the symbols represents a fit to the relation shown in the panel.

Specifications of HBD types: *f*=0.50 for malonic acid (red circles), *f*=0.33 for 3-phenylpropionic acid (green triangles), ethylene glycol (blue squares), glycerol (pink inverse triangles).

7.4. Conclusion

The fluorescence spectroscopic study of choline chloride based DES of different hydrogen bond donors shows interesting properties based on the functional group, number of functional groups and also the nature of alkyl chain attached with the functional groups. The steady state excitation wavelength of C153 dependence study in choline chloride combined with different HBDs show spatial heterogeneity for malonic acid to the greatest extent, feeble for 3PPA and glycerol whereas none for ethylene glycol. Probe of a shorter lifetime supports these conclusions. Increasing temperature removes spatial heterogeneity in these DESs. Dynamic stokes shift is larger for –COOH containing HBD than –OH containing HBD. A uniform decrease is noticed with increasing temperature due to the overall decrease in effective dielectric constant. A significant portion of the total solvation response has been missed due to limited time-resolution employed. Deviation from hydrodynamic dependence on viscosity for solute solvation and rotation has been observed where fractional power-law dependence signalled dynamic heterogeneity in these media. This has resulted substantial decoupling between the measured solvation and rotation times in them. Activation energies estimated for solute rotation show variations with the HBD components constituting these DESs but they are in the range already reported for solute rotation in monohydroxy alcohols with differing alkyl chain lengths.

References

1. Jessop, P. G.; Jessop, D. A.; Fu, D. B.; Phan, L. *Green Chem.* **2012**, *14*, 1245.

2. Ru; Konig, B. *Green Chem.* **2012**, *14*, 2969.

3. Abbott, A. P.; Boothby, D.; Capper, G.; Davies, D. L.; Rasheed, R. K. *J. Am. Chem. Soc.* **2004**, *126*, 9142.

4. Abbott, A. P.; Capper, G.; Davies, D. L.; Rasheed, R. K.; Tambyrajah, V. *Chem. Commun.* **2003**, 70.

5. Francisco, M.; van den Bruinhorst, A.; Kroon, M. C. *Green Chem.* **2012**, *14*, 2153.

6. Francisco, M.; Van den Bruinhorst, A.; Kroon, M. C. *Angew. Chem., Int. Ed.* **2013**, *52*, 3074.

7. Zhang, Q. H.; Vigier, K. D.; Royer, S.; Jerome, F. *Chem. Soc. Rev.* **2012**, *41*, 7108.

8. Biswas, R.; Das, A.; Shirota, H. *J. Chem. Phys.* **2014**, *141*, 134506.

9. Guchhait, B.; Das, S.; Daschakraborty, S.; Biswas, R. *J. Chem. Phys.* **2014**, *140*, 104514.

10. Guchhait, B.; Daschakraborty, S.; Biswas, R. *J. Chem. Phys.* **2012**, *136*, 174503.

11. Guchhait, B.; Gazi, H. A. R.; Kashyap, H. K.; Biswas, R. *J. Phys. Chem. B* **2010**, *114*, 5066.

12. Das, A.; Das, S.; Biswas, R. *Chem. Phys. Lett.* **2013**, *581*, 47.

13. Gazi, H. A. R.; Guchhait, B.; Daschakraborty, S.; Biswas, R. *Chem. Phys. Lett.* **2011**, *501*, 358.

14. Mukherjee, K.; Das, A.; Choudhury, S; Barman, A; Biswas, R.; *J. Phys. Chem. B* **2015**, *xxxx*, xxxx.

15. Das, A.; Das, S.; Biswas, R. *J. Chem. Phys.* **2015**, *142*, 034505.

16. Pal, T.; Biswas, R. *Chem. Phys. Lett.* **2011**, *517*, 180.

17. Perkins, S. L.; Painter, P.; Colina, C. M. *J. Phys. Chem. B* **2013**, *117*, 10250.

18. Perkins, S. L.; Painter, P.; Colina, C. M. *J. Chem. Eng. Data.* **2014**, *59*, 3652.

19. D'Agostino, C.; Harris, R. C.; Abbott, A. P.; Gladden, L. F.; Mantle, M. D. *Phys. Chem. Chem. Phys.*

2011, *13*, 21383.

20. Dai, Y.; Van Spronsen, J.; Witkamp, G.-J.; Verpoorte, R.; Choi, Y. H. *Anal. Chim. Acta.* **2013**, *766*, 61.

21. Sun, H.; Li, Y.; Wu, X.; Li, G. H. *J. Mol. Model.* **2013**, *19*, 2433.

22. Pandey, A.; Rai, R.; Pal, M.; Pandey, S. *Phys. Chem. Chem. Phys* **2014**, *16*, 1559.

23. Maroncelli, M. *Private communication.*

24. *DMABST was received as a gift from Prof. Maroncelli, Penn. State University, USA.*

25. Pradhan, T.; Biswas, R. *J. Phys. Chem. A* **2007**, *111*, 11514.

26. Horng, M. L.; Gardecki, J. A.; Papazyan, A.; Maroncelli, M. *J. Phys. Chem.* **1995**, *99*, 17311.

27. Fee, R. S.; Maroncelli, M. *Chem. Phys.* **1994**, *183*, 235.

28. Horng, M. L.; Gardecki, J. A.; Maroncelli, M. *J. Phys. Chem. A* **1997**, *101*, 1030.

29. Lakowicz, J. R. *Principle of Fluorescence Spectroscopy*; Kluwer Academic Pub: New York, 1999; Vol. 2nd ed.

30. Cross, A. J.; Fleming, G. R. *Biophys. J.* **1984**, *46*, 45.

31. Jin, H.; Li, X.; Maroncelli, M. *J. Phys. Chem. B* **2007**, *111*, 13473.

32. Jin, H.; Li, X.; Maroncelli, M. *J. Phys. Chem. B* **2007**, *111*, 13473.

33. Biswas, R.; Lewis, J. E.; Maroncelli, M. *Chem Phys Lett* **1999**, *310*, 485.

34. Petrowsky, M.; Frech, R. *J. Phys. Chem. B* **2009**, *113*, 5996.

35. Hunger, J.; Stoppa, A.; Schrödle, S.; Hefter, G.; Buchner, R. *Chemphyschem* **2009**, *10*, 723.

36. Mandal, P. K.; Sarkar, M.; Samanta, A. *J. Phys. Chem. A* **2004**, *108*, 9048.

37. Samanta, A. *J. Phys. Chem. B* **2006**, *110*, 13704.

38. Maroncelli, M.; Fleming, G. R. *J. Chem. Phys.* **1987**, *86*, 6221.

39. Richert, R.; Wagener, A. *J. Phys. Chem. A* **1991**, *95*, 10115.

40. Guchhait, B.; Biswas, R.; Ghorai, P. K. *J. Phys. Chem. B* **2013**, *117*, 3345.

41. Biswas, R.; Lewis, J. E.; Maroncelli, M. *Chem. Phys. Lett.* **1999**, *310*, 485.

42. Shirota, H.; Castner, E. W. *J. Am. Chem. Soc.* **2001**, *123*, 12877.

43. Chang, Y. J.; Castner, E. W. *J. Phys. Chem.* **1994**, *98*, 9712.

44. Roy, S.; Bagchi, B. *J. Chem. Phys.* **1993**, *99*, 9938.

45. Nandi, N.; Bagchi, B. *J. Phys. Chem.* **1996**, *100*, 13914.

46. Nandi, N.; Roy, S.; Bagchi, B. *J. Chem. Phys.* **1995**, *102*, 1390.

47. Biswas, R.; Bagchi, B. *J. Phys. Chem.* **1996**, *100*, 1238.

48. Biswas, R.; Bagchi, B. *J. Phys. Chem. A* **1999**, *103*, 2495.

49. Bagchi, B.; Biswas, R. *Adv. Chem. Phys.* **1999**, *109*, 207.

50. Kashyap, H. K.; Pradhan, T.; Biswas, R. *J. Chem. Phys.* **2006**, *125*, 174506.

51. Kashyap, H. K.; Biswas, R. *J. Phys. Chem. B* **2008**, *112*, 12431.

52. Shirota, H.; Segawa, H. *J. Phys. Chem. A* **2003**, *107*, 3719.

53. Das, S.; Biswas, R.; Mukherjee, B. *J. Phys. Chem. B* **2015**, *119*, 274.

54. Egelstaff, P. A. *An Introduction to the Liquid State* Clarendon, Oxford, 1992.

55. Arzhantsev, S.; Jin, H.; Baker, G. A.; Maroncelli, M. *J. Phys. Chem. B* **2007**, *111*, 4978.

56. Ito, N.; Arzhantsev, S.; Heitz, M.; Maroncelli, M. *J. Phys. Chem. B* **2004**, *108*, 5771.

57. Funston, A. M.; Fadeeva, T. A.; Wishart, J. F.; Castner, E. W. *J. Phys. Chem. B* **2007**, *111*, 4963.

58. Waldeck, D. H.; Fleming, G. R. *J. Phys. Chem.* **1981**, *85*, 2614.

Chapter 8

Terahertz Dielectric Relaxation and FTIR studies on Deep Eutectic Solvents of Acetamide + Electrolytes: Anion and Cation Identity

8.1. Introduction

Search for bio-degradable solvents with no or less biological footprint on ecosystems as alternatives to common organic solvents for large scale use in chemical industry is universal. Out of this necessity has emerged a wide of spectrum of reaction media ranging from binary liquid mixtures[1] to electrolyte solutions, supercritical solvents[2,3] to gas-expanded liquids,[4] ionic liquids[5,6] to low temperature transition melts.[7,8] Deep eutectic solvents (DESs), a set of mixtures of solid components at ambient condition which transform to stable liquid phase near room temperature after melting, are an important addition to this growing list of alternative reaction media.[7-18] Fortunately, DESs can be made environmentally benign by suitably choosing components which are biodegradable, relatively cheaper and easy to handle. Acetamide and its methyl derivatives are reported to be biodegradable[19] and therefore DESs made of acetamide in combination with either electrolytes or urea offer a unique solvent systems for industrial applications. Exquisite solvent properties of acetamide due to large dielectric constant[20] and presence of several functional groups have made such DESs an automatic choice for extensive application as green media.

DESs are multi-component systems and are thus subjected to electrostatic, specific and van der Waal's interactions. Deep depression of freezing points of the mixture

components has its roots in extensive inter-species hydrogen bond (H-bond) interactions.[16] For example, in (acetamide + electrolyte) deep eutectics, presence of an amide group stimulates extensive H–bond interaction with the ions followed by interaction between cation and carbonyl group.[21] These interactions lead to ion-amide complexation, and structural frustration at microscopic length-scales. Entropic gain further stabilizes the resultant liquid phase accessed via melting. It is natural then to ask whether avoidance of crystallization through extensive H-bond interaction stamps any characteristic signature on solution structure and dynamics of these DESs. This knowledge is important as relaxation time scales and equilibrium solution properties affect rate of a solution-phase chemical reaction.[22-26]

Although there exist no significant studies revealing spatial molecular arrangements at microscopic lengthscales via x-ray or neutron scattering measurements, fast spectroscopic techniques and simulations of late have attempted to explore the relaxation timescales in several acetamide containing DESs.[27-35] These studies have provided important information regarding relaxation timescales, frictional coupling to solute diffusion, and low-frequency collective dynamics at the sub-picosecond and pico-second level. These studies, however, are unable to decipher solution structural arrangements even-though excitation energy dependence of steady state fluorescence emission measurements involving these media has suggested presence of spatial heterogeneity in (amide+electrolyte) DESs. Earlier dielectric relaxation (DR) measurements, limited within 100 MHz,[15] have interpreted very long relaxation timescales and colossal dielectric constants in terms of heterogeneous solution structure. However, solution dynamics extended to giga-hertz (GHz) and tera-hertz (THz) ranges, which are relevant to ultrafast fluorescence measurements, have not been explored and understood yet. DR measurements of several (acetamide + electrolytes) in the frequency range, $0.2 \le \nu/\mathrm{GHz} \le 50$, have just began to emerge[33], and atomistic simulations started exploring the ion effects on reorientation mechanism of acetamide in such media.[32] However, THz measurements of these

media are still unavailable although the importance of THz measurements in decoding collective intermolecular dynamics of H-bonded systems such as amides is well appreciated.[32,36] This is the motivation for carrying out DR measurements in the THz regime ($0.2 \le \nu/\mathrm{THz} \le 2$) for a few (acetamide + electrolyte) deep eutectics described in this chapter. Electrolytes considered here are lithium nitrate ($LiNO_3$), lithium bromide (LiBr), lithium perchlorate ($LiClO_4$), sodium perchlorate ($NaClO_4$), potassium thiocyante (KSCN) and sodium thiocyanate (NaSCN). In addition, we have carried out infra-red spectroscopic measurements to investigate the dependence on ion-identity of the acetamide-ion interactions and augment the existing literature.[28,29,31]

8.2. Experimental Details

8.2.1. Materials and methods

Acetamide (≥98%, Merck, India), lithium nitrate (≥99%, SRL, India), lithium bromide (≥99%, Sigma Aldrich), lithium perchlorate (≥99%, Fluka), sodium perchlorate (≥98%, Alfa aesar), sodium thiocyanate (≥99%, Sigma Aldrich) and potassium thiocyanate (≥99%, Sigma Aldrich) were all vacuum-dried (~300 K) overnight before use. Different DESs studied had the following compositions: (a) $0.78CH_3CONH_2$ + $0.22LiBr$, (b) $0.78CH_3CONH_2$ + $0.22LiNO_3$, (c) $0.81CH_3CONH_2$ + $0.19NaClO_4$, (d) $0.81CH_3CONH_2$ + $0.19LiClO_4$, (e) $0.75CH_3CONH_2$ + 0.25KSCN, and (f) $0.75CH_3CONH_2$ + 0.25NaSCN. Sample preparation method could be found elsewhere.[22-25,28] All samples except ($0.81CH_3CONH_2$ + $0.19NaClO_4$) were studied before via fluorescence measurements. Preparation protocol remained unchanged for $NaClO_4$ containing DES. In short, 5 gm of sample was measured and transferred in 10 mL vial at room temperature. No inert gas atmosphere was used during weighing and transferring. The sample vials were sealed and heated slowly to ~350 K until it formed a uniform melt. The molten samples were then cooled naturally and kept at room temperature sufficiently long prior to any measurements. Refractive indices (n) and conductivity values used in this work were all taken from ref. 33

8.2.2. Dielectric Relaxation Measurements in THz Regime

Terahertz measurements were done with THz spectrometer - TERA K8, Menlo Systems with 780 nm Er doped fiber laser. The pulse width was <100 fs with a repetition rate of 100 MHz. The laser beam was divided into pump and probe beams of 10mW equal intensity by a polarizing beam splitter. The pump beam further passed through a $\lambda/4$ plate reflecting from a mirror mounted on a motorized delay stage. This reflected beam subsequently excited the THz emitter antenna producing a THz radiation having a bandwidth up to 3.0 THz (>60 dB). Polymer lenses focussed this THz radiation on the sample. The radiation transmitted through the sample was then focused on a THz detector antenna gated by the probe laser beam. The THz antennas are gold dipoles of a gap of 5 μm deposited on LT-GaAs substrate. Experiments were carried out in dry nitrogen atmosphere to avoid any water vapour absorption. The measurements were done in a liquid cell (Bruker, model A 145) with Teflon spacer of 120 μm thickness and z-cut quartz windows. Samples were reloaded four times in the sample cell and 9 full scans were averaged. Each experiment was repeated three times.[37,38]

The amplitude and phase of the THz electric field were measured as a function of time by varying the time delay between the probe and the pump beam. The measured electric field amplitude was Fourier transformed to obtain the frequency dependent power and phase of the transmitted pulse. The frequency dependent absorption coefficient $\alpha(\nu)$ (power attenuation) and refraction index $n(\nu)$ (delay of the THz pulse) were subsequently deduced.[39] Subsequently, collected data were analyzed using a commercial software TeraLyzer.

The relaxation dynamics in various solutions were deduced using the frequency-dependent complex dielectric constant given by the relation[40,41]

$$\varepsilon^*(\nu) = \varepsilon'(\nu) - \left[i\varepsilon''(\nu) + \frac{i\kappa}{2\pi\varepsilon_p \nu} \right] \quad , \tag{8.1}$$

where, κ denotes the dc conductivity of the medium, ε_p the permittivity of free space. $\varepsilon'(\nu)$ is the real part of the complex permittivity, and $\varepsilon_0 = \varepsilon'(\nu \to 0)$. The real $\left(\varepsilon^{'}\right)$and imaginary $\left(\varepsilon^{''}\right)$ dielectric constants are calculated as $\varepsilon' = n^2(\nu) - \kappa^2(\nu)$ and $\varepsilon'' = 2n(\nu)\kappa(\nu)$ where the complex refractive index is $n^*(\nu) = n(\nu) - i\kappa(\nu)$. For conducting solutions such as DESs, the $1/\nu$ divergence at $\nu \to 0$ limit contained in Eq. 8.1 makes accurate determination of ε_0 nontrivial. ε_0 obtained by the extrapolation to zero frequency limit may thus be inaccurate. ε_∞ obtained from the dielectric response in the range 0.2 Thz-2 THz will reflect the inadequacy to access infinite frequency. The dielectric constant at infinite frequency is given by $\varepsilon_\infty = \varepsilon(\nu \to \infty) \approx n^2$ and for complete measurements there should be no undetected components. The imaginary part, $\varepsilon''(\nu)$, represents the dielectric loss component and describes the dissipation of energy within the system originating from the interaction between the externally applied frequency dependent electric field with the dipole fluctuations of the medium.

The frequency dependent changes in $\left(\varepsilon^{'}\right)$ and $\left(\varepsilon^{''}\right)$ can be fitted according to Havriliak-Negami (HN) equation[40],

$$\varepsilon(\nu) = \varepsilon_\infty + \sum_{j=1}^{n} \frac{\Delta\varepsilon_j}{\left[1 + (i2\pi\nu\tau_j)^{1-\alpha_j}\right]^{\beta_j}}, \tag{8.2}$$

where $0 \le \alpha_j < 1$ and $0 < \beta \le 1$, and $\Delta\varepsilon_j$ denotes the magnitude of the dispersion at the j-th relaxation step with the time constant, τ_j. Note $\alpha_j = 0$, $\beta_j = 1$ describes relaxation via the Debye model, whereas $\alpha_j = 0$ corresponds to the Cole-Davidson

(CD) and $\beta_j = 1$ to the Cole-Cole models respectively. These relaxation parameters were determined by simultaneously fitting $\varepsilon'(\nu)$ and $\varepsilon''(\nu)$ by using a non-linear least squares routine. Quality of fits was determined by checking both the 'goodness-of-fit' parameter (χ^2) and residual where χ^2 was defined as follows:[42]

$$\chi^2 = \frac{1}{2m - \ell}\sum_{i=1}^{m}\left[\left(\frac{\delta\varepsilon_i'}{\sigma(\varepsilon_i')}\right)^2 + \left(\frac{\delta\varepsilon_i''}{\sigma(\varepsilon_i'')}\right)^2\right], \qquad (8.3)$$

where m denotes the number of data triples ($\nu, \varepsilon', \varepsilon''$), ℓ the number of adjustable parameters, $\delta\varepsilon_i$ and $\sigma(\varepsilon_i)$ the residuals and standard deviations of the individual data points, respectively. For all the combinations of DESs 4-Debye fits were found to be most suitable. However 3-Debye fits were also good and had been compared with 4-debye fits in the text. Other possibilities of Cole-Cole and Cole-Davidson processes did not result in considerable fits.

FTIR spectra in the 1000−3800 cm^{-1} window were recorded on a JASCO FTIR-6300 spectrometer (absorbance mode) using CaF_2 window. The FTIR spectra of the samples correspond to the difference of absorbance spectra between the measured absorbance of the samples and the measured absorbance of air. Experiments were done at ~ 293K.

8.3. Result and discussions

8.3.1. Terahertz Measurements

Since formation of ion pairs and other complex species in an electrolyte solution can contribute to the measured relaxation spectra, the total relaxation process is likely to be composite in nature with more than one time constants. The asymmetric nature of the Cole-Cole plot shown in Figure A28 suggests non-Debye nature[43-45] of the dielectric response of the DESs under study. We will first study the anion dependence of the measured response for (acetamide + electrolyte) DESs where lithium salts of NO_3^-, Br^- and ClO_4^- and sodium salts of ClO_4^-, SCN^- have been considered.

Figure 8.1

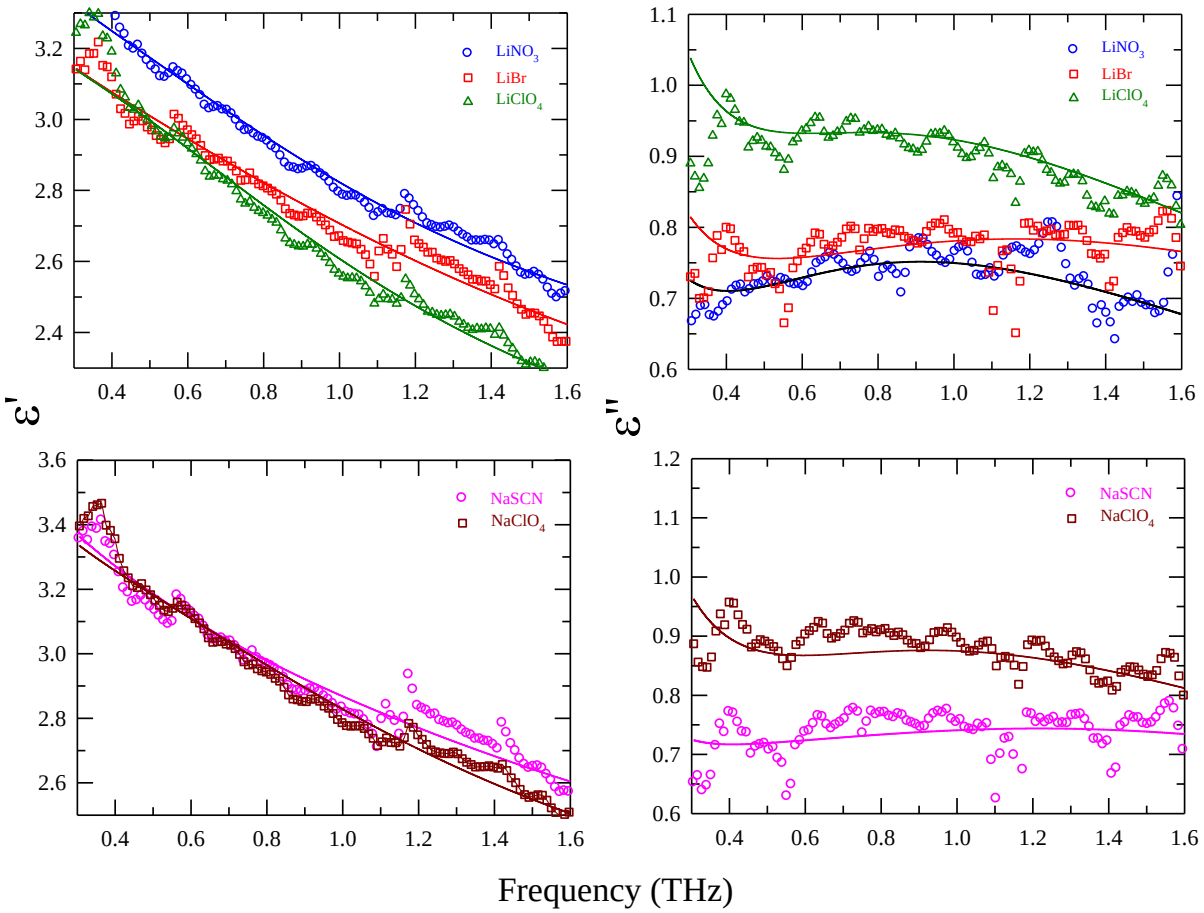

Figure 8.1: The real (ε′) and imaginary (ε″) parts of the measured DR spectra for the (Acetamide + Electrolyte) DES at ~293 K for anions is shown. The upper panels show real and imaginary parts for deep eutectics with lithium salts (perchlorate, bromide and nitrate), and the lower panels present those with sodium salts (perchlorate and thiocyanate). Electrolytes are color coded.

Upper panel of Figure 8.1 shows the anion dependence of the real and imaginary parts of the measured complex DR spectra for DESs containing lithium salts, and the lower panel present the same for DESs containing sodium salts. 4-Debye fits through the data are also shown in the same figure. Few representative residuals are shown in Figure A29. Fit parameters are summarized in Table 8.1. We tried to fit the complex dielectric spectra using 3-Debye process but that resulted in exclusion of the 1-4ps time scale and the resultant fits were not as good as those obtained via 4-Debye fits. Table B14 provides 3-Debye fits and Figure A30 shows a direct comparison for 3-Debye and 4-Debye fits. It is notable that these two procedures yield ε_∞ which are almost equal. Note the maximum undetected portion predicted by the 3-Debye and 4-Debye fits at the high frequency end, $(\varepsilon_\infty - n^2)$, is ~ 0.2 , suggesting these fits are semi-quantitatively correct. Table 8.1 shows that the slower time constants are well separated by almost 10-15 times from the next faster ones, whereas the faster two are sometimes very close. The component with relaxation times in ~10-40ps range dominates the overall relaxation process. Even though the time constant of ~1-4ps is sometimes of negligible amplitude, we could not omit it as that would lead to inaccurate descriptions. Moreover, such a timescale has been clearly observed in the corresponding fs-RIKES measurements.[34] The third component with time constant in ~0.13-0.8 ps range can be real as simulations of orientational relaxation of molten acetamide[32] report such a sub-picosecond component. The fastest time constant has often been fixed at 0.08 ps to obtain reasonable fits and, as a result, carries no signature of ion-identity, although it contributes significantly (upto 8%) to the total observed relaxation. Note also in Figure 8.1 that the fastest relaxation occurs for ClO_4^- containing DESs and the slowest for NO_3^- containing ones.

Next we attempt to assign plausible physical interpretation to the relaxation components detected in the present THz measurements. The component with time constant in ~10-40ps regime is likely to be associated with the collective orientational relaxation. This component has been reported in GHz DR measurements[33] and OHD-RIKES measurements[34] These collective motions originate from extensive networking through inter-species H-bonding involving acetamide molecules and the electrolytes.

A comparison between the viscosities of the system and the time constants reveal no correlation between the two (Table B15). These time constant are therefore clearly not guided by the corresponding solution viscosities. Timescales for ion-pair rotations in the range of tens of picoseconds or longer are reported in literature.[44,46,47] Aqueous systems also show 8 ps relaxation time scale which is ascribed to the cooperative reorientation network[40].

Table 8.1: Parameters obtained from simultaneous fitting of the real (ε') and imaginary (ε'') parts of the measured DR spectra for (Acetamide + Electrolyte) DES at ~293 K are summarized.

Electrolyte	ε_0	$\Delta\varepsilon_1$	τ_1[b] (ps)	$\Delta\varepsilon_2$	τ_2 (ps)	$\Delta\varepsilon_3$	τ_3 (ps)	$\Delta\varepsilon_4$	τ_4 (ps)	ε_∞	$<\tau_{av}>$[d] (ps)	χ^2	n[c]
LiBr	27	23.3[a] (92%)	32.3	0.51 (2%)	1.95	0.32 (1%)	0.238	1.11 (4.4%)	0.09	1.758	29.86	1.03	1.407
$LiNO_3$	25	21.1 (92%)	37	0.80 (3%)	4.62	0.10 (0.5%)	0.875	0.88 (3.8%)	0.136	2.116	34.28	1.19	1.385
$LiClO_4$	33.2	29.4 (94%)	26	0.6 (2%)	3.2	0.63 (2%)	0.128	0.79 (2.51%)	0.08	1.781	24.39	1.02	1.371
$NaClO_4$	22	18.3 (91%)	18.9	0.36 (2%)	1	1.36 (7%)	0.12	0.01 (0.07%)	0.08	1.934	17.35	1.11	1.369
NaSCN	16.4	12.7 (87%)	25.2	0.19 (1.3%)	1	0.502 (4%)	0.309	1.06 (7.3%)	0.081	1.910	22.16	1.12	1.418
KSCN	29	25.1 (92%)	23.4	0.24 (0.08%)	2.5	0.47 (0.17%)	0.333	1.31 (4.8%)	0.08	1.887	21.67	1.08	1.413

a) Number in parenthesis indicates dispersion amplitude of a given dispersion step in percentage.

b) τ_i (i=1-4) are better within ±5% of the reported values.

c) Taken from Reference 33.

d) $< \tau_{av} > = \frac{\sum_{i=1}^{=n} a_i \tau_i}{\sum_{i=1}^{n} a_i}$, where $\sum_{i=1}^{n} a_i = 1$ and $a_i = \frac{\Delta\varepsilon_i}{\sum_{i=1}^{n} \Delta\varepsilon_i}$.

The second time constant (τ_2) n the range,~1-5ps, probably originates from the rotation of either N-H bond vector or C-N backbone.[32] DR measurements in the GHz range also reports similar timescale.[33] Note H-bonded systems like water and monohydroxy alcohols[50] show a relaxation time around 1-3ps. The origin of the third time constant (τ_3) is likely to be the breaking and reformation of H-bonds.[32] Support for such an assignment may be derived from the study of ionic liquid , 1-ethyl-3-methylimidazolium triflate, which reports a timescale ~0.25ps and ascribe to H-bonding dynamics.[46] We would also like to mention here that timescale in ~0.2 ps range has been often observed in aqueous systems and tagged to H-bond making/breaking process[51]. The fastest time constant (τ_4) in ~80-150 fs range cannot show any anion dependence for the reason already discussed. However, collective librations of acetamide, as in water,[52,53] can give rise to such an ultrafast timescale. Note such subpicosecond timescale has been reported for various networked systems that include ionic liquids[46], liquid amides[36,54] and other H-bonded systems[39,47-49,55,56].

Figure 8.2 shows the cation dependence of the real and imaginary components of the measured DR spectra. Here DESs containing the two anions, ClO_4^- and SCN^- at ~293K, have been considered. Residuals are shown in Figure A29. Fit parameters are

summarised in Table 8.1. Note the slowest time constants here follow the viscosity trend and inversely proportional to cation size (see Table B16). The reason may be cation with smaller radius forms stronger networks that slow down overall medium dynamics via increasing viscosity.

Figure 8.2

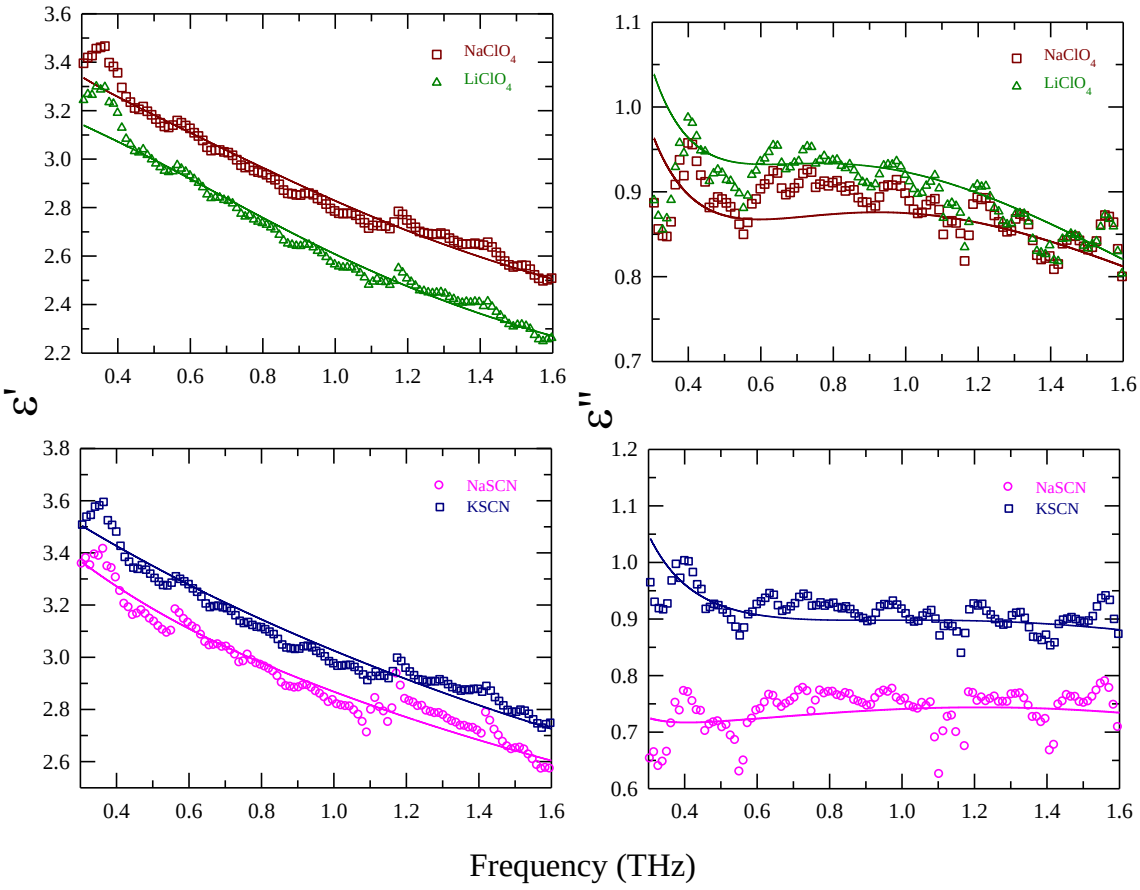

Figure 8.2: The real (ε′) and imaginary (ε″) parts of the measured DR spectra for the (Acetamide + Electrolyte) DES at ~293 K for cations is shown. The upper panels show real and imaginary parts for deep eutectics of perchlorate salts with lithium and

sodium, and lower panels present thiocyanate salts of sodium and potassium. Representations are color coded.

A closer inspection of Table 8.1 reveals that τ_3 carries a signature of the anion effect and in turn strengthens the proposition that anions significantly affect the network formation. τ_3 for ClO_4^- is the smallest among all the anions and is ~0.12 ps for both $LiClO_4$ and $NaClO_4$ containing DESs. On the other hand, it is ~0.3 ps for both the SCN^- containing DESs. NO_3^- containing DES has the highest τ_3 (~0.9 ps) whereas in presence of Br^- it is moderate (~0.24 ps). Since relaxation times vary due to interactions of the ions with acetamide, a decrease in τ_3 can indicate a loss of solvent network and vice-versa. Whether this can be linked to the structure breaking ability of ions is debatable.

Figure 8.3 shows the electrolyte dependence of absorption co-efficient in these DESs. Note the maximum terahertz absorption occurs for systems containing $LiClO_4$ and the minimum for $LiNO_3$ containing DES. With disruption of H-bonding in the solution, the restricted bond movements are freed and bonds become more labile absorbing more of terahertz radiation. This is similar to the increasing of absorption coefficient for water at higher temperature[57]. The derived refractive index plot for (Acetamide+Electrolyte) that decreases with increase frequency is also shown in Figure 8.4. Electrolyte dependence is also evident here.

Figure 8.3

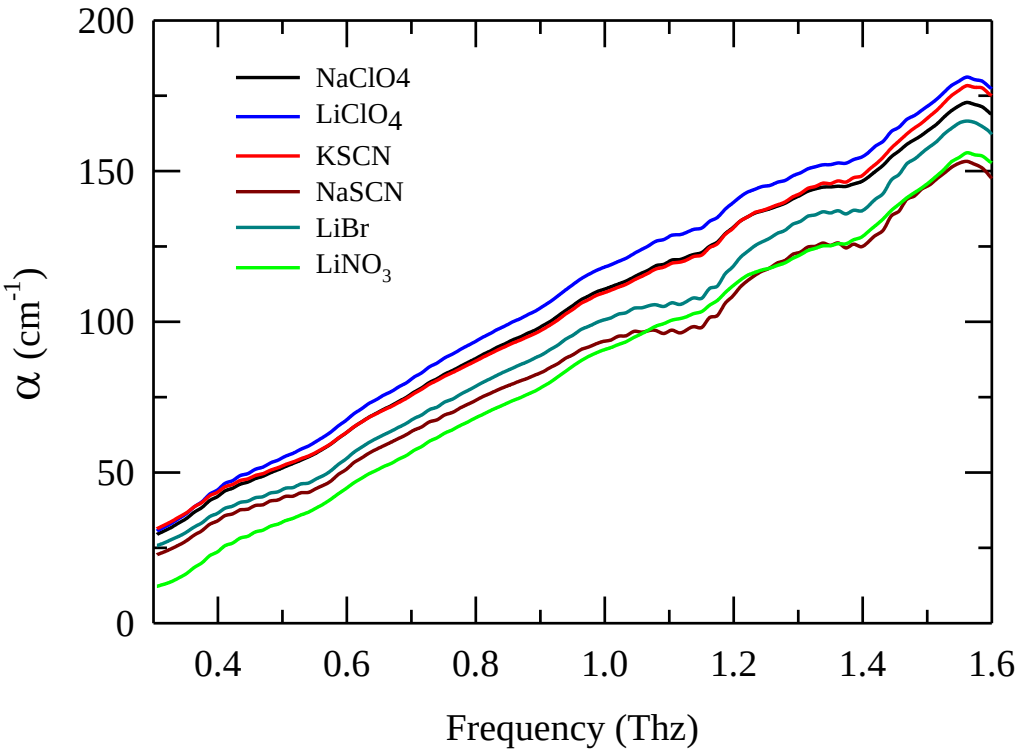

Figure 8.3: Absorption coefficient is plotted against frequency for (Acetamide + Electrolyte) DES at ~293 K. The different combinations are color coded.

Figure 8.4

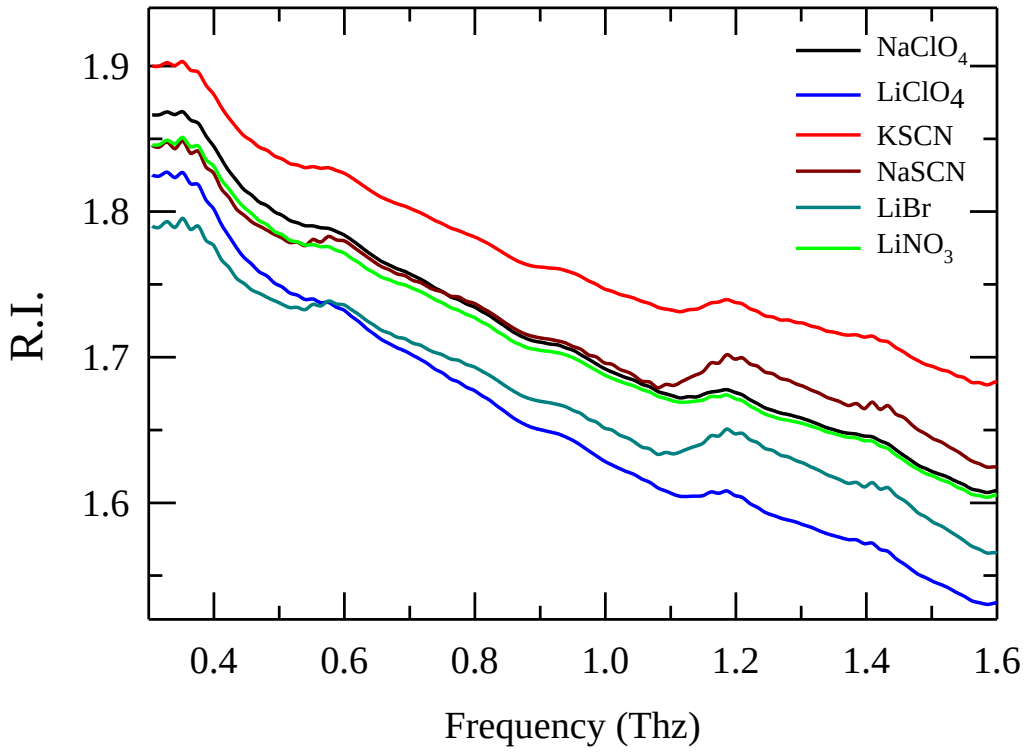

Figure 8.4: Refractive indices are plotted against frequency for (Acetamide + Electrolyte) DES at ~293 K. The different combinations are color coded.

8.3.2. FTIR spectroscopy

FTIR measurements of these (acetamide+electrolyte) systems have been performed in the frequency range, 1000-4000 cm^{-1}. Figure 8.5 presents the results. The upper panel shows the lower frequency region whereas the lower panel describes the higher frequency region. The signature of bands is found to differ significantly compared to the pure liquid acetamide spectra.[58] ClO_4^- , NO_3^- and SCN- containing systems show characteristic bands at 1100 cm^{-1}, 1380 cm^{-1} and 2100 cm^{-1} respectively.[59,60] The N-H rocking motion shows up at 1120 cm^{-1} for (acetamide+ Na/KSCN) and (acetamide+$LiNO_3$/Br) DESs. It is to be noted that this band is submerged for ClO_4^- containing systems because of the relatively much higher intensity of the ClO_4^- band.

C-N stretch is found at 1340 cm^{-1} which is decreased due to co-ordination of oxygen to cation. C-H deformed bands are also seen at 1400 cm^{-1}. In this region the band for (acetamide+$LiNO_3$) DES is noticeably prominent than in other systems. The reason is the common zone of NO_3^- with that of C-N and C-H stretch bands. The amide II (N-H in plane bending) bands occurs at 1610 cm^{-1} which almost overlaps with the amide II (C=O stretch) band at 1670 cm^{-1}. The lower panel shows the N-H band at 3200 cm^{-1} - 3400 $cm^{-1.}$ It is to be noted that the N-H peak at ~3220 cm^{-1} shifts following the sequence: ClO_4^- > $LiNO_3^-$ ~ Na/KSCN > LiBr. One can correlate this variation as decrease of N-H frequency with increasing co-ordination of nitrogen through cation. In addition to these, a band is also seen to be merged with the N-H stretch band which is the band of di/tri/tetramers of acetamide.

Figure 8.5

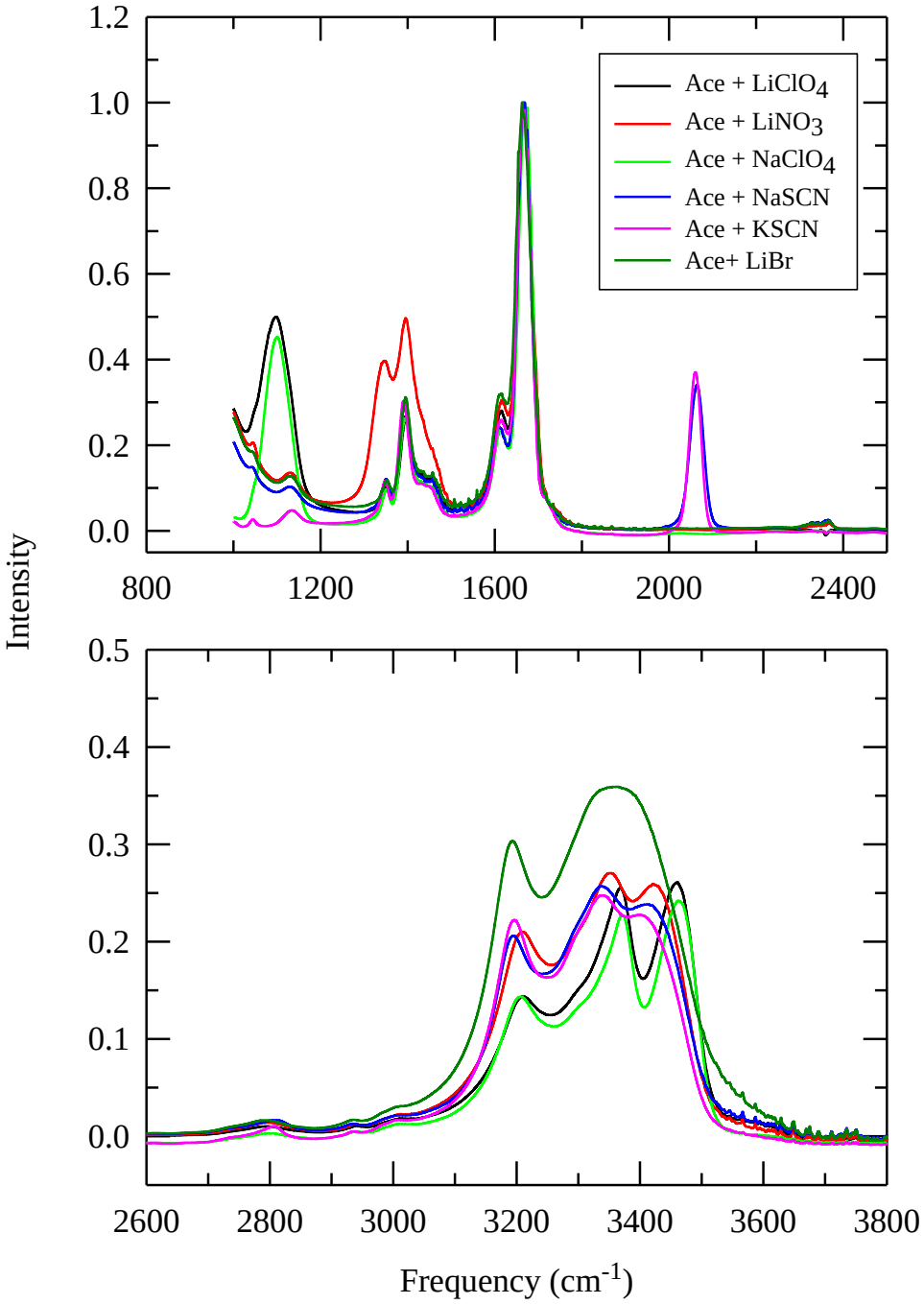
Intensity
Frequency (cm-1)
Ace + LiClO4
Ace + LiNO3
Ace + NaClO4
Ace + NaSCN
Ace + KSCN
Ace+ LiBr

Figure 8.5: The FTIR spectra obtained for different combinations of (Acetamide + Electrolyte) DES (color coded) are shown in two panels. The upper panel shown the variation from 800-2500cm^{-1} and the lower panel shows 2600-3800cm^{-1}.

8.4. Conclusion

In this work we have measured the dielectric relaxation response in the range 0.2-2 THz and FTIR spectra at ~293K for (acetamide+electrolyte) DESs. The real and imaginary parts of the complex DR spectra permittivity have been simultaneously fitted to 4-Debye processes. Plausible mechanisms, based on results from simulations and other experiments, have been attributed to the four time constants reported. The relaxation spectra show both anion and cation dependencies. FTIR measurements show distinct peaks for all the anions. The effect of interactions between the various anions and cations forces deformations in the –CO and –NH_2 regions in the vibrational spectra. Absorption coefficient has been found to be the largest for perchlorate containing DESs, reigniting the issue of structure breaking ability of ions.

References

1. Marcus, Y. *J. Phys. Org. Chem.* **2012**, *25*, 1072.

2. Aaron, M. S.; Keith, H.; Bala, S. In *Gas-Expanded Liquids and Near-Critical Media*; American Chemical Society: 2009; Vol. 1006, p 3.

3. Savage, P. E.; Gopalan, S.; Mizan, T. I.; Martino, C. J.; Brock, E. E. *AIChE Journal* **1995**, *41*, 1723.

4. Jessop, P. G.; Subramaniam, B. *Chem. Rev.* **2007**, *107*, 2666.

5. Heinze, T.; Schwikal, K.; Barthel, S. *Macromol. Biosci.* **2005**, *5*, 520.

6. Ranu, B. C.; Banerjee, S. *Org. Lett.* **2005**, *7*, 3049.

7. Francisco, M.; Van den Bruinhorst, A.; Kroon, M. C. *Angew. Chem., Int. Ed.* **2013**, *52*, 3074.

8. Abbott, A. P.; Harris, R. C.; Ryder, K. S.; D'Agostino, C.; Gladden, L. F.; Mantle, M. D. *Green Chem* **2011**, *13*, 82.

9. Smith, E. L.; Abbott, A. P.; Ryder, K. S. *Chem Rev* **2014**, *114*, 11060.

10. Abbott, A. P.; Capper, G.; Davies, D. L.; Rasheed, R. K. *Chem. Eur. J.* **2004**, *10*, 3769.

11. Francisco, M.; van den Bruinhorst, A.; Kroon, M. C. *Green Chem.* **2012**, *14*, 2153.

12. Berchiesi, G.; Deangelis, M.; Rafaiani, G.; Vitali, G. *J. Mol. Liq.* **1992**, *51*, 11.

13. Vitali, G.; Berchiesi, G.; Barocci, S. *Thermochim. Acta* **1989**, *143*, 205.

14. Berchiesi, G.; Vitali, G.; Plowiec, R.; Barocci, S. *J. Chem. Soc. Faraday Trans. 2* **1989**, *85*, 635.

15. Amico, A.; Berchiesi, G.; Cametti, C.; Di Biasio, A. *J. Chem. Soc. Faraday Trans. 2* **1987**, *83*, 619.

16. Abbott, A. P.; Boothby, D.; Capper, G.; Davies, D. L.; Rasheed, R. K. *J. Am. Chem. Soc.* **2004**, *126*, 9142.

17. Abbott, A. P.; Capper, G.; Davies, D. L.; Rasheed, R. K.; Tambyrajah, V. *Chem. Commun.* **2003**, 70.

18. D'Agostino, C.; Harris, R. C.; Abbott, A. P.; Gladden, L. F.; Mantle, M. D. *Phys. Chem. Chem. Phys.*

2011, *13*, 21383.

19. Jiang, Z.; Hess, S. K.; Heinrich, F.; Lee, J. C. *The Journal of Physical Chemistry B* **2015**.

20. Wallace, R. A. *Inorg. Chem.* **1972**, *11*, 414.

21. Perkins, S. L.; Painter, P.; Colina, C. M. *J. Phys. Chem. B* **2013**, *117*, 10250.

22. Van der zwan, G.; Hynes, J. T. *Chem. Phys.* **1991**, *152*, 169.

23. Nitzan, A. *Chemical Dynamics in Condensed Phases*; Oxford Univ. Press: Oxford, 2006.

24. Van der Zwan, G.; Hynes, J. T. *J. Chem. Phys.* **1983**, *78*, 4174.

25. Pradhan, T.; Biswas, R. *J. Phys. Chem. A* **2007**, *111*, 11524.

26. Pradhan, T.; Gazi, H. A.; Biswas, R. *J. Chem. Phys.* **2009**, *131*, 054507.

27. Das, A.; Das, S.; Biswas, R. *J. Chem. Phys.* **2015**, *142*, 034505.

28. Guchhait, B.; Das, S.; Daschakraborty, S.; Biswas, R. *J. Chem. Phys.* **2014**, *140*, 104514.

29. Guchhait, B.; Daschakraborty, S.; Biswas, R. *J. Chem. Phys.* **2012**, *136*, 174503.

30. Gazi, H. A. R.; Guchhait, B.; Daschakraborty, S.; Biswas, R. *Chem. Phys. Lett.* **2011**, *501*, 358.

31. Guchhait, B.; Gazi, H. A.; Kashyap, H. K.; Biswas, R. *J. Phys. Chem. B* **2010**, *114*, 5066.

32. Das, S.; Biswas, R.; Mukherjee, B. *J. Phys. Chem. B* **2015**, *119*, 274.

33. Mukherjee, K.; Das, A.; Choudhury, S.; Barman, A.; Biswas, R. *J. Phys. Chem. B* **2015**, *xxxx*, xxxx.

34. Biswas, R.; Das, A.; Shirota, H. *J. Chem. Phys.* **2014**, *141*, 134506.

35. Pal, T.; Biswas, R. *Chem. Phys. Lett.* **2011**, *517*, 180.

36. Kashyap, H. K.; Pradhan, T.; Biswas, R. *J. Chem. Phys.* **2006**, *125*, 174506.

37. Polley, D.; Patra, A.; Mitra, R. K. *Chem. Phys. Lett* **2013**, *586*, 143.

38. Samanta, N.; Das Mahanta, D.; Mitra, R. K. *Phys. Chem. Chem. Phys.* **2014**, *16*, 23308.

39. Kindt, J. T.; Schmuttenmaer, C. A. *J. Phys. Chem.* **1996**, *100*, 10373.

40. Bottcher, C. F. J. B., P. *Theory of Electrical Polarization, 2nd ed.;* ; Elsevier: : Amsterdam, The Netherlands, , 1978; Vol. Vol. 2.

41. Kremer, F. S. o., A. *Broadband Dielectric Spectroscopy;*; Springer: : Berlin, Germany, , 2003.

42. Bevington, P. R. *Data reduction and error analysis for the physical sciences,*; McGraw-Hill, : New York, , 1969.

43. Wei, Y. Z.; Sridhar, S. *J. Chem. Phys.* **1993**, *99*, 3119.

44. Asaki, M. L. T.; Redondo, A.; Zawodzinski, T. A.; Taylor, A. J. *J. Chem. Phys.* **2002**, *116*, 10377.

45. Yamada Pittini, Y.; Daneshvari, D.; Pittini, R.; Vaucher, S.; Rohr, L.; Leparoux, S.; Leuenberger, H. *Eur. Polym. J.* **2008**, *44*, 1191.

46. Yamamoto, K.; Tani, M.; Hangyo, M. *J. Phys. Chem. B* **2007**, *111*, 4854.

47. Hunt, N. T.; Turner, A. R.; Tanaka, H.; Wynne, K. *J. Phys. Chem. B* **2007**, *111*, 9634.

48. Biswas, R.; Nandi, N.; Bagchi, B. *J. Phys. Chem. B* **1997**, *101*, 2968.

49. Roy, S.; Bagchi, B. *J. Chem. Phys.* **1993**, *99*, 9938.

50. Li, R. Y.; D'Agostino, C.; McGregor, J.; Mantle, M. D.; Zeitler, J. A.; Gladden, L. F. *J. Phys. Chem. B* **2014**, *118*, 10156.

51. Patra, A.; Luong, T. Q.; Mitra, R. K.; Havenith, M. *Phys. Chem. Chem. Phys.* **2014**, *16*, 12875.

52. Laage, D.; Hynes, J. T. *Science* **2006**, *311*, 832.

53. Ingrosso, F.; Rey, R.; Elsaesser, T.; Hynes, J. T. *J. Phys. Chem. A* **2009**, *113*, 6657.

54. Biswas, R.; Bagchi, B. *J. Phys. Chem.* **1996**, *100*, 1238.

55. Daschakraborty, S.; Pal, T.; Biswas, R. *J. Chem. Phys.* **2013**, *139*, 164503.

56. Born, B.; Weingartner, H.; Brundermann, E.; Havenith, M. *Journal of the American Chemical Society* **2009**, *131*, 3752.

57. Funkner, S.; Havenith, M.; Schwaab, G. *J. Phys. Chem. B* **2012**, *116*, 13374.

58. Kerridge, D. H. *Chem. Soc. Rev.* **1988**, *17*, 181.

59. Narayanan, N. S. V.; Ashokraj, B. V.; Sampath, S. *J. Colloid Inter. Sci.* **2010**, *342*, 505.

60. Miller, F. A.; Wilkins, C. H. *Anal. Chem.* **1952**, *24*, 1253.

Chapter 9

Effects of Mixed Electrolytes on Excited State Intramolecular Charge Transfer Reaction in Common Solvents: Steady State and Time resolved Fluorescence Emission Studies

9.1. Introduction

Charge transfer reactions triggered by photons are important for its' utility in our daily lives[1-5]. Two such life-sustaining processes are photosynthesis and vision. These charge transfer reactions can also be implemented in optoelectronic devices and molecular switches. This area of research received tremendous boost since the discovery of two state emission of 4-*N*,*N*-dimethylaminobenzontrile (DMABN).[1-11] An emission band occurring at a shorter wavelength (blue end) is seen in non-polar solvents whereas polar solvents give rise to an additional emission peak at a longer wavelength[1-5]. The appearance of two distinct emission bands signify an intramolecular charge transfer, indicating one state is being favoured over the other in polar media. Experimental studies, theoretical and semi-emperical quantum mechanical calculations have been done for the molecules in gas phase to compute the difference between these two states[5,6].

Various studies mentioned have suggested that the blue shifted emission (normal fluorescence) occurs from a locally excited state (LE) having the charge distribution similar to that of the ground state. The red shifted emission band, on the other hand, is given by a charge transferred (CT) state which is generated by transfer of electrons within the molecule. On photoexcitation, the molecule is first excited to the locally excited state where charge transfer occurs from the amino group to benzonitrile creating the charge transfer state. The LE state is favoured by less polar environment and CT state would be stabilized by polar solvent through dipole –dipole interaction with dipolar solvent molecules. The twisted intramolecular charge transfer (TICT) model endorses the simultaneous twisting of the bond connecting the amino group and the benzene ring during the charge transfer[1-5]. Viscosity of the environment would affect this twisting mode and in turn would affect the reaction mode of LE to CT transformation. The rate of the reaction ($LE \rightarrow CT$) is also modified by the

dynamical modes as the reaction experiences solvation response via orientational polarisation relaxation of the medium[12,13]. Representative examples of TICT molecules other than DMABN are 4-(1-azetidinyl)benzonitrile (P4C) and 4-(1-pyrrolidinyl)benzonitrile (P5C).

The above discussion makes it clear that solvents of different polarity would remarkably affect the rate of reaction for TICT molecules. Such a topic has been dealt with in the extensive study of different solvents with P4C and P5C.[5] Addition of electrolytes in polar solvent modifies the polarity and solvation response of the medium and significantly alters the due course of the reaction.[14-16] Formation of ion-pairs, triple ions and neutral triple ions are responsible for these changes.[17-47] Solvation dynamics studies in electrolyte solutions of low viscous polar solvents indicate that the solvation times are in nanosecond regime whereas in pure solvent the average solvation time is in sub-picosecond scale[48-51]. Hence it would be of interest to investigate the effect of such slow dynamics on the reactions with time scale of the similar regime. The effects of increasing electrolyte concentration in polar solvents and increasing the size of the cation (keeping the anion fixed) on the reaction static and dynamic properties have already been studied[52]. Here we would like to see how mixed electrolytes in solvent affect these intramolecular charge transfer reactions. Mixed electrolyte systems are formed by mixing more than two electrolytic solid components in solid state or in solvent. Physiochemical properties like viscosity, conductivity, diffusion co-efficient, activity co-efficient, and Gibb's free energy show remarkable changes in presence of mixed electrolytes[53-55]. Ionic potential (charge/radius) of one cation affects the behaviour of the other. One such example is the study of Na^+/K^+ balance in ion channels in biological systems[56,57]. Therefore it is important to study whether the addition of one type of electrolyte would affect the reaction in presence of another electrolyte. Whether the second electrolyte can replace the first without affecting the reaction or affect the overall reaction by retarding or enhancing the reaction is yet unknown for the TICT molecules like P4C and P5C. Data obtained here will help understanding the medium effects on such reactions carried out in deep eutectic solvents.

In this work we have used P4C and P5C as the TICT molecules of interest and $LiClO_4$ and $NaClO_4$ as the electrolytes. Two solvents of different polarities have been chosen – ethylacetate (dielectric constant, $\varepsilon_0 = 6$) and acetonitrile ($\varepsilon_0 = 36$)[58]. So the system is as follows: [xLiClO$_4$+ (0.5-x)NaClO$_4$] (x=0 to 0.5M) in ethyl acetate (EA)/ acetonitrile (ACN).

We have chosen these sets of TICT molecules, electrolytes and solvents because individual studies with these electrolyte and pure solvents are available[5,52,59]. It is worthy to mention here that steady state and time resolved results have been analysed using the convention used earlier.[5,52,59] All experiments were done at ~ 293K.

.

Scheme 1 shows the representation of the TICT molecules (P4C and P5C) along with the pictorial representation of the charge transfer process. **Scheme 2** shows the photoexcitation of a TICT molecule and the subsequent formation of charge-transferred (CT) state where k_f and k_r are respectively the forward and backward rate constants. k_{LE} and k_{CT} represent the net (radiative *plus* nonradiative) rate constants for LE and CT states, respectively. S_0 is the ground state. Interconversion between LE and CT states is the charge-transfer reaction. Two factors affect the interconversion rate. They are twisting of the connecting bond and solvation[5]. With the addition of electrolyte the average polarity of the medium increases,[19,49] favouring the CT formation.

Scheme 1:

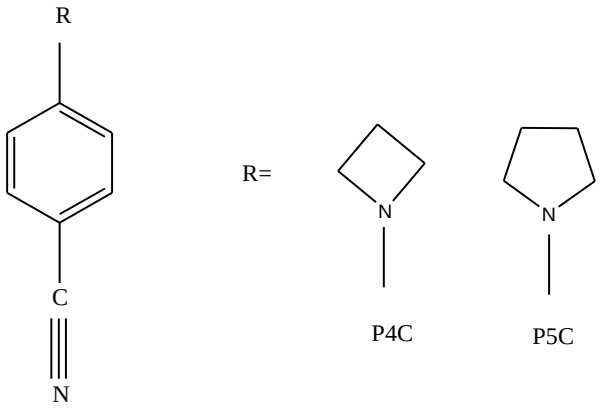

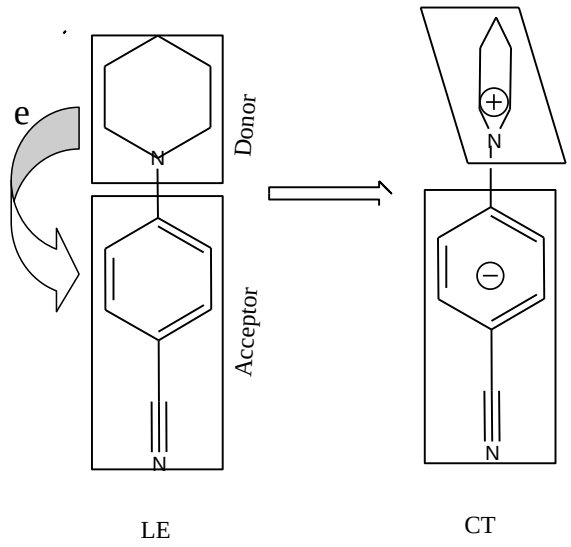

Scheme 2:

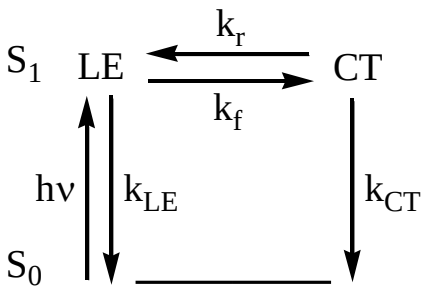

9.2. Experimental Details

4-(1-Azetidinyl)benzonitrile (P4C) and 4-(pyrrolidinyl)benzonitrile (P5C) were synthesized and purified by following the protocol given in Ref. 10 and Ref.11. Ethyl acetate and acetonitrile were used as received (spectrophotometric grade) from Sigma Aldrich. Lithium perchlorate ($LiClO_4$) and sodium perchlorate ($NaClO_4$) were also procured from Sigma Aldrich (anhydrous, 99.5%) and vacuum-dried before use. Solutions were prepared for use by following methods described in Chapter 2. Absorption spectrum was recorded by uv-spectrophotometer (Model UV- 2450, Shimadzu) and the emission spectra were recorded using Fluoromax-3 (Jobin-Yvon, Horiba) after adjusting the absorbance of the solution to 0.1 or less with excitation wavelength fixed at 305 nm. Solvent blanks were subtracted from the emission spectra prior to analysis and converted to frequency representation after properly

weighting the intensity with λ^2. A few samples were bubbled with dry argon gas to investigate the effects of dissolved oxygen on the absorption and emission spectra. These initial runs showed very little or no effects on the overall appearance of the spectra and hence most of the samples were not deoxygenated.

We then deconvoluted each emission spectrum into two fragments by using the emission spectrum of the corresponding TICT molecule in perfluorohexane as mentioned in Ref. 5 This deconvolution provided area under each fragment (measure of population under a particular band) that was then used to calculate the equilibrium constants and change in reaction free energies for the LE to CT conversion. Emission peak frequencies were calculated as follows. Shifts of the emission spectra from the peak of the reference emission spectrum were calculated and added to the *average* peak frequency of the reference emission spectrum. The *average* of the reference emission peak was calculated by averaging the numbers obtained by fitting the upper half of the reference emission spectrum with an inverted parabola, first moment and the arithmetic mean of the frequencies at half intensities on both blue and red ends of the emission spectrum[60-62]. Absorption peak frequencies were obtained by calculating the first moments of the absorption spectra.

Lifetime data for measuring radiative rates for the TICT molecules in electrolyte solutions were obtained from time-correlated single photon counting (Lifespec, Edinburgh Instruments) apparatus with excitation wavelength at 299 for TICT molecules. The effective resolution (fwhm) of the instrument response function with the 299 nm excitation source was ~400 ps. The detail of this instrumentation is discussed elsewhere[60,61] and hence only brief information will be given here. The emission fluorescence has been collected at magic angle at both LE and CT peak positions (of steady-state spectrum). Subsequently, collected decays have been deconvoluted from the IRF and fitted to multiexponential function using an iterative reconvolution algorithm for reasonable accuracy. For a few cases, emission decays have been collected at two or three different emission wavelengths around the LE and CT peaks and average data have been shown for them. Data associated with such cases of different wavelengths are found to vary *insignificantly* and hence are regarded as fluctuations.

Conductivity measurements of electrolyte solutions were performed using a multimeter (*p*H and conductivity) fitted with a conductivity cell of cell constant 0.920 (10%) and standardised with aqueous KCL (~.01M). The electrode was dipped in the sample until equilibrium was

reached and reading becomes stable. After proper calibration, selected samples were checked three times and no significant differences were observed. Densities (ρ) of the samples were measured by an automated temperature-controlled density-cum-sound velocity analyzer (Anton Paar, model DSA 5000) at required temperatures (± 0.5K). Viscosities (η) were measured by AMVn automated micro-viscometer from Anton Paar (falling ball method). Refractive indices were measured by Rudolph J357 automated refractometer. All the experiments were performed at $T = 293 \pm 0.1K$.

9.3. Results and discussion

9.3.1. Transport properties and steady state results

Upper panel of Figure 9.1 shows the variation of the system conductivity with progressive replacement of Na^+ by Li^+ in ethyl acetate. A steady increase in conductivity is noticed upto x= 0.3M after which there is a fall in conductivity. This is probably due to a competition between size of the cation and the cluster formation with organic solvent. Na^+ has a volume of 3.94 $Å^3$ whereas Li^+ is of 1.99 $Å^3$[63]. Therefore when Li^+ progressively replaces Na^+ the conductivity increases due to faster transport of smaller Li^+. With further replacement of Na^+, increase of Li^+ leads to aggregation of Li^+ ions with the organic solvent molecules. Thus cluster formation dominates the interaction and overall conductance decreases with majority of Li^+ in solution.

The complex interaction in the system in the presence of equivalent amount of Li^+ and Na^+ is also observed in the variation trend of viscosity with "x" shown in lower panel of panel of Figure 9.1. As fraction of Na^+ decreases in the system, viscosity increases and maximises at x=0.2 followed by a fall with progressive replacement of all Na^+. It is noteworthy that conductivity as well as viscosity of only Na^+ region (x=0.0) is lesser than only Li^+ region (x=0.5). This is because of larger cluster formation ability of Li^+. It is very interesting to observe increase of both viscosity and conductivity with increase of Li^+ concentration. Such a feature is contrary to hydrodynamic description, and indicates conductivity mechanism other than simple diffusion. For the sake of completeness, Li^+ concentration dependent density and refractive index of the system [xLiClO$_4$+ (0.5- x) NaClO$_4$] in ethyl acetate is shown in Figure A31. Note again here that density is decreasing with x while viscosity is increasing.

Figure 9.1

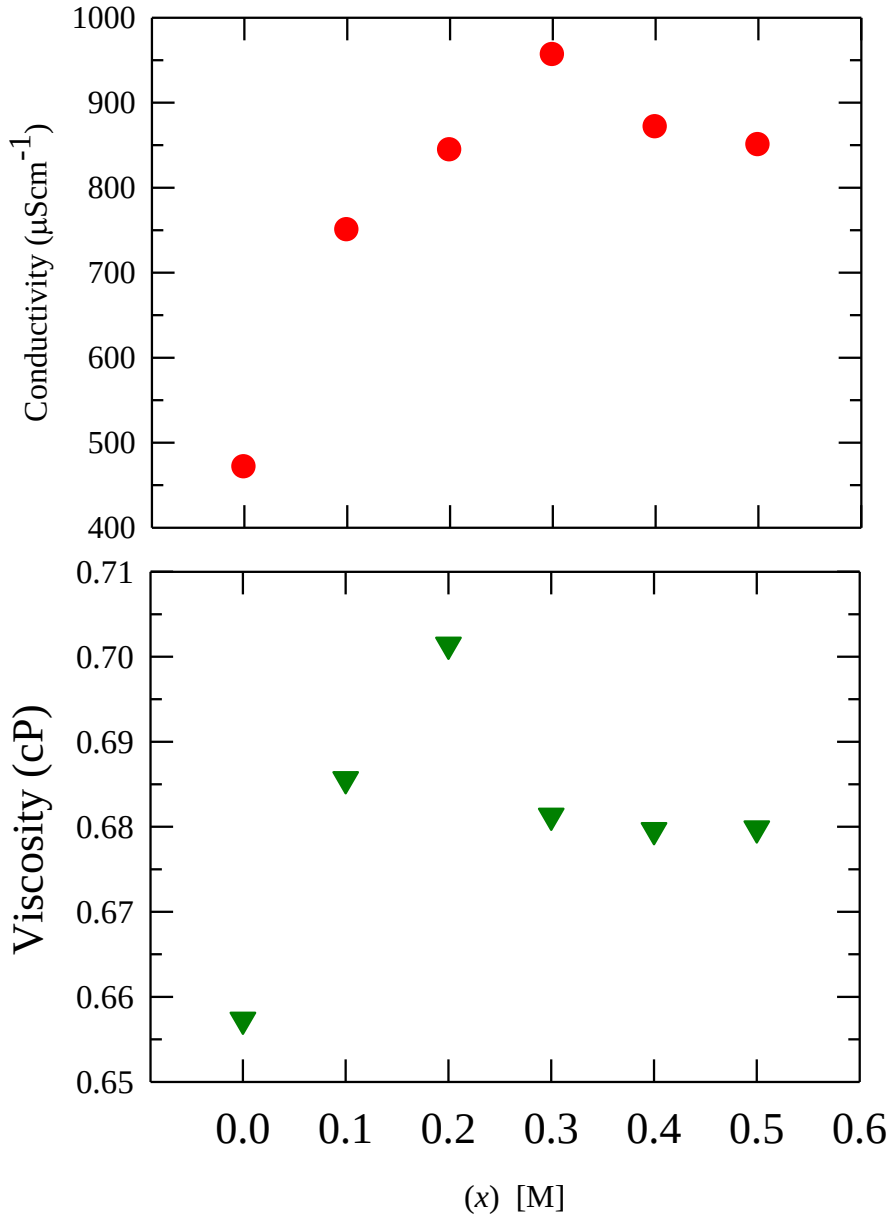

Figure 9.1: Conductivity (μScm^{-1}) and viscosity (cP) are shown in the figure for the increasing [Li^+] represented as *'x'* for the system [*x* $LiClO_4$ + (0.5- *x*)$NaClO_4$] in ethyl aceate at 293K. Error associated with conductivity is ± 10% and for viscosity is ± 5%.

Figure 9.2 represents the absorption and emission spectral envelopes of P4C in acetonirile and ethyl acetate. The same for P5C is given in Figure A32. Cluster formation allows greater solubility of $LiClO_4$ in ethyl acetate although the static dielectric constant of ethyl acetate is one-sixth compared to the highly polar acetonitrile[64]. The shape of the absorption and

emission spectra in presence of mixed electrolyte does not change from that of the pure system. However the response alters with different values of '*x*'. The emission spectra for P4C in ethyl acetate as well as in acetonitrile, show a red shift of the CT state spectra with increasing '*x*'. The difference is due to the greater interaction of electrolytes with ethyl acetate. Figure A32 shows that emission of CT state for P5C is very strong and the intensity distribution for CT and LE states are reversed compared to P4C in the more polar acetonitrile. In ethyl acetate also, amount of CT is very high for P5C.

Figure 9.2

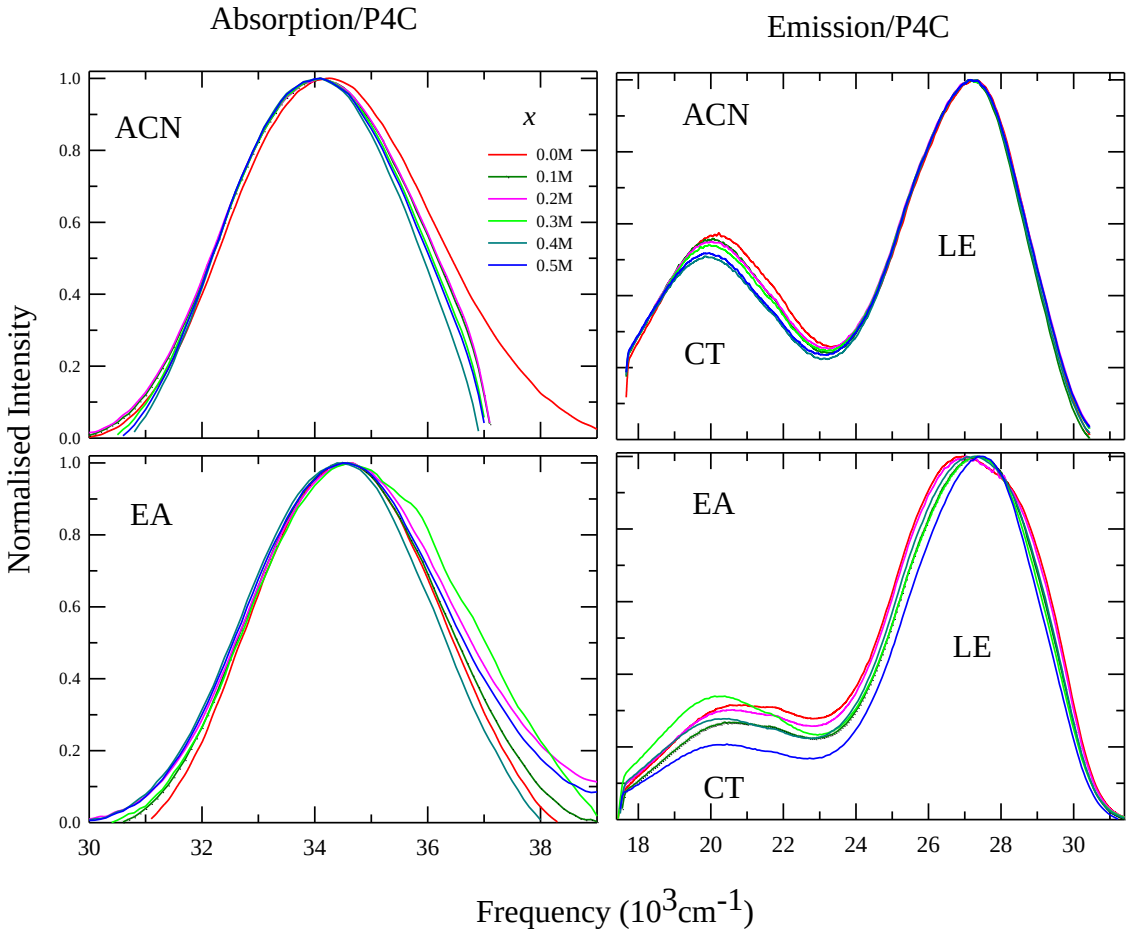

Figure 9.2: Absorption and emission spectra of 4-(1- azetidinyl)-benzonitrile (P4C) is shown for different values of '*x*' (color coded) in the system [*x* $LiClO_4$ + (0.5- *x*)$NaClO_4$] in acetonitrile (upper panel, marked with "ACN") and ethyl acetate (lower panel marked with "EA") at ~293K.

The variation of the spectral properties is shown more quantitatively in Figure 9.3 and Figure 9.4. We see there is an increase in absorption frequency (ν_{abs}) for P4C as Li^+ replaces Na^+ in the system. However the change in behaviour of ν_{abs} and ν_{em} is more prominent in ethyl acetate rather than in acetonitrile owing to the better solubility of the electrolytes in ethyl acetate than acetonitrile.[52] Spectral widths, Γ_{abs} and Γ_{em}, also show similar dependence. The variation of inhomogeneous widths (obtained from following the analysis described in ref. 5) for the LE and CT bands are shown in Figure A33. The irregular variation of the widths is a reflection of the inhomogeneous broadening as a result of microheterogeneous environment formed due to the presence of mixed electrolytes.

Figure 9.3

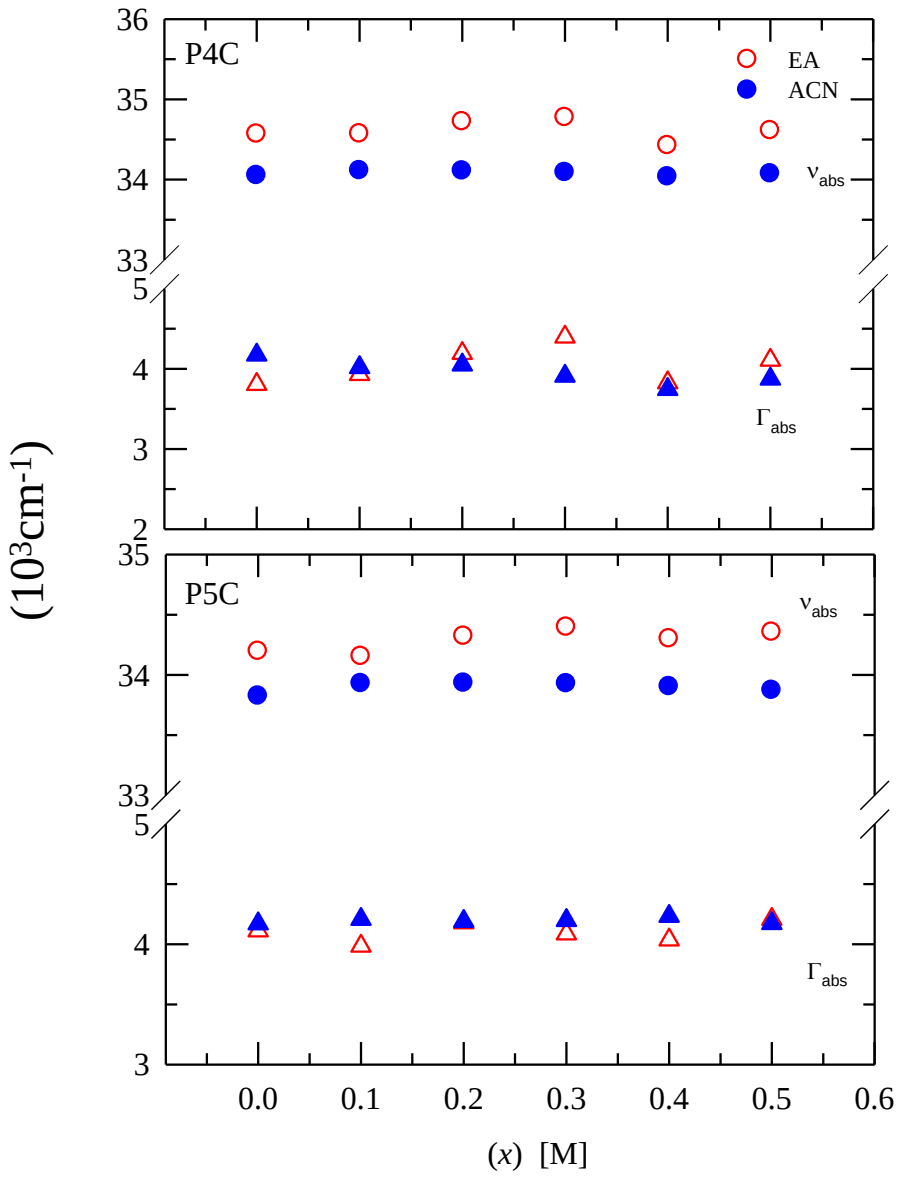

Figure 9.3: Mixed electrolyte concentration dependence of absorption frequencies (ν_{abs}) and line widths (full width at half-maxima, Γ_{abs}) of 4-(1-azetidinyl)benzonitrile (P4C) and 4-(1-pyrrolidinyl)benzonitrile (P5C) for the system [x $LiClO_4$ + (0.5- x)$NaClO_4$] in ethyl acetate (empty symbols) and acetonitrile (filled symbols) are shown. The circles represent ν_{abs} and the triangles are Γ_{abs}.

Figure 9.4

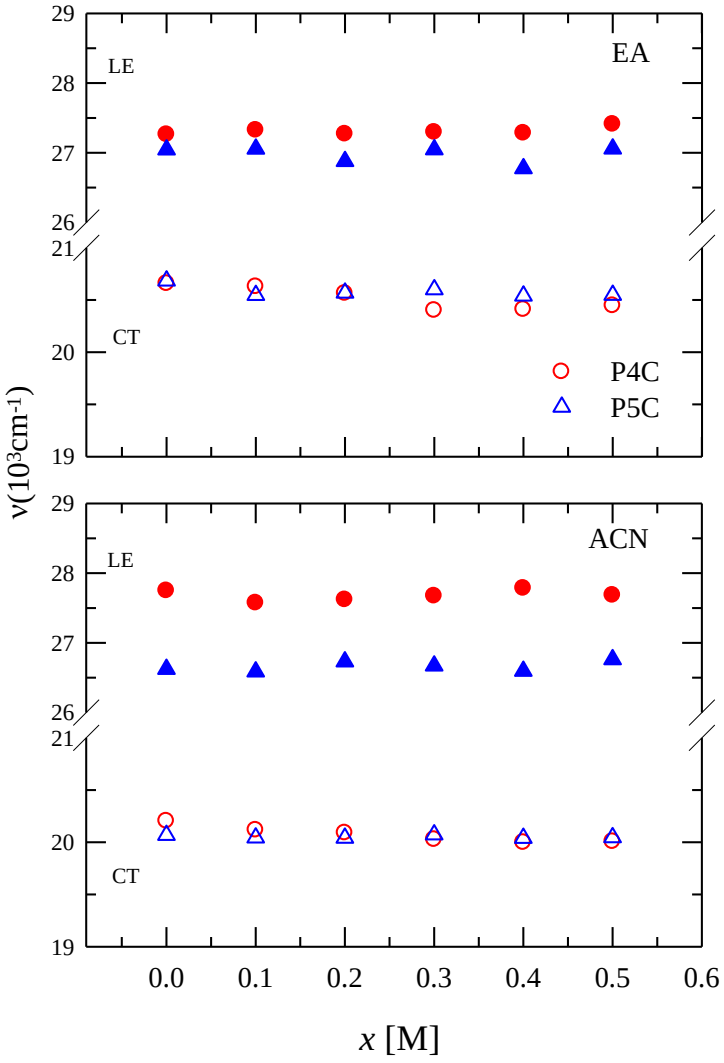

Figure 9.4: Mixed electrolyte concentration dependence of emission (LE and CT) frequencies (ν) of 4-(1-azetidinyl)benzonitrile (P4C) and 4-(1-pyrrolidinyl)benzonitrile (P5C) for the system [x $LiClO_4$ + (0.5- x)$NaClO_4$] in ethyl acetate (EA) and acetonitrile (ACN) are shown. The red circles represent P4C data and the blue triangles are P5C data. Filled symbols indicate frequencies for LE emission whereas CT emission frequencies are denoted by empty symbols.

Figure 9.5 shows the CT/LE ratio (α_{CT}/α_{LE}) for the system [x $LiClO_4$+ (0.5-x) $NaClO_4$] for the two TICT molecules in the solvents. The quantities α_{CT} and α_{LE} signifies the area under the spectral envelope of CT and LE bands respectively. A detailed method for the calculations of α_{CT}/α_{LE} is described elsewhere[65]. A polar environment that favours CT state will give a greater α_{CT}/α_{LE}. Hence the more polar acetonitrile shows a larger α_{CT}/α_{LE} compared to ethyl acetate for both P4C and P5C. Here we see a stronger response in a mixed electrolyte system for P5C than P4C. The ratio of the area under the CT and LE bands also gives the equilibrium constant (K_{eq}) which can be used to obtain the reaction free energy (ΔG_r) by the following equation:

$$\Delta G_r = -RT \ln K_{eq} = -RT \ln\left[\alpha_{CT}\nu_{LE}^{\ 3}/\alpha_{LE}\nu_{CT}^{\ 3}\right] \quad (9.1)$$

A plot showing the variation of $-\Delta G_r$ with the increase of [Li^+] is given in Figure 9.6. This figure essentially follows trends of Figure 9.5. The ($-\Delta G_r$) is larger in acetonitrile than ethylacetate indicating ease of reaction in a more polar medium. For P4C the reaction is unfavourable in ethylacetate. $LE \rightarrow CT$ reaction for P5C is favourable in both solvents. It is notable that the reaction free energies at the both the ends, i.e at 0.5M concentration of Na^+ and Li^+ are almost unchanged. The insensitivity of ΔG_r for TICT reactions with change in cation size of electrolyte has been previously noticed also[52].

Figure 9.5

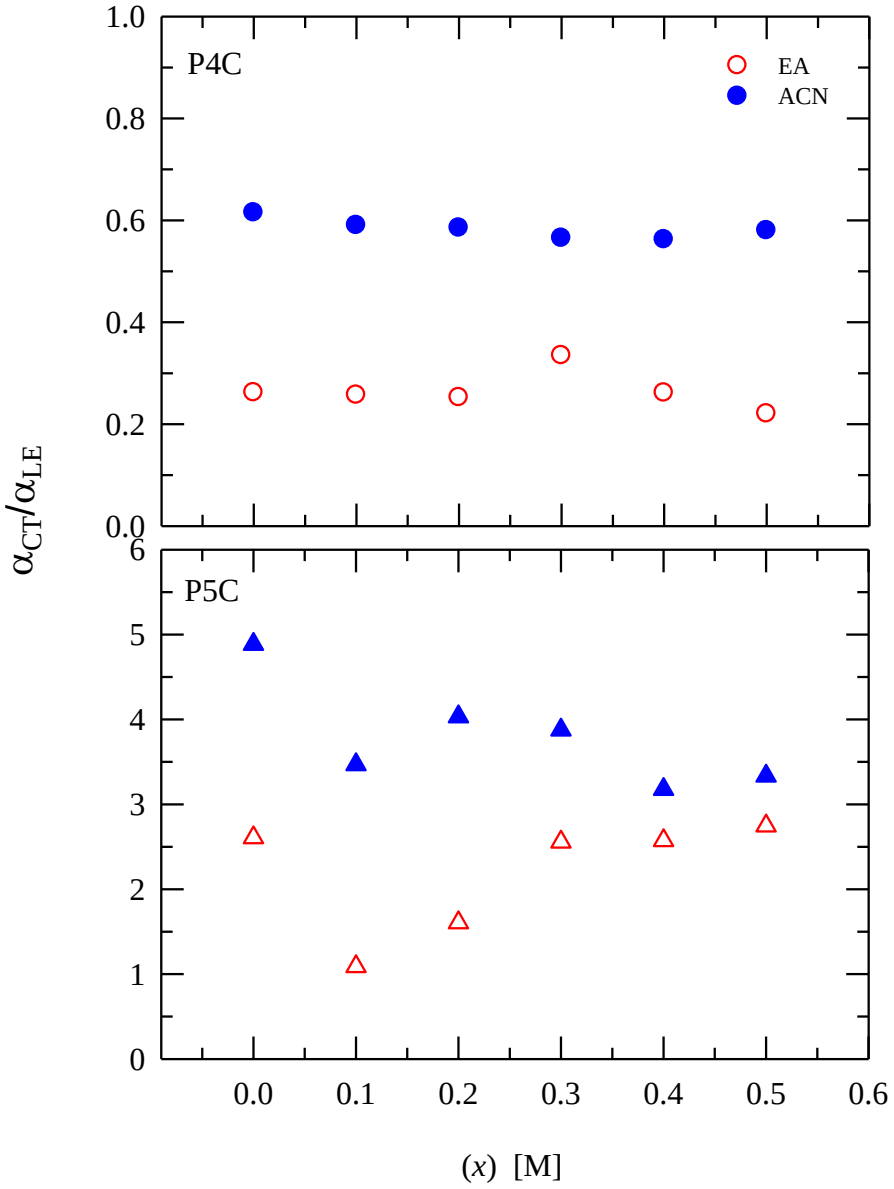

Figure 9.5: Mixed electrolyte concentration dependence (x) of formation of CT and LE population in ethyl acetate (EA, open symbols) and acetonitrile (ACN, filled symbols) of 4-(1-azetidinyl)benzonitrile (P4C) and 4-(1-pyrrolidinyl)benzonitrile (P5C) for the system [x $LiClO_4$ + (0.5- x)$NaClO_4$] are shown here. The ratio ($\alpha_{CT} / \alpha_{LE}$) between areas under the CT and LE bands are obtained after deconvolution as discussed in the text and in ref 5.) the upper panel represents data obtained for P4C and the lower panel shows that of P5C.
The uncertainty for CT band area is typically within (10%).

Figure 9.6

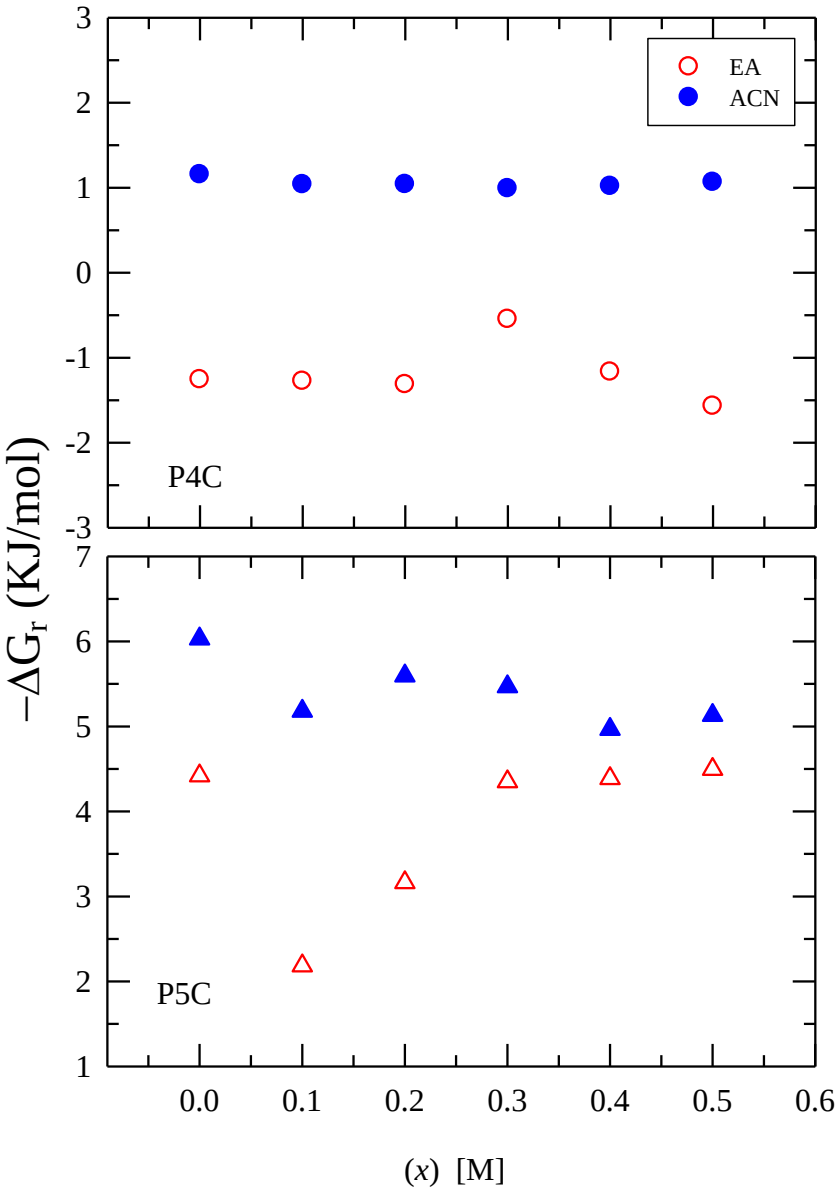

Figure 9.6: Mixed electrolyte concentration dependence (x) for the change in reaction free energy ($-\Delta G_r$) of $LE \rightarrow CT$ conversion for 4 -(1-azetidinyl)benzonitrile (P4C) and 4-(1-pyrrolidinyl)benzonitrile (P5C) for the system [x $LiClO_4$ + (0.5- x)$NaClO_4$] in ethyl acetate (EA, empty symbols) and acetonitrile (ACN, filled symbols) is shown. ΔG_r is obtained from the area ratio (shown in Figure 9.5) by using eq 9.1. Circles in upper panel denote $-\Delta G_r$ for P4C and triangles in the lower panel denotes $-\Delta G_r$ for P5C.

Table 9.1: Mixed electrolyte concentration dependence of fit parameters for the LE emission decays of P4C and P5C for the system [x $LiClO_4$ + (0.5- x)$NaClO_4$] in ethyl acetate (EA) and acetonitrile (ACN) are shown.

(a) P4C in Ethyl acetate + [x $LiClO_4$+ (0.5-x) $NaClO_4$]

x [M]	χ^2	a_1	τ_1 (ps)	a_2	τ_2 (ps)
0.0	1.03	0.69	532	0.31	1857
0.1	1.03	0.70	606	0.30	1723
0.2	1.02	0.73	596	0.27	1762
0.3	1.11	0.65	551	0.35	1477
0.4	1.02	0.61	562	0.39	1385
0.5	1.03	0.51	481	0.49	1324

(b) P5C in Ethyl acetate + [x $LiClO_4$+ (0.5-x) $NaClO_4$]

x [M]	χ^2	a_1	τ_1 (ps)	a_2	τ_2 (ps)
0.0	1.03	0.96	68	0.04	970
0.1	1.13	0.95	87	0.05	1030
0.2	1.02	0.90	94	0.10	1572
0.3	1.11	0.94	91	0.06	947
0.4	1.05	0.95	97	0.05	1129
0.5	1.03	0.95	62	0.05	901

(c) P4C in Acetonitrile + [x $LiClO_4$+ (0.5-x) $NaClO_4$]

x [M]	χ^2	a_1	τ_1 (ps)	a_2	τ_2 (ps)
0.0	1.13	0.94	202	0.06	1939
0.1	1.23	0.94	206	0.06	1759
0.2	1.04	0.91	203	0.09	1456
0.3	1.05	0.93	202	0.07	1418
0.4	1.01	0.92	224	0.08	1470
0.5	1.08	0.91	191	0.08	1208

(d) P5C in Acetonitrile + [x $LiClO_4$+ (0.5-x) $NaClO_4$]

x [M]	χ^2	a_1	τ_1 (ps)	a_2	τ_2 (ps)
0.0	1.13	0.94	73	0.06	1680.9
0.1	1.23	0.94	107	0.06	1442.7
0.2	1.04	0.91	123	0.09	1911.1
0.3	1.05	0.93	152	0.07	1120.5
0.4	1.01	0.92	159	0.08	1202.8
0.5	1.08	0.91	119	0.08	1074.7

9.3.2. Time Resolved Studies

Time resolved decays for P4C and P5C in [xLiClO$_4$+(0.5-x)NaClO$_4$]/acetonitrile and [xLiClO$_4$+(0.5-x)NaClO$_4$]/ethylacetate solutions with x=0.0 to 0.5 have been collected. The kinetic framework used here is that discussed in ref.5. Collected decays were found to best fit to bi-exponential function of time. Such a decay is plotted in Figure A34 along with the fit. The adjacent panel shows the residual which does not show any non-random pattern.[66] The goodness-of-fit parameter (χ^2) and the fitted values are shown in the figure along with the decays. Table 9.1 shows the fitted parameters for the LE decays of P4C and P5C in [x LiClO$_4$+ (0.5-x) NaClO$_4$] solutions of acetonitrile and ethyl acetate. Since the decays were found to be bi-exponentials, we can assert the decay kinetics of the $LE \rightarrow CT$ reaction of P4C and P5C (in acetonitrile and ethyl acetate under mixed electrolyte condition) to classical two state reversible reaction mechanism. This has earlier been formulated in the works of Maroncelli & co-workers[5]. Note that CT decays for the system were also collected for the system and they too were fitted to biexponential functions of time. The CT decays are not shown in the table to avoid complicacy. We will describe one such decay in details here. For x = 0.1, i.e. for [0.1 LiClO$_4$+ 0.4 NaClO$_4$] in ethyl acetate, P4C shows a CT decay (collected at 480nm) with a shorter time constant of 424ps as the rise component and a longer time constant of 2129ps ($\chi^2 = 1.17$). The corresponding LE decay (collected at 360nm) shows a fast component of 606ps (decay constant) which is similar to the rise component of the CT decay. No constraints were used for the fitting process. The likeness of the rise and decay time constants of CT and LE decays indicates that it is the reaction time for the $LE \rightarrow CT$ conversion. Fixing the rise time of the CT decay to the fast time constant of the LE decay yielded a longer time constant of 2201ps with $\chi^2 = 1.21$. Introduction of a third component did not produce better fits. Thus it is seen that mixed electrolytes shows similar biexponential kinetics as unielectrolytic systems[59] in solvents or pure solvents.[5,67].

The reaction time (τ_{rxn}) is considered to be the relatively shorter of the two time constants associated with the LE emission decays according to the convention used earlier in other works with these TICT molecules.[5,16,59,67] Figure 9.7 shows the variation of reaction time (τ_{rxn}) with 'x' for P4C and and P5C for [x LiClO$_4$+ (0.5-x) NaClO$_4$] in ethyl acetate and acetonitrile. The reaction time is seen to be the least in unielectrolyte regions and comparatively larger in the mixed electrolyte region. The addition of Li^+ to NaClO$_4$ – solvent

system increases the reaction time and remains to be high until all Na^+ are replaced by Li^+ (at *x*=0.5M). The pattern of reaction time can be correlated with variation of viscosity (Figure 9.1). The formation of complex aggregates[49,52,59,64] due to the presence of two types of cations causes greater friction to the reaction mode of TICT reaction. Moreover, the reaction time at Na^+ region is mostly similar to Li^+ region for P4C in both the solvents. P5C in ethyl acetate also shows similar reaction time for Na^+ and Li^+ region. However, in acetonitrile P5C strikingly show a considerable difference in reaction time for Na^+ and Li^+.

Figure 9.7

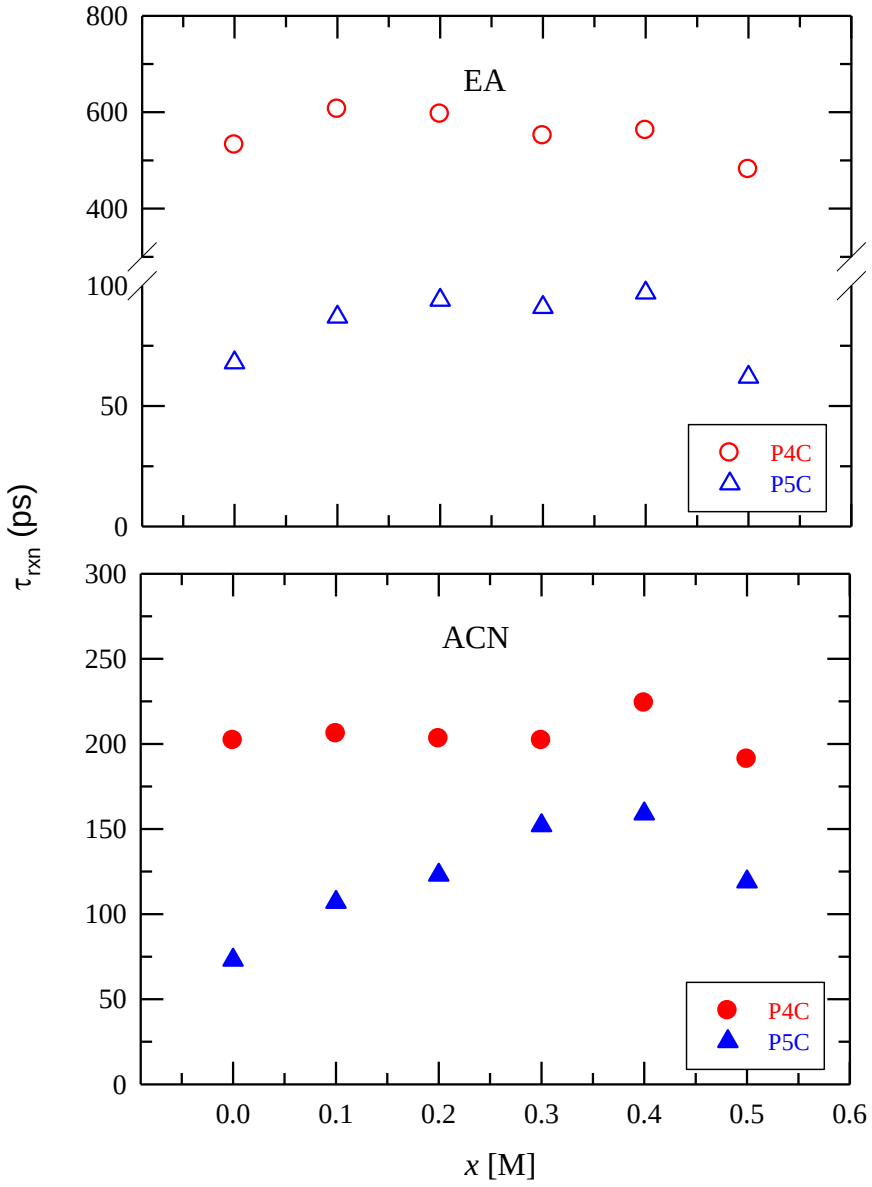

Figure 9.7: Mixed electrolyte concentration dependence (x) of reaction time (τ_{rxn}) of 4-(1-azetidinyl)benzonitrile (P4C) and 4-(1-pyrrolidinyl)benzonitrile P5C for the system [x $LiClO_4$ + (0.5- x)$NaClO_4$] in ethyl acetate (EA, upper panel) and acetonitrile (ACN, lower panel) is shown here. τ_{rxn} for P4C is represented by circles and for P5C by triangles.

Note that τ_{rxn} is the faster time constant as described in text and ref. 5.

Figure 9.8 shows the variation for the forward reaction (k_f) as given in the Scheme 2 and is defined according to earlier convention as follows:

$$k_f = \frac{1}{\tau_{rxn}\left(1 + K_{eq}^{-1}\right)} \qquad (2)$$

Where K_{eq} and τ_{rxn} are defined above.

The forward reaction rate shows similar trend with τ_{rxn} and viscosity for increasing 'x' for the mixed electrolyte system for [x $LiClO_4$+ (0.5-x) $NaClO_4$] in acetonitrile and ethyl acetate for P4C and P5C. k_f decreases as mixed electrolyte region is approached with x= 0.1 to 0.4M. Now if we compare our results to some of the earlier studies[5] it is revealed that through adding of electrolytes the $LE \rightarrow CT$ reaction is slowed down. Table B17 shows the comparison between k_f values obtained for pure solvent[5] and electrolyte solution for the TICT molecules P4C and P5C. Furthermore the forward rate is also slowed in presence of mixed electrolyte system rather than unielectrolyte system.

Figure 9.8

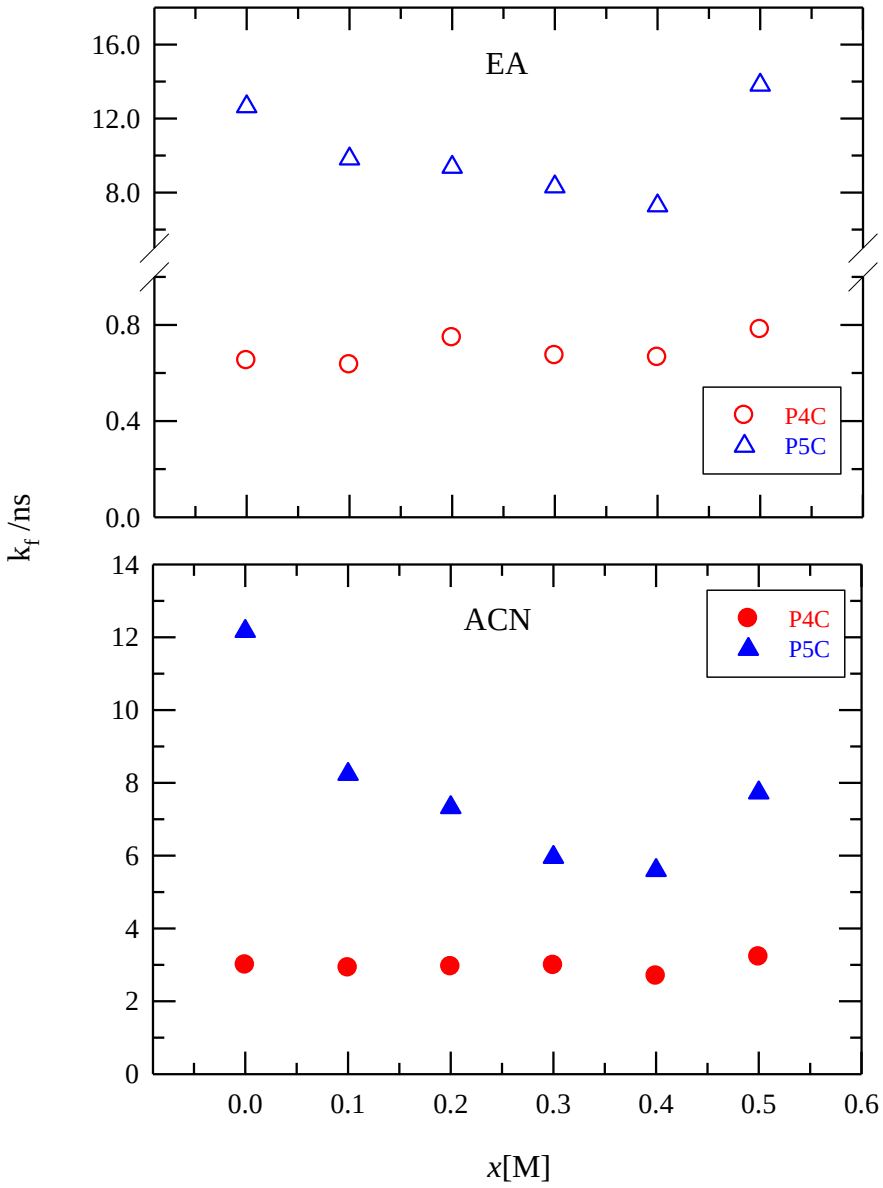

Figure 9.8: Mixed electrolyte concentration dependence (x) of rate of forward reaction (k_f) for $LE \rightarrow CT$ conversion of 4-(1-azetidinyl)benzonitrile (P4C) and 4-(1-pyrrolidinyl)benzonitrile P5C for the system [x $LiClO_4$ + (0.5- x)$NaClO_4$] in ethyl acetate (EA) and acetonitrile (ACN) is shown here. k_f for P4C is represented by circles and for P5C by triangles.

Note that k_f is calculated according to eq. 2 as per the convention of ref. 5.

9.4. Conclusion

The outcome of conducting the mixed electrolyte effect on the reaction rate of P4C and P5C in the two solvents has been quite interesting. In summary, conductivity and viscosity dependence of increasing fraction of '*x*' in the system [xLiClO$_4$+ (0.5-x)NaClO$_4$] in ethyl acetate has indicated a complex behaviour in the middle range where x=0.1 to 0.4M. The high conductivity and the high viscosity is a reflection of complex aggregation process nucleated by two types of cations. From the spectral envelopes, it is clear that P5C is more sensitive than P4C. Also, the CT bands of P5C are very strong in ethyl acetate as well as in acetonitrile. Absorption frequencies show a slight increase in the mid-range of '*x*' for P4C and P5C but are more sensitive in ethyl acetate solution than in acetonitrile. Emission form the CT state is greater in Na^+ rich solution than Li^+ which is guided by the charge/radius (z/r_{ion}) ratio of the cations. The ratio between the CT and LE bands (α_{CT}/α_{LE}) shows minimal change for P4C but P5C indicates strong dependence on '*x*' in ethyl acetate as well as in acetonitrile. α_{CT}/α_{LE} shows an increasing trend with more Na^+. This is also reflected in the change in free energy for the $LE \rightarrow CT$ conversion. The conversion is mostly unfavourable in ethylacetate for P4C whereas favourable for P5C. However, the variation of ($-\Delta G_r$) with '*x*' shows that the reaction is less favoured in presence of mixed electrolyte solution of acetonitrile and ethyl acetate. The variation of τ_{rxn} with '*x*' shows that larger time is required for the conversion in mixed electrolyte than in individual electrolyte solutions of ethyl acetate and acetonitrile. Finally, the rate of forward reaction (k_f) has been compared to show that the $LE \rightarrow CT$ conversion is slower for P5C in individual electrolyte solutions than in mixed electrolyte systems.

References

1. Grabowski, Z. R.; Rotkiewicz, K.; Rettig, W. *Chem. Rev.* **2003**, *103*, 3899.

2. Lippert, E.; Rettig, W.; Bonacickoutecky, V.; Heisel, F.; Miehe, J. A. *Adv. Chem. Phys.* **1987**, *68*, 1.

3. Techert, S.; Zachariasse, K. A. *J. Am. Chem. Soc.* **2004**, *126*, 5593.

4. Zachariasse, K. A.; Druzhinin, S. I.; Bosch, W.; Machinek, R. *J. Am. Chem. Soc.* **2004**, *126*, 1705.

5. Dahl, K.; Biswas, R.; Ito, N.; Maroncelli, M. *J. Phys. Chem. B* **2005**, *109*, 1563.

6. Parusel, A. B. J. *Chem. Phys. Lett.* **2001**, *340*, 531.

7. Rettig, W. *J. Luminesc.* **1981**, *26*, 21.

8. Zgierski, M. Z.; Lim, E. C. *Chem. Phys. Lett.* **2004**, *393*, 143.

9. Al-Hassan, K. A.; Rettig, W. *Chem. Phys. Lett.* **1986**, *126*, 273.

10. Rettig, W. *J. Phys. Chem.* **1982**, *86*, 1970.

11. Rettig, W. *J. Luminesc.* **1980**, *26*, 21.

12. Hynes, J. T., Simon, J. D. *Charge -Transfer Reactions and Solvation Dynamics in Ultrafast Dynamics of Chemical Systems*; Kluwer: Dodrecht, **1994**.

13. Van der zwan, G.; Hynes, J. T. *Chem. Phys.* **1991**, *152*, 169.

14. Barthel, J.; Buchner, R.; Eberspacher, P. N.; Munsterer, M.; Stauber, J.; Wurm, B. *J Mol Liq* **1998**, *78*, 83.

15. Chapman, C. F.; Maroncelli, M. *J Phys Chem-Us* **1991**, *95*, 9095.

16. Pradhan, T.; Gazi, H. A.; Biswas, R. *J. Chem. Phys.* **2009**, *131*, 054507.

17. Bart, E.; Huppert, D. *Chem. Phys. Lett.* **1992**, *195*, 37.

18. Bart, E.; Meltsin, A.; Huppert, D. *Chem. Phys. Lett.* **1992**, *200*, 592.

19. Huppert, D.; Ittah, V.; Kosower, E. M. *Chem. Phys. Lett.* **1989**, *159*, 267.

20. Marcus, Y.; Hefter, G. *Chem. Rev.* **2004**, *104*, 3405.

21. Ittah, V.; Huppert, D. *Chem. Phys. Lett.* **1990**, *173*, 496.

22. Barthel, J.; Deser, R. *J. Solution Chem.* **1994**, *23*, 1133.

23. Barthel, J.; Deser, R. *J. Solution Chem.* **1994**, *23*, 1133.

24. Barthel, J.; Hetzenauer, H.; Buchner, R. *Ber. Bunsen-Ges. Phys. Chem.* **1992**, *96*, 1424.

25. Barthel, J.; Kleebauer, M.; Buchner, R. *J. Solution Chem.* **1995**, *24*, 1.

26. Barthel, J.; Wachter, R.; Gores, H. J.; In Modern Aspects, n.; Bockris, J.; O, M. *Plenum: New York* **1979**, *13*, 1.

27. Buchner, R.; Chen, T.; Hefter, G. *J. Phys. Chem. B* **2004**, *108*, 2365.

28. Buchner, R.; Hefter, G. T.; May, P. M. *J. Phys. Chem. A* **1999**, *103*, 1.

29. Cachet, H.; Cyrot, A.; Fakir, M.; Lestrade, J. C. *J. Phys. Chem.* **1979**, *83*, 2419.

30. Cha, J. N.; Cheong, B. S.; Cho, H. G. *J. Phys. Chem. A* **2001**, *105*, 1789.

31. Chen, T.; Hefter, G.; Buchner, R. *J. Solution Chem.* **2005**, *34*, 1045.

32. Delsignore, M.; Farber, H.; Petrucci, S. *J. Phys. Chem.* **1985**, *89*, 4968.

33. Delsignore, M.; Farber, H.; Petrucci, S. *J. Phys. Chem.* **1986**, *90*, 66.

34. Eberspacher, P.; Wismeth, E.; Buchner, R.; Barthel, J. *J. Mol. Liq.* **2006**, *129*, 3.

35. Fawcett, W. R.; Liu, G. *J. Phys. Chem.* **1992**, *96*, 4231.

36. Fuoss, R. M.; Kraus, C. A. *J. Am. Chem. Soc.* **1933**, *55*, 2387.

37. Fuoss, R. M.; Kraus, C. A. *J. Am. Chem. Soc.* **1933**, *55*, 1019.

38. Kalugin, O. N.; Panchenko, V. G.; V'Yunnik, I. N. *Russ. J. Phys. Chem.* **2005**, *79*, 629.

39. Loring, J. S.; Fawcett, W. R. *J. Phys. Chem. A* **1999**, *103*, 3608.

40. Mollner, A. K.; Brooksby, P. A.; Loring, J. S.; Bako, I.; Palinkas, G.; Fawcett, W. R. *J. Phys. Chem. A* **2004**, *108*, 3344.

41. Petrucci, S.; Eyring, M. *J. Phys. Chem.* **1991**, *95*, 1731.

42. Richardi, J.; Fries, P. H.; Krienke, H. *J. Chem. Phys.* **1998**, *108*, 4079.

43. Rudolph, W. W.; Irmer, G.; Hefter, G. T. *Phys. Chem. Chem. Phys.* **2003**, *5*, 5253.

44. Salomon, M.; Slane, S.; Plichta, E.; Uchiyama, M. C. *J. Solution Chem.* **1989**, *18*, 977.

45. Salomon, M.; Uchiyama, M.; Xu, M.; Petrucci, S. *J. Phys. Chem.* **1989**, *93*, 4374.

46. Salomon, M.; Uchiyama, M. C. *J. Solution Chem.* **1987**, *16*, 21.

47. Spanberg, D.; Hermansson, K. *Chem. Phys.* **2004**, *300*, 165.

48. Bart, E.; Huppert, D. *Chem. Phys. Lett.* **1992**, *195*, 37.

49. Chapman, C. F.; Maroncelli, M. *J. Phys. Chem.* **1991**, *95*, 9095.

50. Huppert, D.; Ittah, V.; Kosower, M. *Chem. Phys. Lett.* **1989**, *159*, 267.

51. Ittah, V.; Huppert, D. *Chem. Phys. Lett.* **1990**, *173*, 496.

52. Pradhan, T.; Biswas, R. *J. Phys. Chem. A* **2007**, *111*, 11514.

53. Hsu, H.L.; Wu, Y.C.; Lee, L.S. *J. Chem. Eng. Data* **2003**, *48*, 514.

54. Hao, L.; Leaist, D. G. *J. Solution Chem.* **1995**, *24*, 523.

55. Kumar, A. *J. Phys. Chem. B* **2005**, *109*, 11743.

56. French, R. J.; Wells, J. B. *The Journal of General Physiology* **1977**, *70*, 707.

57. Korn, S.; Ikeda *Science* **1995**, *269*, 410.

58. Riddick, J. A. B., W. B.; Sakano, T. K. *Organic Solvents*; Wiley: New York, 1986.

59. Pradhan, T.; Biswas, R. *J. Phys. Chem. A* **2007**, *111*, 11524.

60. Horng, M. L.; Gardecki, J. A.; Papazyan, A.; Maroncelli, M. *J. Phys. Chem.* **1995**, *99*, 17311.

61. Biswas, R.; Lewis, J. E.; Maroncelli, M. *Chem. Phys. Lett.* **1999**, *310*, 485.

62. Lewis, J. E.; Biswas, R.; Robinson, A. G.; Maroncelli, M. *J. Phys. Chem. B* **2001**, *105*, 3306.

63. Mukherjee, K.; Das, A.; Choudhury, S; Barman, A; Biswas, R.; *J. Phys. Chem. B* **2015**, *xxxx*, xxxx.

64. Pocker, Y.; Ciula, J. C. *J. Am. Chem. Soc.* **1989**, *111*, 4728.

65. Dahl, K.; Biswas, R.; Ito, N.; Maroncelli, M. *J. Phys. Chem. B* **2005**, *109*, 1563.

66. Bevington, P. R. *Data Reduction and Error Analysis for the Physical Sciences*; McGraw-Hill New York, 1969.

67. Pradhan, T.; Ghoshal, P.; Biswas, R. *J. Phys. Chem. A* **2008**, *112*, 915.

Chapter 10

Conclusions and Future Problems

The main objective in this thesis has been to investigate whether longer-lived heterogeneity is always present in room temperature deep eutectic solvents (DESs) made of components with much higher individual melting points. Our study that included several ionic and non-ionic deep eutectics have revealed that heterogeneity is not a generic feature of DESs; it's rather a reflection of a specific type of complexation or inter-species H-bonding which can even be removed by the addition of another compound competing for complexation via H-bonding. In addition, charge transfer reactions have been studied in these systems to understand how reactions are modified in such complex media. While time-resolved fluorescence technique has been employed to look at the viscosity coupling of relaxation rates and signatures for dynamic heterogeneity, steady state spectroscopic measurements have been carried out to gain knowledge about spatial heterogeneity. Supporting measurements using terahertz dielectric relaxation spectroscopy and Fourier-transformed infra red spectroscopy have also been carried out. Since each of the chapters contain conclusions separately, no separate chapter has been dedicated for over-all conclusion. Rather, a list of interesting and relevant problems have been discussed below which may be studied in future.

10.1. Structure and Dynamics of Deep Eutectic Solvents

Deep eutectic solvents (DES)[1,2] are utilised in various industrial applications[3,4] due to their exquisite solvent properties.[5,6] Although we have explored structural and dynamical aspects of DESs to some extent here, there are still many areas unexplored. The systems of urea-DESs are found to be associated with comparatively faster time scales of relaxation[7]. Using other sophisticated spectral techniques (for e.g. Kerr spectroscopy) and wide-window dielectric relaxation spectroscopy , one can better characterize the faster relaxation timescales and interactions in these media. Detailed investigation by all-atom molecular dynamics simulation can also reveal the correlation between the spatial and dynamical heterogeneities. Most

importantly, X-ray or neutron scattering measurements should be carried out to reveal the origin of the spatial heterogeneity of these systems.

10.2. DESs made of electrolyte and choline chloride

We have dealt with only a few combinations of the DESs of choline chloride in chapters 6 and 7. There are numerous other combinations of other hydrogen bond acceptors and hydrogen bond donors that are used in various industrial solvents.[3,5] The study of spatial and temporal heterogeneity can be extended to these systems in order to find about the interactions that renders them the property of "glassy" liquids.[8,9] Also, we have not conducted any studies on Choline chloride + hydrated metal salts/electrolyte[4] (e.g. $SnCl_2$, $ZnCl_2$, $CrCl_3.6H_2O$) systems. These systems have tremendous utility in electrochemical deposition[10]. For example, using these DESs it has been shown that chromium can be electrodeposited efficiently to yield crack-free surfaces.[10]

10.3. Transport properties of electrolytes in DESs

Development of rechargeable batteries with high energy density has been an area of extensive research over the years.[11,12] Lithium metal anodes are ideally suited as resources as it gives a 5-fold gain in cell energy density[13]. In spite of this, these anodes cannot be used extensively as conventional organic electrolytes are unstable against these, and lead to both poor cyclability and potentially hazardous lithium dendrite formation[14]. At this juncture, Ionic Liquids (ILs) emerged as an alternative that solvate Li-salts and form stable solid−electrolyte interfaces.[15,16] ILs containing bis(trifluoromethanesufonyl)imide ([TFSI]) anion or the bis(fluorosufonyl)imide ([FSI]) anion are found to be amongst the most promising candidates for stable battery generation[17]. While transport properties of neat ionic liquids have been characterized frequently,[18,19] similar studies of DESs containing Li-salts lack proper investigation. Studies of bulk transport properties can provide good estimation for electrochemical performance, with low viscosity and high diffusion being key to high discharge rates.[13] Whereas solvation experiments can give information[20] about the average

environment of Li^+ , MD simulations[21] can be suitably used to extract molecular level information and guidance for smarter use of DESs.[22-25]

10.4. Deep eutectics of Guanidium salts and Urea

The denaturation property of urea by disrupting the noncovalent bonds in the proteins is long known[26]. Ionic guanidine hydrochloride (GuHCl) and guanidine thiocyanate (GuSCN) are also among such denaturating agents.[27,28] Urea forms stable liquids with GuHCl (58°C with 67% Urea) and GuSCN (42°C with 60% Urea)[26]. These moisture-free ionic DESs allow solubility of cytochrome c and bovine serum albumin and have high potential to be used for long-term storage of proteins.[26,29,30]

10.5. Molecular rotors in DESs

Thioflavin-T (ThT), which is a benzothiazole-based cationic dye,[31] is not so emissive in water[32,33] but shows strong emission on binding to amyloid fibrils[34-36]. This is why it is often used as an extrinsic sensor to identify diseases like Alzheimer's disease and Parkinson's.[37,38] ThT is also a molecular rotor by it's structure[39,40]. It undergoes rotation around the single bond connecting the benzothiazole ring and N,N-dimethylaniline which is also responsible for non-radiative decay,[40] leading to low emission yield. This C-C bond rotation is significantly affected by viscosity.[33,41] Molten mixture is a perfect solvent for providing a wide tuneable viscosity range that can regulate the bond rotation and reflect in the emission data.

References

1. Abbott, A. P.; Capper, G.; Davies, D. L.; Rasheed, R. K.; Tambyrajah, V. *Chem. Commun.* **2003**, 70.

2. Abbott, A. P.; Boothby, D.; Capper, G.; Davies, D. L.; Rasheed, R. K. *J. Am. Chem. Soc.* **2004**, *126*, 9142.

3. Smith, E. L.; Abbott, A. P.; Ryder, K. S. *Chem Rev* **2014**, *114*, 11060.

4. Abbott, A. P.; Capper, G.; Davies, D. L.; Rasheed, R. K. *Chem. Eur. J.* **2004**, *10*, 3769.

5. Francisco, M.; van den Bruinhorst, A.; Kroon, M. C. *Angew. Chem., Int. Ed.* **2013**, *52*, 3074.

6. Francisco, M.; Van den Bruinhorst, A.; Kroon, M. C. *Green Chem.* **2012**, *14*, 2153.

7. Das, A.; Das, S.; Biswas, R. *J. Chem. Phys.* **2015**, *142*, 034505.

8. Ediger, M. D. *Annu. Rev. Phys. Chem.* **2000**, *51*, 99.

9. Sillescu, H. *J. Non-Cryst. Solids* **1999**, *243*, 81.

10. Abbott, A. P.; Capper, G.; Davies, D. L.; Rasheed, R. *Inorg. Chem.* **2004**, *43*, 3447.

11. Armand, M.; Tarascon, J. M. *Nature* **2008,**, *451*, 652.

12. Scrosati, B.; Garche, J. *J. Power Sources* **2010**, *195*, 2419.

13. Haskins, J. B.; Bennett, W. R.; Wu, J. J.; Hernandez, D. M.; Borodin, O.; Monk, J. D.; Bauschlicher, J. C. W.; Lawson, J. W. *J. Phys. Chem. B* **2014**, *118*, 11295.

14. Ellis, B. L.; Lee, K. T.; Nazar, L. F. *Chem. Mater.* **2010**, *22*, 691.

15. Xu, J.; Yang, J.; NuLi, Y.; Wang, J.; Zhang, Z. *J. Power Sources* **2006**, *160*, 621.

16. Best, A. S.; Bhatt, A. I.; Hollenkamp, A. F. *J. Electrochem. Soc.* **2010**, *157*, A903.

17. Matsumoto, H.; Sakaebe, H.; Tatsumi, K.; Kikuta, M.; Ishiko, E.; Kono, M. *J. Power Sources* **2006**, *160*, 1308.

18. Tokuda, H.; Hayamizu, K.; Ishii, K.; Abu Bin Hasan Susan, M.; Watanabe, M. *J. Phys. Chem. B* **2004**, *108*, 16593.

19. Borodin, O.; Gorecki, W.; Smith, G. D.; Armand, M. *J. Phys. Chem. B* **2010**, *114*, 6786.

20. Fujii, K.; Hamano, H.; Doi, H.; Song, X.; Tsuzuki, S.; Hayamizu, K.; Seki, S.; Kameda, Y.; Dokko, K.; Watanabe, M. e. a. *J.Phys. Chem. C* **2013**, *117*, 19314.

21. Liu, H.; Maginn, E.; Visser, A. E.; Bridges, N. J.; Fox, E. B. *Ind. Eng. Chem. Res.* **2012**, *51*, 7242.

22. Berchiesi, G. *J. Mol. Liq.* **1999**, *83*, 271.

23. Berchiesi, G.; Rafaiani, G.; Vitali, G.; Farhat, F. *J. Therm. Anal.* **1995**, *44*, 1313.

24. Guchhait, B.; Daschakraborty, S.; Biswas, R. *J. Chem. Phys.* **2012**, *136*, 174503.

25. Guchhait, B.; Gazi, H. A.; Kashyap, H. K.; Biswas, R. *J. Phys. Chem. B* **2010**, *114*, 5066.

26. Parnica, J.; Antalik, M. *J. Mol. Liq.* **2014**, *197*, 23.

27. Privalov, P. L. In *Adv. Protein Chem.*; C.B. Anfinsen, J. T. E., Frederic, M. R., Eds.; Academic Press: 1979; Vol. Volume 33, p 167.

28. Pace, C. N. In *Methods Enzymol.*; C. H. W. Hirs, S. N. T., Ed.; Academic Press: 1986; Vol. Volume 131, p 266.

29. Esquembre, R.; Sanz, J. M.; Wall, J. G.; Monte, F. d.; Mateo, C. R.; Ferrer, M. L. *Phys. Chem. Chem. Phys.* **2013**, *15*, 11248.

30. Mann, J. P.; McCluskey, A.; Atkin, R. *Green Chem* **2009**, *11*, 785.

31. Singh, P. K.; Kumbhakar, M.; Pal, H.; S. Nath *J. Phys. Chem. B* **2010**, *114*, 2541.

32. Maskevich, A. A.; Stsiapura, V. I.; Kuzmitsky, V. A.; Kuznetsova, I. M.; Povarova, O. I.; Uversky, V. N.; Turoverov, K. K. *J. Proteome Res.* **2007**, *6*, 1392.

33. Singh, P. K.; Kumbhakar, M.; Pal, H.; Nath, S. *J. Phys.Chem. B* **2009**, *113*, 8532.

34. Chiti, F.; Dobson, C. M. **2006**, *75*, 333.

35. Gestwicki, J. E.; Crabtree, G. R.; Graef, I. A. *Science* **2004**, *306*, 865.

36. Ban, T.; Yamaguchi, K.; Goto, Y. *Acc. Chem. Res.* **2006**, *39*, 663.

37. Mishra, R.; Winter, R. *Angew. Chem., Int. Ed.* **2008**, *47*, 6518.

38. Gilead, S.; Gazit, E. *Angew. Chem., Int. Ed.* **2004**, *43*, 4041.

39. Singh, P. K.; Kumbhakar, M.; Pal, H.; Nath, S. *Phys. Chem. Chem. Phys.* **2011**, *13*, 8008.

40. Srivastava, A.; Singh, P. K.; Kumbhakar, M.; Mukherjee, T.; Chattopadyay, S.; Pal, H.; Nath, S. *Chem.-Eur. J.* **2010**, *16*, 9257.

41. Kumar, S.; Singh, A. K.; Krishnamoorthy, G.; Swaminathan, R. *J. Fluoresc.* **2008**, *18*, 1199.

Appendix A

Figure A1

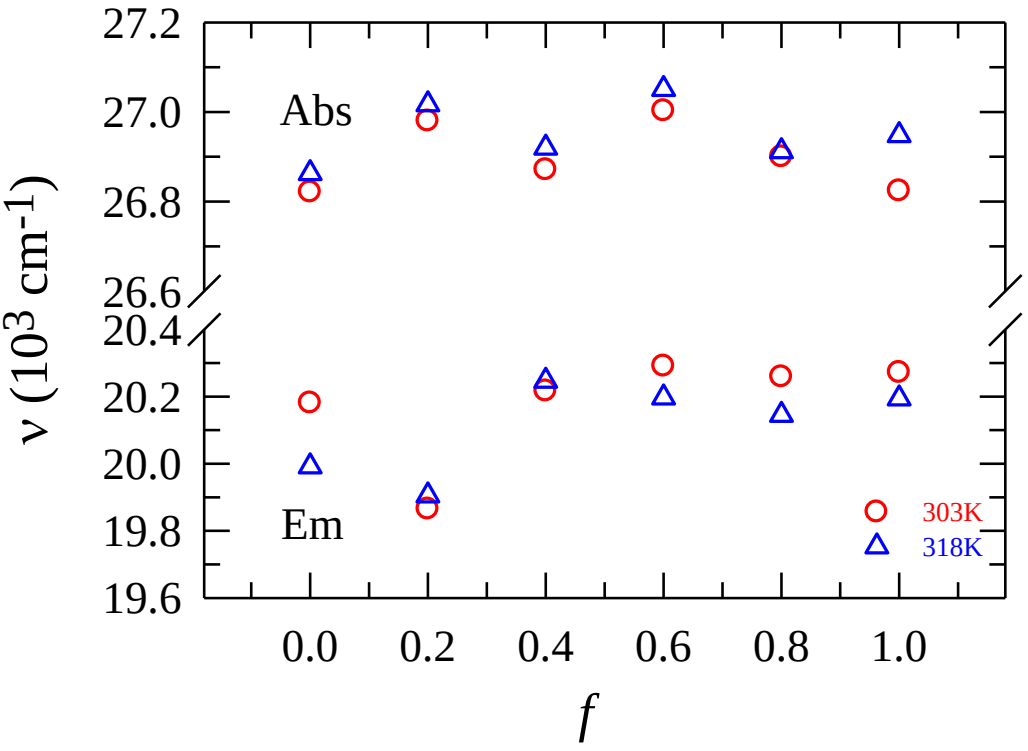

Figure A1: Br^- ion concentration dependence (f) of absorption and emission frequencies (ν) of DTN in $0.78CH_3CONH_2$+ $0.22\{f$LiBr+ $(1-f)LiNO_3\}$ at 303K and 318K (color coded).

Figure A2

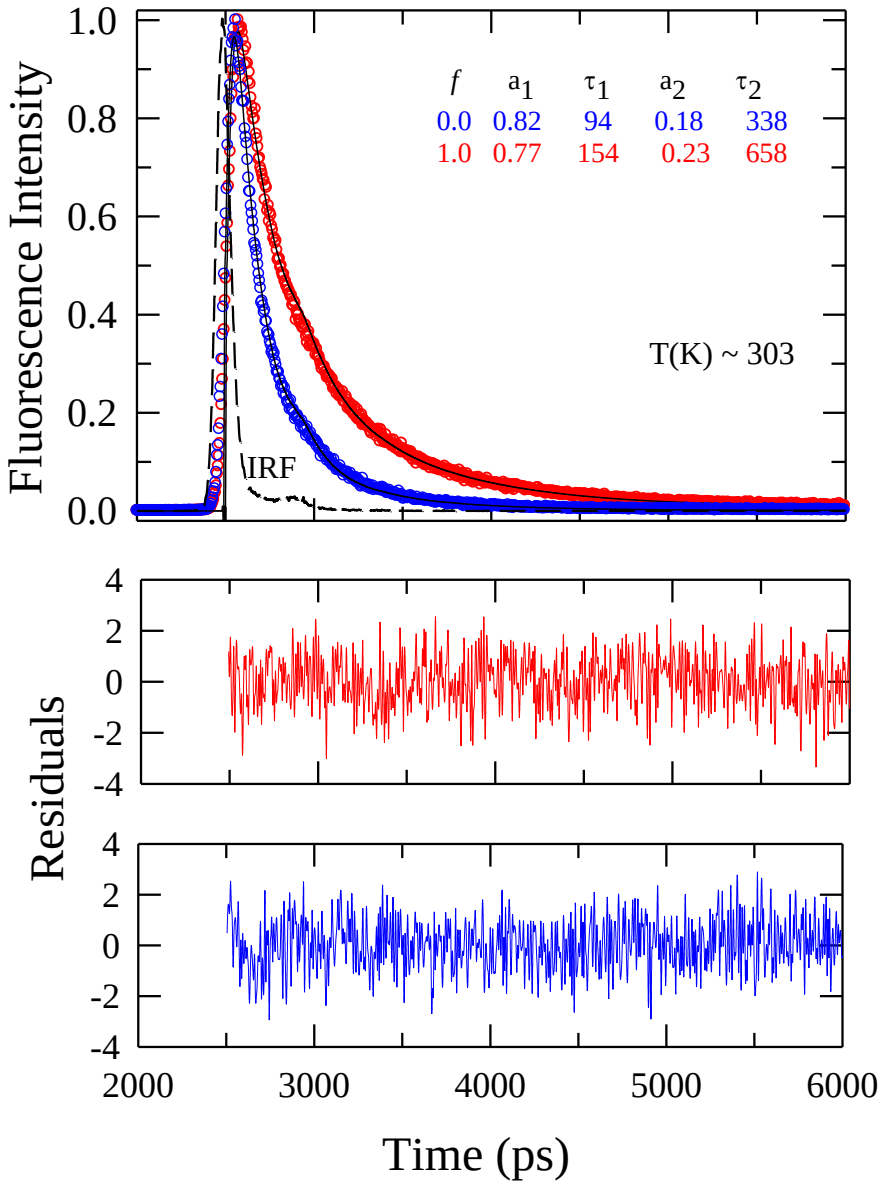

Figure A2: Representative magic angle fluorescence intensity decays collected at the peak wavelengths of the corresponding steady state emission spectra. The circles indicate experimental data and the solid lines are the fits through them. Instrument response function (IRF) is also shown in the same figure (dashed lines). The fitting parameters (time constants are in picoseconds) are shown in the inset. The respective

residuals are also shown (lower panels). The goodness- of- fit parameters are $\chi^2 = 1.07$ and $\chi^2 = 1.20$ for *f*= 0.0 and *f*= 1.0, respectively.

Figure A3

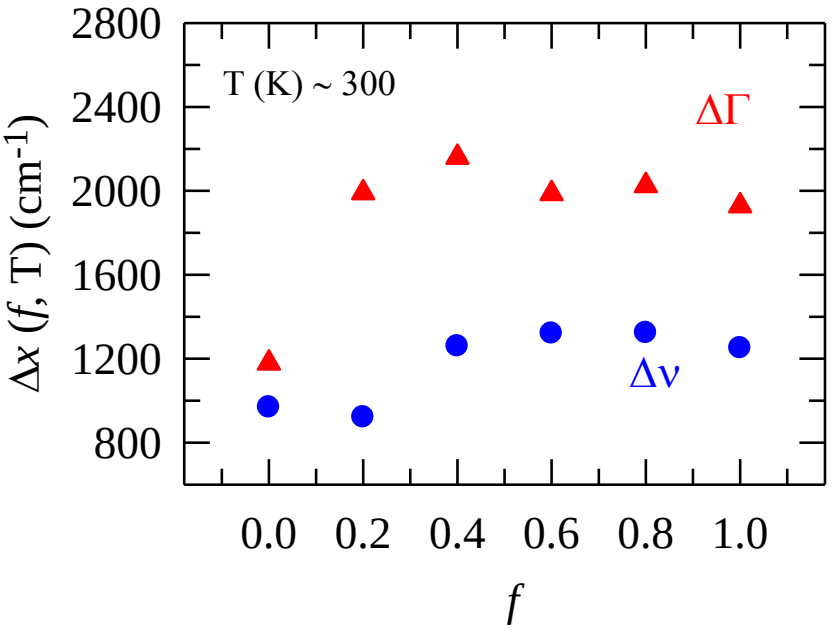

Figure A3: Composition dependence of the total differences (Δx = Δν, ΔΓ) in frequencies and width is shown (color coded) at 303K. Δx (*f*, T) = x(*f*, T, $\lambda_{exc,b}$)- x(*f*, T, $\lambda_{exc,r}$), where $\lambda_{exc,b}$ is the shortest (blue) and $\lambda_{exc,r}$ is the longest (red) wavelengths of excitation.

Figure A4

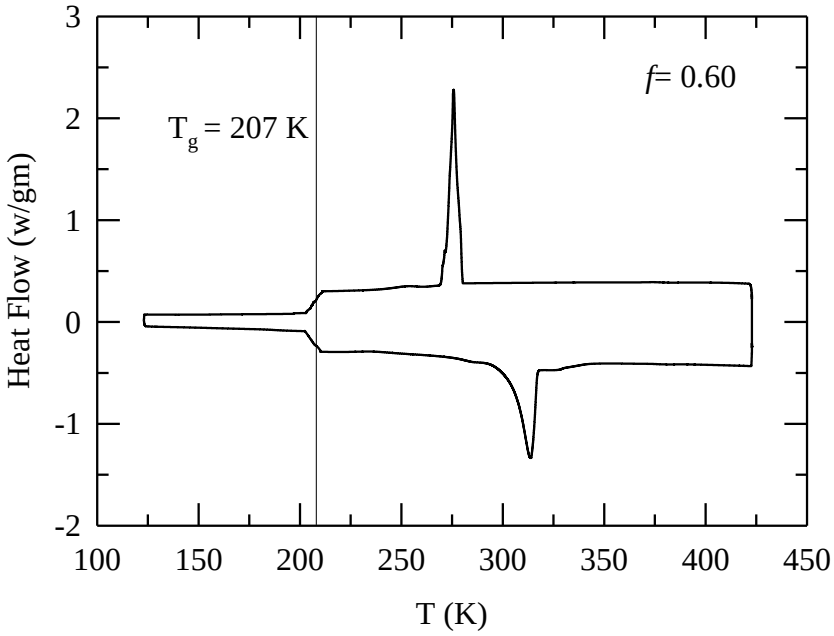

Figure A4: Differential scanning calorimetric trace for [*f*CH_3CONH_2+ (1-*f*)NH_2CONH_2] at *f*=0.6. The glass transition temperature (T_g) is indicated by the vertical line.

Figure A5

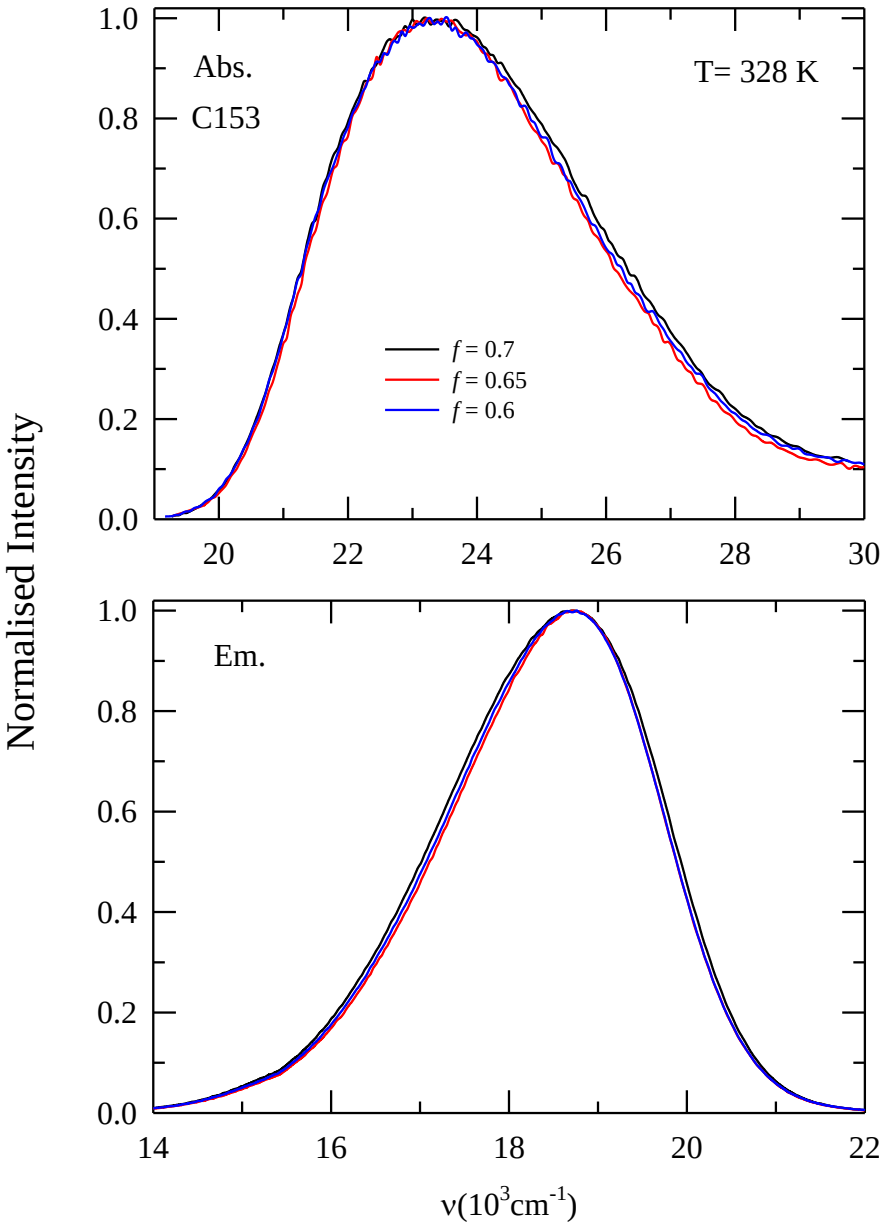

Figure A5: Representative absorption and emission spectra of C153 in [*f* CH_3CONH_2+ (1-*f*) NH_2CONH_2] at 328K at different acetamide mole fractions (*f*).

Figure A6

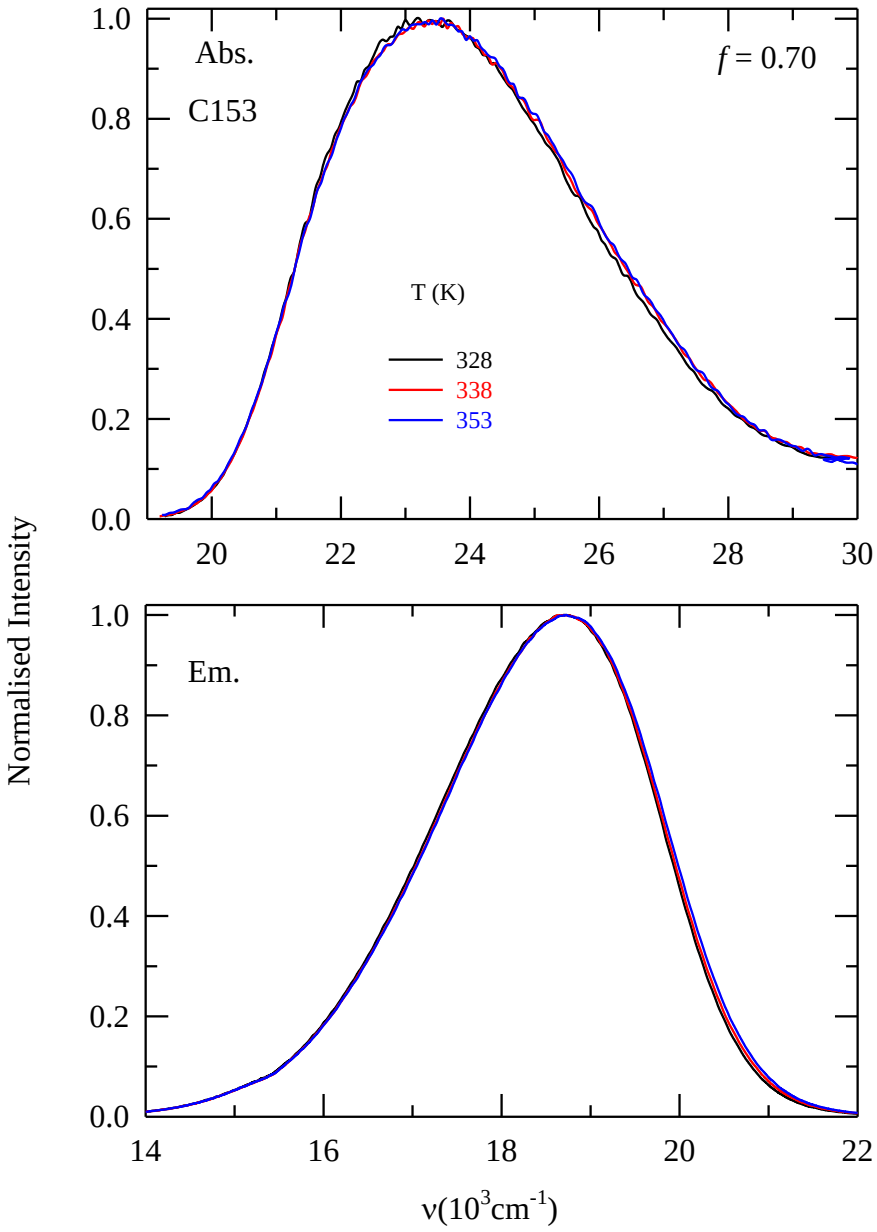

Figure A6: Representative absorption and emission spectra of C153 in [*f* CH_3CONH_2+ (1-*f*) NH_2CONH_2] at *f*=0.70 at different temperatures.

Figure A7

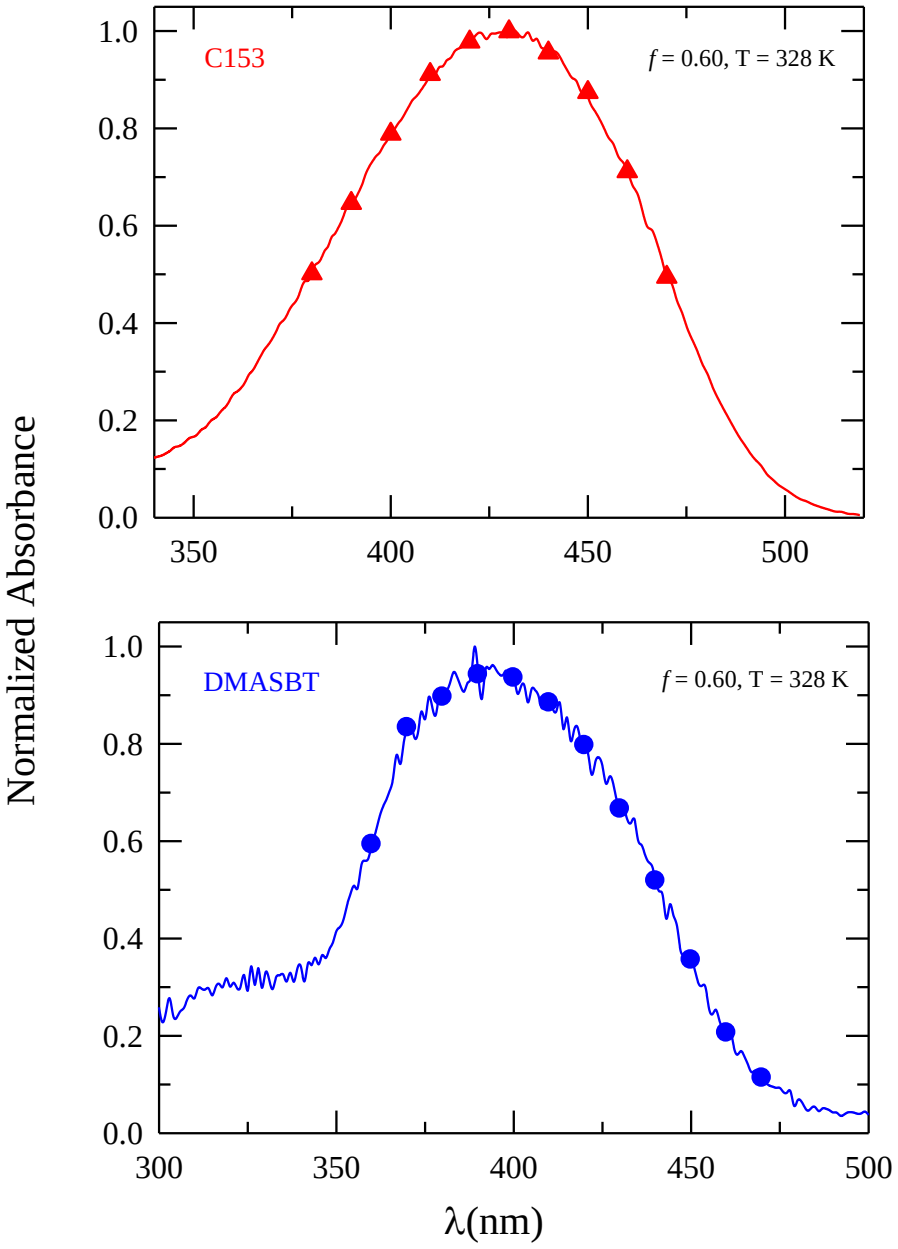

Figure A7: Absorption spectra of C153 and DMASBT in [*f*CH_3CONH_2+ (1-*f*)NH_2CONH_2] at *f*=0.60 at 328 K. Chosen excitation wavelengths are shown by bullets for C153 (red, triangle, upper panel) and DMASBT (blue, circles, lower panel).

Figure A8

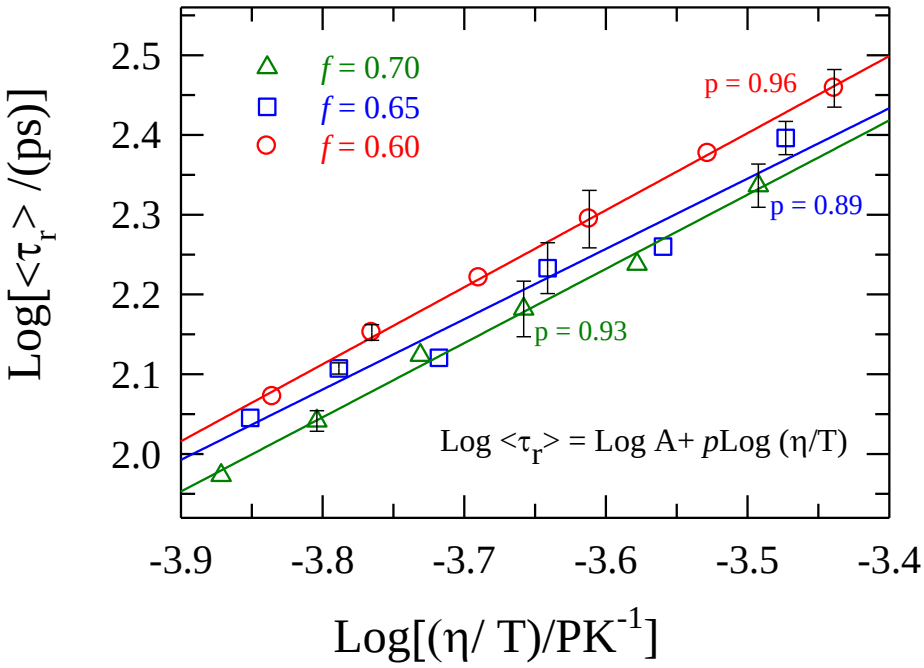

Figure A8: Composition dependence (*f*) of the fraction power, *p*, obtained via fit of the measured rotation times for C153 in [*f*CH_3CONH_2+ (1-*f*)NH_2CONH_2] deep eutectics. While measured data are shown by geometrical symbols, fits through them are by solid lines.

Figure A9

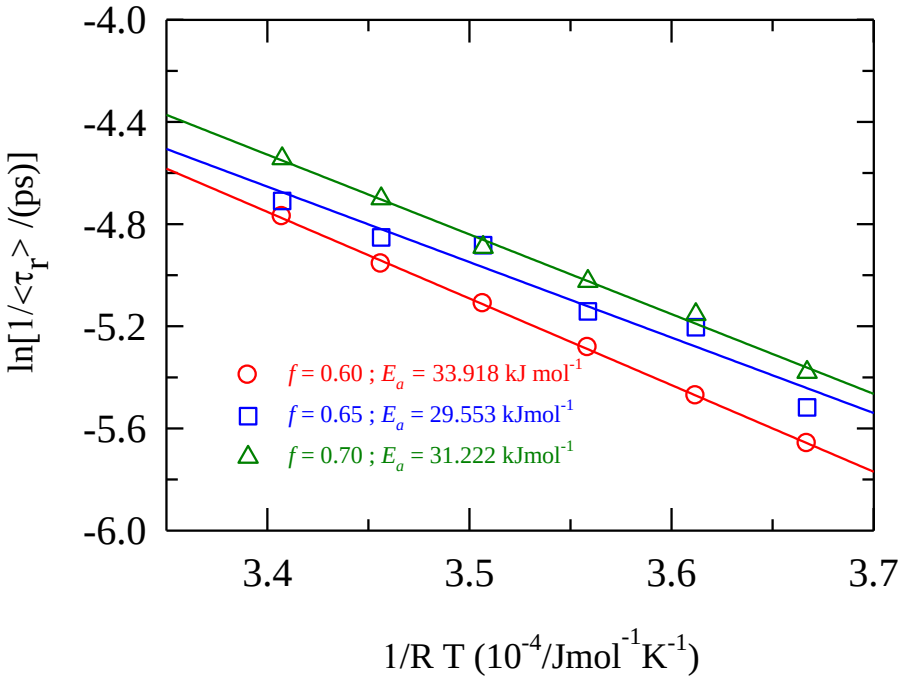

Figure A9: Arrhenius plot of $\ln\left(1/\langle\tau_r\rangle\right)$ versus $1/RT$ for C153 rotation times in [*f*CH_3CONH_2+ (1-*f*)NH_2CONH_2] deep eutectics. Solid lines represent fit through the respective data sets. Composition dependent activation energies (E_a) obtained from fits are shown in the inset.

Figure A10

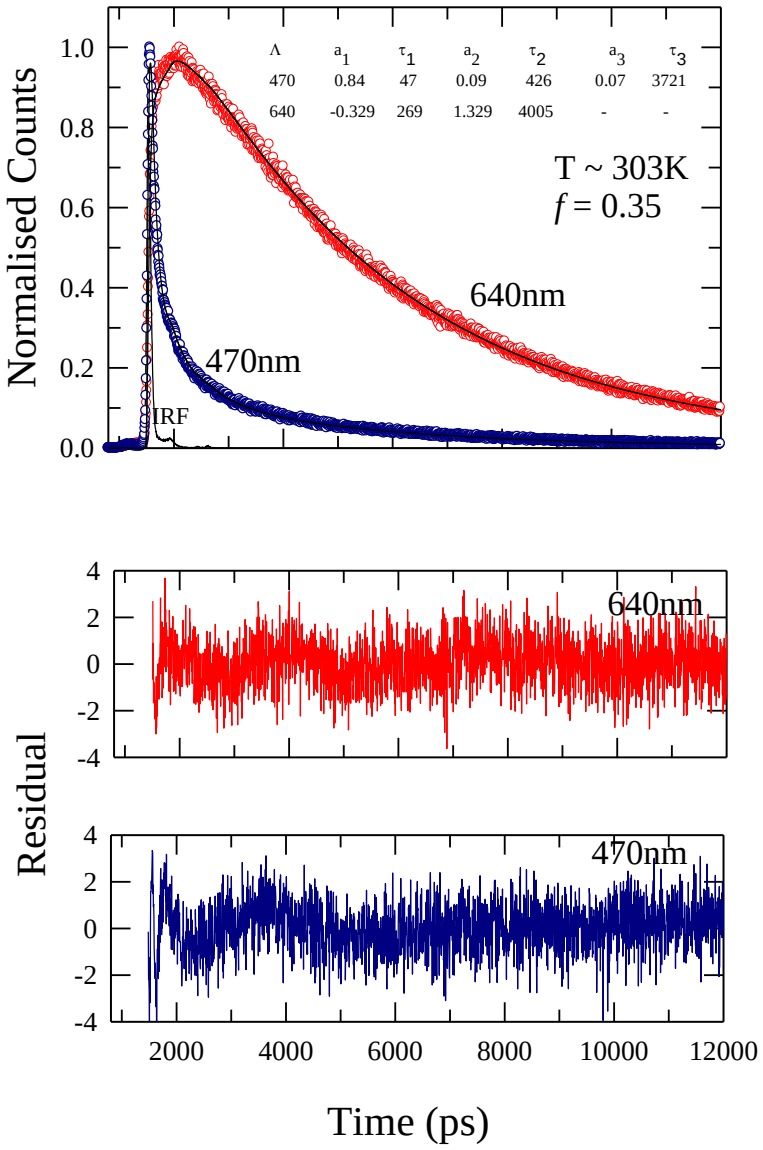

Figure A10: Representative fluorescence intensity decays at blue (470nm) and red (640nm) wavelengths for C153 in molten mixtures of $0.10LiNO_3$ + 0.90[*f* Urea+ (1-*f*) Acetamide] at *f* = 0.35 (T= 303 K). Circles denote the experimental data whereas the solid lines fit through them. Instrument response function (IRF) is also shown in the same figure (dashed lines). The respective residuals (color coded) are presented in the bottom panels. The fit parameters are shown in the inset of the upper panel. Time

constants (τ_i) are in the unit of nanosecond. The Goodness-of-fit parameters (χ^2) in these two wavelengths 470nm and 670nm are 1.08 and 1.01, respectively.

Figure A11

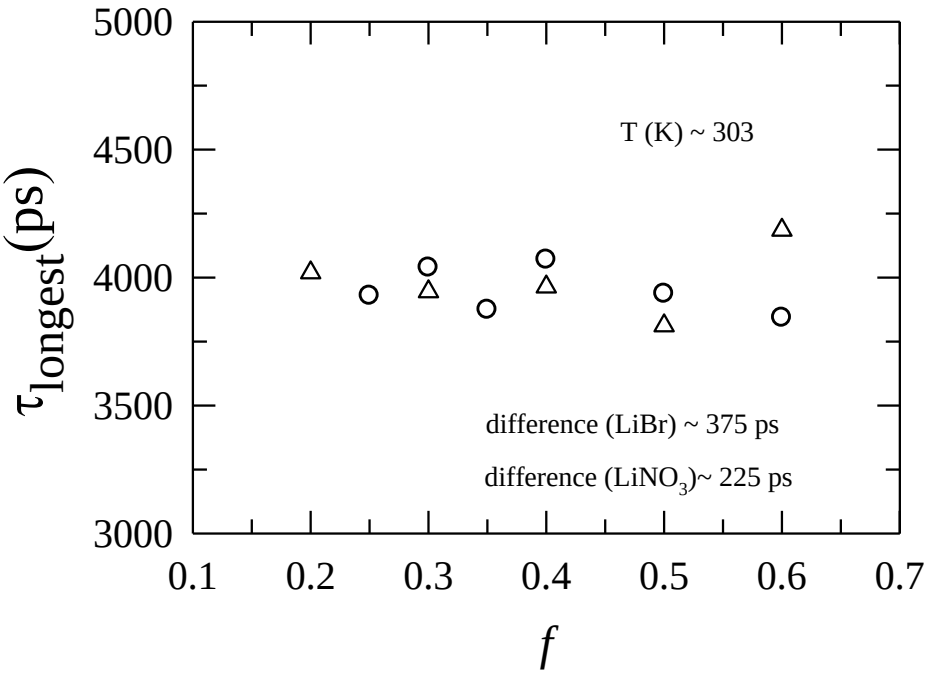

Figure A11: Longest time constant ($\tau_{longest}$ versus fraction of urea (f_{Urea})) (T= 303K) for C153 in 0.10$LiNO_3$/ LiBr + 0.90[*f* Urea+ (1-*f*) Acetamide] has been plotted. These times are obtained from the fits of the collected fluorescence intensity decays at various fractions of urea.

Figure A12

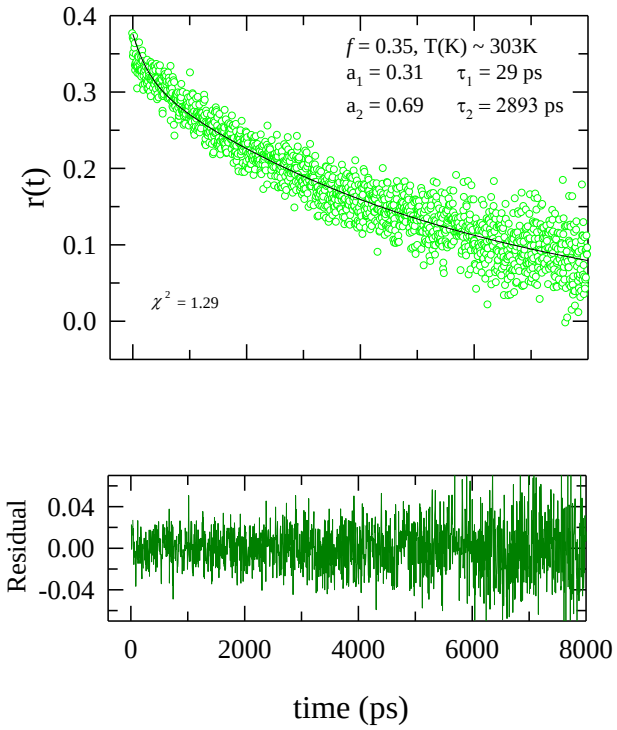

Figure A12: Representative fluorescence anisotropy decay, r(t), of C153 (T = 303K) in the molten mixture of 0.10 $LiNO_3$+0.90 [*f* Urea+(1-*f*) Acetamide] at *f* = 0.35. The circles in the upper panel represent the experimental decay and the solid line through them gives the biexponential fit. The solid line in the panel below represents the residual. The goodness of the fit is about 1.29.

Figure A13

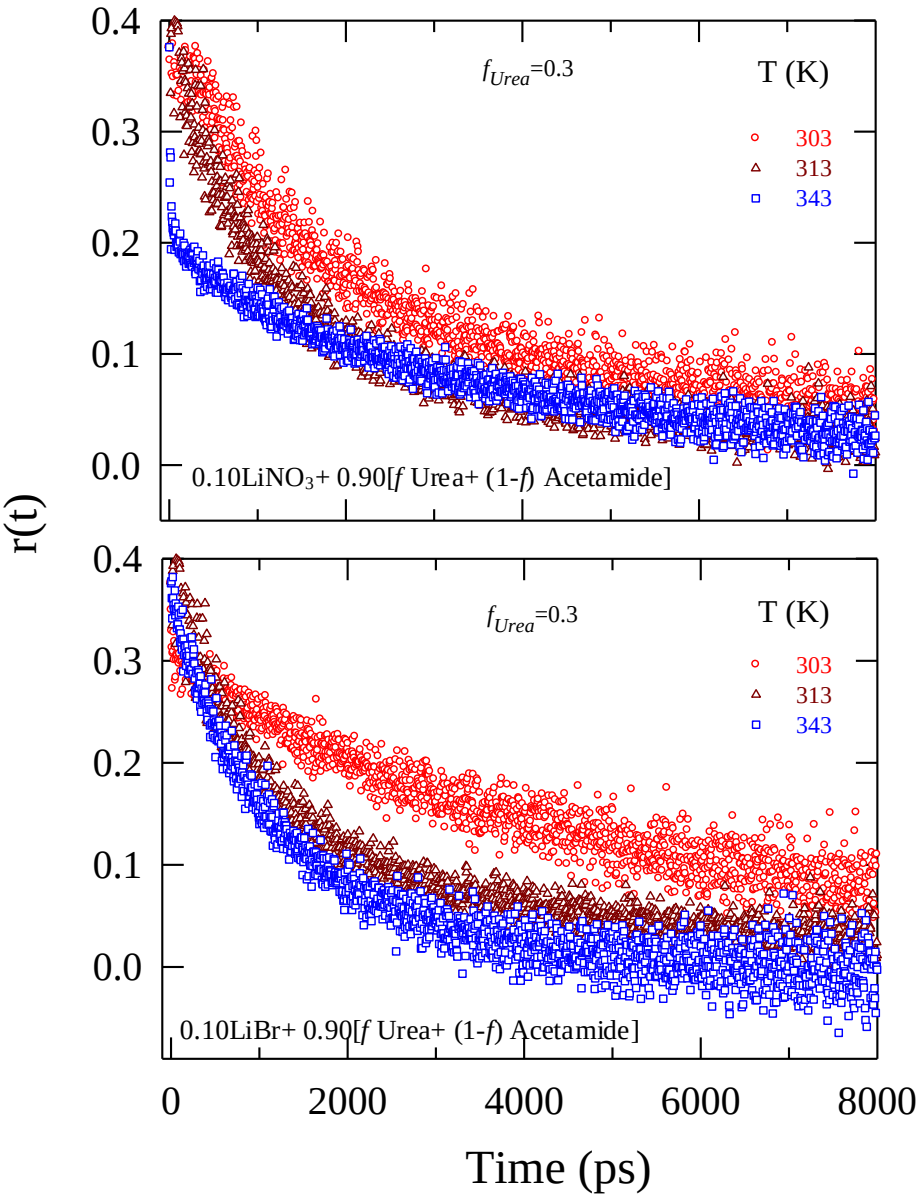

Figure A13: Temperature dependence of fluorescence anisotropy ($r(t)$) decay of C153 in 0.10$LiNO_3$/ LiBr + 0.90[f Urea+ (1-f) Acetamide] at $f = 0.3$. Data representations are denoted in the panels.

Figure A14

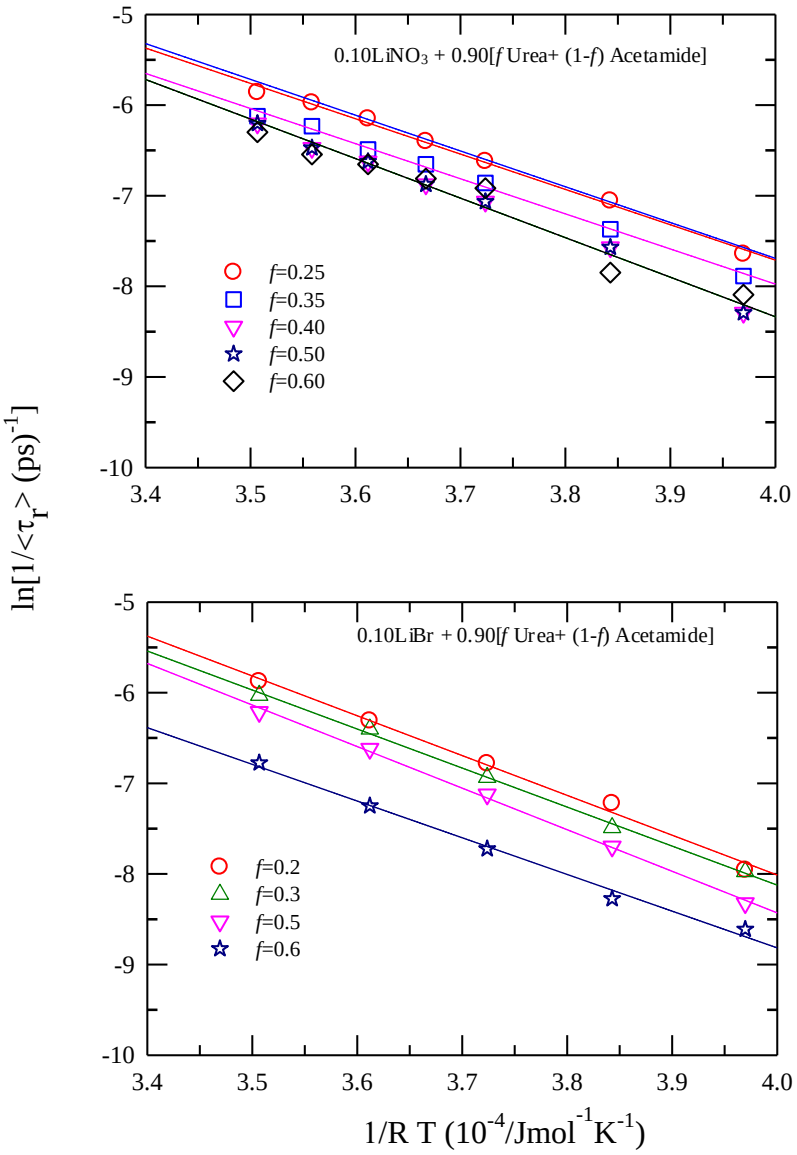

Figure A14: Arrhenius plot of $\ln\left(1/\langle\tau_r\rangle\right)$ versus $1/RT$ for C153 rotation times $<\tau_r>$ in the DES 0.10LiNO$_3$/ LiBr + 0.90[*f* Urea+ (1-*f*) Acetamide] is plotted in the natural log-log form of the equation: $\tau_r = A(\eta/T)^p$. Solid lines represent fit through the respective data sets.

Figure A15

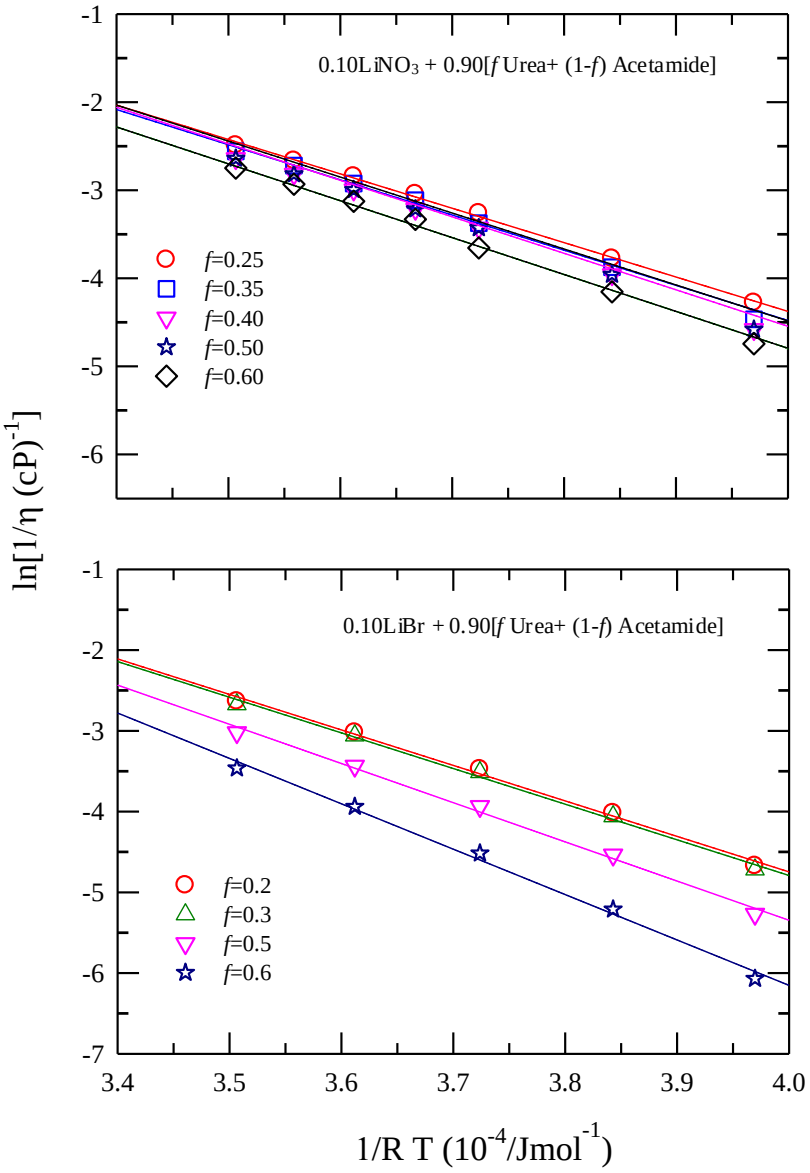

Figure A15: Arrhenius type plot of $\ln(1/\eta)$ versus $1/RT$ for the DES $0.10LiNO_3$/ LiBr + 0.90[*f* Urea+ (1-*f*) Acetamide] is plotted here. Solid lines represent fit through the respective data sets.

Figure A16

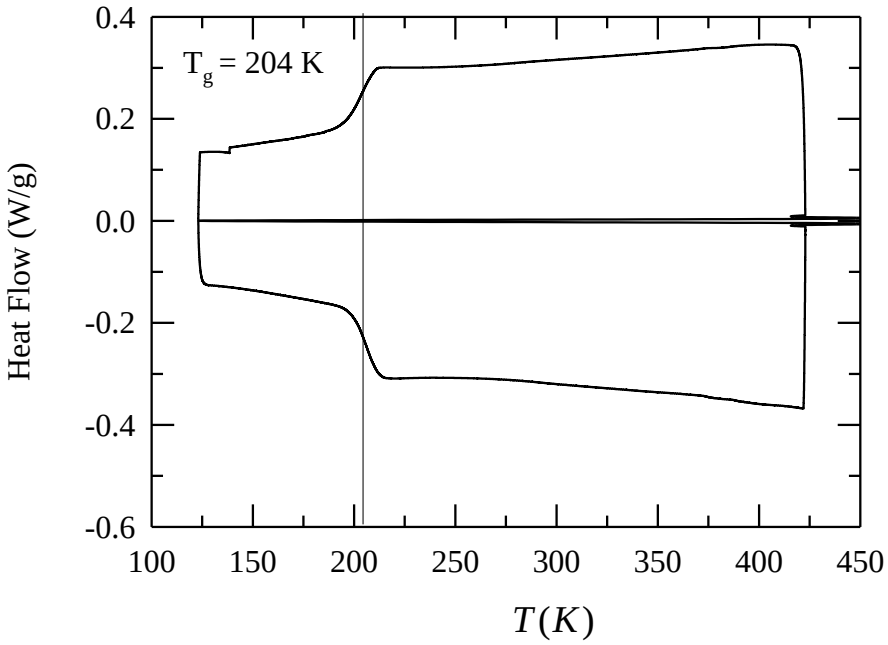

Figure A16: Differential scanning calorimetric trace (heating curve) for the system (0.33Choline chloride+ 0.67Urea) is shown. The glass transition temperatures (*Tg*) is indicated by the vertical line.

Figure A17

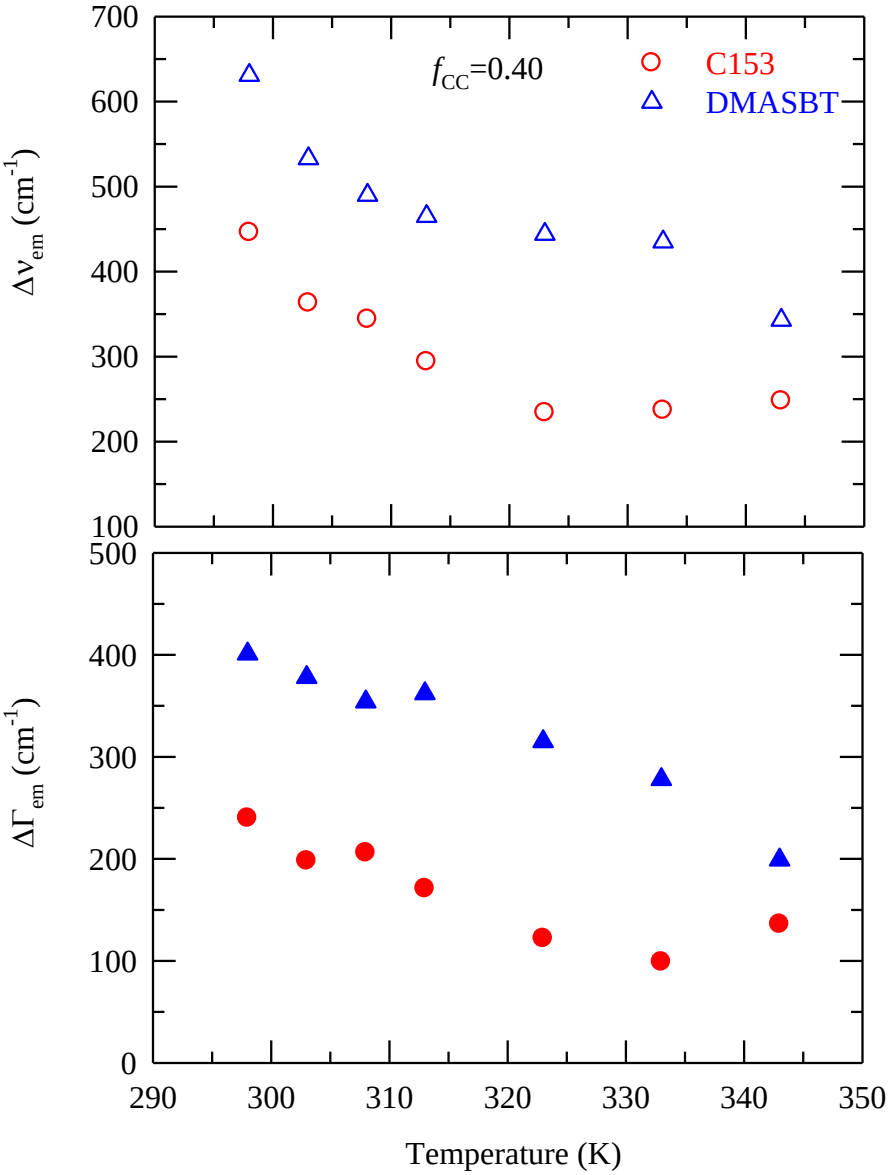

Figure A17: Temperature dependent total differences (Δx) in ν_{em} and Γ_{em} for f= 0.40 in [f Choline chloride**+** (1-f) Urea] are shown in the lower panel. This is defined as $\Delta x(T) = x(T, \lambda_{exc,\,b}) - x(T, \lambda_{exc,\,r})$, x being ν_{em} or Γ_{em} . $\lambda_{exc,\,b}$ and $\lambda_{exc,\,r}$ are the shortest (bluest) and longest (most red) wavelengths used for solute excitation.

Figure A18

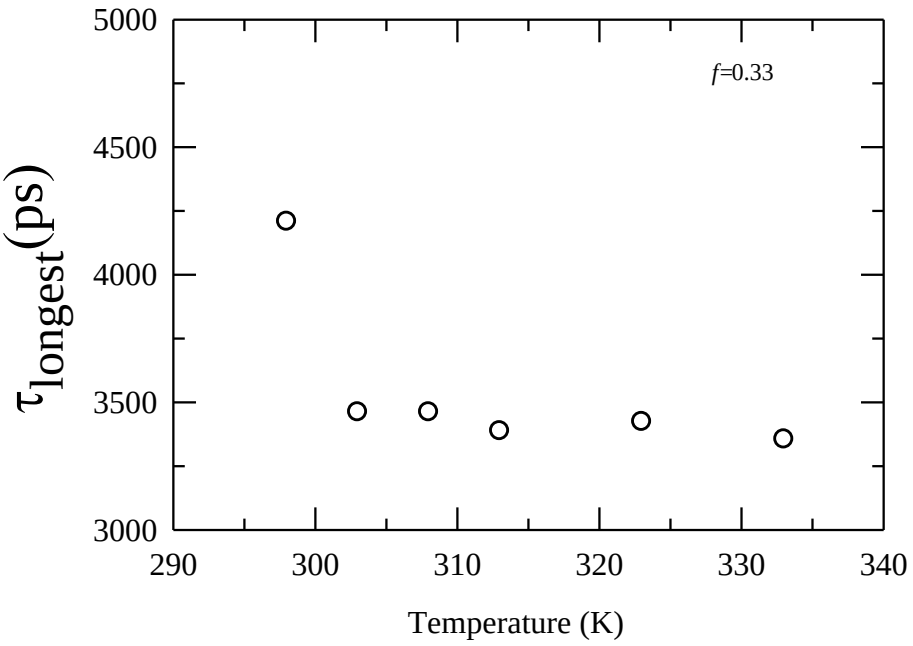

Figure A18: Longest time constant ($\tau_{longest}$) vs Temperature at *f*=0.33 for C153 in [*f* Choline chloride**+** (1-*f*) Urea] has been plotted. These times are obtained from the fits of the collected fluorescence intensity decays at various temperatures.

Figure A19

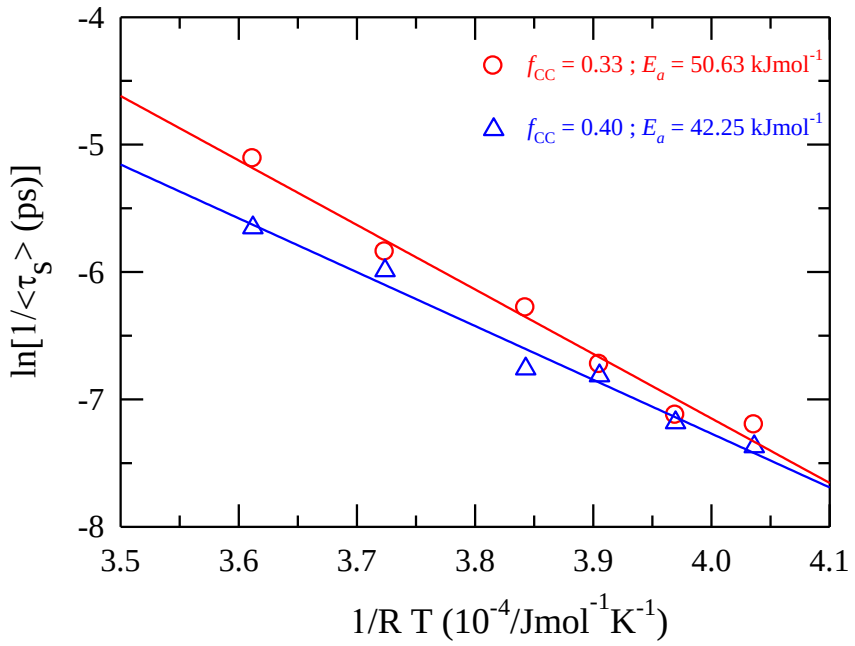

Figure A19: Arrhenius plot of $\ln(1/\langle\tau_s\rangle)$ vs *1/RT* for rotational dynamics of C153 in [*f* Choline chloride**+**(1-*f*) Urea]. The solid lines are the linear fits through the data points. Circles represent natural logarithm of inversion of average solvation times of C153 in the system at *f*= 0.33, and triangles for *f*= 0.40. The respective activation energies are indicated along the legends.

Figure A20

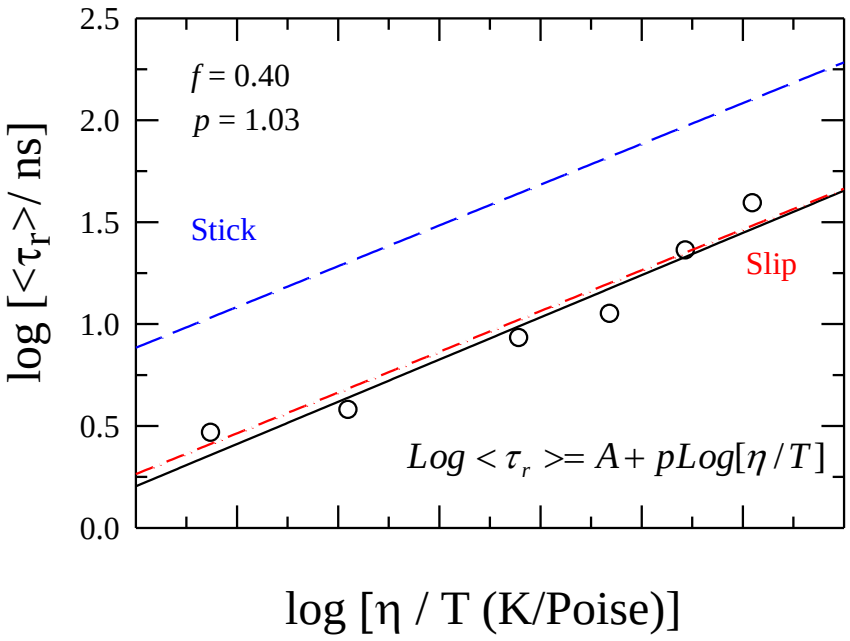

Figure A20: Viscosity coupling of rotation times ($\langle \tau_r \rangle$) for C153 in the system [*f* Choline chloride**+** (1-*f*) Urea] (*f*=0.40) and comparison to hydrodynamic theory is shown in this figure. Temperature dependent measured times are shown as a function of temperature-reduced viscosity (η/T) in a log-log fashion [$Log\langle \tau_r \rangle = A + pLog(\eta/T)$]. Rotation times for C153 at various η/T values from calculation by SDE equation are also shown in broken red and blue lines at the slip and stick boundaries respectively for a comparison.

Figure A21

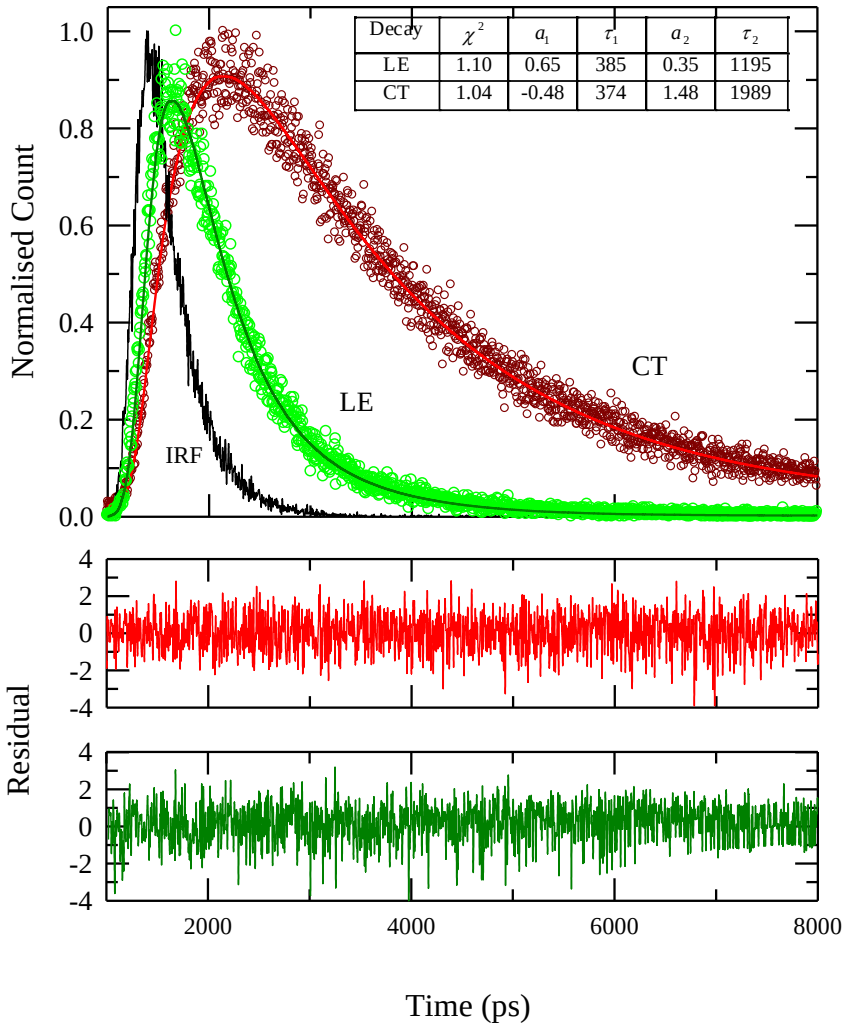

Figure A21: Representative LE and CT emission decays of P4C in [*f* Choline chloride**+** (1-*f*) Urea] (*f*=0.33). The data are represented by circles, and the fit through the data is the solid line. The instrument response function (IRF) is shown by the black line. The fit (biexponential) results are also provided in the upper panel. Residuals are shown in the lower panel.

Figure A22

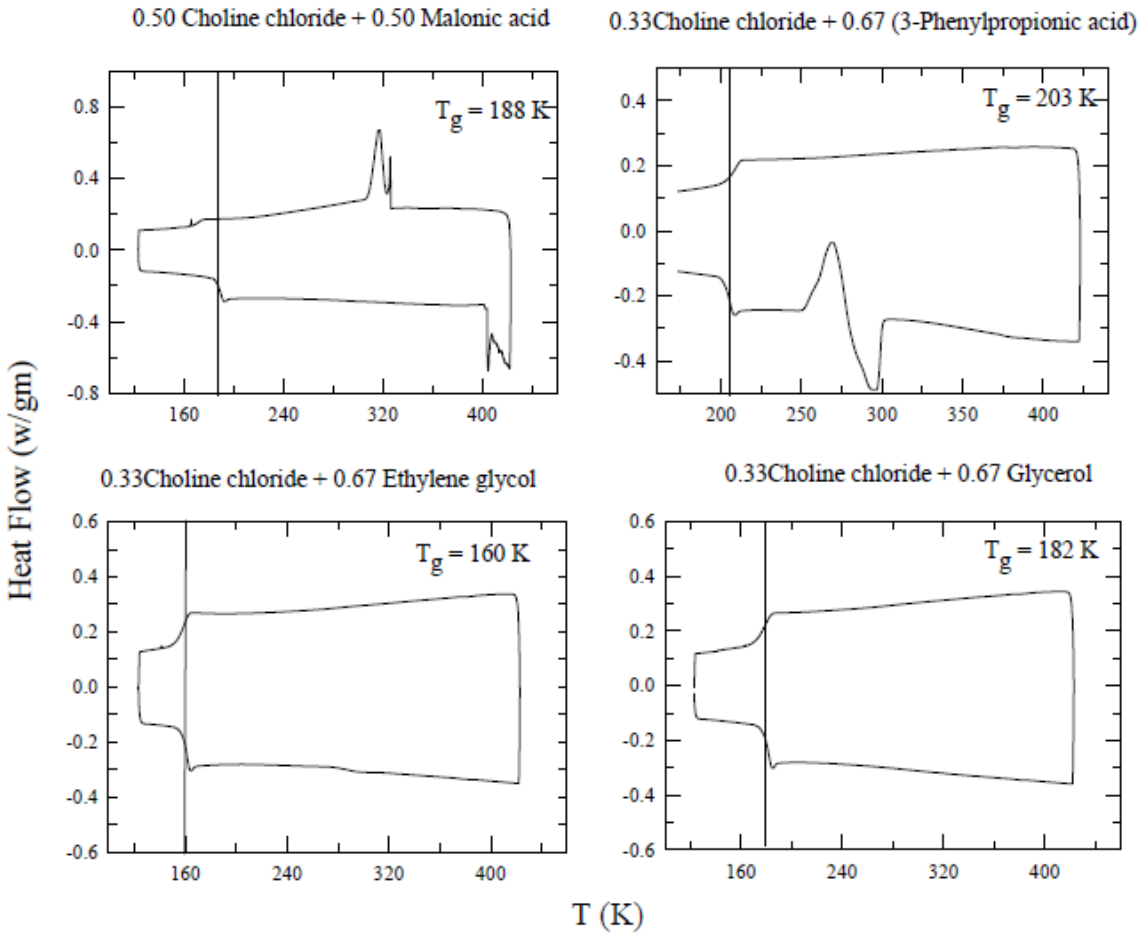

Figure A22: Differential scanning calorimetric traces (heating curve) for all the systems (mentioned in the figures) is shown. The glass transition temperatures (*Tg*) is indicated by the vertical line.

Figure A23

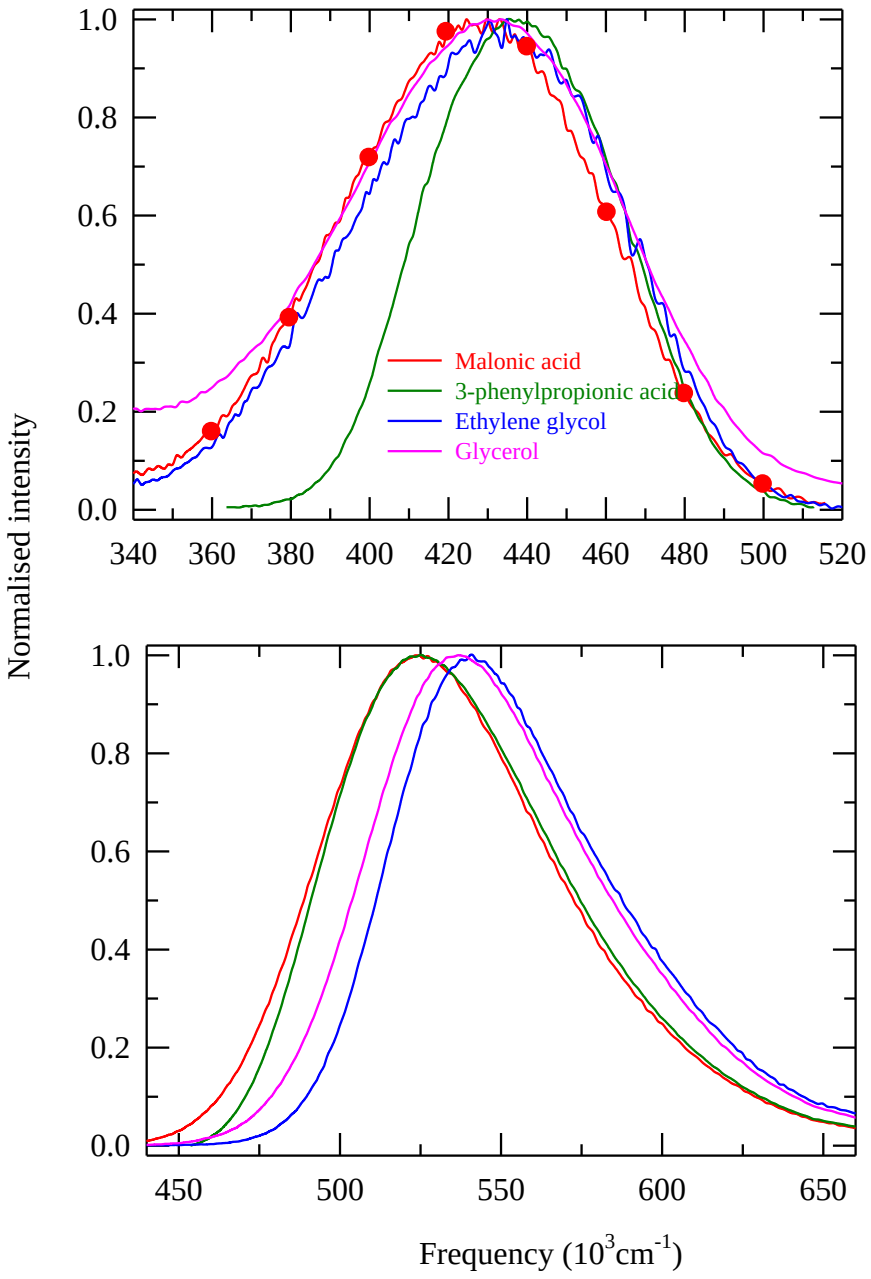

Figure A23: Representative absorption and emission spectra of the DES [*f* Choline chloride**+** (1-*f*) HBD] (color coded) at 293K are shown here. The red filled symbols indicate the wavelengths selected for excitation wavelength dependence studies.

Figure A24

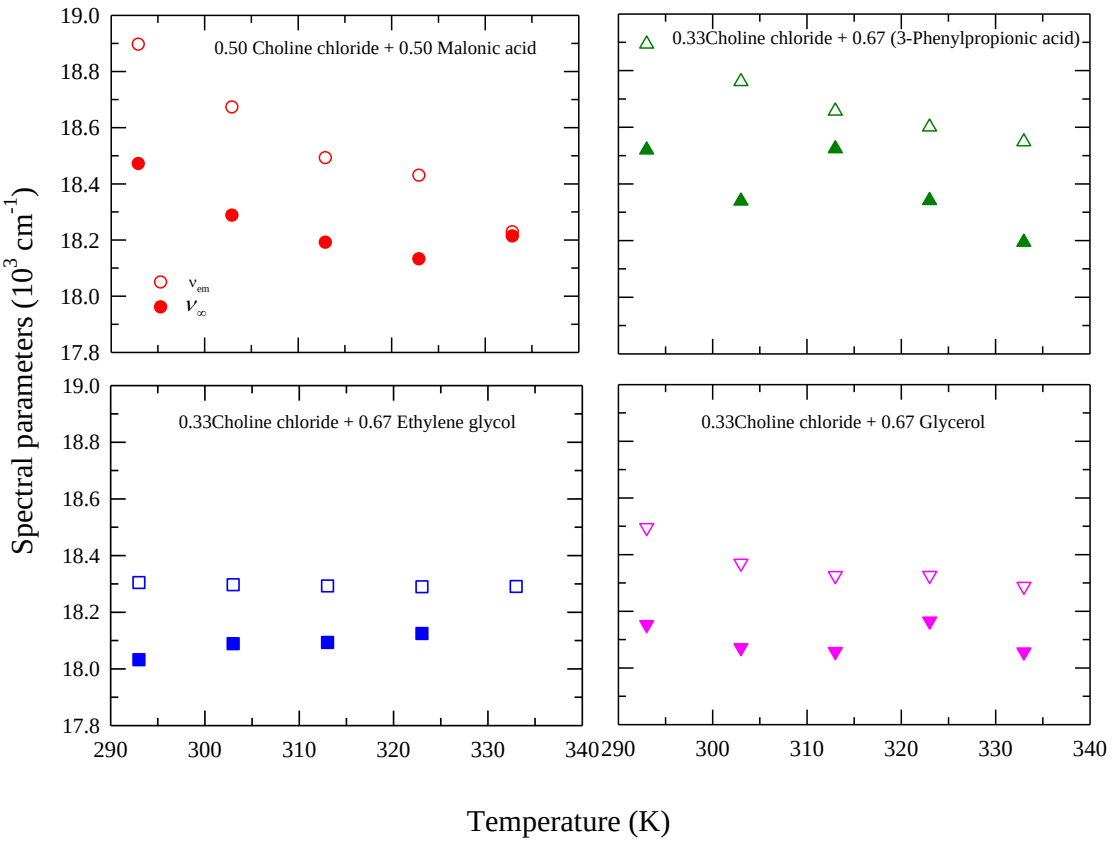

Figure A24: Steady state emission frequencies (ν_{em}) and emission frequencies (ν_{∞}) obtained at time infinity ($t = \infty$) obtained from Fee-Maroncelli method (Ref. 27 of Chapter 7) is shown here for [*f* Choline chloride**+** (1-*f*) HBD] (color coded) at different temperatures.

Figure A25

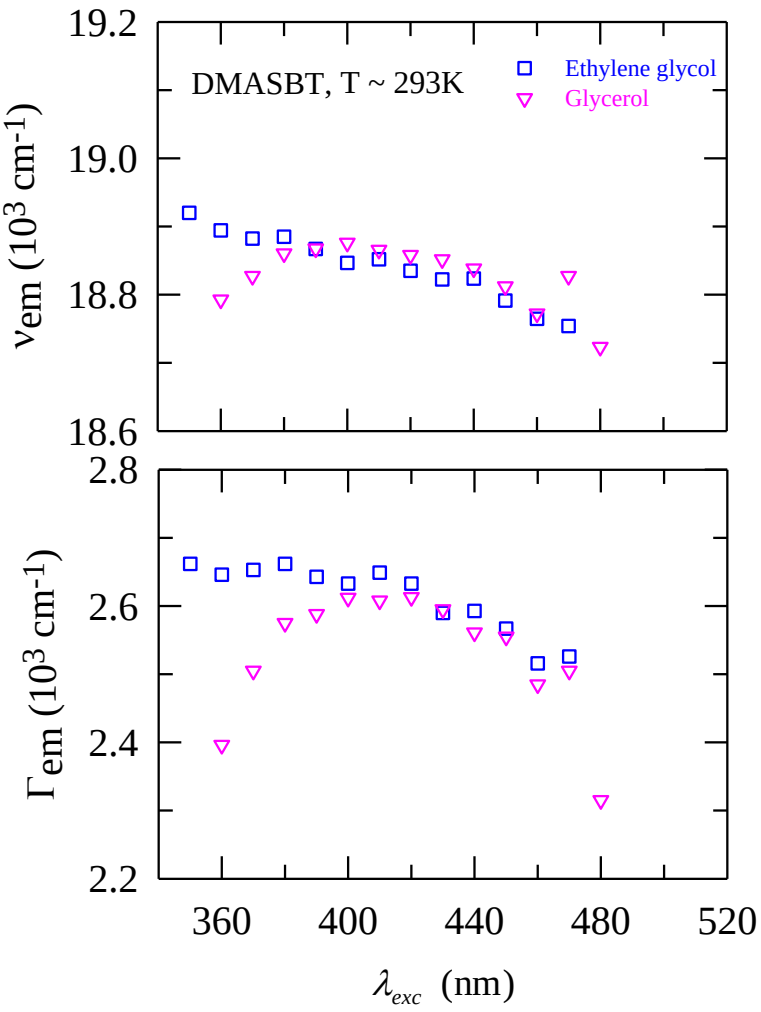

Figure A25: Emission peak frequencies (ν_{em}) and full width at half maxima, *fwhm* (Γ_{em}) for DMASBT in the system of [*f* Choline chloride**+** (1-*f*) HBD] (*f*=0.33) at 293K are plotted against different excitation wavelengths (λ_{exc}). It is to be noted that DMASBT study with malonic acid and 3-phenylpropionic acid could not be performed due to probe-solvent reaction.

Specifications of HBD types: ethylene glycol (blue squares), glycerol (pink inverse triangles).

Figure A26

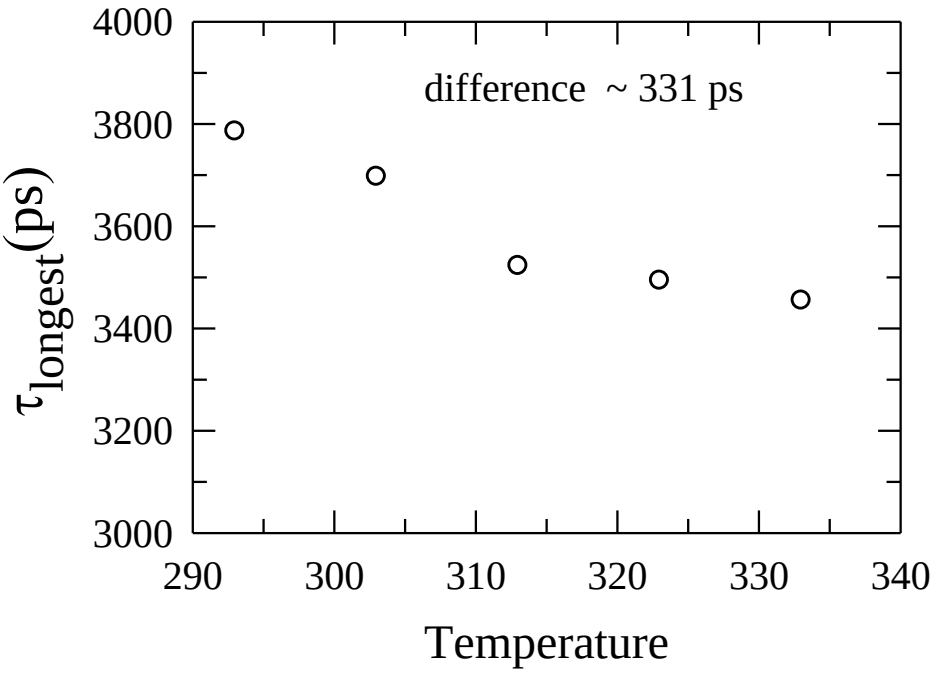

Figure A26: Longest time constant ($\tau_{longest}$ at different temperature) for C153 in [*f* Choline chloride**+** (1-*f*) HBD] where HBD=Malonic acid at *f*=0.50 has been plotted. These times are obtained from the fits of the collected fluorescence intensity decays.

Figure A27

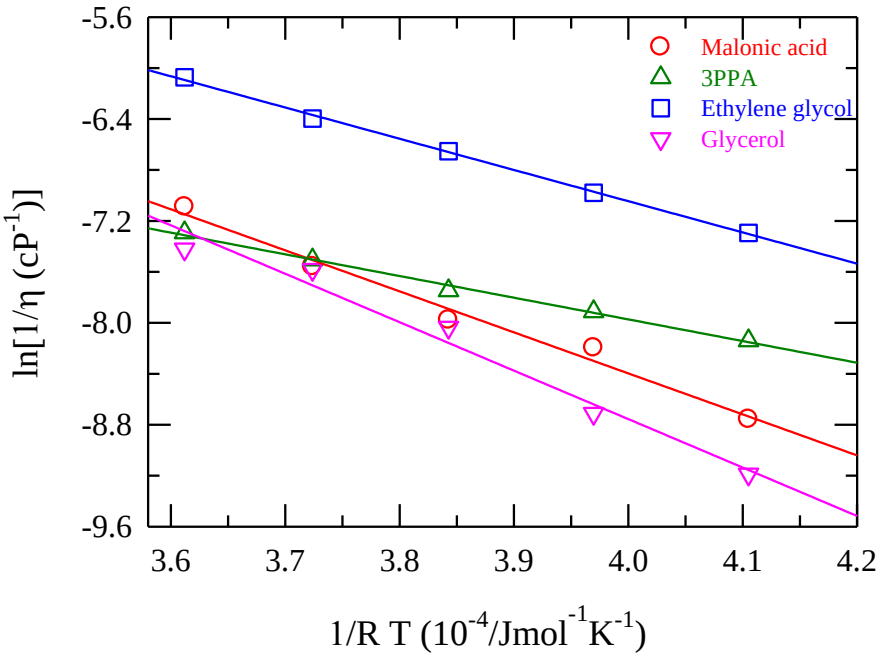

Figure A27: Arrhenius type plot of $\ln(1/\eta)$ versus $1/RT$ for the DES [*f* Choline chloride**+** (1-*f*) HBD] is plotted here. Solid lines represent fit through the respective data sets.

Specifications of HBD types: *f*=0.50 for malonic acid (red circles), *f*=0.33 for 3-phenylpropionic acid (green triangles), ethylene glycol (blue squares), glycerol (pink inverse triangles).

Figure A28

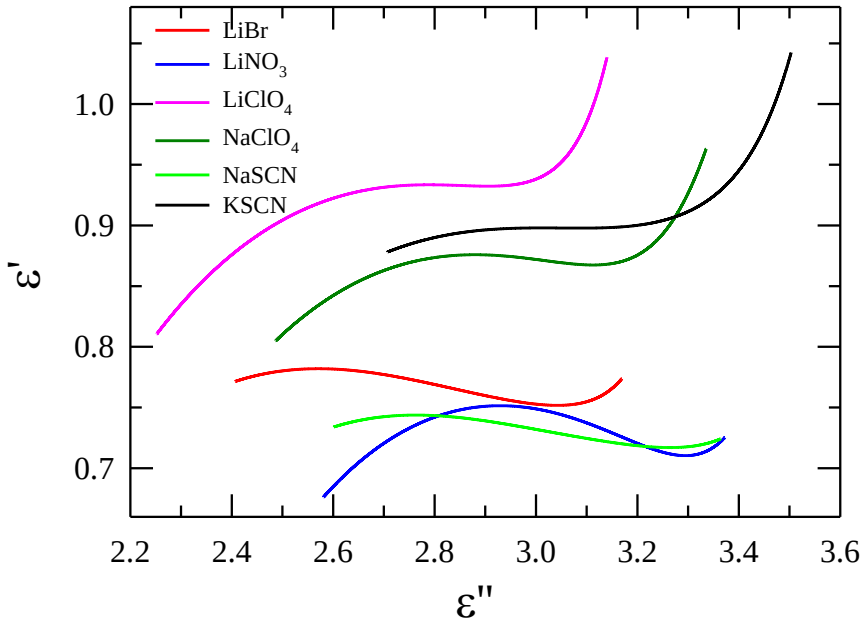

Figure A28: Cole-Cole deviation plots for (Acetamide + Electrolyte) DES at ~293 K are shown here. Each combination is color-coded.

Figure A29

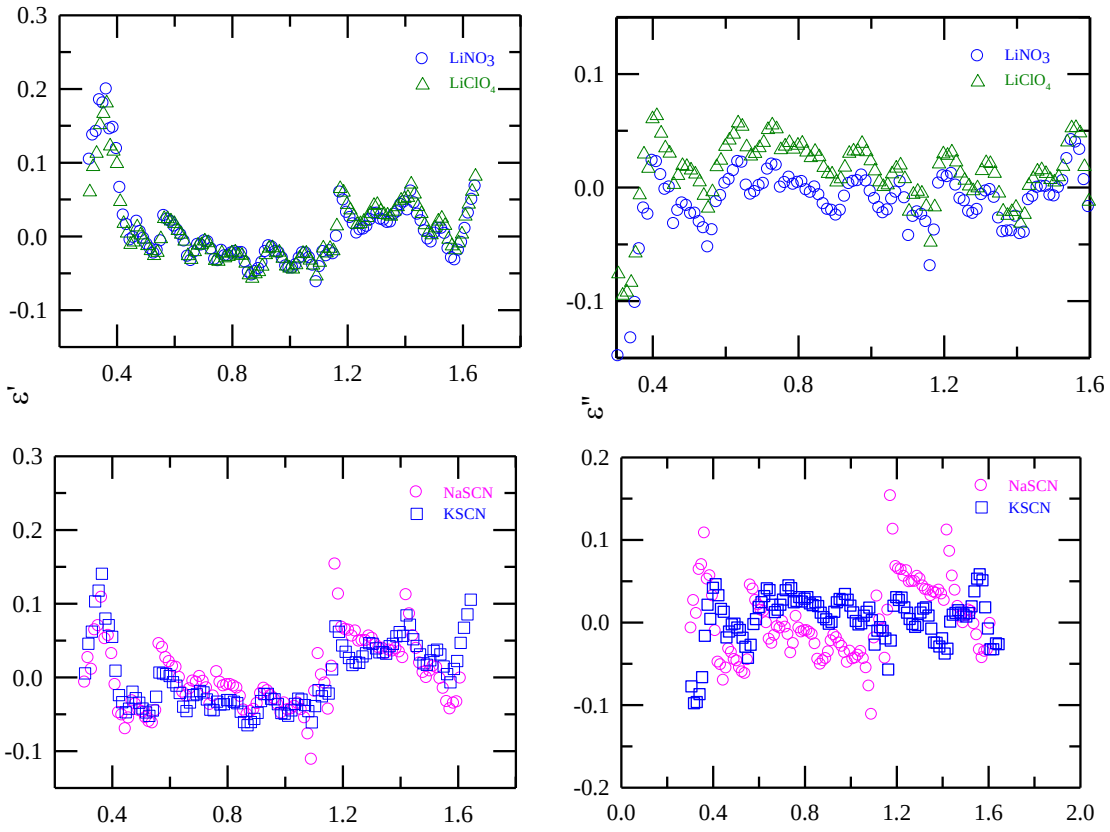

Figure A29: Residuals for 4-Debye simultaneous fits of the real and imaginary parts of the measured DR spectra for (Acetamide + Electrolyte) DESs at ~293 K are shown here. Two sets of electrolytes are considered here in the upper and the lower panel. Representations are color coded.

Figure A30

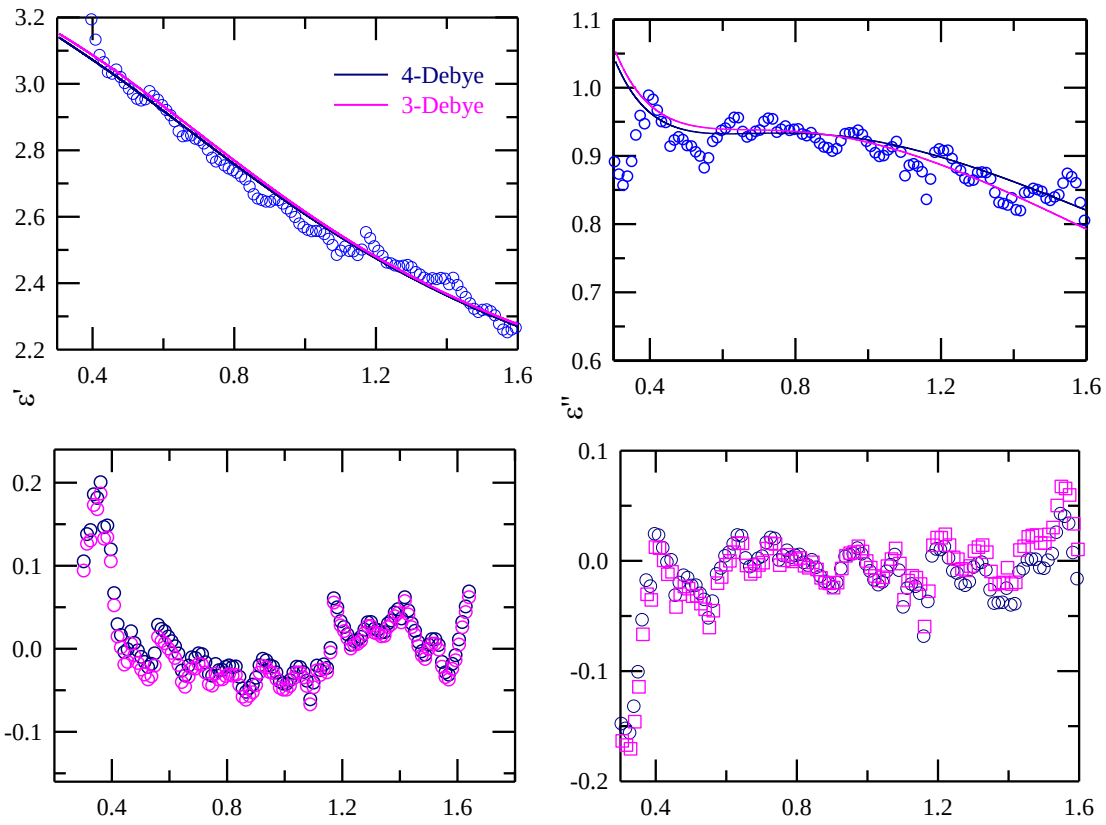

Figure A30: Comparison between residuals from 3-Debye and 4-Debye fits to the measured DR spectra for a representative system, (acetamide + $LiClO_4$), at ~293 K. Residuals shown here correspond to fits to real and imaginary part of the DR spectrum.

Figure A31

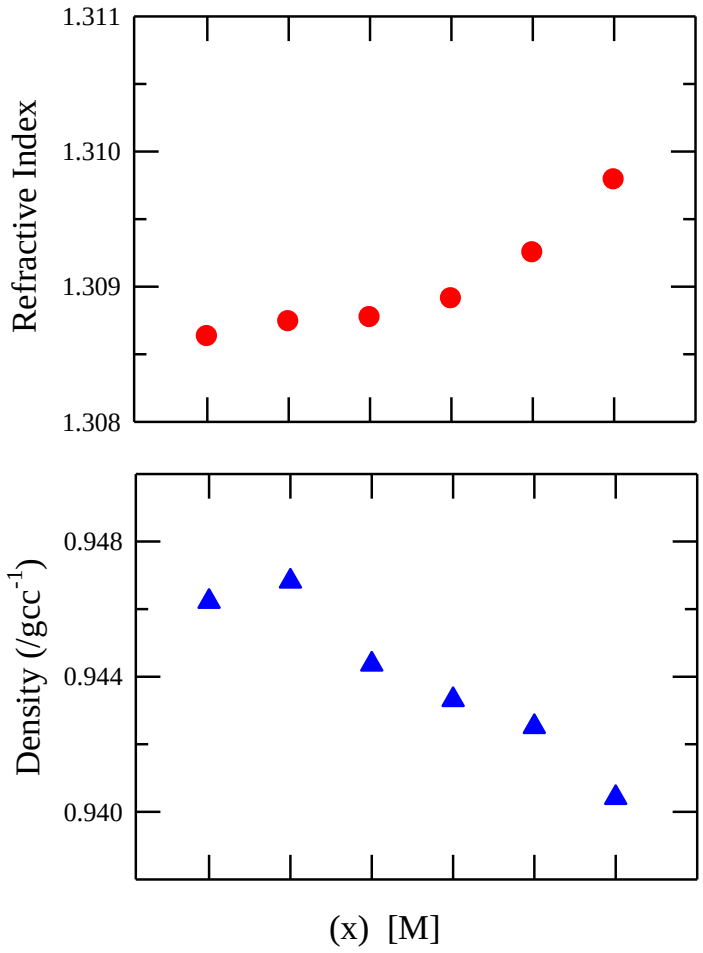

Figure A31: The above figure shows the variation of refractive indices and densities of the system [x $LiClO_4$ + (0.5- x)$NaClO_4$] in ethyl acetate at ~293K.

Figure A32

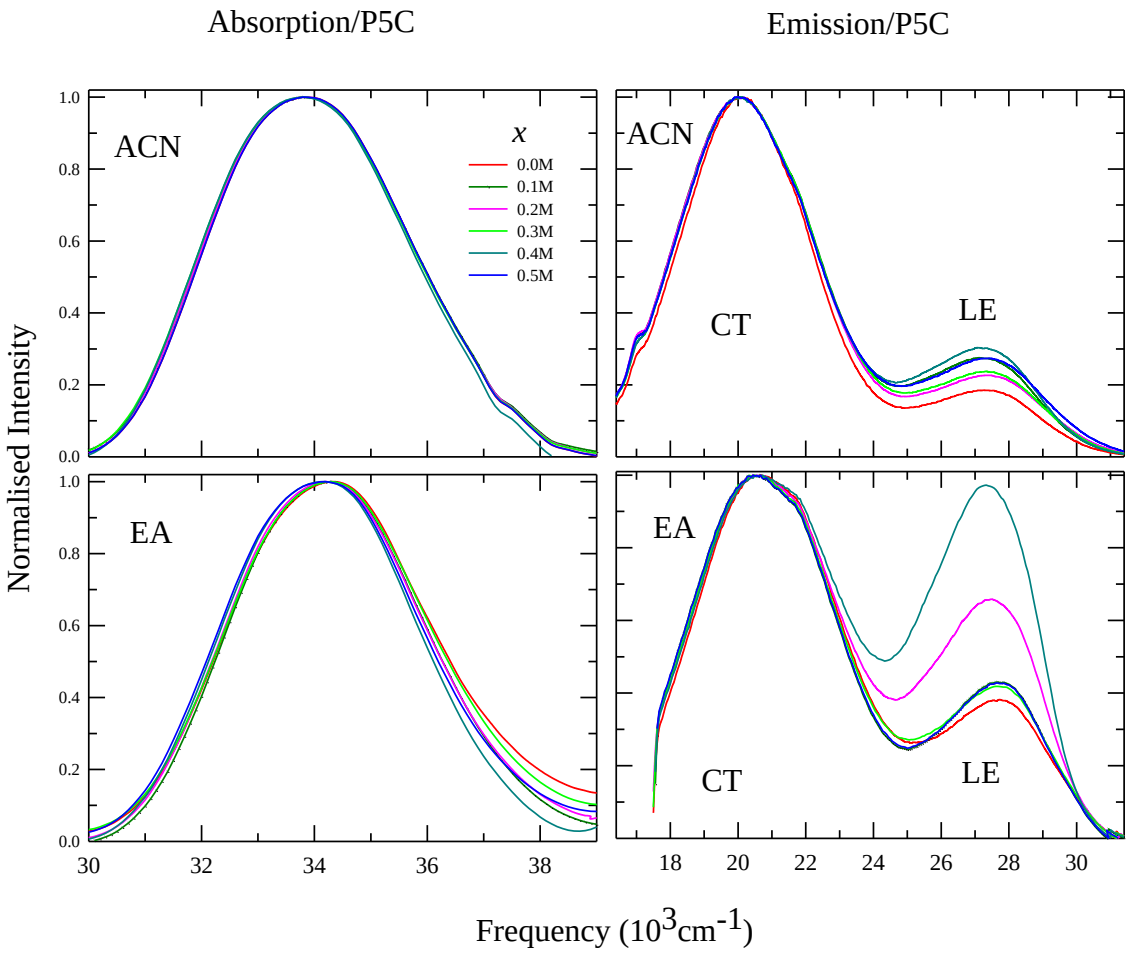

Figure A32: Absorption and emission spectra of 4-(1- pyrrolidinyl)-benzonitrile (P5C) is shown for different values of '*x*' (color coded) in the system [*x* $LiClO_4$ + (0.5- *x*)$NaClO_4$] in acetonitrile (upper panel, marked with "ACN") and ethyl acetate (lower panel marked with "EA") at ~293K.

Figure A33

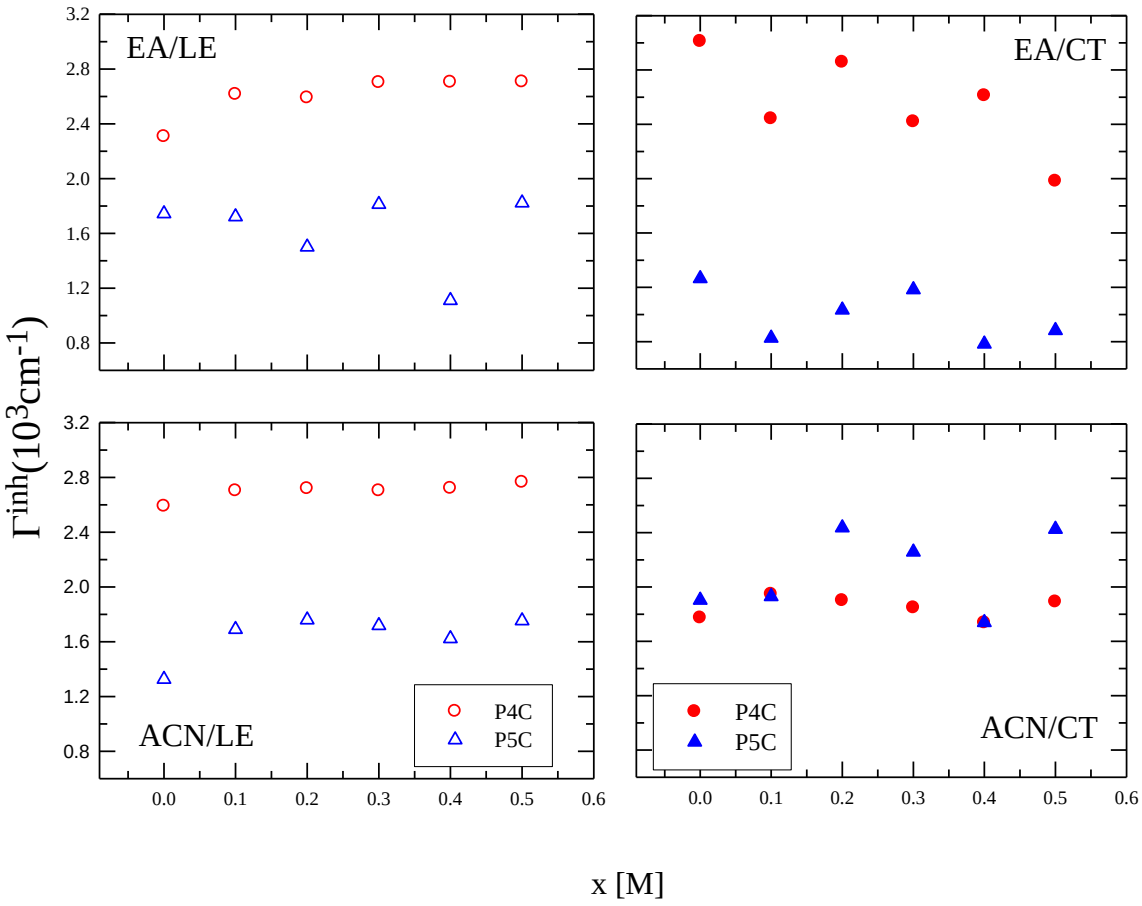

Figure A33: Mixed electrolyte concentration dependence of emission (LE and CT) inhomogeneous line widths (full width at half-maxima, Γ^{inh}) of 4-(1-azetidinyl)benzonitrile (P4C) and 4-(1-pyrrolidinyl)benzonitrile P5C for the system [*x* $LiClO_4$ + (0.5- *x*)$NaClO_4$] in ethyl acetate (upper panel, marked with "EA") and acetonitrile (lower panel, marked with "ACN") are shown. The circles represent the solute P4C and the triangles are P5C respectively. Empty symbols represent LE and filled symbols represent CT line widths. These quantities have been obtained after deconvoluting the experimental emission spectra by broadening and shifting a reference spectrum with a Gaussian function (representing inhomogeneous solvent broadening described in ref. 5 of Chapter 9).

The estimated uncertainty in widths is 300 cm^{-1} (except when the LE is too small).

Figure A34

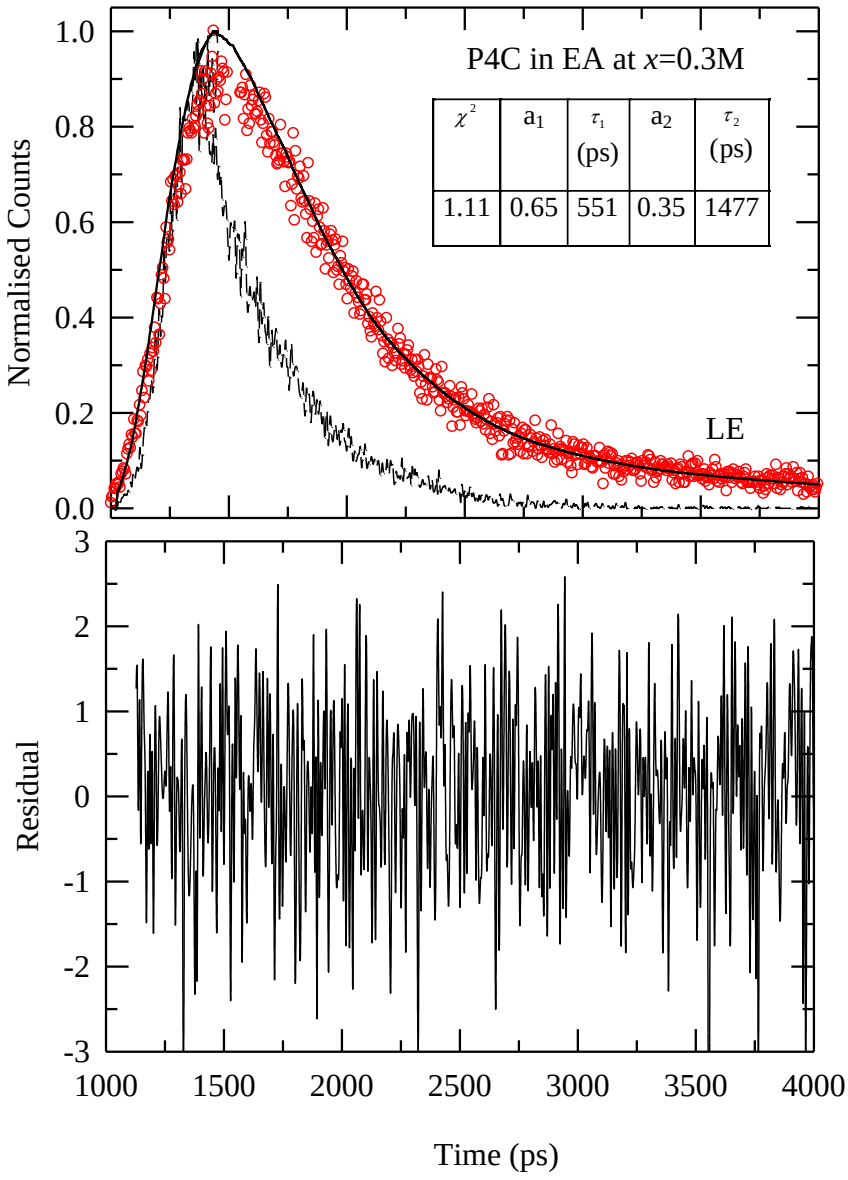

Figure A34: Representative LE emission decay for P4C in [x $LiClO_4$ + (0.5-x)$NaClO_4$] at x=0.3M in ethyl acetate is shown here. IRF is given by the broken black line whereas data are represented by red circles and the the fit is the solid black line through them. Inset provides the fit parameters. The lower panel shows residual obtained for the fit.

Appendix B

Table B1: Fitting parameters of the decays collected at magic angle (55˚) for DTN in $0.78CH_3CONH_2$+ $0.22\{f$LiBr+ $(1-f)LiNO_3\}$ at 303K for various compositions along with viscosity coefficients (η). The calculated $< \tau_{life} >$ is the weighted average of the individual time constants. η values are from Ref. 7 of Chapter 3.

f_{LiBr}	η (cP)	a_1	τ_1 (ps)	a_2	τ_2 (ps)	$= < \tau_{life} >$ (ps)
0.0	210.57	0.82	94	0.18	338	138
0.2	393.67	0.81	90	0.19	346	139
0.4	267.67	0.79	112	0.21	392	171
0.6	609.91	0.81	141	0.19	492	208
0.8	738.89	0.65	129	0.35	505	261
1.0	1311.90	0.77	154	0.23	658	270

Table B2: Composition and temperature dependence of the fitting parameters of the decays collected at magic angle (55˚) for DTN in $0.78CH_3CONH_2$+ $0.22\{f$LiBr+ $(1-f)LiNO_3\}$ along with the viscosity coefficients (η). The calculated $< \tau_{life} >$ is the weighted average of the individual time constants.

T (K)	η (cP)	a_1	τ_1 (ps)	a_2	τ_2 (ps)	$= < \tau_{life} >$ (ps)
$f_{LiBr} = 0.0$						
303	210.57	0.82	94	0.18	338	138
313	109.25	0.91	71	0.09	285	90

318	82.24	0.90	56	0.10	212	71
333	39.35	0.95	45	0.05	190	53
348	21.59	0.98	39	0.02	277	44
f_{LiBr} = 0.2						
303	267.67	0.81	90	0.19	346	139
313	133.34	0.87	63	0.13	277	90
318	98.05	0.89	55	0.11	250	77
333	44.99	0.95	43	0.05	273	54
348	24.27	0.96	34	0.04	274	43
f_{LiBr} = 0.4						
303	393.67	0.75	125	0.25	398	193
313	190.07	0.8	113	0.2	276	146
318	138.88	0.86	92	0.14	213	109
333	64.02	0.91	69	0.09	159	77
348	28.51	0.96	43	0.04	196	49
f_{LiBr} = 0.6						
303	609.91	0.81	141	0.19	492	208
313	278.57	0.88	103	0.12	382	137
318	197.67	0.91	98	0.09	383	120
333	84.69	0.96	66	0.04	414	80
348	30.99	0.97	55	0.03	352	53
f_{LiBr} = 0.8						
303	738.89	0.65	130	0.35	505	261
313	323.40	0.77	97	0.23	429	173

318	225.51	0.81	91	0.19	379	146
333	90.83	0.92	73	0.08	327	93
348	44.62	0.97	61	0.03	406	71
f_{LiBr} = 1.0						
303	1311.90	0.77	154	0.23	658	270
313	534.025	0.87	123	0.13	606	186
318	360.49	0.91	116	0.09	677	167
333	134.53	0.95	83	0.05	925	125
348	64.88	0.96	68	0.04	1016	106

Table B3: Rotational relaxation times as obtained from the anisotropy decays for DTN in the DU melt, [0.78CH_3CONH_2+ 0.22{*f*LiBr+ (1-*f*)$LiNO_3$}] at various '*f*' and temperatures.

f_{LiBr}	T (K)	η (cP)	$< \tau_r >$ (ps)
0.00	303	210.57	1339
	313	109.25	1082
	318	82.24	1048
	333	39.35	821
	348	21.59	532
0.20	303	267.67	1846
	313	133.34	1123

	318	98.05	948
	333	44.99	924
	348	24.27	711
0.40	303	393.67	2009
	313	190.07	1913
	318	138.88	1702
	333	64.02	951
	348	28.51	802
0.60	303	609.91	2613
	313	278.57	2308
	318	197.67	1773
	333	84.69	1006
	348	30.99	814
0.80	303	738.89	2744
	313	323.40	2138
	318	225.51	1191
	333	90.83	993
	348	44.62	887
1.00	303	1311.90	3729
	313	534.025	2355
	318	360.49	2124
	333	134.53	1769
	348	64.88	949

Table B4: Temperature dependence of density (ρ) and viscosity coefficients (η) of [$f$$CH_3CONH_2$+ (1-$f$)$NH_2CONH_2$] DES at different compositions. ([a]T±0.2 K, [b]±5%. [c]T±0.3 K. [d]±2%)

T (K)	Density[a,b] (ρ) (gcc^{-1})	Viscosity[c,d] (η) (cP)
f = 0.60		
328	1.090	11.94
333	1.085	9.87
338	1.083	8.26
343	1.079	7.01
348	1.075	5.98
353	1.070	5.16
f = 0.65		
328	1.101	11.03
333	1.097	9.18
338	1.094	7.72
343	1.091	6.57
348	1.087	5.67
353	1.083	4.97
f = 0.70		
328	1.111	10.56
333	1.107	8.80
338	1.105	7.43
343	1.102	6.37

348	1.099	5.46
353	1.096	4.74

Table B5: Variation of estimated dynamic Stokes shift, $\Delta\nu_{est}^{t}$ (10^3cm^{-1}), for C153 in [*f*CH_3CONH_2+(1-*f*)NH_2CONH_2] deep eutectics with temperatures. The dynamic shift is estimated as $\Delta\nu_{est}^{t} \equiv \left[\nu_{abs.} - \nu_{\infty}(t=\infty)\right]^{mixture} - \left[\nu_{abs.} - \nu_{em.}\right]^{heptane}$, by using the method described in Ref. 58 of Chapter 4. $\Delta\nu^{heptane}$ is measured as 4230 cm^{-1}. We have approximated $\nu_{\infty} \approx \nu_{em}$ (steady state).

Temperature (K)	*f* = 0.60	*f* = 0.65	*f* = 0.70
353	0.856	0.762	0.745
348	0.830	0.810	0.776
343	0.864	0.783	0.766
338	0.871	0.796	0.784
333	0.844	0.807	0.782
328	0.790	0.830	0.801

Table B6: Composition and temperature dependence of the fit parameters of the measured dynamic fluorescence anisotropies, $r(t)$, for C153 in [$f$$CH_3CONH_2$+ (1-$f$)$NH_2CONH_2$]. Calculated $<\tau_r>$ is the weighted average of the individual time constants.

Temp (K)	a_1	τ_1 (ps)	a_2	τ_2 (ps)	$<\tau_r>$ (ps)
f = 0.60					
328	0. 25	15	0.75	381	287
333	0.27	15	0.73	319	238
338	0.28	15	0.72	267	197
343	0.29	15	0.71	228	166
348	0.31	15	0.69	199	142
353	0.31	15	0.69	165	118
f = 0.65					
328	0. 49	15	0.51	416	249
333	0.54	15	0.46	381	182
338	0.42	15	0.58	252	171
343	0.60	15	0.40	311	132
348	0.42	15	0.58	208	128
353	0.41	15	0.59	196	111
f = 0.70					
328	0. 47	18	0.53	393	217
333	0.49	15	0.51	327	173
338	0.50	15	0.50	324	152
343	0.34	15	0.64	200	133

348	0.50	15	0.50	205	110
353	0.76	15	0.24	340	94

Table B7: Viscosities (η) and densities (ρ) as obtained from measurements for $0.10LiNO_3$/ LiBr + 0.90[*f* Urea+ (1-*f*) Acetamide] at various mixture compositions and temperatures are listed below.

(a) $0.10LiNO_3$ + 0.90[*f* Urea+ (1-*f*) Acetamide]

T (K)	η (cP)	ρ (gcc^{-1})
f = 0.25		
303	73.05	1.1502
313	43.69	1.1428
323	26.08	1.1357
328	21.20	1.1318
333	17.16	1.1281
338	14.35	1.1234
343	12.06	1.1207
f = 0.30		
303	83.30	1.1613
313	44.70	1.1540
323	27.40	1.1467
328	22.10	1.1430
333	17.99	1.1393

338	14.84	1.1356
343	12.40	1.1319
f = 0.35		
303	83.2	1.1744
313	46.9	1.1672
323	28.3	1.1600
328	22.80	1.1564
333	18.50	1.1528
338	15.30	1.1491
343	12.90	1.1456
f = 0.40		
303	87.00	1.1812
313	48.13	1.1749
323	29.20	1.1681
328	22.50	1.1648
333	18.61	1.1614
338	15.20	1.1579
343	12.92	1.1544
f = 0.50		
303	99.80	1.2068
313	55.33	1.1996
323	32.02	1.1924
328	26.3	1.1888
333	20.7	1.1852

338	17.6	1.1816
343	14.3	1.1780
f = 0.60		
303	114.78	1.2307
313	63.68	1.2235
323	38.65	1.2162
328	27.95	1.2125
333	22.78	1.2088
338	18.75	1.2052
343	15.62	1.2019

(b) 0.10LiBr + 0.90[*f* Urea+ (1-*f*) Acetamide]

T (K)	η (cP)	ρ (gcc^{-1})
f = 0.20		
303	106.91	1.1875
313	55.64	1.1802
323	32.30	1.1728
333	20.53	1.1653
343	13.93	1.1578
f = 0.30		
303	111.96	1.1960
313	57.91	1.1887

323	33.54	1.1814
333	21.28	1.1740
343	14.46	1.1665
f = 0.40		
303	130.29	1.1909
313	65.59	1.1835
323	36.82	1.1759
333	23.00	1.1680
343	15.50	1.1617
f = 0.50		
303	194.45	1.2554
313	93.46	1.2479
323	51.23	1.2406
333	31.07	1.2332
343	20.52	1.2258
f = 0.60		
303	432.45	1.2962
313	183.40	1.2887
323	91.49	1.2815
333	51.39	1.2743
343	31.93	1.2670

Table B8: Relaxation parameters obtained from bi-exponential fits to *r(t)* of C153 in molten mixture of $0.10LiNO_3$/ LiBr + 0.90[*f* Urea+ (1-*f*) Acetamide] at various mixture compositions and temperatures.

(a) $0.10LiNO_3$ + 0.90[*f* Urea+ (1-*f*) Acetamide]

T (K)	η (cP)	a_1	τ_1 (ps)	a_2	τ_2 (ps)	$< \tau_r >$ (ps)
f = 0.25						
303	73.05	67.12	3103	32.88	15	2088
313	43.69	69.43	1664	30.57	15	1160
323	26.08	68.04	1097	31.96	15	751
328	21.20	61.97	919	38.03	84	602
333	17.16	66.74	695	33.26	15	469
338	14.35	71.31	542	28.69	23	393
343	12.06	65.97	525	34.03	15	351
f = 0.30						
303	83.30	75.14	2940	24.86	60	2224
313	44.70	78.78	2011	21.22	15	1587
323	27.40	70.28	1140	29.72	15	795
328	22.10	63.67	806	36.33	15	519
333	17.99	63.15	690	36.85	24	445
338	14.84	60.57	541	39.43	34	341
343	12.40	61.48	467	38.52	18	294
f = 0.35						
303	83.2	68.56	2893	31.44	29	1992
313	46.9	68.22	1685	31.78	31	1166

323	28.3	64.48	1101	35.52	30	721
328	22.80	63.54	871	36.46	45	570
333	18.50	63.18	728	36.82	24	469
338	15.30	60.61	616	39.39	37	388
343	12.90	58.31	517	41.69	45	320
f = 0.40						
303	87.00	86.50	3076	13.50	15	2662
313	48.13	87.40	1815	12.6	15	1588
323	29.20	86.50	1100	13.50	15	953
328	22.50	82.21	923	17.79	90	775
333	18.61	85.98	763	14.02	15	658
338	15.20	86.88	584	13.12	15	509
343	12.92	74.92	576	25.08	98	456
f = 0.50						
303	99.80	71.77	5450	28.23	299	3992
313	55.33	73.61	2626	26.39	15	1937
323	32.02	74.69	1563	25.31	15	1171
328	26.3	73.99	1297	26.01	30	967
333	20.7	75.10	998	24.90	15	753
338	17.6	70.75	908	29.25	15	647
343	14.3	75.21	652	24.79	15	494
f = 0.60						
303	(114.78)	37.51	1836	62.49	7525	5391
313	(63.68)	35.18	6896	64.82	1595	3460

323	(38.65)	88.53	1356	11.75	15	1202
328	27.95	68.09	1466	31.91	348.7	1109
333	22.78	87.3	886	12.7	15	775
338	18.75	69.99	906	30.01	204	695
343	15.62	88.12	615	11.88	15	544

(b) 0.10LiBr + 0.90[*f* Urea+ (1-*f*) Acetamide]

T (K)	η (cP)	a_1	τ_1 (ps)	a_2	τ_2 (ps)	$< \tau_r >$ (ps)
f= 0.20						
303	106.91	0.38	15	0.62	4610	2855
313	55.64	0.38	28	0.62	2186	1370
323	32.30	0.37	32	0.63	1385	882
333	20.53	0.39	25	0.61	879	550
343	13.93	0.37	15	0.63	556	357
f= 0.30						
303	111.96	0.32	29	0.68	4273	2905
313	57.91	0.29	24	0.71	2507	1787
323	33.54	0.31	42	0.69	1463	1026
333	21.28	0.30	21	0.70	854	602
343	14.46	0.35	36	0.65	619	415
f= 0.40						
303	130.29	0.40	15	0.60	5320	3185

313	65.59	0.38	21	0.62	2404	1502
323	36.82	0.32	38	0.68	1812	1242
333	23.00	0.33	47	0.67	1185	810
343	15.50	0.36	44	0.64	834	553
f= 0.50						
303	194.45	0.30	15	0.70	5915	4118
313	93.46	0.28	15	0. 72	3065	2202
323	51.23	0.27	27	0.73	1690	1241
333	31.07	0.29	15	0.71	1054	750
343	20.52	0.29	15	0.71	703	499
f = 0.60						
303	432.45	0.50	15	0.50	10960	5491
313	183.40	0.40	15	0. 60	6551	3919
323	91.49	0.36	15	0.64	3496	2259
333	51.39	0.33	28	0.67	2087	1407
343	31.93	0.34	39	0.66	1304	875

Table B9: The values of '*p*' for average rotation time ($<\tau_r>$) dependence on temperature reduced viscosities (η) at various fractions of urea in the DES according to the equation $\log <\tau_r> = \log A + p \log(\eta/T)$ derived from $<\tau_r> = A(\eta/T)^p$

f	*p* ($LiNO_3$)	*p* (LiBr)
0.20		0.94
0.25	0.93	
0.30	0.99	0.92
0.35	0.92	
0.40	0.88	0.83
0.50	0.98	0.89
0.60	1.01	0.81

Table B10: The measured values of density (ρ), viscosity coefficient (η) and refractive index (*n*) of the system [*f* Choline chloride+ (1-*f*) Urea)] at *f*= 0.33 and 0.40 at different temperatures are given in the table.

T (K)	η (cP)	ρ (gcc^{-1})	*n*
f= 0.33			
298	1008	1.1955	1.437
303	631	1.1928	1.436
308	411	1.1901	1.435
313	278	1.1874	1.433
318	195	1.1846	1.432
323	141	1.1820	1.431
333	80	1.1768	1.428
f= 0.40			
298	1244	1.1838	1.438
303	932	1.1811	1.436
308	671	1.1785	1.434
313	451	1.1759	1.433
323	214	1.1707	1.430
333	118	1.6567	1.428

Table B11: The values of dielectric constants (ε_0) are shown here as calculated from ref. 52 along with the refractive indices (*n*) and emission frequencies (ν_{em}) of C153 at *f*= 0.33 and 0.40 in the system [*f* Choline chloride+ (1-*f*) Urea)].

T (K)	*n*	ν_{em} (10^3 cm^{-1})	ε_0 Calculated)
f= 0.33			
298	1.437	18.596	14.34
303	1.436	18.391	18.99
313	1.433	18.265	23.50
323	1.431	18.199	26.80
333	1.428	18.149	29.95
f= 0.40			
298	1.438	18.652	13.40
303	1.436	18.472	16.89
313	1.433	18.400	18.81
323	1.430	18.257	23.96
333	1.428	18.191	27.35

Table B12: Parameters Obtained from biexponential fits/ tri-exponential fits to the LE and CT decays of P4C/P5C in [*f* Choline chloride**+** (1-*f*) Urea] at f_{CC}=0.33 at three representative temperatures.

Temp (K)	λ (nm)	χ^2	a_1	τ_1 (ps)	a_2	τ_2 (ps)	a_3	τ_3 (ps)
P4C								
293	LE	1.096	0.65	385	0.35	1195		
	CT	1.039	-0.48	374	1.48	1989		
313	LE	1.005	0.86	287	0.14	719		
	CT	1.021	-0.31	299	1.31	1486		
333	LE	1.147	0.96	120	0.04	797		
	CT	1.156	-0.16	137	1.16	1039		
P5C								
293	LE	1.091	0.56	107	0.29	616	0.15	1938
	CT	1.033	-0.24	238	1.12	1312	0.12	4509
313	LE	1.103	0.74	126	0.17	443	0.09	1704
	CT	1.046	-0.18	202	1.02	807	0.15	3308
333	LE	1.152	0.90	116	0.07	412	0.03	1684
	CT	0.966	-0.11	166	0.94	671	0.17	2056

Table B13. Composition and temperature dependence density (ρ), viscosity coefficients (η) and refractive indices in [*f* Choline chloride**+** (1-*f*) HBD] are shown.

Temp(K)	ρ (gcc^{-1})	η (cP)	Refractive index
Malonic acid, *f*=0.50			
293	1.2339	1092	1.40375
303	1.2272	693	1.40602
313	1.2206	289	1.40832
323	1.2139	186	1.41058
333	1.2073	86	1.41262
3-Phenylpropionic acid, *f*=0.33			
293	1.1189	570	1.45460
303	1.1118	276	1.45159
313	1.1049	149	1.44877
323	1.0980	89	1.44613
333	1.0915	58	1.44389
Ethylene glycol, *f*=0.33			
293	1.1193	50	1.40202
303	1.1136	34	1.40005
313	1.1080	24	1.39757
323	1.1023	17	1.39442
333	1.0967	13	1.39226
Glycerol, *f*=0.33			
293	1.1942	526	1.41780
303	1.1886	265	1.41503
313	1.1831	150	1.41301
323	1.1776	92	1.41104
333	1.1721	60	1.40897

Table B14: Parameters obtained from simultaneous fitting of the real (ε') and imaginary (ε'') parts of the measured DR spectra for (Acetamide + Electrolyte) DES at ~293 K are summarized. Here only the 3-Debye fits are shown.

Electrolyte	ε_0	$\Delta\varepsilon_1$	τ_1[b] (ps)	$\Delta\varepsilon_2$	τ_2 (ps)	$\Delta\varepsilon_3$	τ_3 (ps)	ε_∞	$\langle\tau_{av}\rangle$[c] (ps)	χ^2
LiBr	27	23.69[a] (93%)	32	1.12789 (1.9%)	0.298	0.49271 (4.4%)	0.08	1.689	30.31	1.19
$LiNO_3$	25.2	21.4 (92%)	38.2	1.3073 (2.1%)	4.2	0.5039 (5.6%)	0.114	1.989	35.32	1.26
$LiClO_4$	34	30.776 (96%)	23	1.094 (3.4%)	0.1206	0.242 (0.75%)	0.08	1.888	22.05	1.12
$NaClO_4$	22	18.381 (91%)	22.69	0.9989 (4%)	0.277	0.803 (4.9%)	0.08	1.817	20.68	1.03
NaSCN	16.5	12.847 (88%)	28.44	0.654 (4.5%)	0.403	1.099 (7.52%)	0.08	1.942	25.05	1.22
KSCN	29.1	25.3876 (94%)	20.116	0.6124 (2.3%)	0.2166	1.03465 (3.8%)	0.08	1.965	18.90	1.09

a) Number in parenthesis indicates dispersion amplitude of a given dispersion step in percentage.

b) τ_i (i=1-3) are better within ±5% of the reported values.

c) $<\tau_{av}> = \frac{\sum_{i=1}^{=n} a_i \tau_i}{\sum_{i=1}^{n} a_i}$, where $\sum_{i=1}^{n} a_i = 1$ and $a_i = \frac{\Delta\varepsilon_i}{\sum_{i=1}^{n} \Delta\varepsilon_i}$.

Table B15: Viscosity coefficients (η) and conductivities (κ) of six (acetamide + electrolyte) deep eutectics studied.

DES	η_{293K} (cP)[a]	κ_{293K} (S/m)[b]	κ_{293K} (S/m) (from measurements)
Acetamide + LiBr	1950	0.121	0.141
Acetamide + $LiNO_3$	263	0.095	0.103
Acetamide+$LiClO_4$	220	0.141	0.171
Acetamide +$NaClO_4$	195	0.082	0.145
Acetamide +NaSCN	~2000	0.041	0.055
Acetamide + KSCN	~180	0.23	0.249

a) Viscosity values at ~293 K are obtained from extrapolation of the temperature dependent data available in refs. 28, 29 and 31 from Chapter 8.

b) Conductivity values are used form ref. 33 from Chapter 8.

Table B16: Ion volumes and radii from ref. 33 & 34 from Chapter 8.

Anion	**Volume (nm^3)**	**Radius(nm)**	**Cation**	**Volume (nm^3)**	**Radius(nm)**
Br^-	0.056	0.34	Li^+	0.00199	0.11
NO_3^-	0.064	0.36	Na^+	0.00394	0.14
SCN^-	0.071	0.37	K^+	0.00986	0.19
ClO_4^-	0.082	0.39	-	-	

Table B17: The following table presents the comparison between the forward reaction rate (k_f) for the reaction $LE \rightarrow CT$ for the TICT molecules 4-(1-azetidinyl)benzonitrile (P4C) and 4-(1-pyrrolidinyl)benzonitrile P5C in ethyl acetate (EA) and acetonitrile (ACN) for pure solvents (taken from ref.5 of Chapter 9) and for the systems [0.5M $NaClO_4$ + ACN/EA] and [0.5M $LiClO_4$ + ACN/EA].

	P4C		
System	Pure acetonitrile	Acetonitrile +0.5M $NaClO_4$	Acetonitrile +0.5M $LiClO_4$
k_f /ns	0.034	2.9988	3.2167
System	Pure ethyl acetate	Ethyl acetate +0.5M $NaClO_4$	Ethyl acetate +0.5M $LiClO_4$
k_f /ns	0.008	0.6517	0.7809

	P5C		
System	Pure acetonitrile	Acetonitrile +0.5M $NaClO_4$	Acetonitrile +0.5M $LiClO_4$
k_f /ns	0.51	12.1654	7.7260
System	Pure ethyl acetate	Ethyl acetate +0.5M $NaClO_4$	Ethyl acetate +0.5M $LiClO_4$
k_f /ns	0.15	12.6463	13.8097

Appendix C

Charge transfer reaction in (0.33Choline chloride+ 0.67Urea) deep eutectics:

Absorbance and emission spectra of P4C were collected in [0.33 Choline chloride+ 0.67 Urea] at five different temperatures (shown in Figure C1). Corresponding spectra for P5C is given in the lower panel of the same figure. It may be noted that for both the systems, LE and CT bands show red shift with increasing temperature along with the concomitant increase in intensity of the CT band. The change in frequency and FWHM (for absorption and LE, CT emission spectra) obtained at each temperature is shown in Figure C2. With increase in temperature, red shift is noticed in ν_{abs} accompanied by spectral narrowing. ν_{CT} and ν_{LE} also shows a red shift with increasing temperature. The trends in changing ν_{abs} and ν_{CT} indicate that increasing temperature leads to emission from a more polar environment in comparison to lower temperature. Here, we may also connect with the change in ν_{em} of the non-reactive probe C153 which showed a considerable red shift on increasing temperature discussed in Chapter 6.

Figure C1

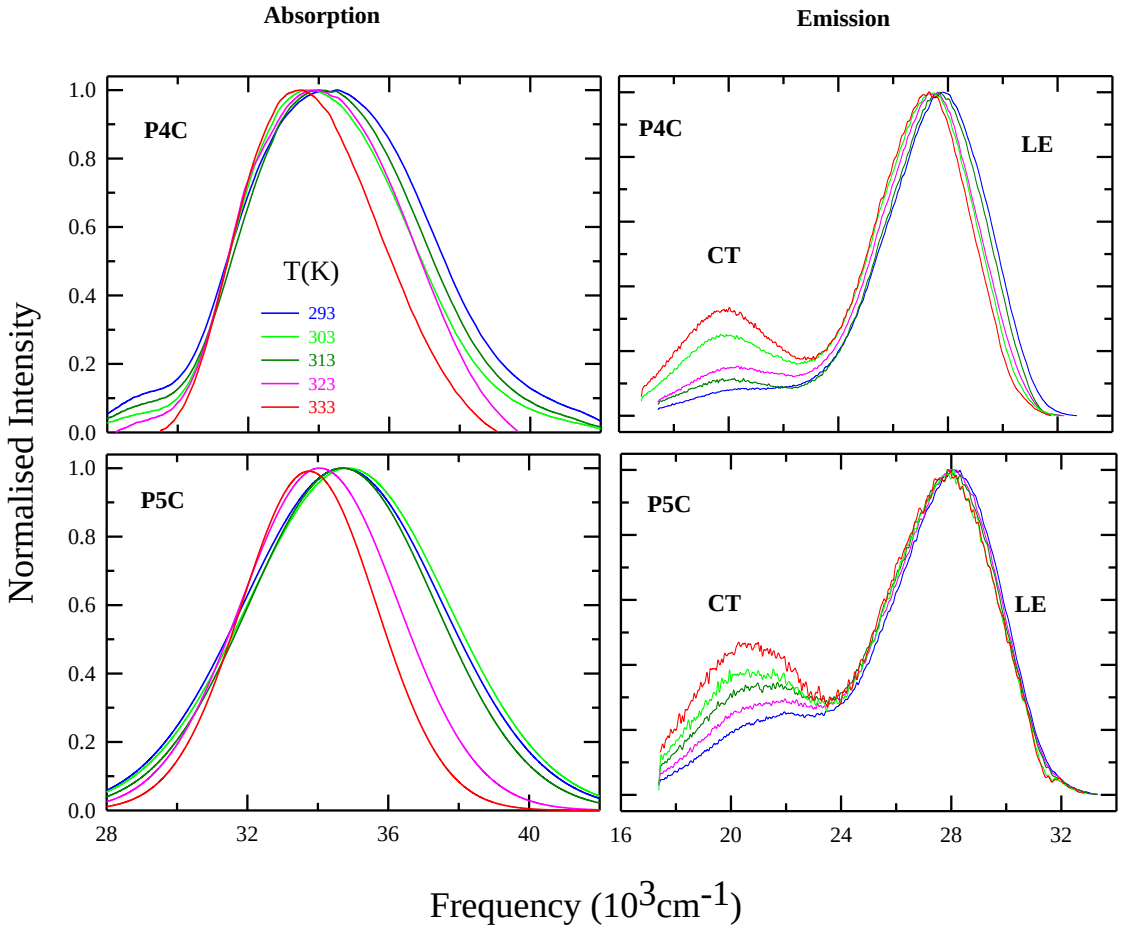

Figure C1: Absorption and emission spectra of P4C (upper panel) and P5C (lower panel) in [*f* Choline chloride**+** (1-*f*) Urea] for *f* =0.33.

Figure C2

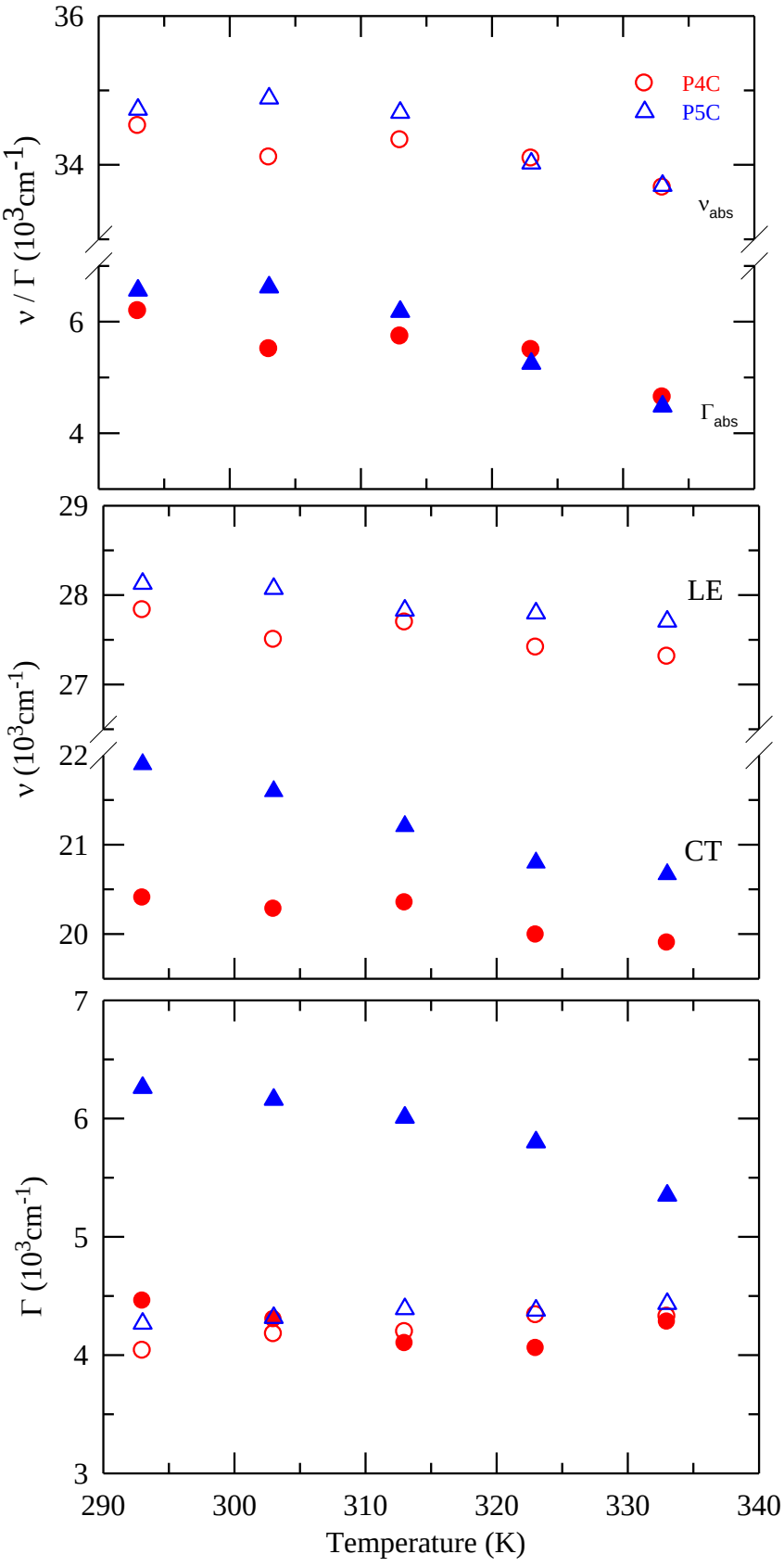
P4C
P5C
ν / Γ (10³cm⁻¹)
ν_abs
Γ_abs
LE
CT
ν (10³cm⁻¹)
Γ (10³cm⁻¹)
Temperature (K)

Figure C2: Temperature dependence of absorption (ν_{abs}) and emission (ν_{LE}, ν_{CT}) peak frequencies and line widths (full width at half-maxima) of the absorption spectra (Γ_{abs}) and LE(Γ_{LE}) and CT(Γ_{CT}) bands of P4C and P5C in [*f* Choline chloride**+** (1-*f*) Urea] at *f*= 0.33. The circles represent the solute P4C, and the triangles are P5C. Filled symbols denote CT and empty symbols denote LE. The uncertainty in frequencies and widths is ($\pm$ 300 cm^{-1}).

Next in Figure C3 we present the ratio of areas under the CT and LE band of the emission envelope denoted by α_{CT}/α_{LE}. For P4C as well as P5C, there is an overall increase in α_{CT}/α_{LE} with rise in temperature. This is evident from emission spectra of P4C and P5C (Figure C1). The increase of α_{CT}/α_{LE} means that the formation of CT state is largely preferred at elevated temperatures. The difference in preference for CT state for the two different molecules is reflected here via higher values of α_{CT}/α_{LE} for P5C.

The equation below (eq. C6) shows the relation between the area under the curves and equilibrium constant (K_{eq}) of the reaction (See scheme 3 of Chapter 6), which gives us the change in free energy (ΔG_r) associated with the $LE \rightarrow CT$ reaction.[1]

$$\Delta G_r = -RT \ln K_{eq} = -RT \ln[\alpha_{CT}\nu_{LE}^3 / \alpha_{LE}\nu_{CT}^3] \qquad \text{(C6)}$$

We have plotted ΔG_r for the $LE \rightarrow CT$ reaction associated with respective molecules against temperature in lower panel of Figure C3. The corresponding calculated properties are summarised in Table C4. The behaviour of ΔG_r is guided by α_{CT}/α_{LE}. For P4C, the conversion of $LE \rightarrow CT$ is slightly favourable only at very

high temperatures. Also, for P5C, the transformation is favourable at higher temperature range. K_{eq} of $LE \rightarrow CT$ conversion for P4C at 333K is about five times than K_{eq} at 293K whereas it is double in case of P5C. k_f (forward reaction rate for $LE \rightarrow CT$) is also tabulated in Table C4.

Figure C3

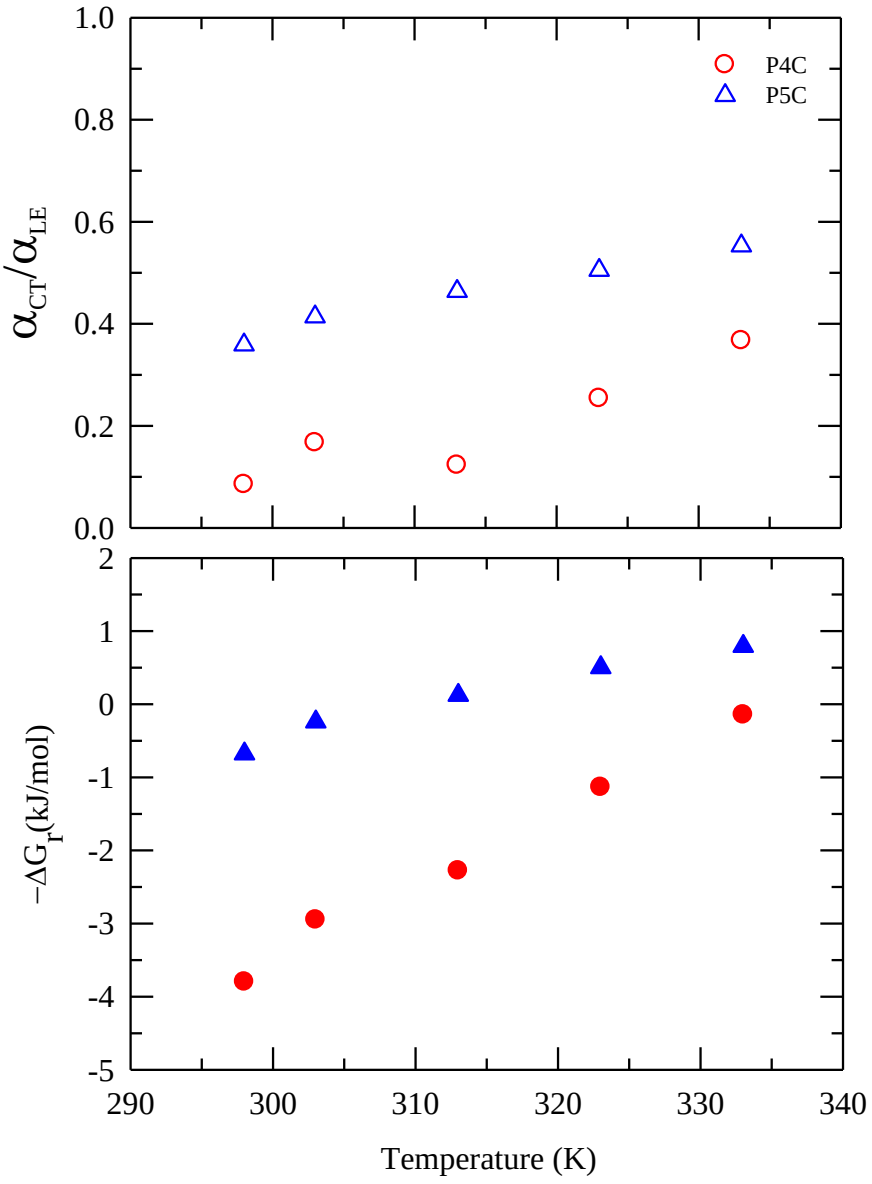

Figure C3: Temperature dependence of formation of CT population in [*f* Choline chloride**+**(1-*f*) Urea] at *f*= 0.33. The ratio between areas under the CT and LE bands (α_{CT}/α_{LE}) are shown in the upper panel. Circles denotes ratio for P4C and triangles represent data for P5C.

The uncertainty for CT band area is typically within (10%).

The lower panel depicts the change in reaction free energy ($-\Delta G_r$) for $LE \rightarrow CT$ conversion for P4C and P5C in [*f* Choline chloride**+** (1-*f*) Urea] at *f*= 0.33.

$-\Delta G_r$ is obtained from the area ratio (shown in upper panel) by eq (C6).

Table C4. Summary of LE-CT reactions for P4C/P5C reactions in [*f* Choline chloride+ (1-*f*) Urea] at f_{CC}=0.33 from at different temperatures.

k_f , K_{eq} and $-\Delta G_r$ are described in text and ref.1.

	P4C		
Temp (K)	k_f /10^{10}s^{-1}	K_{eq}	$-\Delta G_r$ kJ/mol
293	0.208	0.216	-3.80
303	0.318	0.310	-2.95
313	0.434	0.417	-2.28
323	0.544	0.655	-1.14
333	0.873	0.949	-0.15

	P5C		
Temp (K)	k_f /10^{10}s^{-1}	K_{eq}	$-\Delta G_r$ kJ/mol
293	0.466	0.761	-0.68
303	0.416	0.909	-0.24
313	0.427	1.049	0.12
323	0.547	1.205	0.50
333	0.497	1.331844	0.79

Reference

1. Dahl, K.; Biswas, R.; Ito, N.; Maroncelli, M. *J. Phys. Chem. B* **2005**, *109*, 1563.